João Pedro Maurício Rosa
Licenciado

Nanobiophotonics for biomolecular diagnostics

Dissertação para obtenção do Grau de Doutor em Biotecnologia

Orientador: Doutor Pedro Viana Baptista,
Professor Associado com Agregação, FCT/UNL
Co-orientador: Doutor João Carlos Lima,
Professor Associado, FCT/UNL

June 2013

A meus pais

To my parents

ACKNOWLEDGMENTS

The work here presented would not be possible without the support of so many people and institutions that I fear I will forget someone. All the expression of gratitude may not be enough to show the full extent of my thankfulness for all the support throughout the good and bad moments of this journey. However, my most special thanks must be addressed to:

- My PhD advisors, Professors Pedro Baptista and João Carlos Lima, for supporting and putting up with me, for their guidance, advisory and the academic and scientific growth they promoted in me during these years. Thank you for the opportunity of joining the great adventure that was this crazy project. I thank you both for the support, discussions, criticism and dedication to the cause. Most of all, Thank you for believing in me.
I would like to thank Pedro for the constant support and insightful discussions that far exceeded science. Without your pragmatism and vision none of this would have been possible. It is commonly said that "you are who you spend more time with" and I must thank you for who I am now. You have been an example and a beacon in many things. You pushed me and demanded the best of me. You've placed your trust in me and I can only hope not to have let you down. Thank you.
I would like to thank João Carlos for the enthusiastic discussions in science and the lessons in life. For allowing me to grow on my terms and for fuelling the dreams that were essential for this project. I will not forget the opportunities you provided me with and the belief in my competences that you dared to show when I would not. Thank you.

- Fundação para a Ciência e Tecnologia, for the financial support (SFRH/BD/43320/2008) provided to conduct this thesis and to attend national and international scientific meetings.

- The Departament of Chemistry for hosting the doctoral program and the Department of Life Sciences for housing me during these 4 four years. My thanks to all their members as well, for all the support given throughout these years and for providing the conditions to achieve my research goals.

- To João Conde for all the invaluable help with the work in the biosensors. For all the cooperation and endless discussions that lead to numerous breakthroughs and results. I cannot thank you enough for believing it was worth it.

- To Ana, Claudia Fernandes, Claudia Correia, Mara and Sheetal for the work (hands on) that allowed me to explore several avenues simultaneously without losing focus. I can only hope that you enjoyed working with me as I have enjoyed working with you.

"Life is partly what we make it, and partly what it is made by the friends we choose."

Chinese proverb

- À Ana, Carina, Carlota, Carolina, Conde, Crossfire, Fábio, Letícia, Maria, Milton, Revolt e Veigas por terem sido os pilares da minha sanidade e os amigos que eu precisei e tenho a sorte de ter; e ao Artur, Ana Filipa, Ana Marta, Ana Sofia, Carla, César, Equipa, Prof. Folgosa, Inês Gomes, Inês Osório, Isabel, João Avó, Lia, Márcia, Marco, Mário, Marta, Madalena, Margarida, Pedrosa, Quaresma, Renato, Rita e Zé por todos os momentos passados juntos e que fizeram da FCT a minha segunda casa ao longo destes anos.

Ao AVP, Gonçalo, Large, Red e Santo pelas noitadas no laboratório, pelas idas ao fórum e à montra, pela paródia, pelas ideias, pela loucura, pela alegria, pelas futeboladas, pronto! Pelo infinito companheirismo e amizade.

"In the fear and alarm

You did not desert me

My brothers in arms"

Brothers in Arms, Dire Straits

- Ao Large, porque só tu é que sabes.

- A todos os meus amigos. BCMicos: Brunol, Nico, Cati, Sol, Lara, Rols, Hélio, Pips, Luísa, Ropio, Mimi, Andreia. Torrejanos: Carreira, André, Dani, CD, Careca, Ritinha, Lili, Bruno, Ché, Pilas, Sofia, Pedro, Cuba. E aos mais antigos: Filipe, Mafalda, Pedro, Rui José e Rui Pedro. Pela amizade que nem o tempo nem a distância conseguem abalar. Eu não esqueço. Obrigado.

- À Rita pelos anos que me aturou e me apoiou. Pelo que passámos juntos de bom e de mau que nunca vou esquecer. Pelo Thor. Por toda a capacidade de animar e de me suportar quando eu mais precisei. Por toda a dedicação que incondicionalmente mostrou e que eu nem sempre soube retribuir ou reconhecer. Muito Obrigado. Mesmo.

- Às pessoas que me moldaram e marcaram como pessoa profissional, aos meus Professores Margarida e Carlos, Maria Amélia Maia, Fernanda Franco, Felisbela Falcão, Teresa Sirgado, Carlos Silva, Carlos Lopes, Teresa Moura, Nuno Neves e Wanda Viegas.

- À minha família, em particular aos meus avós, os faróis da minha vida e as luzes dos meus olhos. Ao Pedro, meu primo, meu irmão, meu exemplo! À Nenê pela mulher de fogo, as cartadas incompletas e a Ana João. Ao Totó e à Bela por serem mais que tios. Aos meus padrinhos pelo carinho incondicional. E quero deixar um agradecimento muito especial aos meus pais que sempre estiveram nos bastidores a torcer por mim, a apoiar incondicionalmente, a guiar-me. Por tudo o que passaram comigo e por mim. Um muito obrigado. Sem vocês, eu não seria nada.

- To anyone I may have missed in the list above. You may be away from my head at the moment but are surely in my heart! Thank you!

João "Bixo" Rosa

RESUMO

O principal objectivo desta tese foi estudar a modulação de fluorescência induzida por nanopartículas de ouro (AuNPs) em fluoróforos próximos e/ou ligados à sua superfície através de moléculas de ácidos nucleicos. A compreensão do efeito da distância nas propriedades espectrais dos fluoróforos permitiria desenvolver um biossensor para caracterização de sequências de DNA e/ou RNA.

Para estudar os efeitos fotofísicos envolvidos na modulação de fluorescência por AuNPs foi necessário desenvolver uma abordagem experimental que removesse o efeito da interferência óptica causada pela presença de AuNPs. Ao comparar as amostras com soluções referência controladas foi possível determinar o rendimento quântico de fluorescência e o tempo de decaimento de fluorescência de fluoróforos na vizinhança de AuNPs. Durante esta caracterização foram desvendados vários fenómenos não-fotofísicos relacionados com AuNPs, como o efeito do pH local à superfície da AuNP, o acoplamento do oscilador da plasmónica com o momento de transição do fluoróforo ou a agregação de fluoróforos induzido por AuNPs.

O método experimental desenvolvido foi aplicado ao estudo do efeito da distância na modulação de fluorescência induzida por AuNPs. Usando moléculas de DNA como espaçadores, as propriedades fotofísicas de fluoróforos a diferentes distâncias da superfície de AuNPs mostrou uma dependência com a distância correspondente a $1/r^6$.

O conhecimento adquirido sobre sistemas AuNP-DNA-fluoróforo permitiu o desenvolvimento de biossensores optimizados para a detecção semi-quantitativa de RNA. Partindo desse potencial quantitativo, foi possível desenvolver um sistema de controlo e quantificação simultânea de síntese de RNA *in vitro*. A detecção e silenciamento génico *in situ* foi demonstrada em mRNA de EGFP como prova de conceito. Uma estratégia semelhante foi utilizada com sucesso na detecção de siRNA e miRNA endógeno. A aplicação deste sistema à análise de microdelecções e isoformas de RNA foi demonstrada em alvos sintéticos.

PALAVRAS-CHAVE: Fluorescência, Nanodiagnóstico, Nanopartículas, Ouro

ABSTRACT

The main objective of this thesis was to study the fluorescence modulation induced by gold nanoparticles (AuNPs) on fluorophores nearby and/or bonded to the AuNPs' surface through nuclei acid molecules. The understanding of the effect of distance in the spectral properties of fluorophores would allow the development of a biosensor for the characterisation of DNA and/or RNA sequences.

To study the photophysics involved in the fluorescence modulation by AuNPs it was necessary to develop an experimental approach that removed the effect of the optical interference caused by the presence of AuNPs. By comparing the samples with controlled reference solutions it was possible determine the fluorescence quantum yield and fluorescence decay time of the fluorophores in the vicinity of AuNPs. During the characterisation several non-photophysical phenomena involving nanoparticles were unveiled, such as a local pH effect, coupling of the plasmonic oscillator with transition moments of the fluorophore or AuNP-induced fluorophore aggregation.

The developed experimental method was applied to the study of the effect of distance in the modulation of fluorescence caused by AuNPs. Using DNA molecules as spacer, the photophysical properties of fluorophores at different distances of the surface of the AuNPs showed a distance-dependence fitting into a $1/r^6$ dependence.

The knowledge gathered on AuNP-DNA-fluorophore systems allowed for a successful semi-quantitative detection of RNA in solution. The same system showed to be useful for the simultaneous quantification and control RNA synthesis *in vitro*. *In situ* detection and gene silencing was demonstrated by targeting EGFP mRNA as proof-of-concept. A similar approach was successfully achieved in siRNA and endogenous miRNA targets. The application of this system to micro-deletions and RNA isoforms analysis was also demonstrated in synthetic targets.

KEYWORDS: Fluorescence, Gold, Nanodiagnostics, Nanoparticles

SYMBOLS AND NOTATIONS

A – Absorbance

Au-nanobeacon – AuNPs functionalised with hairpin-ssDNA

Au-nanoprobe – AuNPs functionalised with ssDNA

AuNPs – Gold Nanoparticles

b – Absorption path length

C – Concentration

cDNA – complementary DNA (DNA synthesized from mRNA template)

CW – Continuous Wave

DEPC – Diethylpyrocarbonate

DLS – Dynamic Light Scattering

DNA – Deoxyribonucleic Acid

dNTPs – Deoxyribonucleotide Triphosphate

dsDNA – double-stranded DNA

DTNB – 5,5'-dithio-bis(2-nitrobenzoic) acid

DTT – DL-Dithiothreitol

E - Efficiency of energy transfer

EGFP – Enhanced Green Fluorescent Protein

F(λ) – corrected fluorescence intensity in the wavelength range with the total intensity (area under the curve) normalized to the unity

fluorophore@AuNPs – Fluorophore interacting with/functionalized on the AuNP surface

FRET – Förster's or fluorescence resonance energy transfer

GST – Glutathione

h – Plank's constant

I – Fluorescence intensity

I^0_λ - Light intensity of the beams entering a solution

I_λ - Light intensity of the beams leaving a solution

J(λ) – spectral overlap between the donor emission and acceptor absorption spectra

K – Total decay constant

k^2 – Dipole orientator factor

k_{nr} – Non-radiative constant

k_r – Radiative constant

k_T - Rate of energy transfer

LASER – Light Amplification by Stimulated Emission of Radiation

LSPR – Localised Surface Plasmon Resonance

mRNA – Messenger RNA

miRNA – MicroRNA

MTT – 3-(4,5-dimethylthiazol-2-yl)-2,5-diphenyltetrazoliumbromide

n – Refractive index

n(t) – Number of excited molecules at time t following excitation

N_A – Avogadro's number

(N)SET – (Nano)-Surface Energy Transfer

NTP – Ribonucleotide Triphosphate

PBS – Phosphate Buffer Saline

PCR – Polymerase Chain Reaction

PEG – Poly(ethylene glycol)

PM – Photomultiplier

r – Distance from the fluorophore to the nanoparticle or the donor and the acceptor

R_0 – Förster distance

RhB – Rhodamine B

Rh101 – Rhodamine 101

RNA – Ribonucleic Acid

RT-PCR – Reverse Transcription Polymerase Chain Reaction

SDS – Sodium Dodecyl Sulfate

SERS – Surface-Enhanced Raman Scattering

siRNA – Small interfering RNA

SNPs - Single-Nucleotide Polymorphisms

ssDNA – Single-stranded DNA

ssRNA – single-stranded RNA

t – Time

T – Transmittance

TAC – Time-to-amplitude converter

TAE – Tris-Acetate EDTA buffer

TCSPC – Time-correlated single photon counting

TEM – Transmission Electron Microscopy

(WT1)+KTS – *WT1* gene with the isoform containing Lysine-Threonine-Serine

(WT1)-KTS - *WT1* gene with the isoform without Lysine-Threonine-Serine

ε – molar absorptivity coefficient

λ – Wavelength

ν – Light frequency

σ – Molecular absorption cross-section

τ – Fluorescence lifetime

Φ_F - Fluorescence quantum yield

TABLE OF CONTENTS

FIGURES INDEX

TABLES INDEX

CHAPTER 1. General Introduction

Publications associated with this chapter:

Doria G, Conde J, Veigas B, Giestas L, Almeida C, Assunção M, Rosa J, Baptista PV (2012) Noble Metal Nanoparticles for Biosensing Applications. *Sensors*, **12**:1657-1687

Conde J, Rosa J, Lima JC, Baptista PV (2012) Nanophotonics for Molecular Diagnostics and Therapy Applications. *International Journal of Photoenergy*, Article ID 619530

1.1. Background

This first segment of this thesis is intended to provide a clearer perspective on the subject in study. Before presenting the scientific background desirable for a better understanding of the work that follows, I feel it is important to provide a background of its genesis. Hopefully, this will situate the reader as to what were the motivations of the work and explain why the work in this thesis is directed to the optical properties of gold nanoparticles, fluorescence and biosensors rather than any of the numerous other potential topics in the field of nanobiophotonics.

The idea of using the modulation of fluorescence by gold nanoparticles and apply it to diagnostics and biosensing was born from an experimental setback. When I joined the laboratory, the use of gold nanoparticles for diagnostics was already a proficient topic there. The colorimetric properties of gold nanoparticles were already being used for the detection of specific DNA sequences. Simply put, DNA functionalised on gold nanoparticles would hybridise to a specific sequence that, when present, would increase the tolerance of the modified gold nanoparticles to salt-induced colour-changing aggregation. At an optimised ionic force the presence of the target sequence prevents the aggregation that occurs in its absence. Aggregation is followed by a change in the colour of the solution from red to blue.

In 2008, the colorimetric method was still being characterised and one of the main issues revolved around the identification of single nucleotide polymorphisms. This method relies on the efficiency of hybridisation between the probe and the target. When no similar sequences are in solution no hybridisation is possible and the difference between signals is clear. But the identification of sequences that differ only by one base relies on a much thinner hybridisation balance. To understand this balance it is extremely important to assess how many strands are hybridising with the probes in each case. To do this, fluorescently labelled oligonucleotides were being used and its fluorescence in solution was measured after washing. The results were arbitrary. The measurements appeared random and results had no realistic meaning, *i.e.*, more hybridized strands than probe strands, negative amounts of hybridized strands. There was obviously something happening that was not accounted for.

A clearer insight of the literature would be necessary. After a first glimpse, it was interesting to note that the randomness of the results was spread throughout literature. The available information on the effects of metal nanoparticles in fluorescence was not coherent and was even contradictory in some cases. For example, some authors defended a quenching of fluorescence while others presented enhancement.

Within this chaos something was clear: whether quenching or enhancement occurs, metal nanoparticles were modulating fluorescence. Moreover, the conditions in which the experiments were experimentally set up should influence the results. For example, the distance at which the fluorescent

molecules were from the nanoparticle was discussed as relevant to the modulation as well as the size and composition of the nanoparticles.

Further digging into the literature of metal-modulated fluorescence generated even more questions. Can fluorescence be controlled with nanoparticles? What leads to these apparently contradictory results? Can the randomness of results be controlled? Can this distance-dependence effect be used as a ruler? Is it possible to create a gold nanoparticle-fluorescence biosensor?

After meeting with my supervisors, I decided to answer these questions and enter this adventure with their guidance. The answer to these questions would not be quickly or easily answered and it would be a good but difficult challenge (especially for a biologist) that we thought to have little chance of success.

1.2. Nanotechnology, nanobiotechnology and nanobiophotonics

Nanotechnology can be described as the study and control of matter on a nanometre scale. Richard Feynman is considered to be the father of nanotechnology in his famous talk "There's plenty of room at the bottom" at an American Physical Society meeting at Caltech on December 29th, 1959 [1]. However, in the 1850's Michael Faraday had already described the relation between colour and small size of the colloidal particles [2]. Since the 1990's nanotechnology has boomed in terms of publications [3] by revealing the development of new materials and devices with a wide-range of applications, such as electronics, mechanics, medicine, etc. There are two main approaches for preparing nanostructures: top-down and bottom-up approaches. The top-down approach uses eroding procedures such as LASER ablation and lithography to remove and/or shape portions of larger materials. The bottom-up strategy builds the nanoparticle from molecular components, for example chemical synthesis and self-assembly.

Nanosized materials present different properties from the ones observed at the macroscale. These materials have subwavelength sizes in the ultraviolet, visible and infrared region of the light spectrum. Because of this, the interaction of nanomaterials with light is different from the one observed for bulk materials. The study of this issue is usually included in the Nanophotonics field. Nanophotonics-based devices have revolutionized technology and potentiated the development of technologies such as near-field scanning optical microscopy, photoassisted scanning tunnelling microscopy and surface plasmon optics. Nanophotonics can be defined as the science that deals with light-matter interactions at a nanometre scale, providing challenges for fundamental research and opportunities for new technology [4]. Nanophotonics has emerged with the study of new optical interactions, materials, fabrication techniques, and architectures, including the exploration of natural and synthetic structures such as photonic crystals, holey fibres, quantum dots, sub-wavelength structures and plasmonics [5,6].

Another interesting application of nanotechnology was found in biology/biotechnology creating a new field of research referred to as Nanobiotechnology. It can be considered a field that not only concerns the utilization of biological systems to produce functional nanostructures but also concerns the development and application of instruments, originally designed to generate and manipulate nanostructured materials to study fundamental biological processes and structures. Molecular diagnostics is one of the main areas that can benefit from nanobiotechnology, where the unique properties of nanomaterials and nanostructures can give rise to new techniques and methods for better diagnostics [7-9].

The cross-section between nanophotonics and nanobiotechnology creates a very specific field called nanobiophotonics that connects the application of optical properties of nanostructures and its light interacting properties with biology, biotechnology and medicine – Figure 1.1. In fact, the application of this specific field to medicine is a rapidly emerging and potentially powerful approach for disease protection, detection and treatment. The study of the underlying phenomena in nanosurface interaction mediated by biomolecules may provide insights to the development of new detection strategies able to lessen some of the current constraints in biodetection. This nanobiophotonics approach may potentiate the detection capability of biomolecules. The possibilities of this approach are almost unlimited given that minute changes to nanoparticles' size and composition, labelling molecules or fluorophores' properties allow for fine tuning of spectral interaction that can be used for biomolecule detection.

The aim of this thesis is to understand the phenomena involved in nanosurface interaction between gold nanoparticles and fluorophores mediated by biomolecules and explore its potential as sensitive and robust biomolecular sensors.

1.3. Interaction between light and matter

Knowledge of the physical world is based on the interactions between light and matter. This dual behaviour demands the capacity to transfer energy between light and matter. This is achieved by two basic principles, the absorption of light by matter and the capacity of matter to retransform this energy back into light or to other forms of energy.

1.3.1. Light absorption

The first basic principle is normally called absorption and is achieved when a photon of a determined wavelength is absorbed by a molecule. Molecularly, this corresponds to an electronic transition which consists of the promotion of an electron from an orbital of a molecule in the ground state to an unoccupied orbital. The molecule is then said to be in an excited state [10].

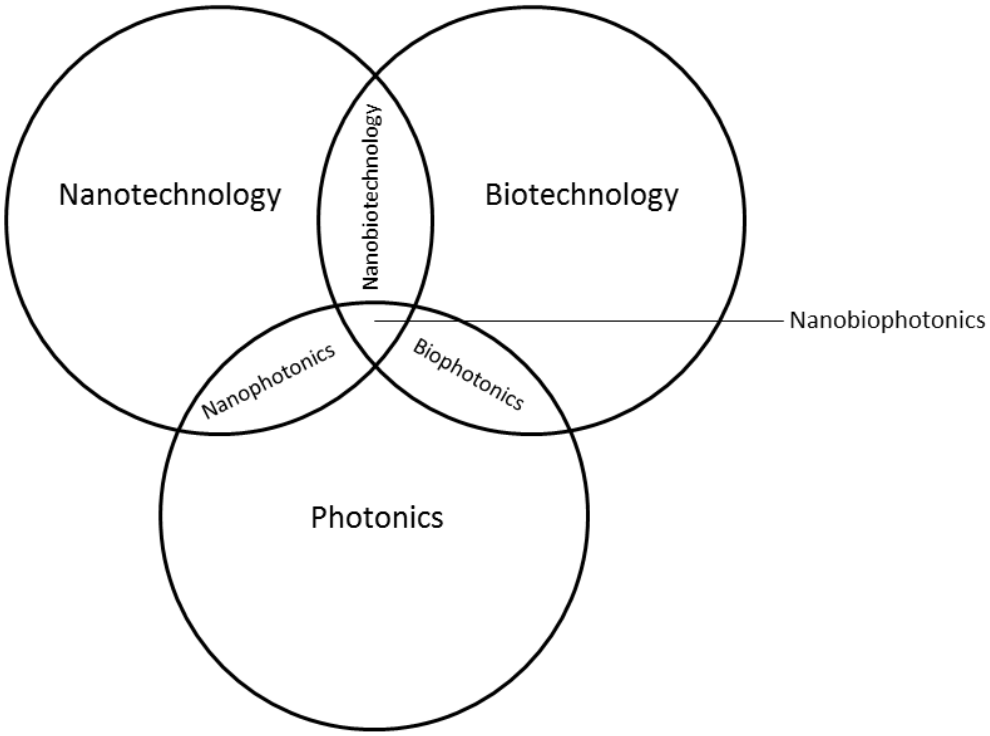

Figure 1.1. Emergence of Nanobiophotonics. Schematic representation of how interacting fields of science lead to Nanobiophotonics.

An electronic transition will only occur if the molecule is irradiated with light with energy corresponding to the energy gap between both states. The energies of the orbitals involved in electronic transitions have fixed values, and as energy is quantised, it would be expected that absorption peaks in spectroscopy should be sharp peaks. However, this is only rarely observed. Instead, broad absorption peaks are seen. The cause for this lies on a number of vibrational energy levels that are available at each electronic energy level, and transitions can occur to and from different vibrational levels as illustrated in Figure 1.2. The situation is further complicated by the fact that different rotational energy levels are also available to absorbing materials (omitted from Figure 1.2.).

Experimentally, the efficiency of light absorption at a specific wavelength (λ) by an absorbing medium is characterized by the absorbance (A) or the transmittance (T), defined as:

$$A(\lambda) = \log \frac{I_\lambda^0}{I_\lambda} \quad \text{(Equaion 1.1)} \quad \text{and} \quad T(\lambda) = \frac{I_\lambda}{I_\lambda^0} \quad \text{(Equation 1.2)}$$

where I^0_λ and I_λ are the light intensities of the beams entering and leaving the absorbing medium, respectively. In many cases, the absorbance of a sample follows the Beer–Lambert Law:

$$A(\lambda) = \log \frac{I_\lambda^0}{I^0} = bC\varepsilon(\lambda) \quad \text{(Equation 1.3)}$$

where ε(λ) is the molar absorptivity coefficient (commonly expressed in $M^{-1}.cm^{-1}$), C is the concentration (in M or $mol.dm^{-3}$) of absorbing species and b is the absorption path length (in cm) [10-13]. Failure to obey the linear dependence of the absorbance on concentration, according to the Beer–Lambert Law, may be due to aggregate formation at high concentrations or to the presence of other absorbing species. Various terms for characterizing light absorption can be found in the literature [10].

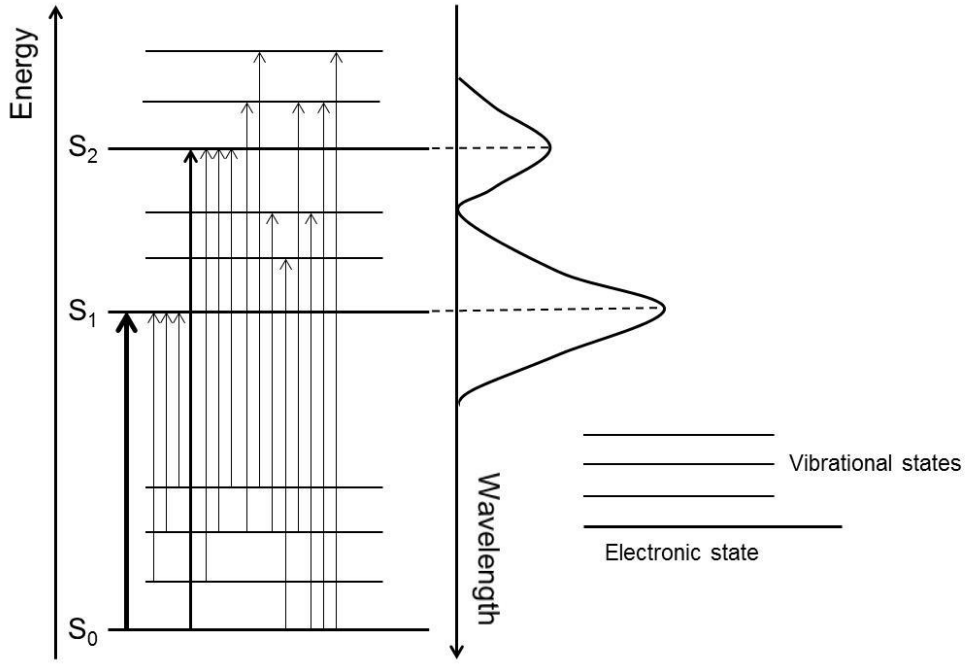

Figure 1.2. Electronic transitions during absorption. Horizontal lines represent electronic states: larger lines represent the fundamental electronic states (S_0, S_1 and S_2) while thinner lines represent vibrational states. Rotational states are omitted. Vertical lines represent the transition of electrons and arrows show the final state of each transition. The right part of the figure represents the correlation of the transitions with its absorption spectrum. Adapted from SpringerImages.

The molar absorption coefficient expresses the ability of a molecule to absorb light in a given solvent. The term molar absorptivity coefficient should be used instead of molar extinction coefficient in most occasions. The molar absorptivity is related to the molecular absorption cross-section (σ) which characterizes the photon-capture area of a molecule. It can be calculated as the molar absorptivity coefficient divided by the Avogadro's number N_A of molecular entities contained in a unit volume of the absorbing medium along the light path:

$$\sigma = \frac{2.303\varepsilon}{N_A} \qquad \text{(Equation 1.4)}$$

In the classical theory, absorption of light can be described by considering the molecule as an oscillating dipole, which introduces an entity called the oscillator strength that is directly related to the

integral of the absorption band. In the quantum mechanical approach, a transition moment is presented in order to characterise the transition between an initial state and a final state. The transition moment represents the transient dipole resulting from the displacement of charges during the transition [10-13].

The use of the Beer–Lambert law deserves further attention. In practical terms, the sample is a cuvette containing a solution. The absorbance must be characteristic of the absorbing species only. Therefore, it is important to note that in the Beer–Lambert Law, the intensity of the beam entering the solution is not the intensity of the incident beam on the cuvette, and that the intensity of the beam leaving the solution is not the intensity of the beam leaving the cuvette. There usually are contributions from reflection and scattering on the cuvette walls and these walls may also absorb light. Moreover, the solvent is assumed to have no contribution, but it may also be partially responsible for a decrease in intensity because of scattering and possible absorption. The contributions of the cuvette walls and the solvent can be taken into account [10,14] by setting an appropriate reference.

1.3.2. Fluorescence

How a molecule decays from an electronic excited state back to ground state is dependent on the situation. One possible pathway is that the decay of the excited state occurs with concomitant emission of a photon. Luminescence is the emission of light from any substance. Luminescence is formally divided into two categories, fluorescence and phosphorescence. The difference between these two categories lies on the nature of the initial and final states. In fluorescence, the excited state and the ground state have the same spin multiplicity and the return to the ground-state is an allowed transition which produces a rapid emission of a photon. In phosphorescence, the spin multiplicity of the excited state and the ground state are different and the return to the ground-state is a forbidden transition which produces slow-rated emission of photon [10,11,14,15].

There are also various non-emissive pathways, such as: dissipation of energy through heat via interactions with the solvent or vibrational or rotational changes; and interactions with second molecules leading to fluorescence quenching or energy transfer. Excited organic molecules can also relax via conversion to a triplet state and follow a secondary non-radiative relaxation step [14].

The processes of absorption to an excited state and relaxation back to the ground state are usually illustrated by the Jablonski diagram. Jablonski diagrams are used in a variety of forms, to illustrate various processes that can occur in excited states. A simplified Jablonski diagram is shown in Figure 1.3. This Jablonski diagram excludes a number of interactions such as quenching, energy transfer and solvent interactions.

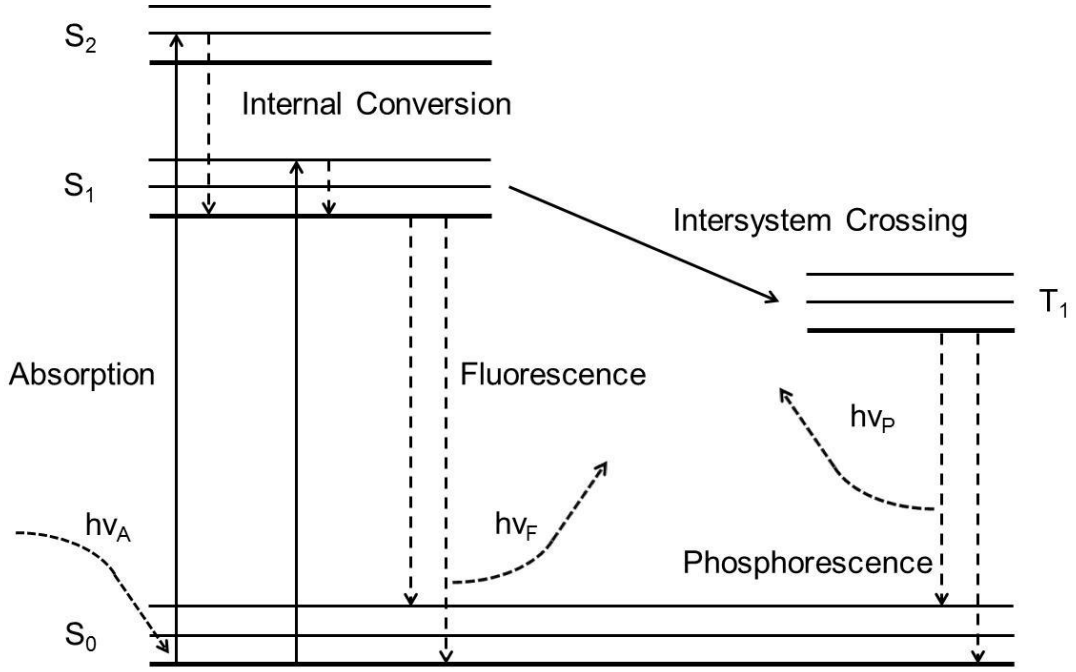

Figure 1.3. Simplified Jablonski diagram. Vertical lines represent electronic transitions and the arrows point the direction of the transition: full lines represent absorption and dashed lines represent luminescence and internal conversion. An electron in the fundamental state can be excited by incident light ($h\nu_A$) which leads to an electronic transition to an excited state. In the excited state this electron will suffer internal conversion and consequently decay to the fundamental state. This electronic transition to the fundamental state can occur non-radiatively or through luminescence: fluorescence ($h\nu_F$) if the electron remains in singlet state or phosphorence ($h\nu_P$) if a change in spin occurs.

The transitions between the ground state and the excited state are represented as vertical lines and show the instantaneous nature of light absorption. Transitions occur in the femtosecond time scale which, in most cases, represents a timescale too short for significant displacement of nucleus of an atom - Franck-Condon principle. Another general property of fluorescence is that the same fluorescence emission spectrum is generally observed irrespective of the excitation wavelength. This is known as Kasha's rule [16], even though Vavilov had previously reported (in 1926) that quantum yields were generally independent of excitation wavelength [17]. Upon excitation into higher electronic and vibrational levels, the excess energy is quickly dissipated, leaving the fluorophore in the lowest vibrational level of S1. This relaxation takes approximately 1 ps. Because of this rapid relaxation, emission spectra are usually independent of the excitation wavelength.

Analytically, the decay of an excited state to the ground state can be expressed as a decay rate. This rate is the sum of the rates associated to each pathway that the excited molecule can take. Therefore a radiative rate (k_r) can be established as the rate at which a molecule decays to the ground state with emission of a photon. Similarly, a rate for each non-radiative pathway also exists. For practical

purposes, in fluorescence studies, all the non-radiative pathways' constants are usually summed up in one single non-radiative constant (k_{nr}).

1.3.2.1. Steady-state and Time-resolved fluorescence

Fluorescence measurements can be broadly classified into two types of measurement: steady-state and time-resolved. Steady-state measurements, the most common type, are performed with constant illumination and observation. The sample is illuminated with a continuous beam of light, and the intensity or emission spectrum is recorded. Because of the nanosecond timescale of fluorescence, most measurements are steady-state measurements. When the sample is first exposed to light, steady state is reached almost immediately. The second type of measurement is time-resolved which is used for measuring intensity decays. For these measurements the sample is exposed to a pulse of light, where the pulse width is typically shorter than the decay time of the sample. The intensity decay is recorded with a high-speed detection system that permits the intensity to be measured on the nanosecond, picosecond and even femtosecond [18-20] timescale. It is important to understand the relationship between steady-state and time-resolved measurements. A steady-state observation is simply an average of the time-resolved phenomena over the intensity decay of the sample [10].

1.3.2.2. Fluorescence Quantum yields and Lifetimes

The fluorescence quantum yield (Φ_F) and lifetime (τ) are perhaps the most important characteristics of a fluorophore. The fluorescence quantum yield is the number of emitted photons relative to the number of absorbed photons. Substances with the largest quantum yields, approaching unity, such as rhodamine molecules, display the brightest emissions. The lifetime is also important as it represents the time available for the excited fluorophore to interact with other components of the system or diffuse in its environment.

The fluorescence quantum yield is the ratio of the number of photons emitted to the number absorbed. Both radiative and non-radiative pathways will depopulate the excited state and account to the amount of excited states formed (amount of absorbed light). The fraction of fluorophores that decay through emission, and hence the quantum yield, is given by:

$$\Phi_F = \frac{k_r}{K} = \frac{k_r}{k_r + k_{nr}} \qquad \text{(Equation 1.5)}$$

The quantum yield can be close to unity if the non-radiative decay is much smaller than the radiative decay, that is $k_{nr} < k_r$.

The lifetime of the excited state is defined by the average time the molecule spends in the excited state prior to return to the ground state. Logically, the smaller the excited-state lifetime the higher is the associated rate, hence:

$$\tau = \frac{1}{K} = \frac{1}{k_r + k_{nr}} \qquad \text{(Equation 1.6)}$$

Fluorescence emission is a random process, and few molecules emit their photons at precisely $t = \tau$. The lifetime is an average value of the time spent in the excited state which means that for an exponential decay 63% of the molecules have decayed prior to $t = \tau$ and 37% decay at $t > \tau$.

The quantum yield and lifetime of the molecules can be modified by factors that affect either of the rate constants (k_r or k_{nr}). Scintillators are generally chosen for their high quantum yields. These high yields are a result of large k_r values when compared to the k_{nr} [10,11,14].

1.3.2.3. Determination of fluorescence quantum yields

The fluorescence quantum yield is related to the efficiency of the fluorescence process. It is defined as the ratio between the number of emitted photons to the number of absorbed photons. The maximum fluorescence quantum yield is 1, which would mean that every absorbed photon results in an emitted photon. Hence, by definition the fluorescence quantum yield is:

$$\Phi_F = \frac{\text{n of emitted photons}}{\text{n o absorbed photons}} \qquad \text{(Equation 1.7)}$$

Although this expression is analytically less practical than Equation 1.7, experimentally, it is clearer in what is needed to determine the fluorescence quantum yield – a quantification of both absorbed and emitted photons. The determination of fluorescence quantum yields is usually associated with high errors due to several technical issues that can occur. For this reason, several methods were developed which can be divided into either absolute or relative methods [11].

Absolute quantum yield determination methods will present a result that is dependent on the technical conditions of its determination. Among the most popular are the integrated sphere method, calorimetric method and light scattering methods.

The integrated sphere method relies on an apparatus called integrated sphere that can be attached to a spectrofluorimeter. The integrated sphere is highly reflective which means that the light entering the sphere can only be either absorbed or collected by the detector. The number of absorbed photons is calculated by comparison of the signal obtained at the excitation wavelength in presence and absence of the sample while the number of emitted photons is a direct reading of the integrated area of the fluorescence spectrum of the sample [21].

Calorimetric methods rely on the changes observed in temperature or volume during irradiation. The basic principle of this approach is the comparison of the observed changes of a non-luminescent molecule and a fluorescent sample with comparable optical densities. The non-luminescent molecule will have a quantum yield of zero, and so, the ratio of the temperature variations in the two solutions provides the fraction of the absorbed energy which is lost non-radiatively in the fluorescent sample. This value is complementary to the fluorescence quantum yield [22].

Light scattering methods rely on molecules that behave as substances that reemit all the photons irradiated upon them without change in wavelength. These molecules are usually called ideal scatterers. Although no absorption or emission occurs, ideal scatterers behave as if they had a quantum yield of 1. The fluorescence quantum yield can then be determined by comparing a molecule's fluorescence with the intensity of light due to Rayleigh scattering from the ideal scatterer solutions with the fluorescence of the sample solutions at the same wavelength [23]. Correction factors have to be introduced in order to account for the different spatial distribution of light from the scattering and fluorescent solutions due to the polarized scattered light and unpolarized fluorescence [24].

Relative quantum yields determination methods are based on the assumption that if two molecules are studied in the same apparatus, absorb the same amount of light, the integrated areas under their corrected fluorescence spectra will be proportional to their fluorescence quantum yields. As such, the relation between quantum yields and fluorescence intensity of two molecules can be expressed as:

$$\frac{I_2}{I_1} = \frac{\Phi_{F2}}{\Phi_{F1}} \frac{A_2}{A_1} \qquad \text{(Equation 1.8)}$$

where Φ_F represents the quantum yields and A represents absorbance at the respective excitation wavelengths. One very important factor for a proper quantum yield calculation using this method is the choice of the adequate reference molecule. Reference molecules should present specific properties in order to be more adequate. The most important of the aspects to take into account are the emission properties of the molecule. The reference molecule should have a broad spectrum with no fine structure and have a high fluorescence quantum yield. Small overlap between absorption and emission spectra is also favourable as it reduces the possibility of self-absorption. The reference and the sample should present similar absorption spectra in order to facilitate the matching of the absorbance of both molecules. For all the presented reasons, it requires a series of suitable reference materials to cover the light spectrum in the visible region [11].

However simple or robust the methods for determination of a fluorescence quantum yield may appear, there are several factors that directly affect its determination. Inner filter effect and self-absorption can be observed at relatively high concentrations. The linear relationship between the concentration of a solute and its fluorescence intensity only applies in solutions of very low absorbance. At higher

concentrations, correction factors must be applied. Working in lower concentrations may also avoid self-absorption in cases where a significant overlap between the absorption and emission spectra exists. Refractive index issues may also rise when reference molecules and sample molecules present different solution optical geometry. The errors due to refractive index changes may exist when the radiation passes from a high to a lower refractive index or by internal reflection of emitted light within the cuvette at all interfaces between zones of different refractive indices. These errors are especially relevant if reference and sample are in different solvents [25]. Other factors such as temperature, polarization of light or photostability may also affect the fluorescence quantum yield determination [11].

1.3.2.4. Determination of fluorescence lifetimes

Prior to further discussion of lifetime measurements, it is important to take another look at the meaning of τ. Consider a sample containing the fluorophore that is excited with an infinitely sharp pulse of light. This excitation results in an initial population (n_0) of fluorophores in the excited state. The excited-state population decays with a rate $k_r + k_{nr}$ according to:

$$\frac{dn(t)}{dt} = (k_r + k_{nr})n(t) \qquad \text{(Equation 1.9)}$$

where n(t) is the number of excited molecules at time t following excitation. Emission is a random event, and each excited fluorophore has the same probability of emitting in a given period of time. This results in an exponential decay of the excited state population:

$$n(t) = n_0 e^{-\frac{t}{\tau}} \qquad \text{(Equation 1.10).}$$

What is observed in a fluorescence experiment is fluorescence intensity. In turn, this intensity is proportional to n(t) [10,13]. Hence, the equation above can also be written in terms of the time-dependent intensity I(t). Integration of Equation 1.10 with the intensity substituted for the number of molecules yields the usual expression for a single exponential decay:

$$I(t) = I_0 e^{-\frac{t}{\tau}} \qquad \text{(Equation 1.11)}$$

where I_0 is the intensity at time 0. The inverse of the lifetime is the sum of the rates which depopulate the excited state and so the fluorescence lifetime can be determined from the slope of a plot of log I(t) versus t, but more commonly by fitting the data to assumed decay models. The lifetime is the average amount of time a fluorophore remains in the excited state following excitation. A typical result is represented in Figure 1.4. This can be experimentally assessed by pulse fluorometry.

Pulse fluorometry is the most popular technique for the determination of fluorescence lifetimes (or decay parameters). Most instruments are based on the time-correlated single photon counting

(TCSPC) method. The basic principle of TCSPC is the probability of detecting a single photon at time t after an exciting pulse is proportional to the fluorescence intensity at that time. After timing and recording the single photons following a large number of exciting pulses, the fluorescence intensity decay curve can be reconstructed.

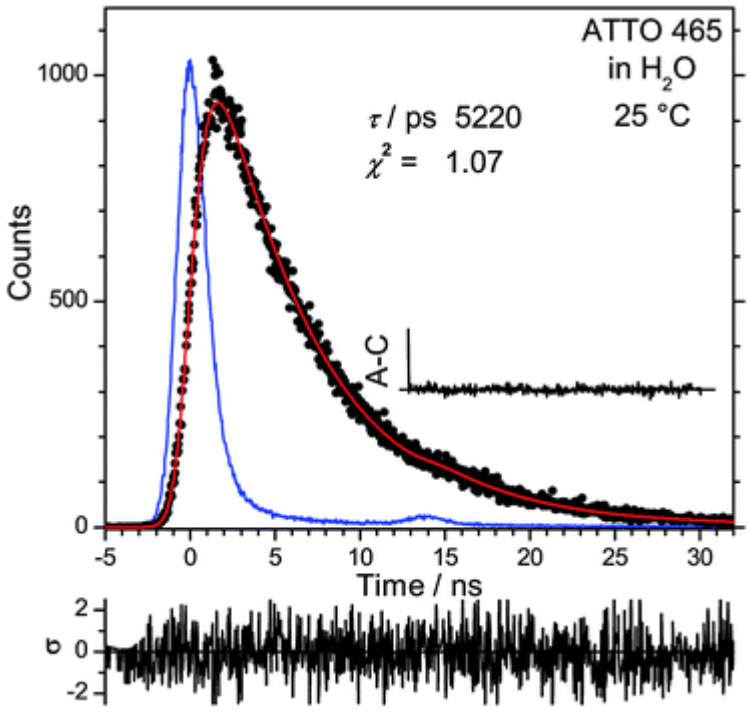

Figure 1.4. Example of a time-correlated single photon counting decay. Representative time-correlated single photon counting decay (black circles) for ATTO 465 in H2O at 25 ˚C (excitation at λ=297 nm, detection at λ=510 nm) [26]. Each circle represents the time taken by one photon to reach the detector since the sample was excited. The linear representations represent the best possible fitting to the experimental points. τ is obtained from the equation of this linear representation.

An electrical pulse associated with the optical pulse is generated and routed to the start input of the time-to-amplitude converter (TAC). Meanwhile, the sample is excited by the optical pulse and emits fluorescence. The optics is tuned so that the photomultiplier detects no more than one photon for each exciting pulse. The corresponding electrical pulse is routed back to the stop input of the TAC. The latter generates an output pulse whose amplitude is directly proportional to the delay time between the start and the stop pulses [27]. The height analysis of this pulse is achieved by an analogue-to-digital converter and a multichannel analyser, which increases by one the contents of the memory channel corresponding to the digital value of the pulse. After a large number of excitation and detection events,

the histogram of pulse heights represents the fluorescence decay curve. The larger the number of events, the better the accuracy of the decay curve. When deconvolution is required, the time profile of the exciting pulse is recorded under the same conditions by replacing the sample with a scattering solution (Ludox – colloidal silica – or glycogen) [10,14].

The excitation source is of major importance. Flash lamps running in air, or filled with N_2, H_2 or D_2 are not expensive but the excitation wavelengths are restricted to the 200–400 nm range. These deliver nanosecond pulses so that decay times of a few hundreds of picoseconds can be measured. Furthermore, the repetition rate is not high and because the number of fluorescence pulses per exciting pulse must be kept below 5%, the collection period may be quite long, depending on the required accuracy (a few tens of minutes to several hours). For long collection periods, lamp drift may become a problem. Lasers as excitation sources are of course much more efficient and versatile but much more expensive. The pulse widths are in the picosecond range with a high repetition rate. This rate must be limited to a few MHz in order to let the fluorescence of long lifetime samples vanish before a new exciting pulse is generated. Synchrotron radiation can also be used as an excitation source with the advantage of almost constant intensity versus wavelength over a very broad range, but the pulse width is in general of the order of hundreds of picosecond or not much less. The time resolution of the instrument is governed not only by the pulse width but also by the electronics and the detector. The linear time response of the TAC is most critical for obtaining accurate fluorescence decays. The response is more linear when the time during which the TAC is in operation and unable to respond to another signal is minimized. For this reason, it is better to collect the data in the reverse configuration: the fluorescence pulse acts as the start pulse and the corresponding excitation pulse as the stop pulse. In this way, only a small fraction of start pulses result in stop pulses and the collection statistics are better. Microchannel plate photomultipliers are preferred to standard photomultipliers, but they are much more expensive. They exhibit faster time responses and do not show a significant colour effect. With mode-locked lasers and microchannel plate photomultipliers, the instrument response in terms of pulse width is 30–40 ps so that decay times as short as 3–4 ps can be measured [10,14].

1.3.2.5. Fluorescence Intensity Quenching

The intensity of fluorescence can be decreased by a wide variety of bi-molecular processes that are usually referred to as quenching. Quenching can be divided into collisional quenching [28,29] and static quenching [29,30]. Energy transfer [31] and electron transfer [32] are amongst the most relevant collisional quenching mechanisms. Quenching can also occur by a variety of trivial, *i.e.*, non-molecular mechanisms, such as attenuation of the incident light by the fluorophore itself or other absorbing species [11].

Collisional quenching occurs when the excited-state fluorophore is deactivated upon contact with some other molecule in solution, usually called quencher. The fluorophore returns to the ground state during an encounter with the quencher but the molecules are not chemically changed in the process. A wide variety of molecules can act as collisional quenchers. Examples include oxygen, halogens, amines, and electron-deficient molecules like acrylamide. The mechanism of quenching varies with the fluorophore–quencher pair. For example, quenching of indole by acrylamide is probably due to electron transfer from indole to acrylamide, which does not occur in the ground state [11]. Quenching by halogen and heavy atoms occurs due to spin–orbit coupling and intersystem crossing to the triplet state [33].

Static quenching or contact quenching, on the other hand, occurs when the molecules form a complex before excitation occurs. The complex has its own unique (non)fluorescence and absorption properties. For example, static quenching often occurs when, due to hydrophobic effects, dyes stack together to minimize contact with water and consequently form aggregates. Planar aromatic dyes that are matched for association through hydrophobic forces can enhance static quenching [14,34,35].

1.3.2.6. Energy Transfer and Electron transfer

Fluorescence intensity can also decrease when a molecule transfers energy to another molecule in its vicinity – energy transfer. Although energy transfer is usually not considered to be quenching, in the general sense energy transfer results in the decrease of fluorescence intensity of the donor excited molecule.

The most commonly known energy transfer mechanism is the Förster Resonance Energy Transfer (FRET) that occurs whenever the emission spectrum of a fluorophore, called the donor, overlaps with the absorption spectrum of another molecule, called the acceptor [36]. Such overlap is illustrated in Figure 1.5. The acceptor does not need to be fluorescent, in which case, it is also a classic quenching mechanism. FRET does not involve emission of light by the donor since it does not derive from a re-absorption of the light emitted from the donor. Hence, there is no intermediate photon in energy transfer mechanisms. The donor and acceptor are coupled by a dipole–dipole interaction. The extent of energy transfer is determined by the distance between the donor and acceptor, and the extent of spectral overlap. The distance at which energy transfer is 50% efficient is called the Förster distance (R_0) [14,36].

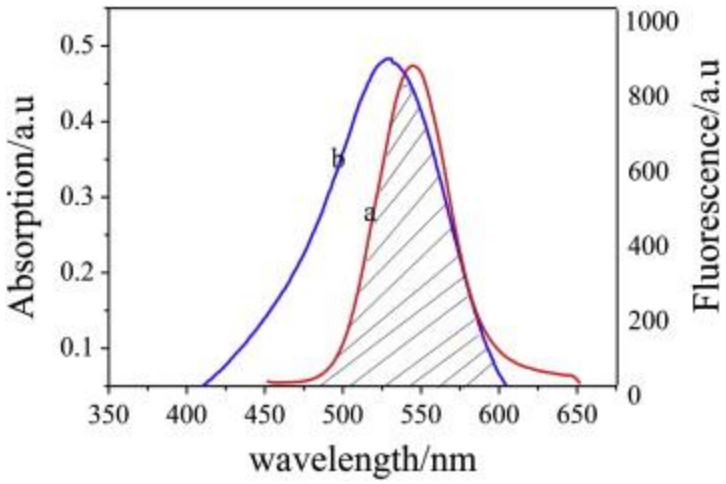

Figure 1.5. Spectral overlap between donor and acceptor. The spectral overlap between the emission spectrum of the donor (a – CdTe quantum dots in this case) and the absorption spectrum of the acceptor (b – neutral red in this case) represents the likeliness with which the energy from an excited electron in the donor will be transferred to the acceptor [37].

The rate of energy transfer $k_T(r)$ can be expressed as:

$$k_T(r) = \frac{1}{\tau_D}\left(\frac{R_0}{r}\right)^6 \qquad \text{(Equation 1.12)}$$

where r is the distance between the donor and acceptor and τ_D is the lifetime of the donor in the absence of energy transfer. The efficiency of energy transfer for a single donor–acceptor pair at a fixed distance is described below:

$$E = \frac{R_0^6}{R_0^6 + r^6} \qquad \text{(Equation 1.13)}$$

Hence the extent of transfer depends on the sixth power of the distance. Fortunately, the Förster distances are comparable in size to biological macromolecules: 20 to 60 Å. For this reason energy transfer has been used as a "spectroscopic ruler" for measurements of distance between sites on proteins [38]. The theory is adjusted for donors and acceptors that are covalently linked, free in solution, or contained in the restricted geometries of membranes or DNA. Additionally, depending on donor lifetime, diffusion can increase the extent of energy transfer [14].

Energy transfer can be reliably assumed to occur whenever the donors and acceptors are within the characteristic Forster distance, as long as a spectral overlap between both molecules occurs. Being a through-space interaction, the energy transfer mechanism is mostly independent of intervening solvent. Resonance energy transfer is a process that does not involve emission and reabsorption of photons. On the contrary, the theory behind energy transfer is based on the concept of molecules as oscillating dipoles with Coulombic interactions. As such, two oscillating dipoles with similar resonance frequency can behave as coupled oscillators [39].

The complexity of FRET is best understood by considering a single donor and acceptor separated by a distance (r). The rate of transfer for a donor and acceptor separated by a distance r is given by:

$$k_t(r) = \frac{\Phi_D k^2}{\tau_D r^6}\left(\frac{9000\ln(10)}{128\pi^5 N_A n^4}\right)\int_0^\infty F_D(\lambda)\varepsilon_A(\lambda)\lambda^4 d\lambda \qquad \text{(Equation 1.14)}$$

Where Φ_D is the quantum yield of the donor in the absence of acceptor, n is the refractive index of the medium, N_A is de Avogadro's number, r is the distance between the donor and acceptor, τ_D is the lifetime of the donor in the absence of acceptor, $F_D(\lambda)$ is the corrected fluorescence intensity of the donor in the wavelength range with the total intensity (area under the curve) normalized to the unity, $\varepsilon(\lambda)$ is the absorption spectra of the acceptor in extinction coefficient units (in typical units of $M^{-1}.cm^{-1}$), k^2 is the dipole orientator factor – usually assumed to be 2/3 as a dynamic random averaging of the donor and acceptor. The integral term, also represented as $J(\lambda)$, corresponds to the spectral overlap between the donor emission and acceptor absorption spectra [14,39].

In practical terms, it is easier to assess the data when it is represented in distances than in transfer rates. So, by assuming that half the donor molecules will decay energy transfer and the other half will decay normally (radiative and non-radiative pathways), R_0 can be estimated as:

$$R_0^6 = \frac{9000\ln(10)\Phi_D k^2}{128\pi^5 N n^4}\int_0^\infty F_D(\lambda)\varepsilon_A(\lambda)\lambda^4 d\lambda \qquad \text{(Equation 1.15)}$$

Once R_0 is known, the rate of energy transfer can be easily calculated (Equation 1.12) as well as the efficiency of energy transfer (Equation 1.13) for a given distance. Using these equations and knowing k^2, n, Φ_D and $J(\lambda)$ and, consequently, R_0, it is possible to calculate the distance between a given pair of donor and acceptor.

David L. Dexter provided another mechanism of energy transfer between two interacting molecules [40]. Dexter's model suggested that an excited donor group and an acceptor group might indeed exchange electrons to accomplish a non-radiative process. Also known as exchange or collisional energy transfer, because it occurs at much shorter distances than Förster energy transfer mechanism, Dexter energy transfer is a process in which two molecules bilaterally exchange their electrons. The excited donor has an electron in the lowest unoccupied orbital that is transferred to the acceptor. The acceptor then transfers an electron in the highest occupied orbital back to the donor. In the end, the acceptor is excited while the donor is in the ground state. Electron exchange is similar to FRET because energy is transferred to an acceptor, depends on spectral overlap of the donor and acceptor and is distance dependent. However, unlike the six-power dependence of Förster energy transfer, the reaction rate constant of Dexter energy transfer exponentially decays as the distance between these two parties increases [14,40]. On account of the exponential relationship to the distance, the exchange mechanism typically occurs within 10 Å, a much shorter distance than the 20-60 Å observed in FRET.

In most donor-fluorophore–quencher-acceptor situations, the Förster mechanism is more important than the Dexter mechanism. With both Förster and Dexter energy transfer, the shapes of the absorption and fluorescence spectra of the dyes are unchanged [14]. The electronic transitions are the same as when the molecules are isolated. Neither Förster nor Dexter mechanisms imply any chemical change in donor or acceptor. On the contrary, both mechanisms only cause the donor molecule to deactivate its' excited state and the acceptor molecule to go from the fundamental state to an excited state. Figure 1.6 schematically resumes both Förster and Dexter mechanisms.

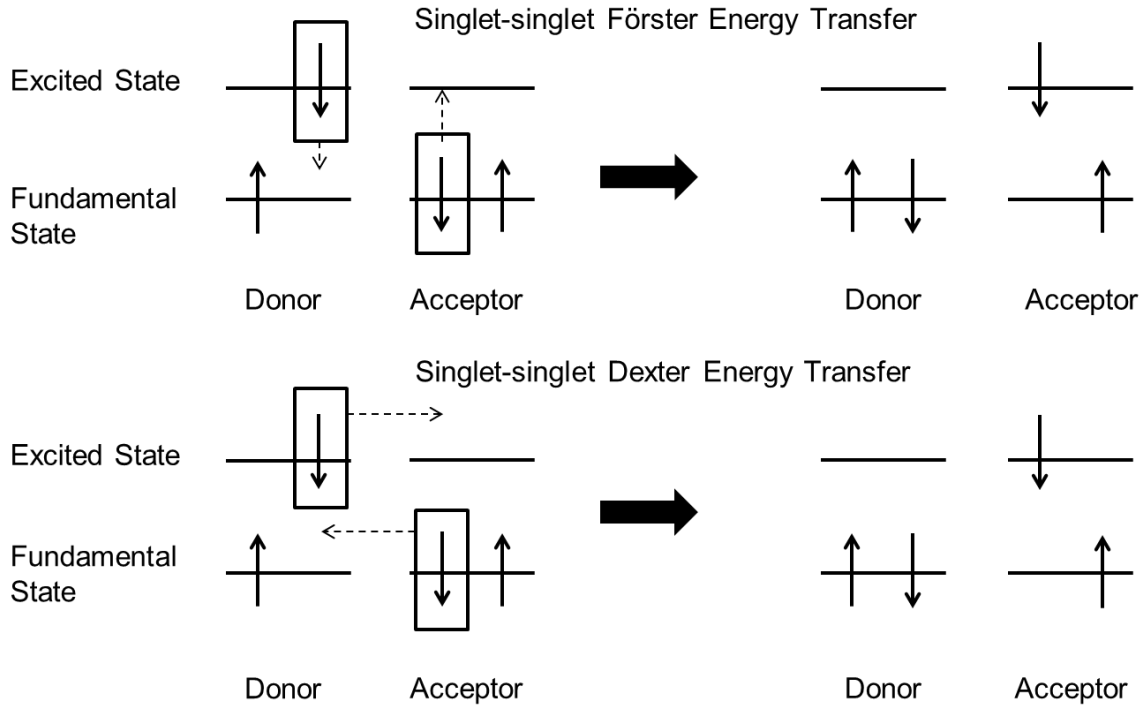

Figure 1.6. Transfer mechanisms between donor and acceptor molecules. Förster resonance energy transfer promotes the deactivation of the excited state of the donor by transferring the energy to the acceptor which, in turn, goes to the excited state. Dexter mechanism does not involve the direct deactivation of the donor excited state rather transferring the excited electron to the acceptor while a fundamental state electron of the acceptor is transferred back to the donor.

1.4. Nanoparticles

Nanoparticle as a term refers to a particle with size comprehended between a few and hundreds of nanometres (10^{-9} m). These can be composed of one or more inorganic compounds, such as noble metals, heavy metals, iron, etc. Most of them exhibit size-related properties that differ significantly from those observed for microparticles or bulk materials. Thus, depending on their size and composition peculiar properties can be observed, such as quantum confinement in semiconductor

nanocrystals, surface plasmon resonance in some metal nanoparticles and superparamagnetism in magnetic materials [41].

Numerous techniques have been developed to synthesize noble metal nanoparticles, including chemical methods (*e.g.*, chemical reduction, photochemical reduction, co-precipitation, thermal decomposition, hydrolysis, etc.) and physical methods (*e.g.*, vapour deposition, laser ablation, grinding, etc.), whose ultimate goal is to obtain nanoparticles with a good level of homogeneity and provide fine control over size, shape and surface properties, in order to better take advantage of their unique physicochemical properties [41].

Metal nanoparticles have size-dependent optical properties that have been explored in many biological applications, such as in medicine and molecular diagnostics. Gold nanoparticles (AuNPs) are among the most extensively studied nanomaterials and have led to the development of various techniques and methods for molecular diagnostics, imaging, drug delivery and therapeutics [42-45]. Metal nanoparticles (including AuNPs) also present significant electronic properties, such as charge storage and conductivity [46] which have been used in memory devices [47-49] and molecular switches [50], and catalytic activity [3,51,52], a property not observed in the bulk material.

AuNPs can be easily synthesized in sizes ranging between 3 and 200 nm in diameter and in different shapes. The most common AuNPs are quasi-spherically shaped, mainly due to their surface energy that favours the formation of spherical particles. One of the most common methods used to synthesize quasi-spherical AuNPs is the chemical reduction of Au(III) to Au(0) ions using sodium citrate as a reducing agent, a method first developed by Turkevich [53] and latter optimized by Frens [54]. In this approach, the citrate acts both as reducing agent and as capping agent which, as the AuNPs form, prevents the nanoparticles from forming larger particles and simultaneously conferring them a mild stability due to electrostatic repulsion between citrate-capped AuNPs [55]. Recent modifications of the Turkevich method have allowed a better distribution and control over the size of the AuNPs, where a range between 9–120 nm can be achieved just by varying the citrate/Au ratio [52,56,57]. Alternatively, many other aqueous- and organic-based methodologies have been developed for the controlled synthesis of different noble metal nanoparticles, including spherical or non-spherical, pure, alloy or core/shell nanoparticles of gold, silver, platinum, palladium and/or rhodium [58-60].

1.4.1. Localized Surface Plasmon Resonance

One of the most important properties of AuNPs is their localized surface plasmon resonance (LSPR) which is seen as a collective oscillation of conduction electrons on the nanoparticles surface that can be generated through the interaction of electromagnetic waves with the nanoparticles surface electrons [61]. This induces dipole moments that oscillate at the respective frequency of the incident wave,

consequently dispersing secondary radiation in all directions. The LSPR presents them with exceptionally high absorption coefficients and scattering properties that allow for higher sensitivity in optical detection methods than conventional organic dyes [62]. AuNP solutions have an intense red colour, which changes to brown when the particles are small (<2 nm) and to violet in the case of bigger nanoparticles. The red colour originates from absorption or scattering of light around 520 nm by localized surface plasmons. Because the particles strongly interact with green light, they appear red. Surface plasmon band arises from collective movements of free electrons, which can follow oscillations of an electric field. The electric field of incident light couples with the conduction band electrons and polarizes them relative to the centre of mass of the nanoparticle [63]. This leads to a charge difference between the opposite surfaces of the nanoparticle, which then acts as a restoring force and causes dipolar oscillation of the electrons [63]. This interaction is schematically represented in Figure 1.7.

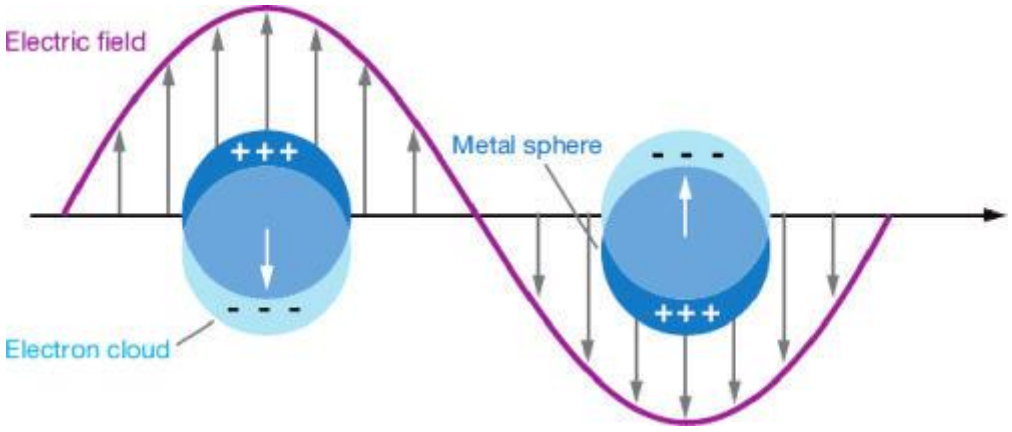

Figure 1.7. LSPR of metal nanoparticles. Schematic representation of how the interaction of the electromagnetic waves with the metal NPs surface electrons generates a surface plasmon resonance [64].

Incident light on the nanoparticles induces the conduction electrons to oscillate collectively with a resonant frequency that depends on the nanoparticles' size, shape, composition, inter-particle distance and environment (dielectric properties) [52,66-69]. A good example is the aggregation of AuNPs. When aggregation of AuNPs occurs, the inter-particle distance decreases substantially, leading to a pronounced change in colour from red to blue due to plasmon coupling between nanoparticles [70]. In addition, changing the composition of the nanoparticles to a different metal or a combination of two or more metals in alloy or core-shell conformation can also affect the LSPR band [71]. The LSPR properties of dispersed spherical metal nanoparticles can be quantitatively predicted by Mie's analytical solution of Maxwell's equations for the scattering of electromagnetic radiation by spherical particles composed of an absorbing or non-absorbing material [72]. Based on Mie's solution some

approaches have been made to calculate the absorption and scattering efficiencies as well as the extinction coefficient of AuNPs with different sizes and shapes [62].

1.4.2. Other optical properties

Excitation of AuNPs with short laser pulses increases the energy of the electrons. In order to return to their initial state, the electrons have to lose the gained energy either as heat (phonons) or as light (photons). Relaxation of the excited gold nanoparticles without emission of photons proceeds through three steps. First, the high temperature electrons distribute their energy among all the electrons by electron-electron scattering in less than a picosecond [73,74]. Second, energy is transferred from electrons to the whole particle via electron-phonon scattering during a few picoseconds [75,76]. The transfer of heat from the nanoparticle to the surrounding medium via phonon-phonon scattering is the third step, which proceeds in hundreds of picoseconds [75,76]. The relaxation time constants are dependent on the excitation energy [77,78], excitation wavelength [73] and surrounding medium [79]. An alternative pathway for relaxation of excited electrons in gold nanoparticles is photon emission [80,81].

1.4.3. Nanoparticle functionalisation

The development of new biosensing and therapeutic applications based on AuNPs has been pushing forward the chemistry for their functionalisation with different moieties such as nucleic acids, antibodies, biocompatible polymers, enzymes and other proteins, in a quest for an increased biocompatibility and targeting specificity [82,83].

Functionalisation of gold nanoparticles is usually achieved either by electrostatic interactions or covalent binding [84-87]. Electrostatic interactions can be performed by mixing charged nanoparticles to molecules with opposite charge which provides very simple and easy to use protocols. On the other hand, this type of interactions are very weak and, consequently, very sensitive to small changes in pH or ionic strength. On the contrary, covalent binding methods provide more stable and resistant functionalisation and are extremely versatile since there are several chemical groups that can chemically react with gold surfaces (especially thiols [88] and amine groups [89]). The fact that the binding to the nanoparticles surface is chemically directed also allows for spatial selectivity and oriented binding of the molecules. As disadvantages, these methods are usually more complex and time-consuming and often require molecules to be modified in order to obtain the chemical groups needed [82].

1.5. Gold nanoparticle-fluorophore systems

Molecular fluorophores in the vicinity of isolated colloidal metal nanoparticles usually experience modulation of their emission and, consequently, of the observable fluorescence [90-92]. Metal nanoparticles can modulate the optical properties of molecules near their metal surfaces, including changes to the radiative and non-radiative rate constants [93,94]. In the case of a fluorophore's emission, nanoparticles have even been proposed both as enhancers and as quenchers [95,96].

1.5.1. Molecular interactions in gold nanoparticle-fluorophore systems

The vicinity of a metal nanoparticle to the photoexcited fluorophore can affect the relaxation of the fluorophore at least via three processes: electron transfer, energy transfer and modification of the radiative rate of the fluorophore. Energy and electron transfer are both non-radiative relaxation routes that become available for the fluorophore when combined with gold nanoparticles. Assuming all three possible pathways can occur simultaneously, then whether enhancement or quenching is observable depends on the balance between changes in radiative vs. non-radiative (including temperature dependent vibrational dumping and energy transfer) and photochemical pathways (*e.g.*, photo-induced electron transfer) [95-97].

1.5.2. Electron transfer mechanisms

Pyrene-functionalised gold nanoparticles were the first gold nanoparticle-based systems for which photoinduced electron transfer was described [84]. In this case, electron transfer takes place from photoexcited pyrenes to 2-3 nm gold nanoparticles. However, this requires a small distance between the nanoparticle and the pyrene molecules [98]. Chlorophyll molecules assembled electrostatically on 8 nm nanoparticles transfer electrons to the particles after photoexcitation [99]. In these systems, close proximity between nanoparticles and fluorescent molecules is required for the electron transfer to take place.

1.5.3. Energy transfer systems

Electron transfer appears to be common in literature but energy transfer phenomena between nanostructures and fluorophores is clearly more explored [85,85,100]. As described before, energy transfer is divided into two major mechanisms, called Dexter and Förster energy transfers. The Dexter mechanism requires overlap of molecular orbitals of donor and acceptor while FRET can take place over longer distances and is based on Coulombic dipole-dipole interactions.

According to the Fermi Golden Rule [101] in the dipole approximation of energy transfer, the energy transfer rate is related to a product of the interaction elements of the donor and the acceptor. A single dipole's interaction elements are dependent on $1/r^3$. Then, on one hand, FRET occurs between two independent and isolated dipoles which derives into an interaction dependent with $(1/r^3)(1/r^3)=1/r^6$ as was described in the previous subchapters. On the other hand, if the interaction occurs between a planar structure (2D dipole array) and an isolated dipole, then the distance dependence becomes associated to $(1/r)(1/r^3)=1/r^4$ [87,101].

FRET between two dipoles can be applied in principle to gold nanoparticle-fluorophore energy transfer. Experiments have shown that energy transfer in systems with gold nanoparticles can range up to 20 nm [102], which is beyond the usual Forster range. An alternative way to face these systems is to treat the fluorophore as a dipole and the gold nanoparticle as a surface, which would lead to a $1/r^4$ dependence of energy transfer rate. This mechanism has been called (nano)-surface energy transfer or (N)SET and has been applied to several fluorophore-gold nanoparticle systems [102,103]. This alternative resembles with typical FRET but R_0 is determined from different physical parameters: quantum yield, the frequency of donor electronic transition, Fermi frequency and wave vector of the metal [102].

Most of this discussion has been shortened into how the experimental results match the theoretical energy transfer rates of FRET or NSET. This problem has been posed in a single common equation, very similar to Equation 1.13 but more ambiguous:

$$E = \frac{R_0^n}{R_0^n + r^n} \qquad \text{(Equation 1.16)}$$

where n=6 means a typical FRET scenario and n=4 means a SET system.

1.5.4. Radiative-rate changes

Gold nanoparticles have also been described to affect the radiative rate of a fluorophore [92,104]. Modification of the fluorophore radiative rate by gold nanoparticles can lead, in optimal conditions, to an enhancement of fluorescence intensity [105]. Change of the fluorophore radiative rate is explained in terms of coupling of molecular and nanoparticles dipoles [104] in which a constructive interference of the dipoles corresponds to increased radiative rate and possible enhancement of fluorescence intensity. Both radiative and non-radiative decays are dependent on the distance between the nanoparticle and the fluorophore and on the orientation of the fluorophore dipole to the particle surface.

1.5.5. Main theoretical approaches on radiative and non-radiative modulation

One of the first models to predict the effect of small dielectric particles on the spectroscopic properties of molecules interacting with them was published by Joel Gersten and Abraham Nitzan in 1981 [93]. The Gersten-Nitzan model predicts the theoretical expressions for the quantum yields, radiative and non-radiative decay rates under the assumption that the nanoparticles are much smaller than the wavelength. The prediction is valid for different sizes, shapes and dielectric constant, which can relate both with the composition of the nanoparticle and the medium. The most important issues taken into account by this model include the total dipole of the system (and not only the nanoparticle), the possible additional induced dipole caused by the presence of the nanoparticle and the relative position of the transition moment relatively to the surface of the nanoparticle (whether they are parallel or perpendicular). One very important issue raised by this model is the complete dependence of the behaviour on the shape, size and dielectric constant of the nanoparticle. Also, it calls attention to the major difference observed when comparing free fluorophores with fluorophores interacting with metal structures and even when comparing between fluorophores interacting with nanoparticles and plane surfaces. The Gersten-Nitzan model is the most used model when studying nanoparticle-fluorophore systems.

Another famous model for nanoparticle-fluorophore systems was proposed by Persson and Lang [106] in 1982 improving an earlier attempt by Chance, Prock and Silbey [94] to analyse similar situations using electrodynamics. Unlike what happens in Gersten-Nitzan model, this model describes the electron-hole pair quenching of excited states near a metal. Instead of considering the effect of a nanoparticle in the excited-state of a molecule it simply assumes the difference in sizes between nanoparticles and fluorophores is so big that the nanoparticles behave as if they were a planar metal structure. Under these assumptions, the dipole is considered to interact with conduction band electrons of the metal, which, in turn, are assumed to move freely in a semi-infinite background. This is the first model to discuss the theoretical modelling on the distance dependence of the nanoparticle-fluorophore interaction as being modulated with $1/r^4$ by a metallic surface.

The quenching and enhancement issue was also empirically described by J. Lakowicz [107] via the Radiating Plasmon model. According to this model the emission or quenching of a fluorophore near a metal structure can be predicted from the optical properties of the metal structures as calculated from electrodynamics, Mie theory and, ultimately, Maxwell's equations. Lakowicz defends that the key issue in metal-modulated fluorescence lays in the nanoparticles' scattering and absorption components of extinction. The Radiating Plasmon model predicts that quenching arises from the absorption component in the extinction spectrum, while enhancement is brought from the scattering contribution, whose relative proportions depend on the nanoparticles' size, shape and composition [62,107].

1.5.6. Experimental approaches on metal-modulated fluorescence

Published data is not consistent in terms of experimental setup. This may be the cause for apparently contradictory reports. Authors analysed different sets of nanoparticles, fluorophores and spacers. Several crucial factors, such as the overlap between plasmon excitation and optical properties of the fluorophore [108,109], the distance between fluorophore [9,10] and the metallic nanosurface and the relative orientation of the excitation dipole and the plasmonic oscillator [110] have been described to influence the final output.

Controlled single-molecule to single nanoparticle studies, reported in two independent studies have shown that quenching and enhancement can occur simultaneously [96,111]. The experiments are based on an isolated nanoparticle in an atomic force microscope (AFM) tip and immobilized fluorophores on a matrix. The AFM system controls distance with very high precision and the fact that both fluorophore and nanoparticle are immobilized permits a very tightly controlled experimental setup. These experiments do not replicate the behaviour of similar systems in solution as they assume one nanoparticle interacting with one fluorophore in a single dipole-orientation relatively to the surface of the nanoparticle.

Most of the work in solution is particularly focused towards the influence of distance on the emission of fluorophores near metal nanoparticles. Chhabra *et al* [112] presented data indicating that quenching efficiency is proportional to $1/r^4$ according to a more recent electrodynamics theory [113,114]. Jennings *et al* also determined the quantum efficiency of FAM and cy5 on 1.5 nm gold nanoparticles to be dependent to $1/r^4$ [87]. On the other hand, earlier data suggested that Gersten-Nitzan model [93] overestimated both radiative and non-radiative constants whilst positively predicting the quantum efficiency of cy5 at several distances of a nanoparticle [92]. The results are not incoherent but do not indisputably show that the quantum efficiency is proportional to $1/ r^4$ rather than $1/ r^6$. The fact that different systems (AuNPs' size, fluorophores, spacers) and different theoretical models are being used by different authors frustrates a global analysis.

In solution, events other than direct fluorescence modulation can occur. Chemical events that may occur on a nanoparticle's surface can merely change the molecules and consequently affect fluorescence. Several possible local environment fluctuations have been suggested, such as pH, salt concentration and local dielectric constant [93,115]; or inter-fluorophore distance dependent quenching like in excimer formation mechanisms [98]. Another key factor for the observed fluorescence modulation is the overlap between the fluorophore's emission and the LSPR of the nanoparticle [109] which in turn also varies with its size, shape and composition.

1.6. Nanoparticles in diagnostics

A range of highly sensitive biosensing methods for nucleic acids, proteins, antibodies, enzymes and other biological molecules have been developed by exploring the gold nanoparticles' physicochemical properties, either based on LSPR or optical modulating properties.

1.6.1. LSPR-based nanodiagnostics methods

Colloidal gold colour change upon aggregation is the best characterized example for diagnostic systems using gold nanoparticles. Most of the colorimetric biosensors based on gold and/or silver nanoparticles have been developed considering these changes in colour generated by the plasmon coupling between nanoparticles upon aggregation, while other methods have used the LSPR properties of the noble metal nanoparticles just as a colourful reporter (*i.e.*, making use of their scattering and/or absorbance properties). Some are based on the unspecific adsorption of biomolecules to non-functionalised noble metal NPs, while others are based on functionalised noble metal nanoparticles for increased specificity.

In the case of the non-functionalised nanoparticles, Li *et al*. took advantage of the differential propensity of ssDNA and dsDNA adsorption to AuNPs to develop a biosensor for DNA detection [116]. The free bases of ssDNA molecules interact electrostatically with the negatively charged surface of the citrate-capped AuNPs, which confers an increased stability to the nanoparticles upon increasing ionic strength. On the other hand, dsDNA molecules adsorb much less to the nanoparticles' surface and do not provide stability to increasing ionic strength induced aggregation of the nanoparticles. Based on these observations, Li and co-workers combined AuNPs with citrate capping with a polymerase chain reaction (PCR) procedure, using ssDNA probes complementary to the amplicon. Whenever the template of the PCR is amplified, the ssDNA probes hybridize with the amplicon and consequently become unavailable to adsorb to the gold NPs' surface. This way, a positive result (*i.e.*, target amplification) yields a colorimetric change from red to blue upon salt addition, while in a negative result the colour remains unchanged. This approach has also been successfully explored for the detection of single-nucleotide polymorphisms (SNPs) [117,118], ultraviolet (UV)-induced mutagenic or carcinogenic DNA dimers [119], or to directly detect unamplified hepatitis C virus RNA isolated from clinical specimens [120]. Similarly, Xia and co-workers used the same approach to develop a nearly "universal" biosensor to detect a broad range of targets including nucleic acids, proteins, small molecules and inorganic ions, using conjugated polyelectrolytes and different ssDNA aptamers or probe molecules that mediated the target detection [121].

Other approaches have used noble metal nanoparticles functionalised with different biosensing molecules (*e.g.*, ssDNA, antibodies, proteins or enzymes) in order to increase specificity of the methods. In 1996, Mirkin *et al.* described the use AuNPs functionalised with thiol-modified ssDNA probes (Au-nanoprobes) that would form a cross-linking network upon detection of a complementary ssDNA target by both Au-nanoprobes [122]. This cross-linking network leads to the aggregation of the AuNPs causing a red-shift in the LSPR absorbance band to 574 nm – Figure 1.8.. This approach also allowed the identification of single nucleotide polymorphisms by controlling the temperature of denaturation of the cross-linked network, which presents a sharp melting transition [123,124]. When combined with a rolling circle amplification technique, this method allows the detection of single point mutations with 1 fM sensitivity [125].

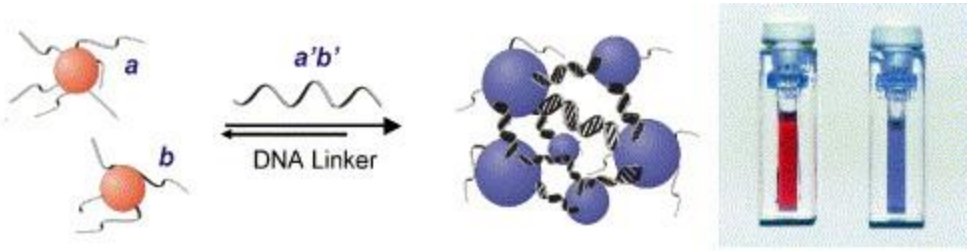

Figure 1.8. Cross-linking method. A mixture of gold nanoparticles with surface-immobilized non-complementary DNA sequences (a, b) appears red in colour. When a complementary DNA sequence (a'b') is added to the solution, the particles are aggregated causing a red shift in the LSPR, thus, appearing purple in colour. An example is shown in the upper right where monodisperse particles (red) are aggregated using a complementary DNA linking sequence (purple) [124].

Other methods for specific nucleic acid detection using AuNPs functionalised with ssDNA probes have been developed based on their differential non-cross-linking aggregation mediated by the increasing ionic strength of the solution [126-132]. In the case of the non-cross-linking method developed by Baptista and co-workers, the differential aggregation of the Au-nanoprobes is evaluated upon salt addition to discriminate the presence of complementary, mismatched and non-complementary targets in solution [127-132]. An increase in ionic strength is produced by addition of salt which will induce the aggregation of the Au-nanoprobes. The presence of a fully complementary target increases the stability of the Au-nanoprobes, while non-complementary targets will not protect the Au-nanoprobes from aggregation – Figure 1.9. Mismatched targets will be less effective in protecting the Au-nanoprobes from aggregation due to less efficient hybridisation and less stable structural conformation. This method has been thus far successfully applied to the detection of pathogenic agents [128,130] and SNP/single point mutations [132,133], as well as in gene expression analysis without the need for reverse transcription [129,131].

1.6.2. Raman spectroscopy based nanodiagnostics methods

A different approach was developed in 1974 when Fleishmann and co-workers demonstrated for the first time that Raman signals from different types of molecules could be dramatically enhanced by their adsorption to silver surfaces [134], as well as on other metals, as later demonstrated. Since then, the use of metal nanoparticles for surface-enhanced Raman scattering (SERS), mostly gold and silver nanoparticles, has led to the development of a wide variety of new biosensors for the detection of nucleic acids, antibodies, proteins and other biological molecules [135,136].

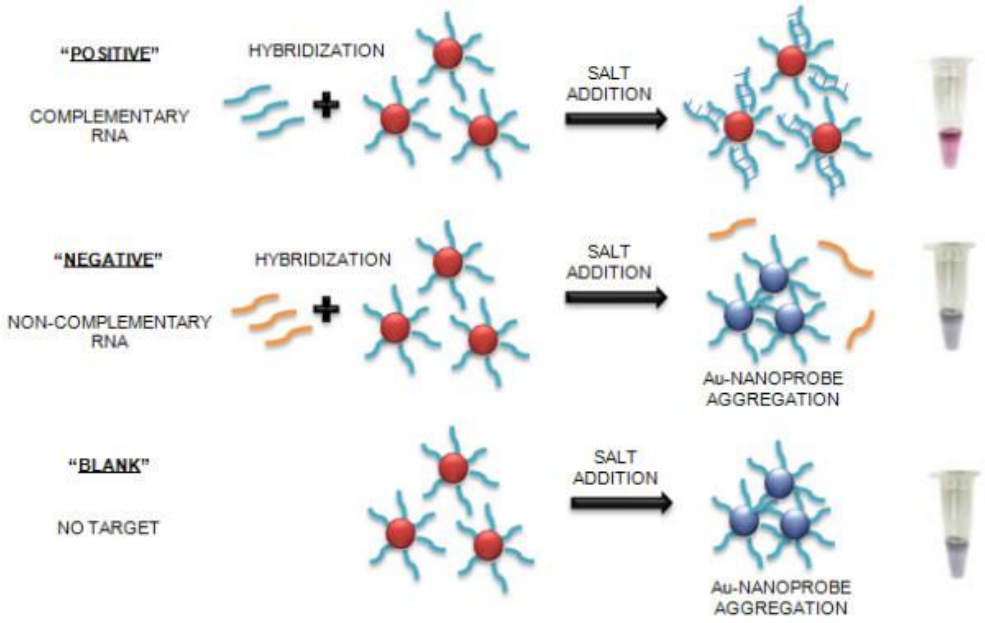

Figure 1.9. Schematic representation of a non-crosslinking method. The assay is based on the increased stability of the Au-nanoprobes upon hybridisation with the complementary target in solution, while non-hybridized Au-nanoprobes easily aggregate once the solution's ionic strength is increased [129].

Unlike absorption-based phenomena, Raman spectroscopy is based in a change of frequency when light is inelastically scattered by molecules or atoms resulting in a molecular fingerprint, information on molecular structure or intermolecular interaction of a specific process or molecule. The potential of Raman spectroscopy as biomedical diagnostics tool is rather low due to its low cross-section (~10-30 cm^2) that results in low sensitivity [137]. However, in 1977 two groups independently described the use of noble metal surfaces to enhance the Raman scattering signal of target molecules [138,139] - SERS. Jeanmaire and Van Duyne proposed a two-fold electromagnetic field enhancement that was later associated with the interaction between the incident and scattered photons with the nanostructure's LSPR [140]. Simultaneously, Albrecht and Creighton suggested the source of the enhancement to be caused by a specific interaction between an adsorbate to the nanoparticle surface. Briefly, a charge transfer from the adsorbate into the empty energetic levels on the metal surface or

from the occupied levels of the nanoparticle's surface to the adsorbate [141-143]. The SERS detection of specific biomolecules mediated by noble metal nanoparticles can be either accomplished directly or indirectly, through the association with a molecule with an intense and characteristic Raman signature, typically a fluorescent dye. Most of the methods based on SERS have taken similar approaches to those already described in colorimetric assays. For example, by exploring the electrostatic adsorption of some biomolecules to the nanoparticles' metal surface some groups have created a metallic layer made of gold or silver nanoparticles aggregates to perform the detection of biomolecules and metabolites by SERS. Gogotsi *et al.* developed a SERS label-free biosensor based on a glass coated with AuNPs to detect and quantify nicotinic acid adenine dinucleotide phosphate (NAADP) molecules, which is a calcium secondary messenger that plays a crucial role in intracellular Ca^{2+} release [144]. This system allowed for the rapid detection of 100 μM NAADP without any special sample purification or labelling, making it an important tool for the study of normal cell function and cancer development. The use of conjugated noble metal nanoparticles was also explored in SERS-based biosensors for a more versatile and specific detection of biomolecules. In most cases, a probe (*e.g.*, DNA, antibody) is functionalised to the nanoparticle or an aggregated layer of nanoparticles such as to create a sandwich conjugation with a Raman-labelled probe upon target detection, thus generating the SERS signal. An interesting combination of magnetic iron/gold core-shell nanoparticles with gold nanorods has also been used to specifically enumerate *E. coli* in water samples in a rapid and sensitive test [145]. In this case, the magnetic nanoparticles are used to concentrate the bacteria, improving the Raman signal by concentration, and the posteriorly added gold nanorods serve as Raman signal enhancers.

1.6.3. Fluorescence based nanodiagnostics methods

Methods based on the quenching of fluorescence have been proposed for DNA detection. May one of the simpler consists of fluorophore-labelled ssDNA electrostatically adsorbed onto gold nanoparticles [146], where the presence of a complementary target triggers des-adsorption of the newly formed dsDNA from the nanostructures due to the electrostatic variation between ssDNA and dsDNA, and fluorescence emission is restored.

As for functionalised with thiol-modified oligonucleotides has been explored in different conformations. Tang and co-workers proposed a method to probe hydroxyl radicals using an AuNP-oligonucleotide-FAM system where the hydroxyl radical promotes strand breakage and consequent release of FAM, restoring the previously quenched fluorescence [147]. The same quenching mechanism was used to detect specific DNA strands using two probes (one with an AuNP label and another labelled with TAMRA) that hybridize to two DNA sequences near each other [148], bringing the probes close enough to quench fluorescence emission. Phillips and co-workers developed an array

of AuNP–conjugated polymer constructs for bacterial sensing [149]. The efficient quenching ability of AuNPs coupled with the molecular-wire effect of conjugated polymer compounds generated a pronounced fluorescence response mediated by the binding strength of the bacterium to the AuNP. Through this approach, the authors successfully differentiated twelve different bacteria using only three systems. On another approach, noble metal nanoprobes can be combined with dye-labelled ssDNA probes to detect specific nucleic acid targets by FRET/NSET mediated mechanisms – Figure 1.10 B. One method is to design such probes to harbour complementary and contiguous sequences to the target, in such way that upon target hybridisation the dye is forced to approach the nanoparticle's surface and the fluorescent signal consequently decreases [148] – Figure 1.10C. Another method is to hybridize the dye-labelled ssDNA directly to the nanoprobes and detect specific target DNA sequences based on strand displacement of the fluorescent probe [150]. For example, in the presence of a fully complementary long ssDNA targets, the short dye-labelled DNA strand is displaced and, as a result, the fluorescence that was initially quenched by the nanoparticle is restored. Through this approach, the signal-to-noise ratio and detection limit of 50 pM is significantly improved when compared to similar probes using organic acceptors as reported by Mo and co-workers [150].

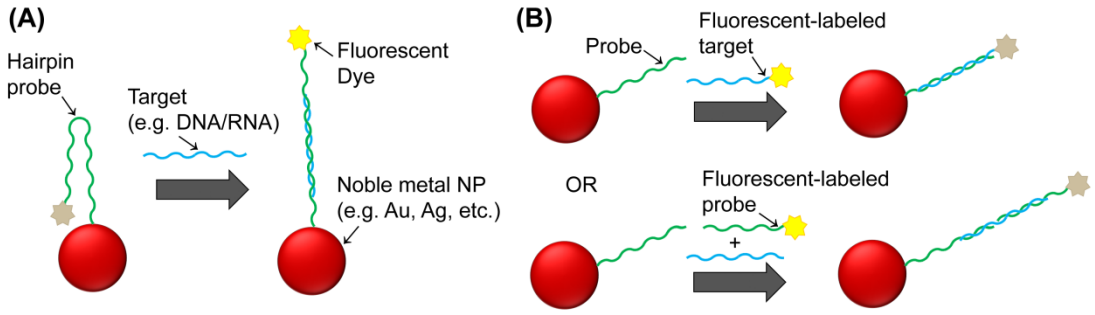

Figure 1.10. Different approaches for fluorescent-based noble metal NPs biosensing. (A) molecular nanobeacon and (B) other nanoprobes. Distance to the nanoparticle determines the fluorescence signal that is observed. Distances are not represented to the scale [A151].

Particular interest has been given to hairpin-DNA functionalised nanoparticles. In this, case, the hairpin structure leads the fluorescent dye moiety to the proximity of the nanoparticle's surface and, consequently, to the quenching of fluorescence. In the presence of a complementary DNA/RNA target, the hairpin structure is disrupted by target hybridisation and fluorescence is restored. Several methods have been developed based on this approach to monitor specific nucleic acid hybridisations as well as cleavage processes mediated by nucleases, mainly using AuNPs [146] – Figure 1.10A. For example, Dubertret and co-workers reported the use of molecular nanobeacons based on 1.4 nm AuNPs to detect single-base mismatches in DNA with a 100-fold increase in sensitivity when compared to conventional molecular beacons [152]. Similarly, Benia *et al*. used molecular nanobeacons based on

13 nm AuNPs to successfully detect a mutation associated to cystic fibrosis using just 1 nM of target [153]. They have also shown that the use of AuNPs larger than 13 nm for molecular nanobeacons is not recommended due to the fact that larger nanoparticles present relevant quenching efficiency even at large fluorophore–nanoparticle separation lengths, despite the fact that they could carry a higher number of molecular beacons.

Proteins have also been probed through nanoparticle fluorescence-mediated systems, for example human blood proteins have been let to interact with fluorescent AuNPs and detected through quenching [154]. In another example, a sandwich immunoassay using AuNPs quenching has been proposed for the detection of the protein cardiac troponin T by its interaction with two different antibodies, one attached to AuNPs and the other labelled with fluorescent dyes [155]. By means of an opposite modulation, infrared fluorescent nanoparticles showed enhanced fluorescence when interacting with protein [156]. Guirgis and co-workers developed an immunoassay to detect malaria based on the fluorescence quenching of Cy3B-labeled recombinant Plasmodium falciparum heat shock protein 70 (PfHsp70) upon binding to AuNPs functionalised with an anti-Hsp70 monoclonal antibody [157]. Upon competition with the free antigen, the Cy3B-labeled recombinant PfHsp70 is released to solution resulting in an increase of fluorescence intensity. The interaction of human blood proteins with AuNPs has also been studied by letting the proteins interact with fluorescent AuNPs and performing the detection through quenching [154].

1.7. Scope of the thesis

The expansion of nanobiophotonics led to a boom in innovative tools for several adjacent scientific fields. The potential of the application of nanophotonics devices to diagnostics is one of the most explored areas and the influence of nanoparticles on fluorescence is one of the main focuses. Gold nanoparticles are already vastly used in diagnostics and the possibility to use fluorescence-modulated systems has widened the horizons for a broad range of sensitive and adaptable systems. One interesting topic lies on the distance-dependence of the modulation of gold nanoparticles on fluorescence.

Nonetheless, the background behind the interaction between nanoparticles and fluorophores is still unclear. There are several proposed theoretical models and these are arguably capable of describing what is observed in experimental data. Moreover, optical interferences caused by nanoparticles' presence in solution are not usually taken into account, *i.e.*, optical filter created by the nanoparticles, the light scattered back from the nanoparticles, physic-chemical changes at the surface of nanoparticles. These effects are only very rarely considered and may play an important part in the experimental characterization of the nanoparticle-fluorophore systems.

Considering this issue, a nanoparticle-fluorophore system was developed to explore an experimental approach for the photophysical characterization of a fluorophore at the surface of AuNPs. The approach should rely on the experimental assurance that the reference fluorophores were in the same optical conditions of those of the AuNP-fluorophore conjugates. The relevance of introducing corrections for the inner filter effect and the reabsorption of the emitted light caused by AuNPs was assessed. In order to understand the underlying mechanisms involved in emission changes, it was essential to accurately determine the radiative and non-radiative rate constants. This demanded independent measurements of fluorescence quantum yields and fluorescence decay-times. The developed approach also allowed an evaluation of the distance influence in the effect of the nanoparticles on the emission of the fluorophores using ssDNA strands with crescent number of nucleotides as spacer molecules.

Finally, this thesis demonstrated the advantages of applying the studied fluorescent nanorulers with gold nanoparticles to biosensing in complex and challenging biological problems such as monitoring and controlling RNA synthesis *in vitro* and *in situ*. The potential of the distance-dependence of this nanobiophotonics system was further explored by assessing microdeletion *in vitro*.

CHAPTER 2. Materials and Methods

2.1. General Information

All chemicals were purchased from Sigma Aldrich in the highest purity available and used without further purification unless stated otherwise. All oligonucleotides were purchased from STAB Vida (Lisbon, Portugal). All aqueous solutions were sterilized using autoclave when possible or sterile filters as an alternative. All aqueous solutions used for RNA handling were prepared with milli-Q water (18.3 MΩ.cm at room temperature) treated with Diethylpyrocarbonate (DEPC, 0.1% (v/v)) for at least 16 hours before being sterilized in the autoclave.

Absorption spectra were recorded on a Nicolet Evolution 300 UV/Visible spectrophotometer (Thermo Electron Corporation, USA). Fluorescence spectra were recorded on a Fluorescence Spectrophotometer Cary Eclipse with Peltier thermostated accessory (Varian, USA). The emission spectra related to the characterization of the system (Chapter 4) were collected with 2.5 nm slit bandwidth for excitation and emission. The emission spectra related with the application of the system to biological applications (Chapter 5) were collected with 5 nm slit bandwidth for excitation and emission. Absorption and emission spectra related to the characterization of fluorophores at the surface of AuNPs were recorded using standard 1x1 cm quartz cuvettes (101-QS, Hellma Analytics, Germany). Absorption and emission spectra related to the characterization of oligonucleotide modified with fluorophores at the surface of AuNPs were recorded using Ultra-microvolume quartz cuvettes 105.202-QS and 105.251-QS, respectively.

2.2. Oligonuleotides

Table 2.1. Unmodified oligonucleotides

Oligonucleotide	Nucleotide Sequence (5'-3')
RepNB_comp	TGAAACACAAACTTGAACAGCTA
NEG	GGGTGGTGCAAATAGTAACGG
MYCforward	GCTCATTTCTGAAGAGGACTTGT
MYCreverse	AGGCAGTTTACATTATGGCTAAATC
T7-MYCforward	TAATACGACTCACTATAGGGAGAGCTCATTTCTGAAGAGGACTTGT
T7 primer	TAATACGACTCACTATAGGGAGA
WT1+KTS	GGACTCATACAGGTAAAACAAGTGAAAAGCCCTTCAGCTG
WT1-KTS	GGACTCATACAGGTGAAAAGCCCTTCAGCTG
NEG2	TGTCGATCAGCTGGTCCACCGAACGAACAAGGCTGTGT CCTCGG
Antisense target	CACCAUGGAGAGCGACGA
anti EGFP siRNA	Sense: GCAUGACCAACAAGAUGAAUU Antisense: UUCAUCUUGUUGGUCAUGCUU
nonsense siRNA	Sense: AAUUCUCCGAACGUGUCACGUUU Antisense: UUUUAAGAGGCUUGCACAGUGCA
EGFP forward	AGCTTCGAATTCTGCAGTCG
EGFP reverse	GGCTGATTATGATCTAGAGTC
miR-21 target	UAGCUUAUCAGACUGAUGUUGA
miR-21 loop	TGTTGCCATGAGATTCAACAGTCAACATCAGTCTGATAAGCTACCCGACA
miR-21 forward	GCCGCTAGCTTATCAGACTGATGT
β-actin forward	ATAGCACAGCCTGGATAGCAAC
β-actin reverse	CACCTTCTACAATGAGCTGCGT

Table 2.2. Oligonucleotides modified at 5' with Thiol-C6 group and/or at 3' with a fluorophore

Oligonucleotide	Nucleotide Sequence (5'-3')	Modifications
oligotest	CCAAGCTACTATTTG	5'-Thiol-C6 and 3'-6-FAM
SNSET12	CCGTTACTATTT	5'-Thiol-C6 and 3'-6-FAM
SNSET15	CCGTTACTATTTGCA	5'-Thiol-C6 and 3'-6-FAM
SNSET20	CCGTTACTATTTGCACCACC	5'-Thiol-C6 and 3'-6-FAM
SNSET25	CCGTTACTATTTGCACCACCGTCTA	5'-Thiol-C6 and 3'-6-FAM
SNSET50	CCGTTACTATTTGCACCACCGTCTAACTATCCATACCTAGTCACTGATGC	5'-Thiol-C6 and 3'-6-FAM
Reporter_NB	TTTGCATAGCTGTTCAAGTTTGTGTTTCATGCAAA	5'-Thiol-C6 and 3'-cy3
Inhibitor_NB	TTTGCATCTCCCTATAGTGAGTCGTATTATGCAAA	5'-Thiol-C6 and 3'-6-FAM
MYCforward_cy5	GCTCATTTCTGAAGAGGACTTGT	3'-Cy5
WT1_S_FAM	TTCGCGCAGCTGAAGGGCTTTTCACTTGTTTTACCTGTATGAGTCCCGCGAA	5'-Thiol-C6 and 3'-6-FAM
antisense Au-nanobeacon	TTTGCCTCGTCGCTCTCCATGGTGGGCAAA	5'-Thiol-C6 and 3'-cy3
WT1+KTS_cy5	GGACTCATACAGGTAAAACAAGTGAAAAGCCCTTCAGCTG	3'-Cy5
WT1-KTS_cy5	GGACTCATACAGGTGAAAAGCCCTTCAGCTG	3'-Cy5
NEG2_cy5	TGTCGATCAGCTGGTCCACCGAACGAACAAGGCTGTGT CCTCGG	3'-Cy5
anti-siRNA Au-nanobeacon	TTTGCCGCATGACCAACAAGATGAAGGCAAA	5'-Thiol-C6 and 3'-cy3
anti-miR Au-nanobeacon	TTTGCCTCAACATCAGTCTGATAAGCTAGGCAAA	5'-Thiol-C6 and 3'-cy3
nonsense Au-nanobeacon	TTTGCCCCGTTACTATTTGCACCACGGCAAA	5'-Thiol-C6 and 3'-cy3

2.3. AuNPs synthesis

All AuNPs synthesis were preceded by a careful treatment of the materials used. Namely, all glass materials were previously immersed overnight in freshly prepared *aqua regia* (1:3, HNO_3:HCl) and later washed with milli-Q water (18.3 MΩ.cm at room temperature). All metal materials used during synthesis were covered with Teflon and Milli-Q H2O was used in all solutions.

2.3.1. Citrate reduction method

AuNPs were prepared using the citrate reduction method described by Turkevich [53] and later adapted with slight modifications by Lee and Miesel [158]. In a 500 mL round bottom flask, 225 mL of X mM $HAuCl_4$ were brought to a boil while vigorously stirring. While in reflux, 25 mL of Y mM sodium citrate were quickly added and the mixture was kept refluxing for 15 min with continuous stirring. The concentration of $HAuCl_4$ and citrate was adjusted in the attempt to synthesize AuNPs with different sizes. The values of X and Y for the tried synthesis are shown in Table 2.2. The colloidal solution was left to cool to room temperature while keeping the continuous stirring and was then transferred to a 250 mL Erlenmeyer flask with a ground glass cap, covered with aluminium foil and stored in the dark at room temperature. The AuNPs were later characterized by Transmission Electron Microscopy (Hitachi 8000, Japan), Dynamic Light Scattering (DLS) and UV/Vis Spectroscopy and their concentration was determined using the Lambert-Beer law with theoretical extinction coefficients calculated with the Mieplot v4107 program.

2.3.2. Citrate and sodium borohydride co-reduction method

AuNPs were prepared using a citrate and sodium borohydride co-reduction method described by Zou *et al* [159] with slight modifications. Namely, in a 100 mL Erlenmeyer, 2.5 mL of a solution of Y mM of citrate were added to a solution of 95 mL of X mM of $HAuCl_4$ in vigorous stirring. After 1 min 2.5 mL of a solution of Z mM of $NaBH_4$ were added to the mixture. The colloidal solution was stirred for an additional 5 min and stored in the dark at room temperature. The values of X, Y and Z for the tried synthesis are shown in Table 2.2. The AuNPs were later characterized by Transmission Electron Microscopy (Hitachi 8000, Japan), Dynamic Light Scattering (DLS) and UV/Vis Spectroscopy.

Table 2.3. AuNPs synthesis reaction mixtures

Method	$[HAuCl_4]$ (X)	[Citrate] (Y)	$[NaBH_4]$ (Z)
Citrate1	1.00 mM	38.8 mM	n/a
Citrate2	1.22 mM	52.0 mM	n/a
Citrate3	0.68 mM	35.0 mM	n/a
Co-red1	0.25 mM	0.25 mM	0.50 mM
Co-red2	0.15 mM	0.25 mM	0.10 mM
Co-red3	0.25 mM	0.25 mM	0.20 mM
Co-red4	0.15 mM	0.25 mM	0.20 mM
Co-red5	0.25 mM	0.25 mM	0.10 mM
Co-red6	0.20 mM	0.25 mM	0.10 mM
Co-red7	0.20 mM	0.25 mM	0.20 mM
Co-red8	0.15 mM	0.25 mM	0.25 mM
Co-red9	0.20 mM	0.25 mM	0.25 mM
Co-red10	0.25 mM	0.25 M	0.25 mM

2.4. AuNPs functionalisation

2.4.1. AuNPs functionalisation with fluorophores

2.4.1.1. AuNPs functionalisation with SAMSA

2.4.1.1.1. Preparation of SAMSA fluorescein

A small amount of SAMSA [(5-((2-(and-3)-S-(acetylmercapto)succinoyl)amino)fluorescein)] (Invitrogen, USA) powder was resuspended in 100 µL of NaOH 1M and incubated for 15 min in the dark at room temperature. After the incubation period 900µl of water were added to the solution. This solution can be used for subsequent experiments or used as stock if stored at -80ºC and protected from light. SAMSA should not be stored for long periods of time because it is already activated. The concentration of each batch was determined using the Lambert-Beer law of diluted solutions of the stock (ε_{SAMSA}=80000 $M^{-1}.cm^{-1}$). All manipulation of SAMSA was performed on ice.

2.4.1.1.2. Functionalisation of SAMSA@AuNPs surface

The previously prepared SAMSA solution was brought to pH8 by dilution with Phosphate Buffer 10 mM, pH8, 0.05% SDS to yield activated-SAMSA. The activated-SAMSA was then added to the nanoparticles and incubated overnight for functionalisation. The SAMSA@AuNP conjugates were centrifuged at 16000g for 20 min, the supernatant removed and the NPs resuspended in fresh buffer. This washing step was repeated five more times in order to remove every trace of non-bonded SAMSA, and absorption spectra of the supernatants taken after each washing step to ensure complete removal of non-bonded SAMSA.

2.4.1.2. AuNPs modification with Rhodamine 101 and Rhodamine B

Functionalisation of AuNPs with Rhodamine molecules was attained by mixing AuNPs and Rhodamine 101 (Rh101) or Rhodamine B (RhB) in water and incubating for 16 hours with mild agitation at 20ºC. The mixture was then centrifuged at 16000g for 20 min at 20 ˚C. The supernatant was saved for subsequent analysis and the sample resuspended in bi-distilled water.

2.4.2. AuNPs functionalisation with thiolated oligonucleotides

2.4.2.1. Simple AuNPs functionalisation with thiolated oligonucleotides

The thiolated oligonucleotides were suspended in 1mL of 0.1M DL-dithiothreitol (DTT), extracted three times with ethyl acetate and further purified through a desalting NAP-5 column (Pharmacia Biotech, Sweden) using 10 mM phosphate buffer (pH 8) as eluent. Following oligonucleotide quantification via UV/Vis spectroscopy (based on number of moles - OD_{260} proportion given by the manufacturer for each oligonucleotide batch), each oligomer was added to the AuNP solution in a 100:1 ratio. AGE I solution (2% (w/v) SDS, 10 mM phosphate buffer (pH 8)) was added to the mixture to achieve a final concentration of 10 mM phosphate buffer (pH 8), 0.01% (w/v) SDS. The solution was incubated at room temperature for 20 min. Afterwards, the ionic strength of the solution was increased sequentially in 50 mM NaCl increments by adding the required volume of AGE II solution (1.5 M NaCl, 0.01% (w/v) SDS, 10 mM phosphate buffer (pH 8)) up to a final concentration of 10 mM phosphate buffer (pH 8), 0.3 M NaCl, 0.01% (w/v) SDS. Following the last addition, the solution was left to rest for additional 16 hours at room temperature. Then, the functionalised Au-nanoprobes were centrifuged for 20 min at 21460g, the oily precipitate washed thrice with 10 mM phosphate buffer (pH 8), and redispersed in 10 mM phosphate buffer (pH 8). The resulting Au-

nanoprobes were stored in the dark at 4°C until further use and characterized by UV/Vis Spectroscopy and TEM.

2.4.2.2. Simultaneous co-functionalisation with thiolated oligonucleotides and PEG chains

The co-functionalisation of AuNPs with thiolated oligonucleotides and PEG chains was achieved by following the proceeding described in section 2.4.2.1. with modifications. Namely, after the addition of AGE I the solution was sonicated for 10 seconds using an ultrasound bath and incubated at room temperature for 20 min. After this period, 0.045 mg/mL of O-(2-Mercaptoethyl)-O'-methyl-hexa(ethylene glycol), $C_{15}H_{32}O_7S$ was added to the mixture and incubated for another 20 min at room temperature. Afterwards, the ionic strength of the solution was increased sequentially in 50 mM NaCl increments by adding the required volume of AGE II solution (1.5 M NaCl, 0.01% (w/v) SDS, 10 mM phosphate buffer (pH 8)) up to a final concentration of 10 mM phosphate buffer (pH 8), 0.3 M NaCl, 0.01% (w/v) SDS. After each increment, the solution was sonicated for 10 seconds and incubated at room temperature for 20 min before the next increment.

Also, the functionalised Au-nanobeacons were centrifuged for 20 min at 21460g, and the oily precipitate washed three times with DEPC-treated H_2O instead of 10 mM phosphate buffer (pH 8), and redispersed in DEPC-treated H_2O to a final concentration in Au-nanobeacons of 15 nM. The resulting Au-nanobeacons were stored in the dark at 4ºC and were characterized by UV/Vis Spectroscopy and Transmission Electron Microscopy.

2.4.2.3. Sequential co-functionalisation with PEG chains and thiolated oligonucleotides

The co-functionalisation of AuNPs with thiolated oligonucleotides and PEG chains was achieved by following the proceeding described in section 2.4.2.2. with modifications.

Namely, a solution containing 10nM of the AuNP solution was mixed with 0.003mg/mL of a commercial hetero-functional poly(ethylene glycol) (PEG) [O-(2-Mercaptoethyl)-O'-methyl-hexa(ethylene glycol), C15H32O7S, 356.48 Da] in an aqueous solution of SDS (0.028%). Then, NaOH was added to a final concentration of 25 mM and the mixture incubated for 16 hours at room temperature. Excess PEG was removed by centrifugation (21.460 ×g, 30 min, 4ºC), and quantified by a modification of the Ellman's Assay [160] (see section 2.5.1.2.3.). The level of PEG coverage on the AuNP was evaluated to be corresponding to 30% of saturation of the gold's surface. After, the stem-looped oligonucleotides modified with 3'-Cy3 and 5'-Thiol-C6 (STABVIDA) were added as described in section 2.4.2.1. The resulting Au-nanobeacons were characterized by Dynamic Light Scattering (Zetasizer, Malvern), Zeta Potential (Zetasizer, Malvern), UV/Vis Spectroscopy and Transmission Electron Microscopy.

2.5. Nanoconjugates characterization

2.5.1. AuNPs functionalisation assessment

2.5.1.1. Quantification of fluorophores at the AuNPs' surface

2.5.1.1.1. Quantification of SAMSA on the AuNPs' surface

The average amount of SAMSA per AuNP was determined by three independent methods:

i) differential absorption spectroscopy performed by subtracting the naked AuNPs absorption spectrum from that of the SAMSA@AuNP conjugates (particular attention was paid to SAMSA's range of absorption), and the obtained spectra used to calculate the concentration of SAMSA using the Lambert-Beer Law ($\varepsilon SAMSA=80000 M^{-1}cm^{-1}$);

ii) subtractive assessment of fluorophore in the supernatant via accumulation of fractions retrieved from all the washing steps. The supernatants were obtained after centrifugation at 16000 ×g for 20 min at 20˚C. A standard curve with known concentrations of SAMSA was prepared in Phosphate Buffer 10 mM, pH8, 0.05% SDS (see Appendix II, Figure A1), and the concentration of non-bonded SAMSA interpolated (the amount of SAMSA bonded to the AuNPs was calculated by subtracting the non-bonded SAMSA from the initially added SAMSA);

iii) reduction of the bond between the AuNPs and SAMSA by addition of 0.1M DTT (Dithiothreitol) and incubation overnight at room temperature. The aggregated AuNPs were centrifuged at 16000g for 20 min at 20˚C and the supernatant analysed by fluorescence spectroscopy (using a calibration curve as described in ii) – see Appendix II. Figure A2).

2.5.1.1.2. Quantification of Rhodamine 101 and Rhodamine B on the AuNPs' surface

The average amount of Rh101 and RhB per AuNP was determined by subtractive assessment of fluorophore in the supernatant. This was retrieved from the UV/Visible spectrophotometric analysis of the supernatants of all the washing steps. The amount of fluorophore adsorbed to the AuNPs was calculated by subtracting amount of fluorophore measured in the supernatant from the amount of fluorophore initially added.

2.5.1.2. Quantification of functionalised oligonucleotides and PEGs on the AuNPs

2.5.1.2.1. Quantification of functionalised oligonucleotides on the AuNPs' surface after simple functionalisation

The amount of fluorophores/oligonucleotides per AuNP was determined by subtractive assessment of the number of fluorophores/oligonucleotides in the supernatant via accumulation of fractions retrieved

from all the washing steps. A standard curve with known concentrations of fluorophore/oligonucleotide was prepared in phosphate buffer 10mM, pH8 (see Appendix II, Figures A3 and A4), and the concentration of non-reacted fluorophore/oligonucleotide interpolated (the amount of fluorophore/oligonucleotides bonded to the AuNPs was calculated by subtracting the amounts captured in the supernatants from the initially added fluorophore/oligonucleotide).

2.5.1.2.2. Quantification of functionalised oligonucleotides on the AuNPs' surface after simultaneous co-functionalisation with PEG

The amount of fluorophores/oligonucleotides per AuNP was determined by subtractive assessment of the number of fluorophores/oligonucleotides in the supernatant via accumulation of fractions retrieved from all the washing steps. A standard curve with known concentrations of fluorophore/oligonucleotide was prepared in phosphate buffer 10 mM, pH 8 (see Appendix II, Figure A5), and the concentration of non-reacted fluorophore/oligonucleotide interpolated (the amount of fluorophore/oligonucleotides bonded to the AuNPs was calculated by subtracting the amounts captured in the supernatants from the initially added fluorophore/oligonucleotide).

2.5.1.2.3. Quantification of PEG chains on the AuNPs' surface after sequential co-functionalisation with thiolated oligonucleotides

The excess of thiolated chains in the supernatants is quantified by interpolating a calibration curve set by reacting 200 μL of stock solution of the O-(2-Mercaptoethyl)-O'-methyl-hexa(ethylene glycol) in 100 μL of phosphate buffer 0.5 M (pH7) with 7 μL of 5,5'-dithio-bis(2-nitrobenzoic) acid (DTNB) 5 mg/mL in phosphate buffer 0.5 M (pH7), and measuring the absorbance at 412 nm after 10 minutes. The linear range (Appendix II, Figure A6) for the O-(2-Mercaptoethyl)-O'-methyl-hexa(ethylene glycol) chain obtained by this method is 0.0002–0.035 mg/mL (Abs412 = 26.034×[PEG, mg/mL] + 0.0627). The number of exchanged chains is given by the difference between the amount determined by this assay and the initial amount incubated with the AuNPs. There is a point at which the nanoparticle becomes saturated with a thiolated layer and is not able to take up more thiolated chains - maximum coverage per gold nanoparticle, *i.e.,* 0.01mg/mL of O-(2-Mercaptoethyl)-O'-methyl-hexa(ethylene glycol) (Appendix II, Figure A6). The Au-nanobeacons were functionalised with 0.003 mg/mL of O-(2-Mercaptoethyl)-O'-methyl-hexa(ethylene glycol) corresponding to 30% of PEG saturation of AuNPs' surface (190.29±19.56 chains per nanoparticle).

2.5.1.2.4. Quantification of functionalised oligonucleotides on the AuNPs' surface after sequential co-functionalisation with PEG

The average number of oligonucleotides functionalised per nanoparticle was assessed following complete displacement of the thiolated oligonucleotides (beacons) from the AuNP by means of 0.12mM β-Mercaptoethanol incubation for 48h. After 48 hours at room temperature, the solutions were centrifuged at 14500g for 20 min. The concentration of beacon in the supernatant was measured by monitoring the emission spectra of FAM (Excitation at λ=490 nm) or Cy3 (Excitation at λ=530 nm). All the AuNPs samples and the standard solutions of the thiol-oligonucleotide beacon were kept at the same pH and ionic strength and calibration for all measurements. Fluorescence emission was converted to molar concentrations of the thiol modified oligonucleotide by interpolation from a standard linear calibration curve (see Appendix II, Figure A7 and A8). Standard curves were prepared with known concentrations of beacon using the same buffer pH, salt, and β-Mercaptoethanol concentrations. The average number of molecular beacon strands per particle was obtained by dividing the oligonucleotide molar concentration by the AuNP concentration.

2.5.2. Nanoconjugates physical characterization

2.5.2.1. Transmission Electron Microscopy analysis

Samples of nanoparticles were sent to Instituto de Ciencia e Engenharia de Materiais e Superfícies (ICEMS/IST), Portugal, for TEM analysis. The samples were prepared by depositing 10 µL of the as-prepared colloidal suspensions in carbon copper grids, washing twice with 10 µL of Milli-Q water, and air dried. TEM was performed with a HITACHI H-8100 microscope operated at 200 kV. Particle size and polydispersity were determined from the TEM pictures using the imaging software Adobe Photoshop CS5, and by analysing at least 500 NPs.

2.5.2.2. Dynamic Light Scattering

The hydrodynamic diameter of the citrate capped AuNPs was determined by DLS using the Zetasizer Nano ZS system (Malvern Instruments Ltd, England). A total volume of 800 µL of 1 nM of sample containing AuNPs or Au-nanobeacons was first stabilized for 15 minutes at 25ºC and then a total of 15 measurements with a minimum of 15 runs each were registered. The results were analysed using the software provided by the equipment manufacturer.

2.5.2.3. Zeta potential analysis

The samples of Au-nanobeacons were let to stabilize for 15 minutes at 25ºC and then a total of 30 zeta potential measurements with 30 runs each were registered by using a Zetasizer Nano ZS (Malvern Instruments Ltd, England) system. The results were analysed using the software provided by the equipment manufacturer.

2.5.2.4. Au-nanobeacon behaviour in a reductive environment

To evaluate whether the reductive cell environment would cause detachment of the beacon from the AuNPs' surface, the Au-nanobeacons resistance to DTT or glutathione (GST) was evaluated. To mimic the behaviour in the intra-cellular milieu, 1 nM of the Anti-miR-21 Au-nanobeacon was incubated with 5, 10 and 100mM of DTT or GST (Sigma-Aldrich) at 37°C for up to 24h. Fluorescence intensity was measured in a PerkinElmer LS45 Fluorescence Spectrometer (Varian) using an Ultra-Micro quartz cell (Hellma) programmed to incubate the reactions for 1440 min (24 hours) at 37°C at 15 minutes intervals (excitation/emission, 530 nm/560 nm) (Appendix II, Figure A10). The curves show that for concentrations of reducing agent between 5 and 10 mM, the Au-nanobeacon remains in its closed conformation, which demonstrate that, under physiologic intracellular conditions, observable Au-nanobeacon fluorescence is solely due to hybridisation to specific target.

2.5.3. Photophysical characterization of the nanoconjugates

2.5.3.1. Time-dependent spectrophotometry characterization of fluorophores@AuNPs

2.5.3.1.1. Time-dependent UV/Visible Spectrophotometry of fluorophores@AuNPs

Experimental assessment of the extinction coefficient variation of SAMSA, Rh101 and RhB in the vicinity of AuNPs was performed by differential spectra taken in a double-beam spectrophotometer. After establishing a baseline using two 1nM AuNPs solutions in both sample and reference beams, a 1nM gold nanoparticle solution was positioned in the reference beam while a solution containing 1nM of AuNPs and freshly added fluorophores was positioned on the sample beam. The first spectrum was recorded immediately after the addition of the fluorophore and spectra hence forward were recorded with two hour intervals between 2 hours and 10 hours. A last spectrum was taken after 16 hours.

2.5.3.1.2. Time-dependent spectrofluorometry of fluorophores@AuNPs

Experimental assessment of the extinction coefficient variation of SAMSA, Rh101 and RhB in the vicinity of AuNPs was performed by spectrofluorometry. A cuvette containing 1 nM of AuNPs and freshly added fluorophores was positioned on the holder. The first spectrum was recorded immediately

after the addition of the fluorophore and spectra hence forward were recorded with two hour intervals between 2 hours and 10 hours. A last spectrum was taken after 16 hours.

2.5.3.2. Fluorescence quantum yields determination

2.5.3.2.1. Reference Molecules

Fluorescence quantum yields (Φ_F) were determined by the relative method using the fluorescence emission of reference solutions (Fluorescein, 5-FAM and SAMSA) for the same absorbance conditions. When applicable, to ensure identical absorbance, solutions were prepared using 1nM of AuNPs. Each fluorophore was used at a concentration that ensures an absorbance at 490 nm of 0.1. Fluorescence quantum yields for Fluorescein, 5-FAM and SAMSA in Phosphate Buffer 10mM, pH5, 0.05% SDS were calculated using Fluorescein in basic ethanol as reference. The attained data were used to calculate the Φ_F of the same fluorophores using each other as reference in presence and absence of AuNPs.

2.5.3.2.2. SAMSA@AuNPs

For the SAMSA@AuNP conjugates, absorbance of the fluorophore was that corresponding to the concentration of fluorophore bonded to the AuNPs according to the Lambert-Beer Law. All Φ_F determinations were performed in Phosphate Buffer 10mM, pH8, 0.05% SDS. The same was done for 5-FAM in Phosphate Buffer 10mM, pH5, 0.05% SDS in the absence of AuNPs. Excitation was at λ=490 nm for every experiment and absorbance for both samples and references was matched at this wavelength for Φ_F determinations.

2.5.3.2.3. Nanoprobes

As for nanoprobes, Φ_F determinations were performed in phosphate buffer 10 mM, pH8 for SNSET probes (Excitation wavelength of λ=490 nm). As a reference solution, the same number of oligonucleotides that was determined to be was added to 1 nM of AuNPs in the same buffering conditions.

2.5.3.3. Time-resolved Fluorescence Spectroscopy Measurements

Fluorescence lifetimes (τ) of Reference molecules, SAMSA@AuNPs and nanoprobes were measured via time correlated single photon counting technique (TCSPC) using two different home-built equipment:

1. Fluorescence decays were measured via the Time Correlated Single Photon Counting technique (TCSPC) using a home-built equipment. The samples were excited at 460 nm using a nanoLED (IBH). The electronic start pulses were shaped in a constant fraction discriminator (Canberra 2126) and directed to a time to amplitude converter (TAC, Canberra 2145). Emission wavelength (520 nm for SAMSA and oligonucleotide-FAM or 550 nm for Rhodamine 101) was selected by a monochromator (Oriel 77250) imaged in a fast photomultiplier (9814B Electron Tubes Inc.), the PM signal was shaped as before and delayed before entering the TAC as stop pulses. The analogue TAC signals were digitized (ADC, ND582) and stored in multichannel analyser installed in a PC (1024 channels, 1.95 ns/ch) until 5000 counts were reached.

2. Fluorescence decays were measured using a home-built picosecond TCSPC apparatus described elsewhere [161]. The samples were excited at 532 nm (picosecond Spectra Physics mode-lock Tsunami* Laser (Ti:Saphire) Model 3950 with repetition rate of about 82 MHz and tuning range 700-1000 nm, pumped by a Millenia Pro-10s, frequency-doubled continuous wave (CW), diode-pumped, solid-state laser). A harmonic generator model GWU-23PS (Spectra Physics) is used to produce the second and third harmonic from Ti:Saphire laser exciting beam frequency output. The samples were measured at 520 nm and the horizontally polarized output beam from the GWU (second harmonic) was first passed through a ThorLabs depolarizer (WDPOL-A) and after by a Glan-Thompson polarizer (Newport 10GT04) with vertical polarization. Emission at 90˚ geometry collected at magic angle polarization was detected through an Oriel CornerstoneTM 260 monochromator by a Hamamatsu microchannel plate photomultiplier (R3809U-50). Signal acquisition and data processing were performed employing a Becker & Hickl SPC-630 TCSPC module. Fluorescence decays and the instrumental response function where collected (4096 channels, 0.814 ps/ch), until 5000 counts at maximum were reached.

The analysis of the decays was carried out with the method of modulating functions extended by global analysis as implemented by Striker *et al* [162].

2.5.4. Au-nanobeacons specificity

The capability to recognize the specific target of the Au-nanobeacons was evaluated by incubating each Au-nanobeacon at 1 nM with a complementary and a non-complementary target in phosphate buffer at pH 7. This amount of target was added so that the number of DNA strands on each Au-nanobeacon was in a 1:5 proportion with the respective target. FAM or Cy3 fluorescence intensity as function of incubation time was measured every 2 min throughout 120 min with an incubation temperature of 37°C. FAM was excited at λ=490 nm and the respective fluorescence was collected in the 500-700 nm interval while cy3 was excited at 530 nm and its respective fluorescence corrected in

the 560-800nm interval. The area of the spectra was calculated and total intensity was plotted in function of time. In some cases only the initial and final points were assessed.

Reporter and Inhibitor Au-nanobeacons were also tested under the same conditions but with the reaction buffer used in the experiment (see section 2.6.6): 200 mM Tris-HCl at pH 7.9, 30 mM $MgCl_2$, 50 mM NaCl, 10 mM spermidine and 10 mM of each NTP.

2.6. Molecular and Cell Biology

2.6.1. cDNA production

2.6.1.1. RNA extraction

Total RNA extracted from HL-60 cells, HCT-116 cells and kidney samples using TRIsure™. HL-60 and HCT-116 cells were directly lysed in the culture flask by adding 1ml of TRIsure™ per 10cm^2 of growth area and pipetting the cell lysate several times to ensure sufficient cell disruption. Around 75 mg of Kidney samples were homogenised in 1 ml of TRIsure™. The samples with TRIsure™ were then incubated for 5 min at room temperature and 200 µL of chloroform (4˚C) was added. The tubes was securely closed and vigorously shaken by hand for 15 s. The samples were incubated for 3 min at room temperature and centrifuged at 12,000 x g for 15 min at 4°C. The aqueous phase (transparent and upper phase) was transferred to another tube and the organic phase (green and lower phase) and interphase (white and pasty layer) were discarded. The aqueous phase was mixed with 500 µL of isopropyl alcohol (4°C) and incubated samples for 30 min at -20°C and then transferred to -80°C for least another 2 h. After incubation, the samples were centrifuged at 12,000 x g for 10 min at 4°C. The supernatant was removed and the pellet was washed with 1 mL of 70% ethanol, vortexed and centrifuged at 7500 x g for 5 min at 4°C. The excess of 70% ethanol was removed and the pellet was air-dried (or with the help of a speed-vac). The resulting pellet was then ressuspended in DEPC-treated water by slow pipetting the solution up and down and, in some cases, incubation for 10 min at 55-60°C. The extracted RNA was used right away or otherwise stored at -80°C.

2.6.1.2. RT-PCR

2.6.1.2.1. Reverse Transcription

The extracted RNA was subjected to reverse transcription (RT) for cDNA synthesis with Revert-AidTM M-MuLV Reverse Transcriptase (Fermentas, Vilnius, Lithuania) according to the manufacturer's specifications, using 20 µM of the appropriate reverse primer (MYCreverse, WT1reverse), annealing at 42°C for 1 h and 70°C for 10 min to reverse transcriptase inactivation.

2.6.1.2.2. PCR

Gene specific primers (MYCforward and MYCreverse, WT1forward and WT1reverse) were then used for the amplification of the cDNA. PCR amplification of the *c-myc* specific fragment was performed in duplicate on a MyCycler Thermocycler (Biorad) in 25 µL using 1 µM of primers, 2.5mM dNTPs with 1 U Taq DNA Polymerase (Amersham Biosciences, GE Healthcare, Europe, GmbH), with the following thermal cycling conditions:

1. 5 min 95˚C
2. 30 s 95˚C ←
3. 30 s 62˚C 30 cycles
4. 30 s 72˚C →
5. 5 min 72˚C

PCR amplification of the WT1 RNA specific fragment was performed in duplicate on a DNAengine Thermocycler (Biorad) in 25 µL using 1 µM of primers, 2.5mM dNTPs with 1 U Taq DNA Polymerase (Amersham Biosciences, GE Healthcare, Europe, GmbH), with the following thermal cycling conditions:

Long program

1. 5 min 95˚C
2. 3 min 95˚C ←
3. 1 min 30 s 62˚C 45 cycles
4. 6 min 72˚C →
5. 5 min 72˚C

Short program

1. 5 min 95˚C
2. 1 min 95˚C ←
3. 45 s 62˚C 30 cycles
4. 45 s 72˚C →
5. 5 min 72˚C

Mixed program

1.	5 min	95˚C	
2.	30 s	95˚C	
3.	30 s	55˚C	5 cycles
4.	30 s	72˚C	
5.	30 s	95˚C	
6.	30 s	62˚C	25 cycles
7.	30 s	72˚C	
8.	5 min	72˚C	

The resulting fragments were stored at 4˚C. Confirmation of correct PCR products was performed by agarose gel electrophoresis with TAE 1x (40mM Tris, 20mM acetic acid, 1mM EDTA) using conditions according to the amplicon's size and with GelRed™ staining.

2.6.2. Preparation of competent *E. coli* cells*

Escherichia coli cells were inoculated on a LB agar (1% (w/v) tryptone, 0.5% (w/v) yeast extract, 171 mM NaCl, 1.4% (w/v) of Agar, pH 7) plate and incubated at 37ºC overnight. A colony was inoculated in 125 mL SOB (2% (w/v) tryptone, 0.5% (w/v) yeast extract, 10 mM NaCl, 2.5 mM KCl, 10 mM MgCl2, 10mM MgSO4, pH 7) in a 500 mL flask, at 20ºC with vigorous shaking to OD600 = 0.5 (normally 24 - 36 hours). The flask was placed on ice for 10 min. Cells were pelleted by spinning at 1663 g for 10 min at 4ºC. The cells were gently resuspended in 40 mL ice-cold TB and stored on ice for 10 min. Cells were pelleted by spinning at 1663 g for 10 min at 4ºC. Cells were gently resuspended in 5 mL ice-cold TB and 350 µL DMSO (DMSO was stored at -20ºC o/n before use). Competent cells were aliquoted in 200 µl fractions and stored at -80ºC.

2.6.3. Cloning

2.6.3.1. Ligation

WT1 amplicons's band of interest was extracted, avoiding exposure to UV light, and purified using the GFX™ PCR DNA and Gel Band Purification Kit, following manufacturer's instructions and using 50 µL of sterile milli-Q H2O as eluent. Using the GeneJET™ PCR Cloning Kit, 100 ng of the extracted DNA was inserted into a linearized blunt-end pJET1 cloning vector, following the manufacturer's Sticky-End protocol.

*Adapted from [163]

2.6.3.2. *E. coli* transformation

Two microliters of the ligation product were added to 20 µL of *E.coli* competent cells and stored on ice for 30 min. A plasmid resulting of the transformation of pJET1 with the manufacturer's provided fragment was used as positive control and as negative control the ligation product was replaced by sterile milli-Q water. The cells were then submitted to a heat shock at 42ºC for 90 seconds and rapidly transferred to ice. After 2 min on ice, 80 µL of SOC medium (similar to SOB medium but with 20 mM of sterile glucose after autoclaving SOB medium) were added and the cells were incubated for 1 hour at 37ºC. After incubation, 100 µL of the transformed competent cells were cultured on LB agar plates with 100 µg/mL ampicillin. The plates were left at room temperature until liquid had been absorbed and then incubated at 37ºC overnight. A selected transformed colony was resuspended in 25 µL of sterile milli-Q water. Two microliters of transformed cells were used to perform PCR using pJET1Fw and pJET1Rev primers to confirm insert ligation. The remaining cells were inoculated in 2 mL of LB medium with 100 µg/mL ampicillin and incubated at 37ºC o/n with agitation. Stock solutions of the transformed cells were prepared by adding 300 µL of glycerol to 700 µL of culture, and stored at -80ºC. The remaining volume of culture was used to extract and purify the cloned plasmid.

2.6.4. *E. coli* plasmid extraction and purification

An *E. coli* colony was inoculated in 2 mL of LB medium and 100 µg/mL ampicillin and incubated at 37ºC o/n with agitation. Cells were pelleted by spinning at 16,000 g for 2 min at 4ºC in 1.5 mL eppendorfs. The supernatant was discarded and the pellet was resuspended in 100 µL of ice-cold AL I solution. After 5 min on ice, 200 µL of AL II solution was added and mixed by inversion. After 5 min on ice, 150 µL of AL III solution was added and vigorously mixed by vortex. After 5 min on ice, the lysate was centrifuged at 21,460 g for 5 min at 4ºC. The supernatant was transferred to a sterile eppendorf and 2 volumes of ice-cold 100% ethanol were added. The plasmid DNA was left to precipitate at -20ºC overnight (or at -80ºC for 2 hours). Afterwards, the precipitate was centrifuged at 21,460 g for 15 min at 4ºC and the supernatant was discarded. The pellet was washed with 500 µL of ice-cold 70% ethanol. The pellet was left to dry at room temperature (or with the help of a speed-vac) and resuspended in 50 µL of sterile milli-Q water. RNAse A was added to a final concentration of 25 µg/ml and incubated for 1 hour at 37ºC. Two extractions with 1 volume of phenol were performed, followed by one extraction with chloroform. DNA was again precipitated at -20ºC overnight with 2 volumes of ice-cold 100% ethanol. Afterwards, the precipitate was centrifuged at 21,460 g for 15 min at 4ºC and the supernatant was discarded. The pellet was washed with 500 µL of ice-cold 70% ethanol.

The pellet was left to dry at room temperature (or with the help of a speed-vac) and resuspended in 50 μL of sterile milli-Q water.

2.6.5. Transcription template preparation and purification

The amplification product obtained in section 2.6.1.2.2 was re-amplified using the same reaction conditions and thermal cycling as above except for the forward primer that was replaced for T7-MYCforward primer. The resulting fragment was then PCR amplified using primers MYCreverse and T7 primer as described above and purified through band gel extraction. Confirmation of correct PCR products was performed by 2% agarose gel electrophoresis stained with GelRed™. This amplification product was used as template for *in vitro* transcription reactions related to MYC sequences.

2.6.6. Monitoring RNA synthesis *in vitro*

Standard *in vitro* transcription was performed in 100 μL reaction containing *in vitro* transcription buffer (200 mM Tris-HCl (pH 7.9), 30 mM $MgCl_2$, 50 mM NaCl, 10 mM spermidine), 10 mM of each NTP, 0.6 μg of DNA template, and 30 U of T7 RNA polymerase (Fermentas, Vilnius, Lithuania) according to the manufacturer's protocol. For the real time quantification experiments, 1 nM of the reporter Au-nanobeacon (labelled with Cy3) was added to each transcription reaction. When using the inhibitor Au-nanobeacon (labelled with FAM), 1 nM was also added to the reaction mixture. All measurements were performed during incubation of the reactions for 120 min at 37°C by recording the fluorescence intensity of the Au-nanobeacon every 2 min at an excitation wavelength of 490 nm or 530 nm for FAM-labelled or Cy3-labeled Au-nanobeacon, respectively. After the measurements, the enzyme was heat inactivated for 15 min at 75°C.

All transcription reaction products were also evaluated on a 3% agarose gel electrophoresis with GelRed™ staining. Product quantity determination was performed by pixel intensity/counting using ImageJ™ imaging software as previously described [164].

2.6.7. Monitoring RNA *in situ*

2.6.7.1. Cell culture and EGFP vector transfection

HCT-116 cells (from colorectal carcinoma) were grown in Dulbecco's modified Eagle's medium with Glutamax (DMEM, Invitrogen) with 10% heat inactivated foetal bovine serum (Invitrogen), 100 U/ml penicillin and 100 μg/ml streptomycin (Invitrogen) and maintained at 37ºC in 5% CO_2. Cells were seeded at a density of 1×105 cells/well in 24-well plates and grown for 24 hours prior to transfection of the EGFP vector (pVisionGFP-N vector 4.7 kb, Biovision) encoding for green fluorescent protein,

VisionGFP, optimized for high expression in mammalian cells. On the day of transfection, EGFP vector (1μg per well) was added cells at approximately 50% confluence with 2μg of Lipofectamine 2000 (Invitrogen) and Opti-MEM® Reduced Serum Medium (Invitrogen) according to the manufacturer's recommendations.

2.6.7.2. EGFP silencing

2.6.7.2.1. EGFP silencing with Antisense Au-nanobeacon

After 24 hours of EGFP transfection, cells were treated with 30 nM of Antisense Au-nanobeacons in Opti-MEM® Reduced Serum Medium (Invitrogen). After 48 hours, cells were washed with 1× PBS, lysed in water and collected for analysis of EGFP silencing, RNA extraction and confocal imaging. Fluorescence was measured at least 3 times in a Cary Eclipse spectro*fluorimeter* (Varian) using an Ultra-Micro quartz cell (Hellma) by taking the area under the curve from 495 to 650 nm. EGFP fluorescence values were normalized to the bulk protein concentration determined via the Bradford assay (Thermo Scientific), and then normalized against the controls to determine per cent knockdown of EGFP.

2.6.7.2.2. EGFP silencing via siRNA and Au-nanobeacon silencing of siRNA pathway

After 24 hours of EGFP transfection, cells were treated with 10 nM of siRNA for EGFP using 1.5 μg of Lipofectamine 2000 (Invitrogen) and Opti-MEM® Reduced Serum Medium (Invitrogen) according to the manufacturer's recommendations. EGFP silencing was evaluated as described above. For Au-nanobeacon silencing of siRNA evaluation, 10 nM (concentration of beacon on NP) of Anti-siRNA Au-nanobeacon were added to the media with 10 nM of siRNA with several delays of incubation (0.5, 1, 3, 6 and 24 hours). After 48 hours, the cells were washed in 1× PBS, lysed with water and collected for analysis of EGFP recovery as above.

2.6.7.3. microRNA-21 silencing using Au-nanobeacons

Cells were seeded at a density of 1×105 cells/well in 24-well plates and grown for 24 hours prior to incubation with 10, 30 and 50 nM Anti-miR-21 Au-nanobeacon for 24, 48 and 72 hours. After 24, 48 and 72 hours, cells were washed with 1× PBS, lysed and collected for RNA extraction and confocal imaging.

2.6.8. Real-time RT-PCR

2.6.8.1. Real-time RT-PCR after *in vitro* transcription

To evaluate the expression of the *c-myc* transcript, Real-time RT-PCR was performed. Real-Time PCR amplification was performed in a Corbett Research Rotor-Gene RG3000 using SYBR GreenER Real-Time PCR Kit (Invitrogen) according to manufacturer's specifications in 50 µl reactions containing 6 µl of cDNA from HCT-116 cells, 1× SYBR Green SuperMix and 200 nM of primers – MYCforward and MYCreverse. The amplification cycle conditions consisted of:

1. 2 min 50˚C
2. 10 min 95˚C
3. 30 s 95˚C
4. 30 s 60˚C
5. 30 s 72˚C
6. 10 min 72˚C

50 cycles

Data was collected from three independent experiments.

2.6.8.2. Real-time RT-PCR after silencing

Total RNA was extracted from the cell line as explained earlier and used for qRT-PCR to evaluate expression of EGFP, miR-21 and β-actin. cDNA was attained by subjecting 1µg of total RNA to Reverse Transcriptase with 200U of Revert-AidTM M-MuLV Reverse Transcriptase (Fermentas) according to the manufacturer's specifications, using 20 µM of EGFP and β-actin reverse primers and miR-21 loop primer, annealing at 42°C for 1 h and 70°C for 10 min to reverse transcriptase inactivation.

Real-Time PCR was performed in a Corbett Research Rotor-Gene RG3000 using SYBR GreenER Real-Time PCR Kit (Invitrogen) according to manufacturer's specifications in 50 µl reactions containing 2 µl of cDNA from HCT-116 cells, 1× SYBR Green SuperMix and 200 nM of the appropriate primers. The amplification conditions consisted of:

1. 2 min 50˚C
2. 10 min 95˚C
3. 30 s 95˚C
4. 30 s 52˚C 40 cycles
5. 30 s 72˚C
6. 10 min 72˚C

All data originated from three independent experiments. PCR amplification products were subjected to agarose gel electrophoresis (2% agarose, TBE 1×, 75 minutes at 90V, GelRed™ staining visualized under UV light) to confirm amplicons' molecular weight: 158 bp (β-actin), 792 bp (EGFP) and 75 bp (miR-21). As the difference of PCR amplification efficiency of EGFP, miR-21 and β-actin products was less than 5%, qRT-PCR data were derived from 2-ΔΔCT using β-actin expression levels as reference [fold-induction was calculated by the Ct method as follows: ΔΔCT = (Ct EGFP(or miR-21) – Ct β-actin)treated for EGFP(or miR-21) - (Ct EGFP(or miR-21) – Ct β-actin)untreated] [165].

2.7. Confocal Microscopy

All confocal microscopy samples were prepared as described above for EGFP silencing and recovery and miR-21 silencing. Cells were fixed with 4% paraformaldehyde in PBS for 15 min at 37ºC and mounted in ProLong® Gold Antifade Reagent with DAPI (Invitrogen) to allow for nuclear staining. Images of cells were taken with a Confocal Laser Point-Scanning Microscope Zeiss LSM 510 META. Once optimized, the same microscope settings were used throughout. The laser lines used for excitation were 405 nm for DAPI (nucleus), 480 nm for EGFP, and 561 nm for Cy3 (Au-nanobeacons).

2.8. Cytotoxicity evaluation

Standard MTT [3-(4,5-dimethylthiazol-2-yl)-2,5-diphenyltetrazoliumbromide] reduction assay (Invitrogen) was performed to determine cytotoxicity following transfection with Au-nanobeacons, siRNA and ssRNA complexes as described above. After 24 hours, 100 µl of Au-nanobeacons were added to the wells and cells further incubated for 48 and 72 hours. Following medium removal, cells were washed twice with sterile PBS and incubated for 2 hours with 300 µl of fresh medium with serum supplemented with 16.7 µl of sterile MTT stock solution (5 mg/mL in PBS). Next, medium was removed, formazan crystals resuspended in 300 µl of dimethyl sulfoxide (Sigma), and absorbance measured at 540 nm as a working wavelength and 630 nm as reference using a Microplate reader

Infinite M200 with Absorbance module (Tecan, Switzerland). Cell viability was normalized to that of cells cultured in the culture medium with PBS treatment.

2.9. Statistical analysis

All statistical analysis were performed with SPSS statistical package (version 15, SPSS Inc., Chicago, IL) using a Paired-Sample T-test. All experiments, unless otherwise stated, were performed in triplicate. All error bars used in this report are ± standard deviation of at least three independent experiments.

CHAPTER 3. Component analysis

The literature on the use of AuNPs as modulators of fluorescence for the development of biosensors is vast but not always clear. Reports presented by different groups on this subject are not always comparable in what concerns both photophysical studies and biological applications. As described in Chapter 1, there are several factors that can influence metal-induced modulation of fluorescence, such as the overlap of the spectra from NPs and fluorophores, the physical properties of the NPs (composition or size) or even the properties of the fluorophores. The different experimental setups used in different experiments can be the cause for such apparent disparity among published data. Often, the complexity of the used systems is not thoroughly analysed and particular properties of the nanoparticles such as the surface capping or the specific characteristics of the medium are overlooked. On the other hand, the application to biological scenarios usually takes nanotechnology devices as tools and neglects the understanding of the interaction between the involved nano-elements and their build-on components.

In order to understand the metal-induced fluorescence modulation and later use as a biological sensor it was necessary to choose a system that could be used for the photophysical characterization and compatible with biological environments. Having this in mind, Chapter 3 tours through the choice of each element used for posterior work during the thesis and provides a previous understanding of the properties of the AuNPs, fluorophores and spacers as well as a first practical approach on the construction of the systems to be used later in the photophysical studies and nanodiagnostics.

3.1. Gold Nanoparticles

Literature shows an extensive use of gold nanostructures both as models for photophysics studies and diagnostic and therapeutic applications. Another popular option could be the use of silver nanoparticles. In fact, the most relevant studies about enhancement with metal nanostructures use silver nanostructures [166-168]. Silver nanostructures have been applied for the development of several diagnostic methodologies [73,133,169]. However, functionalisation is not as easy to achieve with silver as it is with gold nanostructures which would negate the possibility of using simple nanoconjugates. In practical terms the use of gold nanostructures is more convenient than any other, not only because of the fluorescence modulation properties, that are to be explored in this thesis, but also because of its higher biological compatibility when compared to other nanostructures, especially in terms of toxicity [170]. Moreover, the shape of the nanoparticles is relevant in both their spectra and their biocompatibility. In this matter, spherical nanoparticles seem to have an edge since they present an LSPR peak that is more defined and is in the visible region of the spectrum [171] as well as presenting less toxicity [172]. Under this logic, spherical AuNPs were chosen for further utilization in detriment of silver or gold-silver alloy nanoparticles.

3.1.1. Gold Nanoparticles optical properties

The interaction of an electromagnetic field with small, colloidal metallic spheres was first theoretically described by Mie [72]. By solving Maxwell's equations he established the means to predict the dependence of the plasmon band position and intensity on the size and surroundings of the metal sphere. In this work, the spectra of gold nanoparticles with increasing size in aqueous solution were predicted using the implementation of Mie's equations available in the software Mieplot [173] (prediction of Mie scattering using Cext/Cabs/Csca vs. wavelength of a gold sphere in water - IAPWS at 25 ˚C). Mieplot does not predict the molar extinction coefficient of nanoparticles but allows the prediction of their absorption cross-section. The molar extinction coefficient is related to the absorption cross-section as shown in Equation 3.1:

$$\sigma = 1000 \ln(10) \frac{\varepsilon}{N_A} = 3.82 \times 10^{-21} \varepsilon \qquad \text{(Equation 3.1.).}$$

Figure 3.1 shows the extinction spectra of nanoparticles from 30 nm (lowest distinguishable line) and 100 nm (highest extinction coefficient spectrum). A clear shift in the local surface plasmon resonance is observable for nanoparticles bigger than 40 nm along with an increase in the extinction coefficient. For nanoparticles with size ranging from 5 nm to 20 nm there is no observable change in the LSPR peak but the increase in molar extinction with the size of the nanoparticle is visible. Figure 3.2. depicts the calculated spectra for nanoparticles with size ranging from 5 nm to 20 nm according to Mie's solution of Maxwell's equations.

Mie's solution does not only predict the spectra of spherical metallic nanoparticles but also allows a theoretical assessment of its scattering and absorption component. The behaviour of both components with the increasing AuNPs size was also calculated using Mieplot [173] and the extinction coefficient at the peak was selected for the LSPR extinction coefficient and for both its components as shown in Figure 3.3 and 3.4. According to the figures, smaller nanoparticles have a very little contribution from the scattering component to the extinction coefficient and the absorption component is completely dominant for nanoparticles up to 40 nm. Only nanoparticles larger than 40 nm start to show some relevant contribution from the scattering component to the extinction coefficient – Figure 3.4. On the contrary, AuNPs larger than 85 nm present a dominant scattering component in the extinction coefficient. Light reaching AuNPs with this range of sizes will be largely scattered back rather than absorbed.

It is important to notice that the radiating plasmon theory proposed by Lakowicz suggests that the way a molecule in the proximity of a nanosurface is influenced can be dependent on the proportion between the absorption component and the scattering component of the extinction [15,107]. Thus, the

use of smaller AuNPs will lead to a scenario more favourable to quenching and bigger AuNPs to one more favourable to enhancement.

3.1.2. Nanoparticle synthesis and characterization

The synthesis of AuNPs can be achieved by several different methods [174]. In order to produce nanoconjugates soluble and stable in aqueous solution it is important to produce AuNPs that can maintain in water. One of the most used methods for the production of stable AuNPs in water is the citrate reduction method [53]. This method uses citrate molecules both as reducing agent for the gold salt and to cap the AuNPs. In the end, capped AuNPs interact with the surrounding medium through the capping. In this case, citrate molecules are negatively charged at close to neutral pH which provides a superficial negative charge to the AuNPs. When reduction is achieved and the capping complete, the citrate reduction method produces AuNPs that are soluble in water and very stable over long periods. This method allows the preparation of stable AuNPs between 9 nm and 120 nm [56] but the production of AuNPs bigger than 30 nm implies the loss of monodispersity and spherical shape. To produce citrate-capped AuNPs smaller than 9 nm, a stronger reducing agent is needed. This is achieved by adding $NaBH_4$ to the reaction mixture. In this situation the citrate works mainly as capping agent. The reaction is more spontaneous to the point that heating is no longer needed [158]. By using the citrate reduction method and the co-reduction with $NaBH_4$ it is possible to produce AuNPs between less than 2 nm up to 120 nm that are capped with citrate and stable in water for long periods.

Several AuNPs synthesis methods were tested based on the citrate reduction method and the co-reduction method with $NaBH_4$. The obtained AuNPs were characterized by UV-Vis spectroscopy and Dynamic Light Scattering (DLS). An example of the DLS results is shown in Appendix II, Figure A9. The wavelength of the LSPR peak and the Z-average size ± distribution width – calculated using the intensity tool of the software provided by the manufacturer (Zetasizer Nano ZS system, Malvern Instruments Ltd, England) – are resumed in Table 3.1. After the synthesis all batches presented a reddish colour. However, after a short time (described in table 3.1.) some of the batches progress to a blue/purple colour which is attributed to aggregation [122].

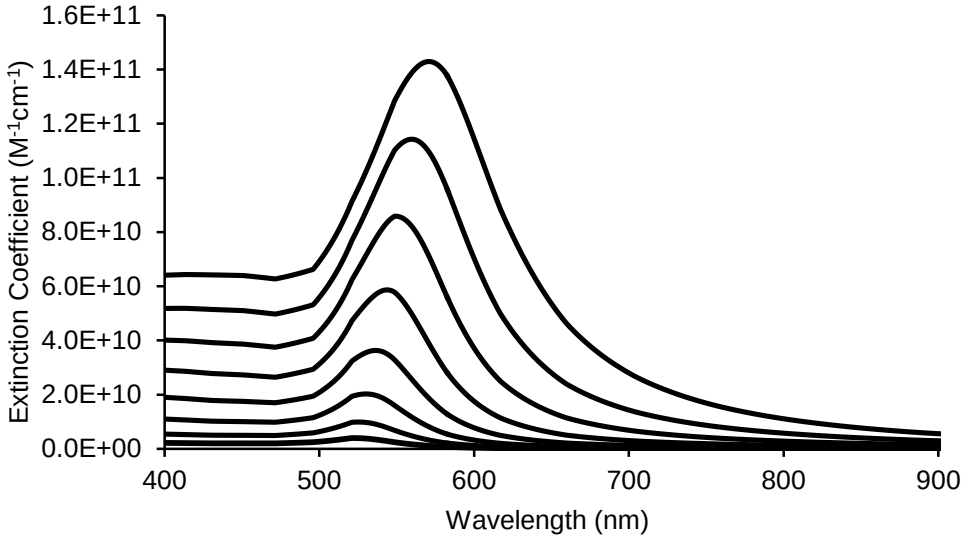

Figure 3.1. Theoretical absorption spectra of nanoparticles with different sizes. Theoretical absorption spectra of nanoparticles with size ranging from 30 nm (lower distinguishable line) to 100 nm (higher distinguishable line) in 10 nm intervals. The spectra were calculated using Mieplot [173] to obtain the absorption cross-spectra (σ) which is directly related to the extinction coefficient.

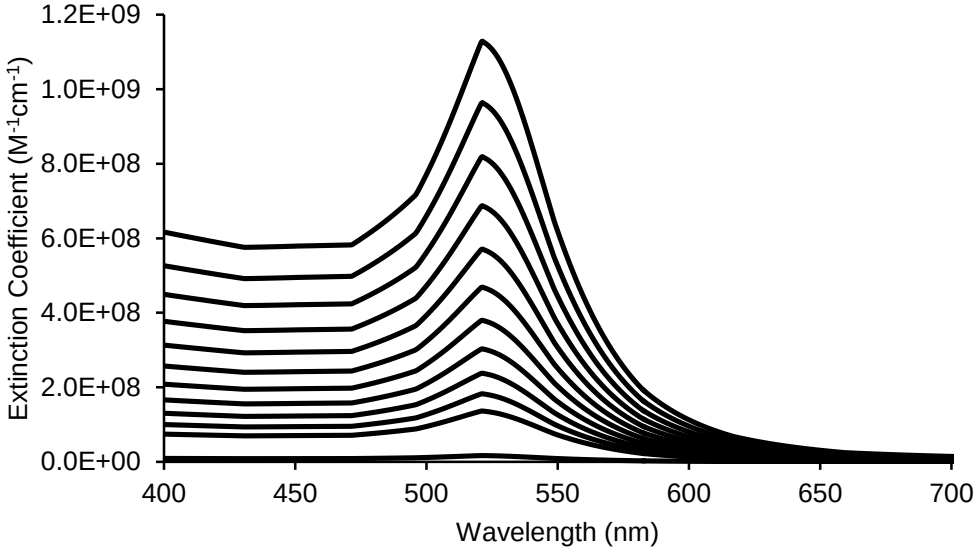

Figure 3.2. Theoretical absorption spectra of smaller nanoparticles with different sizes. Theoretical absorption spectra of nanoparticles with size ranging from 20 nm (higher distinguishable line) to 10 nm (higher distinguishable line) in 1 nm intervals. The lowest spectrum corresponds to 5 nm nanoparticles. The spectra were calculated using Mieplot [173] to obtain the absorption cross-spectra (σ) which is directly related to the extinction coefficient.

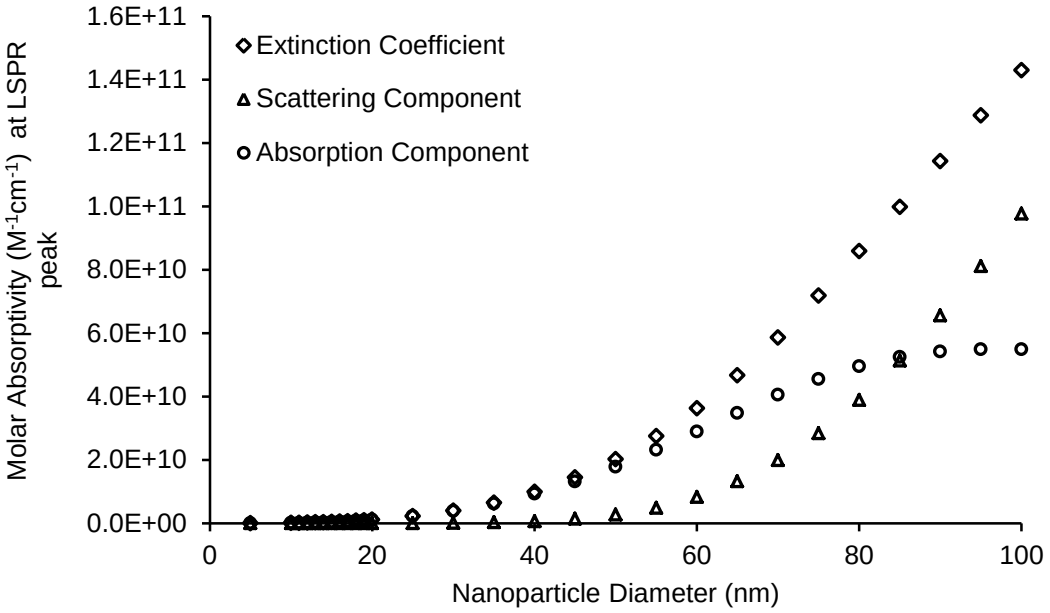

Figure 3.3. Extinction coefficient variation with AuNPs diameter. Extinction coefficient (diamonds), scattering component (triangles) and absorption component (circles) of AuNPs with sizes ranging from 5 nm to 100 nm. The values are obtained at the maximum of each spectrum.

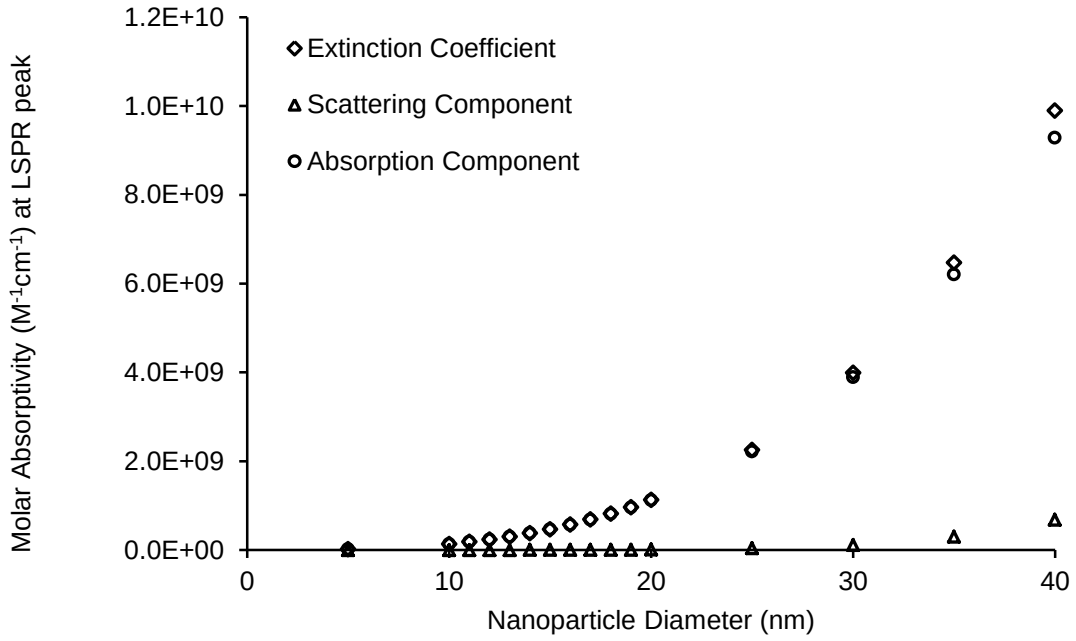

Figure 3.4. Extinction coefficient variation with AuNPs diameter. Extinction coefficient (diamonds), scattering component (triangles) and absorption (circles) component of AuNPs with sizes ranging from 5 nm to 40 nm. The values are obtained at the maximum of each spectrum.

When using the citrate reduction method, synthesis with different proportions of gold salt and citrate were arranged in order to produce AuNPs with different sizes. Citrate1 method is the most used citrate method to produce spherical AuNPs with 13-15 nm while citrate2 and citrate3 are adaptations with higher citrate:$HAuCl_4$ ratios (see Section 2.3.1 and Table 2.3 for more detailed information). Since the citrate molecule is both reducing and capping agent then an increase in the citrate:$HAuCl_4$ ratio should change the superficial area that the citrate molecules can accommodate as well as the electrochemical potential for gold reduction. Both these effects should lead to smaller AuNPs. It is of note that the nanoparticles attained via citrate3 method were not possible to characterize using DLS. Spherical AuNPs smaller than 9 nm produced by the citrate reduction method were never described in literature, which suggests that the DLS results for citrate3 should be taken with reserve. Also, the size of the AuNPs produced using citrate1 is a little larger than expected. DLS measures the hydrodynamic radius of nanoparticles that is larger than the AuNP metallic core but these AuNPs seem to be slightly larger than expected even after considering the hydrodynamic radius.

As for the AuNPs produced using the co-reduction method, only 3 of the 10 batches produced stable and monodispersed AuNPs. Curiously, the batches with AuNPs bigger than 10 nm or with bimodal distribution aggregated soon. The AuNPs produced with co-red1 precipitated during synthesis. There is no apparent relation between the conditions used since the only thing in common in co-red2, co-red7 and co-red8 is also common to the other batches. Co-red2 and co-red7 produced AuNPs with similar size while co-red8 produced smaller AuNPs.

From the 13 experimental conditions, 6 different stable batches were achieved with sizes of 19 nm, 11 nm, 8 nm and 5 nm. One of the batches could not be characterized by DLS but since it was also stable, it was considered for further analysis.

3.1.3. Gold nanoparticles functionalisation test

Whether the synthesized AuNPs can be used for further studies is not only dependent on their physical properties to modulate fluorescence but also on their potential as scaffold for other molecules.
To assess the potential of the produced AuNPs for the work developed in this thesis, all the AuNPs were subjected to a simple functionalisation with a thiolated oligonucleotide (oligotest) using the protocol as described in section 2.4.2.1. . This functionalisation protocol was already standardly used in the laboratory and widely described in literature [122,127,130,131] and oligotest had previously been used to functionalised AuNPs produced using the citrate1 method.

Table 3.1. LSPR peak and hydrodynamic diameter of the synthesized AuNPs

Method	LSPR wavelength (nm)	Z-average size (nm) ± d.w./2	Stability
Citrate1	519	19.00 ± 6.89	Stable after 2 years
Citrate2	520	11.08 ± 4.06	Stable after 3 months
Citrate3	521	≤ 1	Stable after 3 months
Co-red1	523	-	Aggregated immediately
Co-red2	518	8.9 ± 3.4 nm	Stable after 3 months
Co-red3	524	2.5 ± 0.8 nm 28.7 ± 12.7 nm	Aggregated after 1 month
Co-red4	512	2.8 ± 1.6 nm 50 ± 13 nm	Aggregated after 1 week
Co-red5	523	1.4 ± 0.4 9.5 ± 8.6 nm	Aggregated after 3 months
Co-red6	522	15.55 ± 6.64	Aggregated after 1 month
Co-red7	518	8.2 ± 3.5	Stable after 3 months
Co-red8	514	5.2 ± 1.7	Stable after 3 months
Co-red9	522	12.7 ± 6.1	Aggregated after 1 month
Co-red10	528	0.8 ± 0.3 nm 20.6 ± 8.6 nm	Aggregated after 1 week

All batches except citrate1 aggregated during functionalisation. This method has a salt aging process that is characterized by a controlled increase in ionic strength of the medium that is believed to increase the functionalisation yield. Citrate-capped AuNPs are known for their colorimetric changes upon increasing of the medium ionic strength. With an increase in salt concentration, in this case NaCl, the ionic shielding effect of the medium reduces the repulsion between the negatively charged AuNP's capped with citrate, leading to the destabilization of the colloid and aggregation of the particles. In absence of functionalised oligotest, these AuNPs tend to aggregate and precipitate [122,130] at the higher salt concentrations. So, if the AuNPs were only mildly stable, the increase in salt concentration may have induced the aggregation of the AuNPs. On the contrary, the AuNPs produced with citrate1 were stable after the functionalisation protocol indicating that the functionalisation was successful. This lead to the decision to use AuNPs synthesized with citrate1 in the following work.

3.1.4. AuNPs used in the following work

Three batches of AuNPs were synthesized using the citrate1 method. All batches were characterized by UV-Vis Spectroscopy and Transmission Electron Microscopy (TEM) - see Figure 3.5. Considering the calculated mean diameter from all the batches and comparing with the calculations made in the previous section, it is expectable that the AuNPs solutions present only residual scattering components. Still, even if only 0.1% of the extinction is attributed to scattering, it will present an extinction coefficient between 10^5 and 10^6, still considerably higher than the molar absorptivity of regular organic fluorophores.

3.2. Fluorophores

A very important component of the system is the molecule which photophysical properties are going to be modulated. A better initial understanding of the system would be required to properly choose fluorophores for future work. Due to the absence of coherent literature in the matter fluorophores were chosen according to experimental needs. The behaviour of the system was unknown at this point and that lead to the choosing of a fluorophore that simplified the system. That was achieved by choosing a fluorophore that could be bonded directly to the AuNP, preferably with a thiol group, thus permitting the system to be washed until only the AuNPs functionalised with the fluorophore were in solution for analysis. This restriction left only a few options like SAMSA, sulforhodamine or some fluorophores from the BODIPY family. From these only SAMSA was both soluble in water and commercially available. SAMSA is a fluorescein derivative, which means that its absorption and emission spectra are in the same region of the visible spectrum as the LSPR of the AuNPs and presents a relatively high quantum yield (Φ_F=0.6) and a fluorescence decaytime of 4ns in phosphate buffer at pH=8.2 [175].

After an initial understanding of the system a second fluorophore would be needed. In the case of succeeding in the interaction between AuNPs and fluorophores with overlapping spectra, other fluorophores that present less overlapping should be studied. Another desirable property would be a quantum yield near unity. If a molecule presents Φ_F=1 then for each absorbed photon there is one photon that is emitted. This also means that the constants associated with the decay of the excited electron are all related to radiative process if no other interfering mechanisms occur, *i.e.*, energy transfer. By choosing a fluorophore with Φ_F=1it would be possible to analyse the effect of the AuNPs on k_r without further interference. This way, the origin of a possible enhancement phenomenon could be traced. Less spectral overlapping can be easily achieved by choosing fluorophores that emit at longer wavelengths than the AuNPs LSPR. It was mentioned before that only SAMSA filled the conditions needed to covalently link (thiol derivative commercial availability), hence, molecules able to interact with the AuNPs through electrostatic attraction leading to adsorption at or close to the

AuNPs surface were chosen. Since the AuNPs are citrate-capped they should present a dominant negative charge surrounding the surface. Hence, fluorophores with a positive charge at the working pH (pH 8) should present a tendency to partitionate to the surface layer of the nanoparticle. These characteristics led to the choosing of Rhodamine 101 and Rhodamine B.

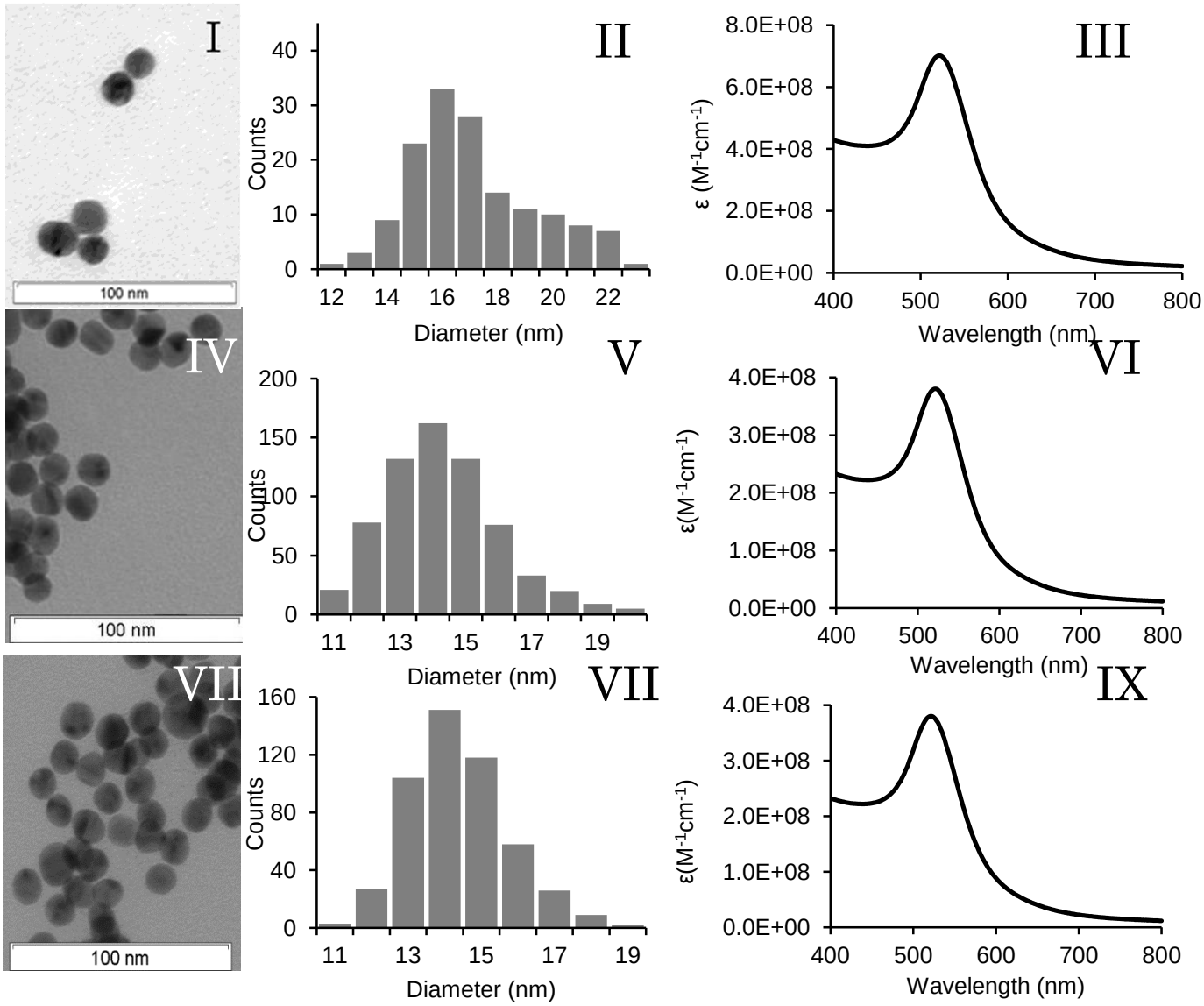

Figure 3.5. Characterization of the synthesized AuNPs. I, IV and VII – Transmission electron microscopy (TEM) of batch A, B and C, respectively. II, V and VIII – Size distribution of the synthesized AuNPs of batch A, B and C, respectively. The nanoparticles were determined to be 17.2 ± 2.9 (n=151), 14.4 ± 2.0 (n=501) and 14.6 ± 1.7 (n=501). III, VI and IX – Absorbance Spectrum of AuNPs of batch A, B, C and D, respectively.

3.3. Introducing spacer - DNA

A more complex system was required to be able to study the effect of distance in the interaction between AuNPs and fluorophores. The idea was to apply the system for biomolecule detection when properly controlled and so the introduction of a spacer that could also be used as a probe was needed. In this scenario one obvious solution was the utilization of DNA as spacer between the AuNP and the fluorophores. On one hand, DNA molecules provide a semi-rigid structure [166] that can provide a support for the fluorophores. On the other hand, DNA strands can be controlled both in size (number of bases), which is important when studying distance-dependent phenomena, and in sequence, which is relevant when using this sequence to hybridize with complementary targets.

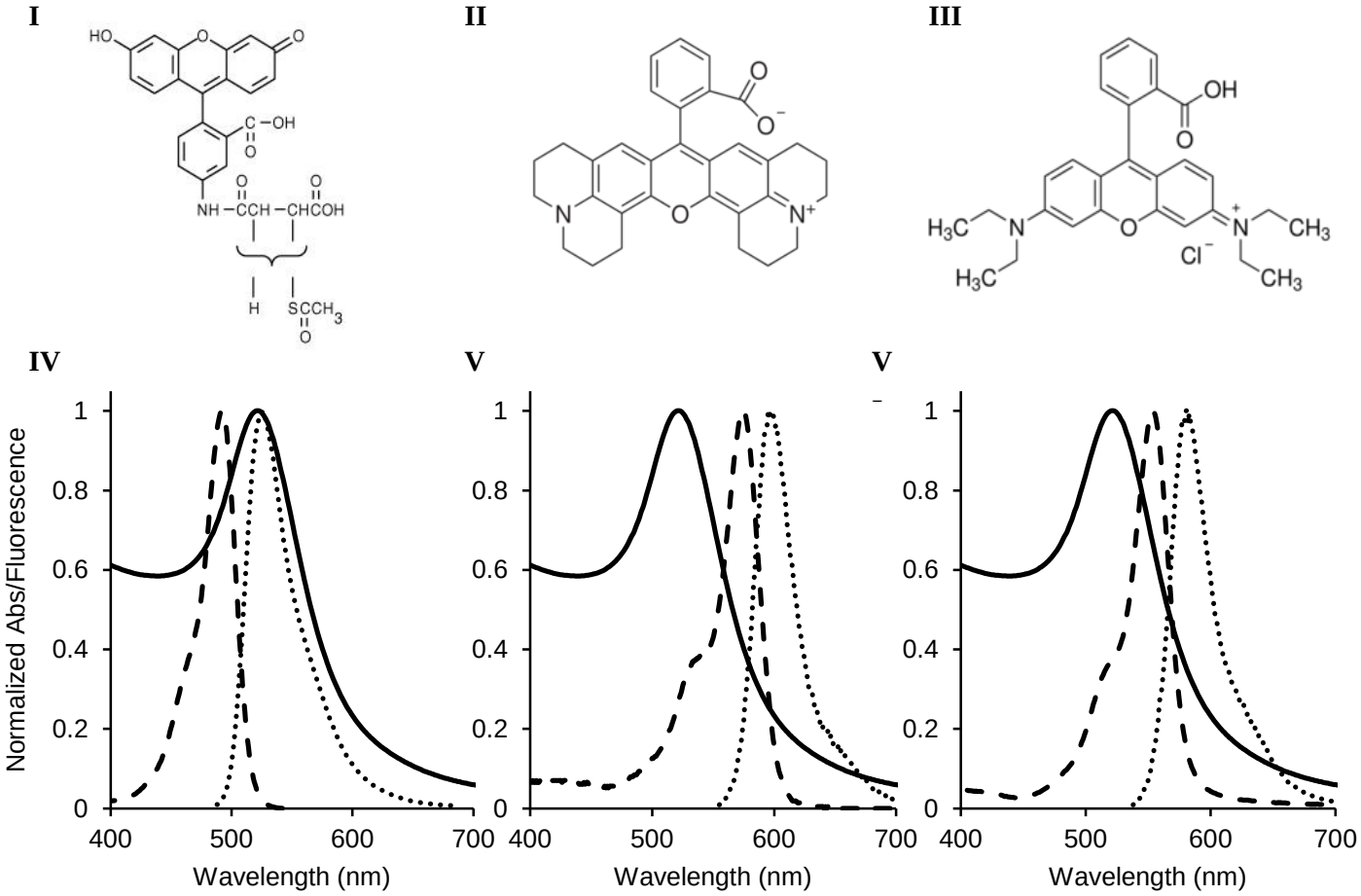

Figure 3.6. Structure and spectra of the chosen fluorophores. The molecular structure of SAMSA (I; as provided by Invitrogen), Rhodamine 101 (II; as provided by Sigma) and Rhodamine B (III; as provided by Sigma) is shown. The absorption (dashed line) and emission (dotted line) spectra of SAMSA (IV), Rhodamine 101 (V) and Rhodamine B (VI) are also shown. The black lines represent the absorption spectrum of the AuNP solution obtained via citrate1 and used in the experiments with the fluorophores.

CHAPTER 4. Fluorophore interactions with gold nanoparticles

Publications associated with this chapter:

Rosa J, Lima JC, Baptista PV (2011) Experimental photophysical characterization of fluorophores on the vicinity of gold nanoparticles. *Nanotechnology*, **22**(41):415202

Rosa J, Lima JC, Baptista PV - Portuguese Patent application PAT 105354 (25/10/2010) - "Célula de espectrofotometria para análise diferencial das propriedades ópticas de amostras líquidas" ("Spectrophotometry cuvette for the differential analysis of optical properties of liquid samples")

A better understanding of the modulation of fluorescence by gold nanoparticles must begin by the realization that not all the observable changes in the emission of nearby molecules are necessarily a direct influence of the nanoparticles on the photophysical properties of these molecules. As discussed in Chapter 3, the extinction of the nanoparticles is composed of both absorption and scattering and holds very high coefficients when compared even to the brightest fluorophores. Chapter 4 describes a study of the effects of gold nanoparticle on the molecules at their surface, with special emphasis on the absorption and emission properties.

4.1. Optical interference of gold nanoparticles

It is extremely difficult to photophysically characterize a fluorophore in close vicinity to AuNPs. AuNPs usually possess extinction coefficients at least three orders of magnitude higher than the majority of fluorophores, and it is difficult to account for the optical interference caused by their presence in solution. Most of the work concerning this topic relies on pure theoretical models that do not take into consideration all conditions associated with the presence of AuNPs in solution. For example, how much light was absorbed by a fluorophore, how much of the emitted light was re-absorbed by the AuNPs or how much of the AuNP's extinction is scattered back to the fluorophore or absorbed back by the AuNPs are effects usually neglected.

4.1.1. Cuvette development

For a more comprehensive approach of the interactions occuring between AuNPs and fluorophores in its vicinity, it is important to understand how much optical effects can lead to miscalculation of photophysical characteristics and perhaps help understand why there are inconsistent results in literature on this topic. Therefore, it is extremely important to be able to quantify how much light is being optically filtered by AuNPs. For this purpose, a two-compartment cuvette that allows to physically separate AuNPs from a fluorophore in solution without removing the optical interference caused by the high absorptivity of the nanoparticles was invented. Figure 1 shows drawings of two different views of the two-compartment cuvette (Portuguese Patent: PAT 105354).

The cuvette was designed so that the distance between the centre compartment and the outer cuvette wall was the same for all sides. Compartment Z is 5 mm wide and compartment Y is 2.5 mm in total, meaning that both Y1 and Y2 are 1.25mm each.

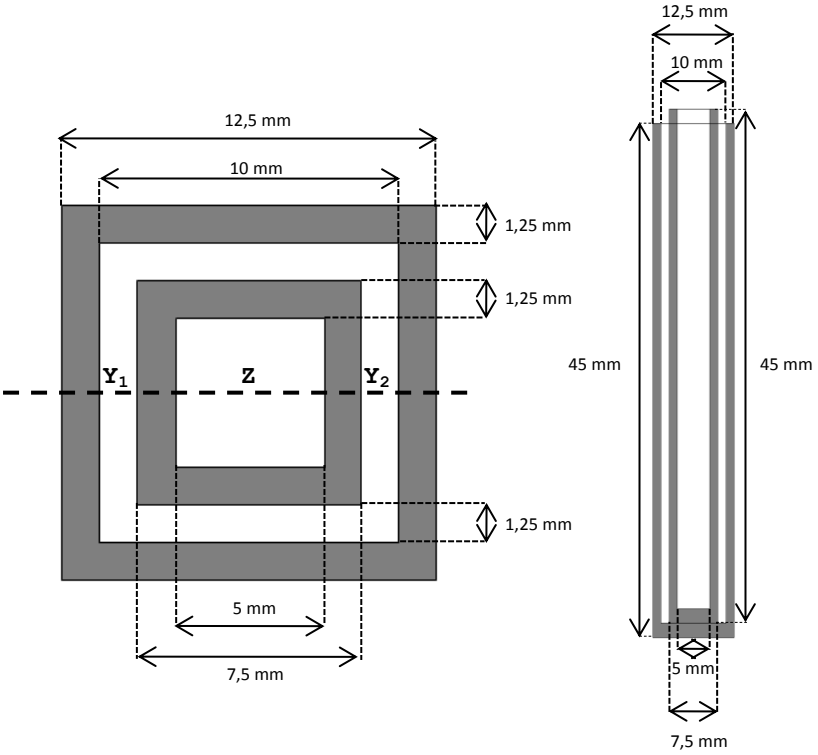

Figure 4.1. Two-compartment cuvette. Schematic representation of the axial and sagittal views of the proposed two-compartment cuvette. Y_1, Y_2 and Z represent the lightpaths for each zone of the cuvette. The horizontal dashed line represents a possible lightpath.

This instrument was conceived to be used as simulation of optical filtering without physical mixture of the AuNPs and the fluorophores. Since the objective was to study the effects of the presence of the AuNPs in the optical path on both absorption and fluorescence, the cuvette was designed with two concentric compartments. The centre compartment will pose a physical isolation of the fluorescent components while allowing the system to be used in a regular spectro*fluorimeter*. The outer compartment holds the AuNPs surrounding the inner compartment. This configuration permits the testing of AuNPs as optical filter of both incident light and exiting light simultaneously.

4.2. Absorbance interference

A light beam going through the cuvette will go through both solutions as it would go through a standard cuvette with a mixture. However, in order to compare spectra obtained using this cuvette it is essential to correct the concentrations for the path length in each situation. The comparison between the absorbance or transmittance of two solutions in different compartments and its mixture (wether in a regular cuvette or in the two-compartments cuvette) can only be made with the proper correction on

the components' concentrations according to Lambert-Beer law. Light transmittance for a given path length (b_X) is given by the following expression

$$T = \int_0^b I_0 e^{-\varepsilon C b_X} \qquad \text{(Equation 4.1)}$$

where T is transmittance, I_0 is the intensity of incident light, ε is the extinction coefficient of a compound, C is the concentration of the compound. In a scenario of a two-compartment cuvette containing two solutions equation 1 transforms into

$$T = k \int_0^b I_0 e^{-\varepsilon_a C_a b_{Y1}} e^{-\varepsilon_b C_b b_Z} e^{-\varepsilon_a C_a b_{Y2}} \qquad \text{(Equation 4.2)}$$

where a and b are two different compounds and Y and Z are the compartments of the cuvette (see Figure 4.1) and k is a geometrical factor associated with extra interaction of light with the cell walls and different mediums. The separation of the compartment Y in two blocks is due to the fact that light goes through the compartment Y twice. Notice that $X = Y1 + Y2 + Z$. If the same solution is present in both compartments of our cuvette then equation 2 becomes equation 1. In a situation of the mixture of a and b in all the compartments, the transmittance equation is

$$T = k \int_0^b I_0 e^{-\varepsilon_{a^*} C_{a^*} b_X - \varepsilon_{b^*} C_{b^*} b_X} \qquad \text{(Equation 4.3).}$$

in which lowcase a^* and b^* are the compounds in separate and lowcase a and b are the compounds when mixed together. To study if an interaction between two components of a solution is dependent on physico-chemical contact rather than just optical interference it is only necessary to match equations 2 and 3 and see if the resulting spectra are coincindental. How corrected concentrations can be used to match the theoretical transmittance or absorbance is exemplified in Figure 4.2. If the experimentally obtained spectra do not overimpose then the interaction is dependent on direct physical contact between a and b rather than on a optical effect.

The proposed cuvette and methodology were tested by mixing 0.96 µM SAMSA (Invitrogen) with 1 nM of 17nm gold nanoparticles. SAMSA has a thiol group that bonds to AuNPs. SAMSA was activated according to the manufacturer and then mixed with AuNPs in Phosphate buffer (10 mM, pH 8) with 0.05% SDS. This solution was measured in a classic 1x1cm cuvette. Using equation 4.2, we corrected the concentrations of SAMSA and AuNPs to 1.54 µM and 2.87 nM, respectively, to be used in the two-compartment cuvette. The absorption of both cuvettes was the same. The two-compartment cuvette was placed in the reference beam of a double-beam spectrophotometer and the classic cuvette was placed in the sample beam. If only optical interactions were to occur no difference would be observed. However, a clear difference can be observed as shown in Figure 4.3. With time this difference increases indicating a reaction between SAMSA and AuNPs is occuring.

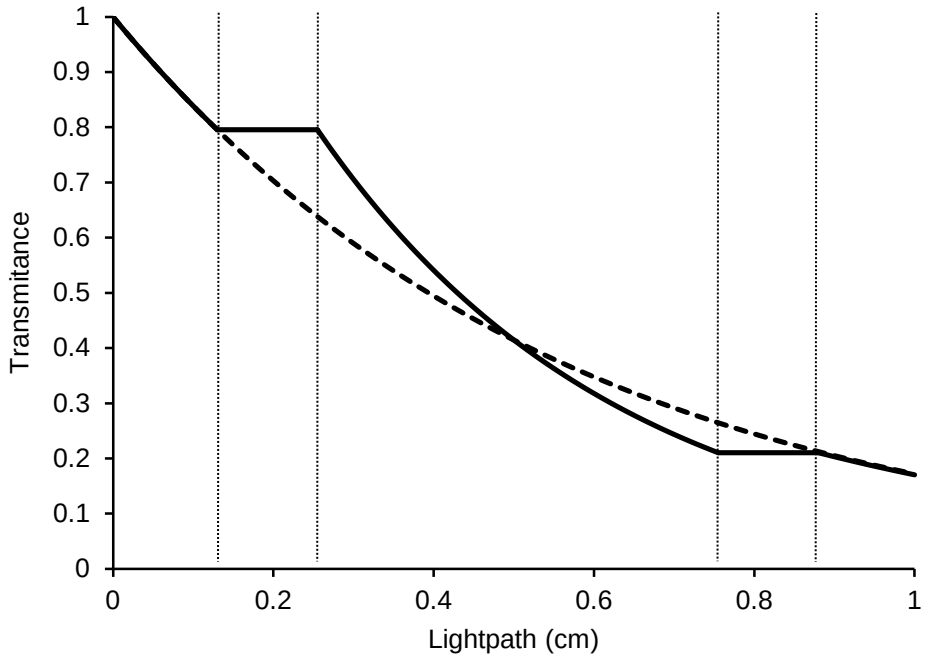

Figure 4.2. Light transmittance through absorption cuvettes. Light transmittance through a regular cuvette (dashed line) and the presented two-compartment cuvette (solid line). The dotted vertical lines represent medium interfaces in the two-compartment cuvette. In the two-compartment cuvette, light goes through AuNPs medium and into a quartz wall where no absorption occurs. Then light enters the fluorophores solution in the inner compartment and again through a quartz wall. Finally light enters the AuNPs solution and leaves the cuvette through the outer cuvette wall (not represented).

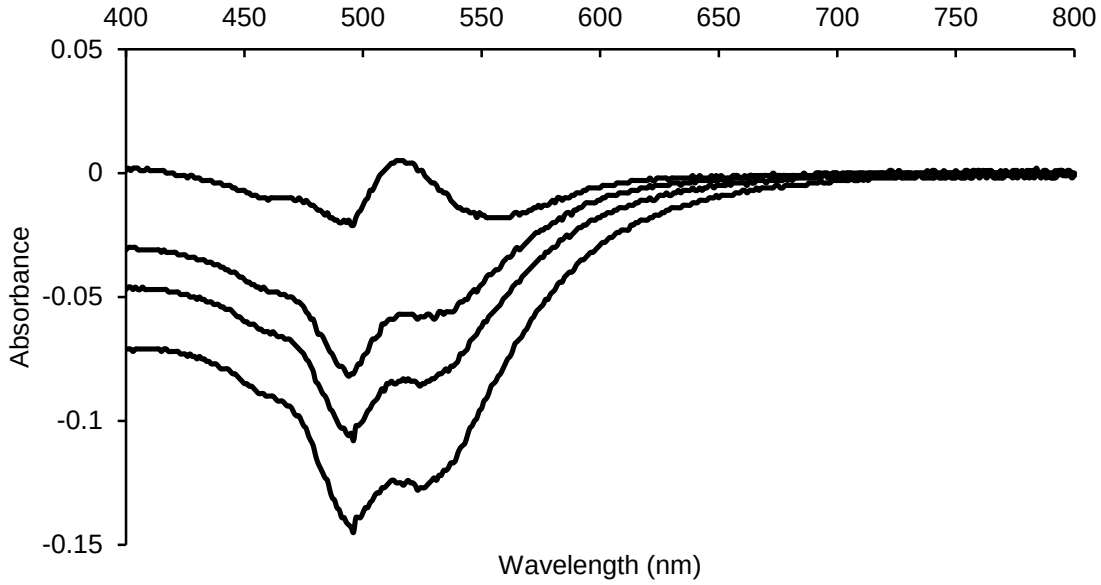

Figure 4.3. Differential spectra of the functionalisation of SAMSA on AuNPs. Differential spectra of SAMSA while bonding to the surface of AuNPs. A solution containing mixed SAMSA with AuNPs was placed in the sample beam in a regular cuvette while the reference cell holder had the two-compartment cuvette with corrected amounts of AuNPs in the outer compartment and SAMSA in the inner compartment. Spectra were taken immediately after adding SAMSA and after 1h, 2h and 3h.

4.3. Emission Interference

The optical interference of AuNPs in fluorophores' emission when in close proximity to their surface was also tested. Since the cuvette does not allow to study the optical filter created by the AuNPs on the incident light and exiting light independently, the combined effect of these phenomena was assessed. The two-compartment cuvette was used to compare either 0.96 μM of SAMSA or 0.75 μM of Rhodamine B in the inner compartment and water in the outer compartment with the same solution of SAMSA or Rhodamine B in the inner compartment and 2.5 nM of 17 nm gold nanoparticles in the outer compartment. Figure 4.4 shows the obtained spectra. About 65% of the measured emission disappears for SAMSA and about 19% of the Rhodamine B. Together, these results clearly show that the mere presence of AuNPs in the optical path can change the amount of light measured in emission. The introduction of AuNPs on the optical path not only decreases the amount of light that reaches the fluorophore in the inner compartment but also reabsorbs the resulting emmited light. This "optical filter" effect can induce serious misanalysis in fluorescence quantum yields determination. Relative quantum yield determination is based on the assurance that the reference molecules and the sample molecules are in the exact same optical conditions. The mere presence of the AuNPs on the optical path promotes a decrease in fluorescence readings and this is not due to fluorescence modulation but rather due to causing less light to reach the fluorophores and reabsorption of the emmited light. If the reference molecules are not posed with the same interference it will lead to an overestimation of quenching phenomena if observed.

The fact that the AuNPs filter is less effective with Rhodamine B than with SAMSA is due to the fact that the spectral interference depends on the extent of the spectral overlap between exciting light and AuNPs absorption and also between AuNPs absorption and fluorophore emission. This appears to be quite intuitive but it represents a massive setback in the analysis of fluorophore interactions with AuNPs because energy transfer processes are also dependent on the overlap between acceptor AuNP's absorption and donor fluorophore's emission in typical FRET [92,104] or SET [87,108] mechanisms.

4.4. Nanoparticle-fluorophore systems

Since the mere presence of AuNPs has been shown to change how incident light reaches the fluorophores there is a need to create a setup that allows for the determination of the photophysical parameters of the fluorophores when in presence of the gold nanoparticles.

To do so the quantum yield and fluorescence decay times of the fluorophores when interacting with the nanoparticles must be determined. Although the decay times can be determined in a quite straightforward measurement, the determination of the quantum yield proves to be quite troublesome. Normally, quantum yields can be determined by absolute [22,23] or relative methods [10,11].

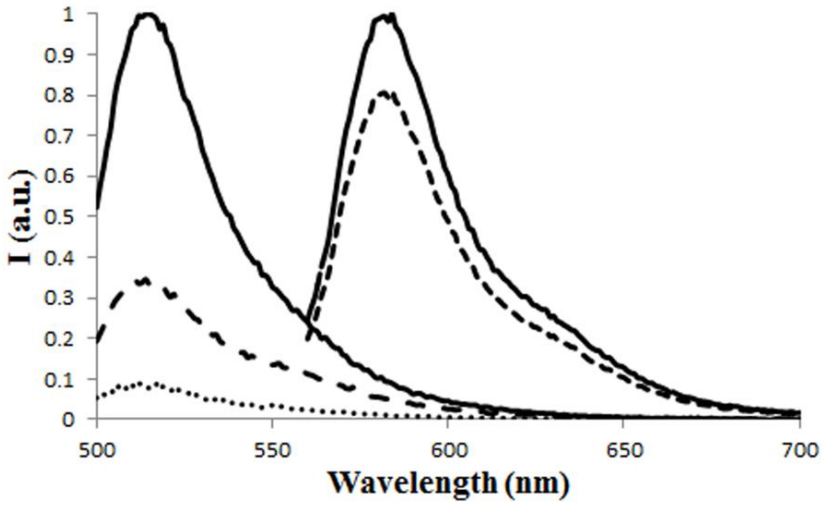

Figure 4.4. Emission spectra of SAMSA and Rhodamine B in presence and absence of AuNPs. The represented spectra correspond to the fluorophore in the inner compartment with and without AuNPs in the outer compartment. The emission spectra of SAMSA has a peak at 520 nm and the emission spectra of Rhodamine B has a peak at 580 nm. Full lines represent each fluorophore in inner compartment with water in the outer compartment, dashed lines represent the fluorophores in the inner compartment with gold nanoparticles in the outer compartment and the dotted line represents the emission of SAMSA bonded to gold nanoparticles in the same optical conditions.

Absolute methods usually rely on knowing the amount of photons that are being irradiated into a solution and quantifying the amount of photons that is being emitted using integrating spheres. When in presence of AuNPs this cannot be correctly assessed because of the phenomena described in the above sections. Quantifying the interference caused by the AuNPs in both the amount of photons that reaches the fluorophores and the reabsorption of the emitted light is not easy. On the other hand, relative quantum yield determination requires that a reference molecule with known quantum yield could be measured in the exact same optical conditions. To do so in presence of AuNPs requires that the interference with the AuNP's is all accounted for.

For a comparison between the molecule in study and the reference fluorophore to be accurate both molecules must absorb the same amount of light in similar regions of the spectra (the same absorbance at the exciting wavelength) and be in the same physic-chemical conditions. Since the objective lies in studying the effect of AuNPs in the fluorescence of nearby molecules so AuNPs must be present in solution. Therefore, instead of removing the AuNPs from the scenario, AuNPs were added to the reference fluorophore instead. This way the optical hindrance caused by the AuNPs is represented in the reference solution as well.

4.4.1. Experimentally controlled reference solutions

A fully characterized fluorophore in the presence of AuNPs is required to use as reference for classic relative Φ_F determination, ensuring the same optical conditions for both sample and reference. To do so, it is crucial that the reference fluorophore does not show variation of its photophysical properties in presence of AuNPs. This will ensure that when calculating Φ_F, the amount of light absorbed by the reference fluorophore does not change and emission re-absorption is accounted for. Furthermore, to be used as reference fluorophore for photophysical studies in presence of metal NPs, it is required that its k_r and k_{nr} remain constant both in presence and absence of AuNPs, which will mean that there is no observable interaction between the reference molecule and the AuNPs.

To determine whether there is any change in the fluorophores' photophysical properties, three similar fluorophores were used and their Φ_F determined using each other as reference both in absence and presence of AuNPs. Fluorescein, 5-FAM and SAMSA were chosen as reference fluorophores. SAMSA and 5-FAM are fluorescein derivatives so their general photophysical behaviour will be similar, making them very good reference molecules for each other. SAMSA can later be activated to expose its thiol group to the AuNPs' surface, yielding SAMSA@AuNP conjugates.

To avoid working with solutions with absorbance higher than 1, a solution of 1 nM AuNPs (ε=7.01×10^8 $M^{-1}cm^{-1}$) was used throughout the studies, which is within the well-defined range of concentrations for biomolecule detection applications. Also, higher concentrations of AuNPs result in excessively high absorbance impeding correct detection of the fluorophores' emission and for the absorbance spectra to be in the range of the spectrophotometer. Furthermore, working with higher concentrations of AuNPs could result in AuNP aggregation or fluorophore degradation, adding extra variables to the already complex experimental setup.

Data in Table 4.1 shows that Φ_F remains unaltered in presence of AuNPs, suggesting that there is no observable photophysical interaction between AuNPs and either one of the reference fluorophores (fluorescein, 5-FAM or SAMSA) at these concentrations. The fluorescence decay times were independently determined for the same experimental and optical conditions used for the Φ_F determination. No variation was observed, both for Φ_F and τ, which documents that the photophysical properties of the tested fluorophores are not being influenced by the AuNPs.

4.4.2. Quasi-covalently bonded-fluorophores

Having reference molecules that do not interact or change their photophysical properties when in presence of AuNPs allows for the determination of the quantum yields of molecules interacting with the AuNPs. By functionalising the AuNPs with fluorophores that bond quasi-covalently to its surface allows for subsequent washing steps that permit the fluorophore@AuNP complex to be studied

without interference from non-interacting species, *i.e.*, non-functionalised fluorophores. For this purpose SAMSA was activated and functionalised at the surface of spherical AuNPs with 17 nm in diameter.

Table 4.1. Experimental photophysical characterization of fluorophores in presence and absence of AuNPs. Top: Cross-determined Φ_F of the reference fluorophores in presence (+AuNPs) and in the absence (-AuNPs) of AuNPs; Bottom: Decay times of the same reference fluorophores in presence and absence of AuNPs.

sample / reference	Fluorescein		5-FAM		SAMSA	
	-AuNP	+AuNP	-AuNP	+AuNP	-AuNP	+AuNP
Fluorescein	-	-	0.80 ± 0.01	0.77 ± 0.05	0.60 ± 0.02	0.61 ± 0.07
5-FAM	0.79 ± 0.02	0.81 ± 0.04	-	-	0.60 ± 0.01	0.59 ± 0.05
SAMSA	0.80 ± 0.02	0.79 ± 0.03	0.81 ± 0.04	0.81 ± 0.07	-	-
τ (ns)	3.78 ± 0.06	3.75 ± 0.06	3.81 ± 0.05	3.79 ± 0.05	3.74 ± 0.11	3.77 ± 0.14

4.4.2.1. Local pH effect and quantification of SAMSA@AuNPs

As mentioned above, activated SAMSA will bond covalently to the AuNPs' surface, allowing for photophysical characterization at ground-zero distance. Prior to accurate photophysical characterization of SAMSA@AuNP, precise quantification of SAMSA at the AuNPs' surface needed to be performed, *i.e.*, to determine the Φ_F of SAMSA@AuNP, it is necessary to know what fraction of the total absorbed light can be attributed to SAMSA. For that purpose, the absorption spectrum of the naked AuNPs was subtracted from that of SAMSA@AuNP, where the resulting spectrum ought to correspond to SAMSA bonded to the AuNPs.

The dotted line in Figure 4.5 depicts the absorption spectra of SAMSA@AuNP in phosphate buffer pH8. The resulting spectrum does not match that of *free* SAMSA attained under the same experimental conditions. Instead, the profile matches that of a fluorescein derivative at an acidic pH. To confirm this 5-FAM and SAMSA were titrated the respective absorption spectra retrieved – Figure 4.6.

The data shown in Figure 4.6 is clear about the similarities between SAMSA and 5-FAM spectral variation with pH. Moreover, the spectrum of SAMSA@AuNP in Figure 4.5 and the spectrum of 5-FAM at pH 5 in Figure 4.6 have clear resemblance. It was not possible to compare SAMSA@AuNP with SAMSA at pH 5 because SAMSA precipitates. Still, with similar behaviour shown by both molecules, it is legitimate to compare SAMSA@AuNPs with 5-FAM.

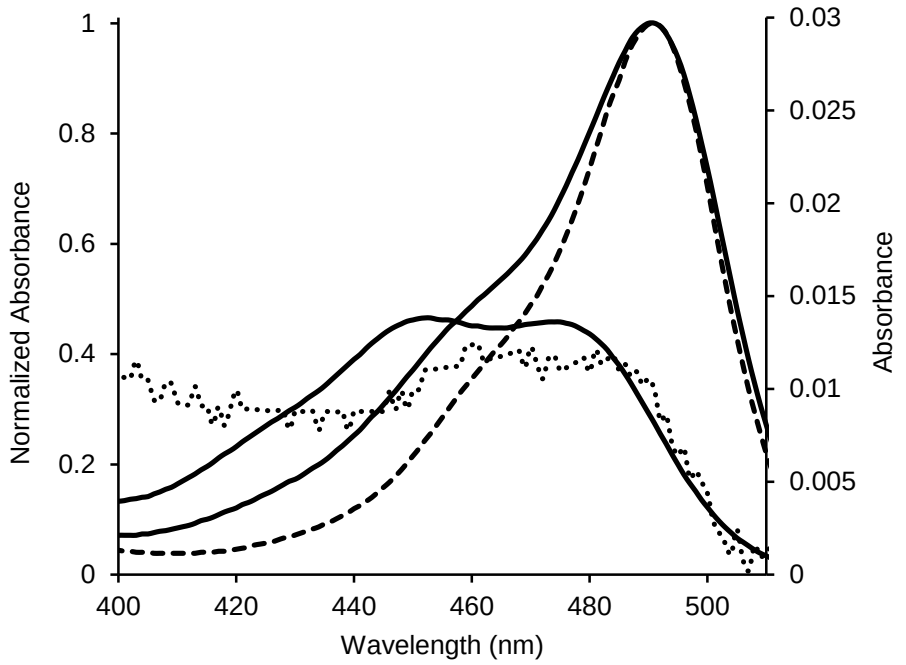

Figure 4.5. Absorbance of SAMSA and SAMSA@AuNPs. Spectra of 5-FAM at pH5 and pH8 (full line), SAMSA at pH8 (dashed line) and SAMSA@AuNP (dotted line). The spectral profile of SAMSA@AuNPs (differential spectrum obtained from subtracting the AuNPs absorption spectrum from that of SAMSA@AuNP) resembles that of 5-FAM's at pH5.

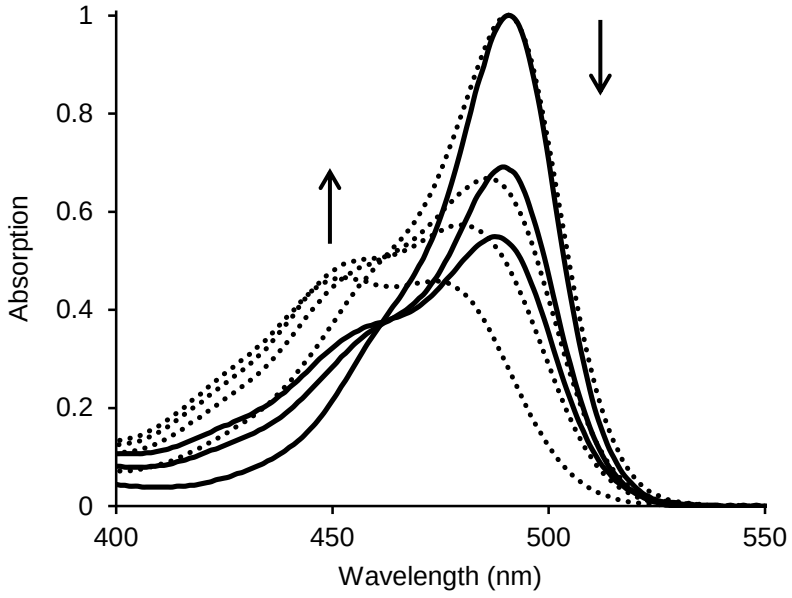

Figure 4.6. Titration of SAMSA and 5-FAM. Spectra of 5-FAM (dotted lines) and SAMSA (full line) at pH ranging from 5 to 8 are plotted. The higher absorbing spectrum of both molecules is at pH 8 and the lower at pH5. The arrows indicate the direction of the changes observed in the spectra.

This simple approach revealed that SAMSA@AuNP is likely to be sensing a pH around pH 5, the pH at the AuNPs' surface. The acidic pH is probably due to the negatively charged citrate molecules in the capping and a pH effect on fluorescence at close vicinity of AuNPs has been previously suggested [115].

To circumvent this issue two alternative methods were followed to correctly ascertain how much light was being absorbed by SAMSA: supernatant analysis and reduction of the SAMSA-thiol-Au bond. The Au:SAMSA ratio was 1:470±87 and 1:454±20, respectively.

4.4.2.2. Effect of the local pH on Φ_F and τ_F determination

The differential analysis of the AuNPs' spectra revealed a local pH effect that is relevant for the subsequent determination of Φ_F. The difference in absorbance at the excitation wavelength caused by the pH in the fluorophore needs to be taken into account, as well as the Φ_F of the fluorophore at pH 5. It is demonstrated above that non-activated SAMSA at pH 8 can be used as a reference in presence of AuNPs but this change in absorption cannot be assessed using SAMSA. To estimate what would be the loss of absorption in SAMSA if it was soluble at pH 5, the absorbance of 5-FAM and SAMSA at λ=490 nm as function of pH was plotted – Figure 4.7. The trendlines observed in both SAMSA and 5-FAM are almost superimposed which credits an extrapolation of the absorption of SAMSA at pH 5. It is now possible to determine the Φ_F of SAMSA@AuNP using:

$$\Phi_{\mathrm{SAMSA@AuNP}} = \frac{\mathrm{I_{SAMSA@AuNP}}}{\mathrm{I_{AuNP+SAMSA(pH8)}}} \times \frac{\mathrm{A_{(pH8)}}}{\mathrm{A_{(pH5)*}}} \times \Phi_{\mathrm{SAMSA(pH8)}} \qquad \text{(Equation 4.4)}$$

where I is the integrated area of the emission spectrum and A is the absorbance of the solution at the exciting wavelength. $A_{SAMSA(pH5)}{}^{*}$ represents the corrected absorbance of SAMSA at pH 5 and $I_{AuNP+SAMSA(pH8)}$ represents the integral of the emission of SAMSA in the presence of AuNPs. For a complete characterization of SAMSA@AuNP, τ_F were determined as before for the reference fluorophores. Due to the pH issue previously discussed, and for comparison purposes, 5-FAM Φ_F and τ_F at pH 5 and pH 8 were also determined and are shown in Table 4.2.

4.4.2.3. Determination of k_r and k_{nr}

From the experimental data, k_r and k_{nr} can be calculated for 5-FAM, SAMSA and SAMSA@AuNP considering that the intensity of light reaching the fluorophore at the surface and free in solution is the same. However, the intensity of light reaching the fluorophore (I^0) at the surface ought to be suffering the influence of the scattered light back from the AuNP, the amplification of the light field due to the

SPR together with a different environment with concomitant change to the refractive index. Therefore, when retrieving k_r and k_{nr}, the attained constants are affected by a factor related to the ratio of the intensity of light reaching the fluorophore (I^0) and refractive index (n).

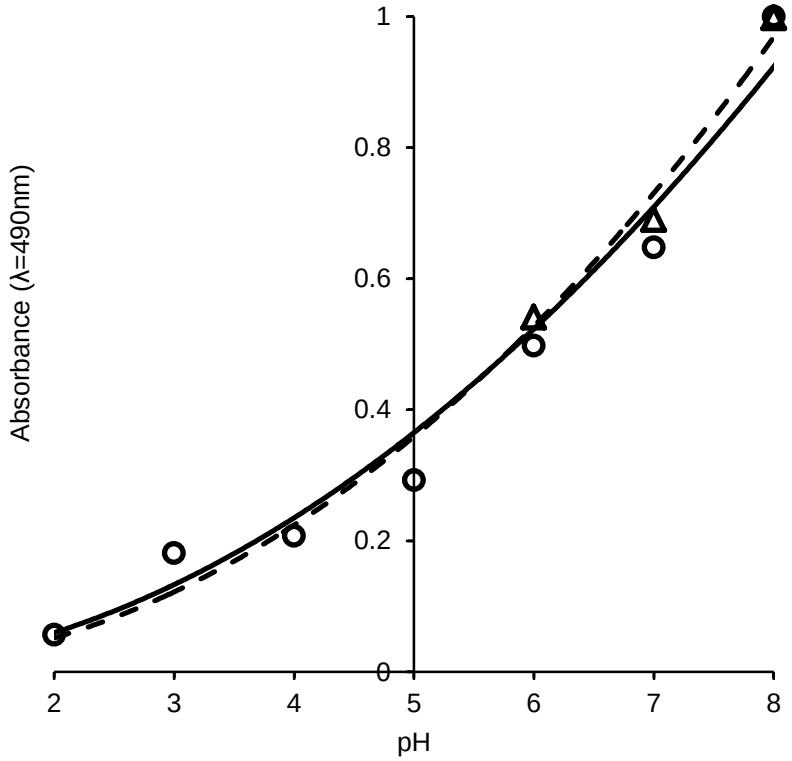

Figure 4.7. Absorbance of 5-FAM and SAMSA at λ=490 nm. Absorption at 490nm as function of pH for 5-FAM (circles) and SAMSA (triangles) with corresponding trendline (full line) and (dashed line). The trendlines are defined by the power function: y=0.015x1.9473 (R^2 = 0.973) and y = 0.012x2.1123 (R^2 = 0.975) for 5-FAM and SAMSA, respectively.

Using a relative quantum yield determination method fluorescence intensity of SAMSA@AuNPs can be established by:

$$\frac{I_{SAMSA@AuNP}}{I_{SAMSA(pH8)}} = \frac{I^0_{SAMSA@AuNP}}{I^0_{SAMSA(pH8)}} \times \frac{A_{SAMSA@AuNP}}{A_{SAMSA(pH8)}} \times \frac{\Phi_{SAMSA@AuNP}}{\Phi_{SAMSA(pH8)}} \times \frac{{n_{SAMSA(ph8)}}^2}{{n_{SAMSA@AuNP}}^2}$$

(Equation 4.5.)

where I is the fluorescence intensity on each case, I^0 is the light intensity reaching a fluorophore, n is the refractive index of the medium, A is the absorbance and Φ is the fluorescence quantum yield. SAMSA@AuNP refers to SAMSA when bound to the AuNP and SAMSA (pH 8) refers to SAMSA free in a solution with AuNPs at pH 8. If the equation is rearranged to single out $\Phi_{SAMSA@AuNP}$ and if the absorption is considered to be appropriately corrected (including pH variations) then this equation becomes:

$$\Phi_{SAMSA@AuNP}{}' = \Phi_{SAMSA@AuNP} \times \frac{I^0_{SAMSA@AuNP}}{I^0_{SAMSA(pH8)}} \times \frac{n_{SAMSA(pH8)}{}^2}{n_{(SAMSA@AuNP)}{}^2}$$

(Equation 4.6.)

It is not easy to experimentally assess neither $I^0_{SAMSA@AuNP}$ nor $n_{SAMSA@AuNP}$. However I of SAMSA free and bound to AuNPs can be measured and $\Phi_{SAMSA(pH8)}$ has already been calculated. Separating measurable incognita from immeasurable ones:

$$\Phi_{SAMSA@AuNP} \times \frac{I^0_{SAMSA@AuNP}}{I^0_{SAMSA(pH8)}} \times \frac{n_{SAMSA(pH8)}{}^2}{n_{SAMSA@AuNP}{}^2} = \frac{I_{SAMSA@AuNP}}{I_{SAMSA(pH8)}} \times \Phi_{SAMSA(pH8)}$$

(Equation 4.7.)

So, defining $\Phi_{SAMSA@AuNP}$' as the measured fluorescence quantum yield of SAMSA at the surface of AuNP, one can understand its relation to the real Φ_F through equation 4.8:

$$\Phi_{SAMSA@AuNP}{}' = \frac{I^0_{SAMSA@AuNP}}{I^0_{SAMSA(pH8)}} \times \frac{n_{SAMSA(pH8)}{}^2}{n_{SAMSA@AuNP}{}^2} \times \Phi_{SAMSA@AuNP}$$ (Equation 4.8.).

This light intensity factor propagates through the determination of k_r and k_{nr}. The constants calculated using $\Phi_{SAMSA@AuNP}$' will be called k_r' and k_{nr}'. To calculate k_r' and k_r the following expressions can be used:

$$k_r = \frac{\Phi_{SAMSA@AuNP}}{\tau} \qquad k_r{}' = \frac{\Phi_{SAMSA@AuNP}{}'}{\tau}$$ (Equation 4.9. and 4.10.)

To deduct the relation between k_r' and k_r, $\Phi_{SAMSA@AuNP}$' can be substituted. From here,

$$k_r' = \frac{I^0_{SAMSA@AuNP}}{I^0_{SAMSA(pH8)}} \times \frac{n_{SAMSA(pH8)}{}^2}{n_{SAMSA@AuNP}{}^2} \times \Phi_{SAMSA@AuNP} \times \frac{1}{\tau}$$ (Equation 4.11.)

and substituting $\Phi_{SAMSA@AuNP}$:

$$k_r{}' = \frac{I^0_{SAMSA@AuNP}}{I^0_{SAMSA(pH8)}} \times \frac{n_{SAMSA(pH8)}{}^2}{n_{SAMSA@AuNP}{}^2} \times k_r$$ (Equation 4.12.).

About the non-radiative rate constant, k_{nr} is obtained with:

$$k_{nr} = \frac{1}{\tau} - k_r$$ (Equation 4.13.).

However, only k_r' can be measured and the obtained result corresponds to k_{nr}':

$$k_{nr}{}' = \frac{1}{\tau} - k_r{}'$$ (Equation 4.14.).

Therefore, substituting τ^{-1} and k_r', the light intensity factor propagates into k_{nr} as:

$$k_{nr}' = k_{nr} + k_r + \frac{I^0_{SAMSA@AuNP}}{I^0_{SAMSA(pH8)}} \times \frac{{n_{SAMSA(pH8)}}^2}{{n_{SAMSA@AuNP}}^2} \times k_r \qquad \text{(Equation 4.15.),}$$

which simplifies to,

$$k_{nr}' = k_{nr} + k_r\left(1 - \frac{I^0_{SAMSA@AuNP}}{I^0_{SAMSA(pH8)}} \times \frac{{n_{SAMSA(pH8)}}^2}{{n_{SAMSA@AuNP}}^2}\right) \qquad \text{(Equation 4.16.).}$$

Using the deducted formula k_r, k_r', k_{nr} and k_{nr}' were calculated as shown in Table 2. Data show that bonding of SAMSA to the AuNPs leads to an increase both in k_r' and k_{nr}'. The increase in k_{nr}' may be associated to an increase of available pathways for the relaxation to the ground state, in accordance to what has been previously advocated [107].

For k_r', which has been directly calculated from experimental data, the 6 fold increase is not so easily attributable. This k_{nr}' increase corresponds to an observable increase in fluorescence, *i.e.*, a "radiative enhancement". How much of this enhancement arises from the light field enhancement or real k_r change cannot be effectively determined. Emission increase has been previously associated to a local field enhancement of fluorescence in the vicinity of AuNPs [96,97]. Analysis of data related to 5-FAM, indicates that variation due to the pH effect is negligible.

As for k_{nr}', SAMSA@AuNP shows a remarkable increase when compared to SAMSA, even considering that k_{nr}' is the lower limit of the real k_{nr}, indicating that the fluorophore is suffering a strong effect derived from being located at the surface of the AuNP. This effect is probably due to the strong overlap between SAMSA emission and AuNP absorption, which favours the energy transfer quenching mechanism. Again, comparison with the k_{nr}' values for 5-FAM shows a very small contribution from the pH to the observed effect.

Table 4.2. Φ_F, τ_F, k_r' and k_{nr}' for SAMSA@AuNP, SAMSA, 5-FAM at pH 5 and pH 8

	SAMSA@AuNP	SAMSA	FAM pH 5	FAM pH 8
Φ_F	0.11 ± 0.01	0.60 ± 0.02	0.51 ± 0.03	0.80 ± 0.02
τ (ns)	0.12 ± 0.06	3.74 ± 0.11	3.07 ± 0.02	3.81 ± 0.05
k_r' ($\times 10^8$ s^{-1})	9.40	1.60	1.69	2.10
k_{nr}' ($\times 10^8$ s^{-1})	739	1.07	1.63	0.525

Decreasing k_r values have been reported for fluorophores bonded to AuNPs when compared to those free in solution [175], and AuNPs smaller than 40 nm in diameter have been linked to a radiative quenching effect [107]. However, this data shows an increase of the k_r'. Also, in the tested experimental conditions, it is clear that the non-radiative processes are being favoured when compared to the radiative processes. Together, these results seem to indicate that there is a balance of effects, in agreement to what has been previously proposed by Lakowicz that associated the enhancement of fluorescence at the vicinity of a metal nanosurface to the scattering component of absorption [107].

4.4.2.4. Evaluating scattered light effect

One question still persists. How to assess how much of the scattered light reaches the fluorophores? It is reasonable to assume that closely located fluorophores (or at the surface) absorb most of the light scattered back from AuNP but distant fluorophores will receive increasingly less light as distance to the AuNP' surface, *i.e.*, there is a light dilution factor. This light dilution factor needs to be taken into account in quantum yield determination when comparing fluorophores spatially concentrated and close to the AuNPs' surface with those spread throughout the entire solution. To evaluate the dilution effect on the scattered light, two situations were simulated: i) the effect of the spatial distribution of the 450 SAMSA molecules bonded to one AuNP, and ii) when all the 450 SAMSA molecules are evenly dispersed in solution around each AuNP – Figure 4.8.

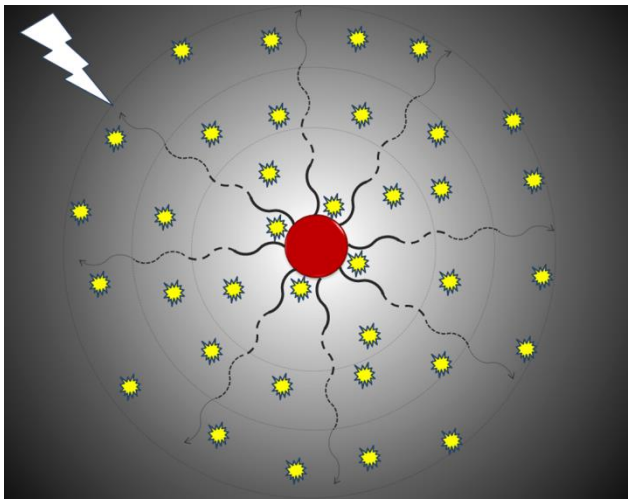

Figure 4.8. Schematic representation of the spatial dilution of scattered light from the AuNP. The red sphere represents one AuNP and the stars represent the fluorophores, localized within concentric coronas (dotted circumferences). The lightning symbolizes the incident light into the solution and the wave arrows represent the scattered light, where the full line shows strong intensity that decreases with distance to NP (dotted arrow line). The shades of grey for each corona suggest the dilution effect upon the scattered light reaching the fluorophores within that region of space around the AuNP.

The first scenario is simpler to assess since one can easily imagine a spherical AuNP with all fluorophores bond to its surface and absorbing the scattered light, *i.e.*, all fluorophores are at the same distance to the centre of the AuNP (r=8.5nm). However, in the second scenario, the free fluorophores are dispersed in solution around the AuNP at varying distances to the surface. Hence, a situation where the fluorophores are evenly distributed within theoretical spherical coronas centred on the AuNP's geometrical centre was assumed. The volume of each AuNP alone was estimated, assuming that every AuNP is equidistant from each other, and the radius of this sphere corresponds to the maximum distance a fluorophore can be from any AuNP (730 nm in this scenario). The radial distribution in three-dimensional space ($g_V(r)$) of the fluorophores was estimated using a function dependent on the distance to the centre of the AuNP (r), previously described by Tanemura [176]:

$$g_V(r) = \frac{1}{4\pi r^2} \times \frac{dK_V(r)}{d(r)} \qquad \text{(Equation 4.17.)}$$

where $\frac{dK_V(r)}{d(r)}$ is a density factor dependent on the distance and $\frac{1}{4\pi r^2}$ is spatial factor of dilution for each distance.

Assuming one AuNP upon which 450 fluorophores are bonded (as determined in section 4.2.2.), the amount of light that is diluted results from the direct comparison of the surface area of the *inner* (at the surface) and *outer* (free in solution) spheres,

$$\text{Dilution} = \frac{g_V(ri)}{g_V(rii)} = \frac{\frac{1}{4\pi ri^2} \times \frac{dK_V(r)}{d(r)}}{\frac{1}{4\pi rii^2} \times \frac{dK_V(r)}{d(r)}} = \frac{4\pi ri^2}{4\pi rii^2} = \frac{ri^2}{rii^2} \qquad \text{(Equation 4.18.).}$$

For ri the radius of the nanoparticle was used because every SAMSA molecule will be at its surface, *i.e.*, 8.5 nm. As for rii, the mean distance between fluorophores freely distributed in solution and the AuNP needed to be determined. First, the volume ascribed to each AuNP was calculated:

$$V_{singleAuNP} = \frac{V_{solution}}{\text{number of AuNPs}} = \frac{2.00 \times 10^{-6} m^3}{1.20 \times 10^{12}} = \times 1.66 \times 10^{-18}\, m^3/\text{AuNP}$$

(Equation 4.19.)

from where the maximum distance at which a fluorophore would be under the influence of a single AuNP can be calculated using the equation for the sphere volume

$$V_{singleAuNP} = \frac{4}{3}\pi {r_{max}}^3 \qquad \text{(Equation 4.20.)}$$

resulting in $r_{\max} = 2.00\times10^{-6} m$. Knowing the maximum distance a fluorophore can be from the AuNP' centre and that 450 fluorophores are inside this volume, the spatial distribution of the fluorophores as function of the distance to the NP centre can be determined

$$\sum_{8.5\times10^{-9}}^{734\times10^{-9}} \frac{K_V(r)}{d(r)} = 450$$

(Equation 4.21.)

and is given by $K_V(r) = 2.71\times10^{12}$.

This allowed for calculation of the number of fluorophores at each corona and the average mean distance to the NP, *i.e.*, 551 nm. With this value, and bearing in mind what is presented above, the light dilution factor can be calculated:

$$\text{Dilution} = \frac{\text{ri}^2}{\text{rii}^2} = \frac{(551\times10^{-9})^2}{(8.5\times10^{-9})^2} = 4205.5 \qquad \text{(Equation 4.22.).}$$

This means light is diluted in a factor of approximately 4200 times before it reaches a fluorophore free in solution when compared to a fluorophore bound to its surface.

This experimental data shows a 6 fold increase in k_r' of SAMSA bonded to the AuNP when compared to the free fluorophore. Scattered light was estimated to be 4200 times stronger at the surface at the surface than at the average distance at which the fluorophores are of the surface when in solution. This dilution factor is about 717 times larger than the increase in the measured radiative enhancement. This data supports the idea that the calculated value (k_r') is not indeed the *real* k_r. Even considering that the scattered light is only one of the sources of light available to the fluorophores, this simulation questions whether the increase of the k_r does in fact occur or if a radiative enhancement compiling both k_r variations and effective incident light changes occurs instead. The same AuNPs at the same concentrations are present and, therefore, optical filter effects can be assumed to be the same in both situations which discards any influence due to this parameter as hypothesis. If a similar spatial analysis was to be done while comparing two different sets of nanoparticles (*i.e.*, different sizes, different composition), then other parameters would have to be taken into account (*i.e.*, scattering cross-section).

4.4.3. Adsorbed fluorophores

Until this point, the effect of AuNPs on fluorophores that are chemically attached to their surface and that have a complete spectral overlap with their LSPR was studied. This provided the tools to handle the obtained data and how to circumvent the problems posed by the presence of AuNPs in solution.

Still, the interaction of fluorophores that do not overlap as much with the LSPR is required to understand how the enhancement/quenching dichotomy works. Moreover, since no other attachable fluorophores are available, the study of fluorophores that are in solution and establish adsorption equilibriums requires further insight. Rhodamine 101 (Rh101) and Rhodamine B (RhB) were chosen for subsequent studies. The reasons for which Rh101 and RhB were chosen lie on three different aspects. Firstly, at our working pH (pH 8) both rhodamine molecules are positively charged, which promotes adsorption on the negatively charged AuNPs' surface. Secondly, the fact that both Rh101 and RhB have less spectral overlap with the AuNPs than SAMSA. And finally, Rhodamine 101 has a published quantum yield very close to 1 [177,178] RhB has a quantum yield around 0.6 [178], which means that in case of an increase in the measured k_r could show significant evidence to support the idea that the light scattered back from the AuNPs can be a major cause of the fluorescence enhancement.

4.4.3.1. Absorption of Rhodamine B at AuNPs' surface

The interaction of RhB and AuNPs was assessed using a double beam spectrophotometer. By placing a solution containing of AuNPs in the reference beam while a mixture of RhB and AuNPs were placed in the sample beam. A solution of 10 μM of RhB and 1 nM of AuNPs was prepared. Figure 4.9 (full line) shows the typical spectra of RhB in water. With time, the absorption of RhB decreases, stabilizing after 16 hours. The final spectrum shows 15% less absorbance than the initial amount as seen in the dashed line of Figure 4.9.

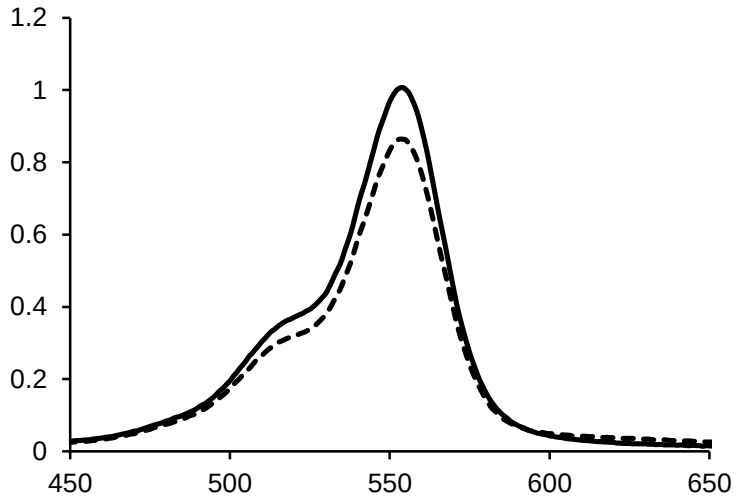

Figure 4.9. Differential spectra of RhB in presence of AuNPs. Differential spectra of RhB after mixing with AuNPs. One spectrum was taken right after mixing (full line) and another after 16 hours of equilibration (dashed line).

The interaction of RhB with AuNPs also induces an absorption decrease that affects the determination of both k_r and k_{nr} as occurred with SAMSA. At this point several hypotheses can be dropped such as a local pH effect, similar to what happened with SAMSA, or some kind of aggregation as can be found in literature [35]. The first hypothesis is not excluded but is not very probable since changes in pH are not expected for RhB at this range of pH [179], especially considering that the surface of the AuNPs appears to be even more acidic than solution pH. As for the second hypothesis, it is a lot more probable since the concentration of RhB used is much lower than the concentration at which aggregation is described [35]. Nonetheless, while this work was still in progress, a much more plausible explanation was suggested in the literature [180]. According to the authors a decrease in the absorption of RhB in presence of AuNPs can be explained by the coupling of optical transitions of the RhB and plasmonic oscillations in AuNPs.

It would be interesting to see how coupling with AuNPs would affect the photophysics of RhB using a similar system to the one used with SAMSA. To do so it would be necessary to know the amount of RhB interacting with the AuNPs. By centrifuging the AuNPs and analysing the supernatant this would be very simple to achieve. However, the interaction with RhB seems to decrease the stability of the AuNPs and leads to AuNP aggregation that was observed every time centrifugation was tried. Since the AuNPs form aggregates, it is impossible to know whether the RhB molecules that were interacting with them will maintain this interaction or be released back to solution. Without this quantification it is impossible to assess how the absorption of RhB@AuNP is changing which denies the follow up work on photophysics. An analysis on the modulation of fluorescence of RhB during the interaction with AuNPs was also attempted but the obtained results were unsystematic. This also denies a global analysis of the interaction between this pair.

4.4.3.2. Absorption of Rhodamine 101 at AuNPs' surface

The strategy used for RhB was also followed for Rh101. The differential absorption spectra of the solution containing 1.3 µM Rh101 and 1 nM of AuNPs were recorded every two hours for 16 hours after mixing both components as shown in Figure 4.10.

During incubation, a clear change to the absorption spectra is observable with a significant decrease of the absorption peak at 573 nm, and the appearance of additional absorption bands at 475 nm and 511 nm. After 10 hours, no further changes were detected indicating that adsorption equilibrium was achieved. These spectral changes are absent from Rh101 solutions without AuNPs and have never been reported. Though novel for Rh101, Rhodamine 6G and RhB aggregation was shown to induce similar spectral changes in the milimolar concentration range [35,181]. This may suggest that either

the AuNPs induce aggregation of Rh101 at lower concentrations, or some interaction of the optical transitions of Rh101 and the AuNPs is suggested to occur with Rh101 when adsorbed to AuNPs [180]. Other causes, like the pH at the surface of the AuNP as discussed for SAMSA are less likely since Rh101 does not present spectral changes in water between pH5 and 8 as shown in Appendix V.

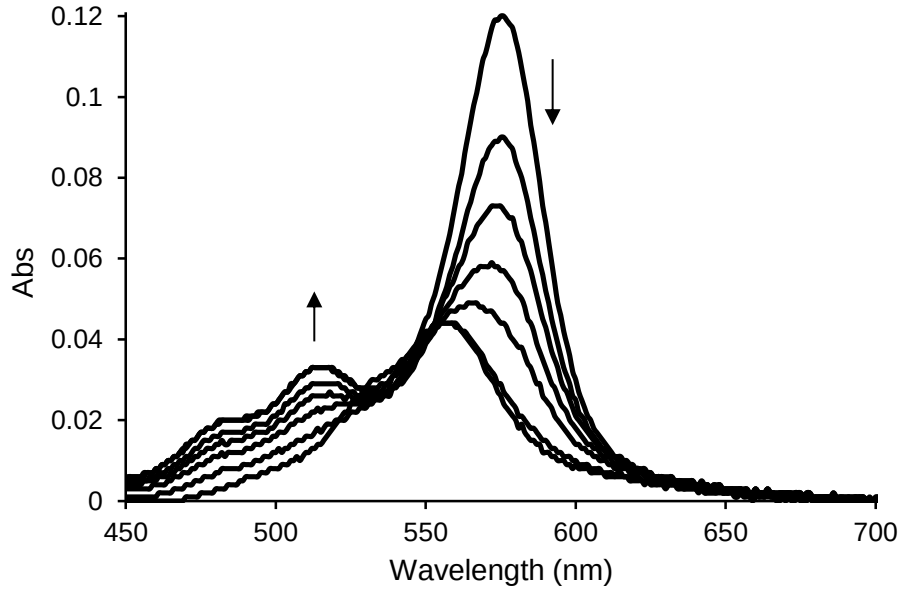

Figure 4.10. Rh101 absorption spectra over time in presence of AuNPs. Differential absorption spectra of Rh101 mixed with AuNPs using AuNPs as reference at two hour intervals for 10 hours and then after 16 hours. The absorption spectrum with highest value at 570 nm was recorded immediately after mixing (0 hours).

Whatever is cause for the change in absorption, this will affect the amount of absorbed light at the excitation wavelength and will, once again, introduce significant error in interpreting the photophysical parameters, *i.e.*, there will be a reduction in emission intensity due to reduction of the amount of light absorbed by Rh101 and this reduction can be erroneously assigned to excited state quenching if the changes in absorbance are not taken into account.

4.4.3.2.1. Determination of the molar absorptivity of Rh101@AuNP

For a quantitative analysis of the AuNP-Rh101 interaction, the number of fluorophores that are in fact interacting with the AuNPs' surface must be determined. Since a mixture of Rh101 interacting with the AuNPs and free Rh101 will coexist in the vial, the absorption spectrum reflects the absorption of the mixture. To split the individual contributions, the mixture was centrifuged 3 times and the amount of Rh101 in the supernatants measured using UV/Vis absorption spectroscopy. As little as 5.66% of the added Rh101 was recovered in the supernatants, meaning that 1.23 µM were interacting with or at

the surface of the AuNPs. This corresponds to 84% coverage of the AuNPs' surface, assuming that one Rh101 molecule has a dimension of 7Å x 6Å and that the AuNPs are 14 nm in diameter (see Chapter 3, batch 2 of cit1 method).

The free Rh101 shows an absorbance peak of 0.117 at 573 nm. After the partition equilibrium to the AuNPs is complete, the absorbance at 573 nm decreases to 0.029. Using the concentrations of free and adsorbed Rh101 and the extinction coefficient of free Rh101 (ε(573nm)=90000 $M^{-1}cm^{-1}$ [182]), the extinction coefficient of the adsorbed Rh101 can be estimated through equation 4.23:

$$\mathrm{Abs(total)} = \mathrm{C(Rh101)}\varepsilon\mathrm{(Rh101)b} + \mathrm{C(Rh101@AuNP)}\varepsilon\mathrm{(Rh101@AuNP)b}$$

(Equation 4.23)

where C(Rh101) and C(Rh101@AuNP) are the concentrations of Rh101 free in solution and at the AuNPs' surface, respectively; ε(Rh101) and ε(Rh101@AuNP) are the molar absorptivity at 573 nm of Rh101 free in solution and at the AuNPs' surface, respectively. From here, ε(Rh101@AuNP)=18246 $M^{-1}cm^{-1}$ at 573 nm is obtained.

The observed changes, be it in the case of aggregation or coupling, will have a strong impact on the photophysical analysis as, upon adsorption to the nanoparticle and considering the excitation wavelength (absorption maximum observed in water, 573 nm) Rh101 absorbs significantly less light when compared to free Rh101. Consequently, a low fluorescence response will be observed not due to quenching of the excited state but rather to the decrease in absorption at the excitation wavelength.

4.4.3.2.2. Fluorescence modulation of AuNPs on Rh101

The experimental setup used in 4.3.2 was repeated but the emission of Rh101 was monitored to assess the impact on the photophysical parameters leading to quenching or enhancement of fluorescence. To avoid corrections relative to the amount of light absorbed by Rh101 in the free/adsorbed condition, the isosbestic point was chosen as excitation wavelength (λ=546 nm). Figure 4.11 shows the emission spectra as function of time.

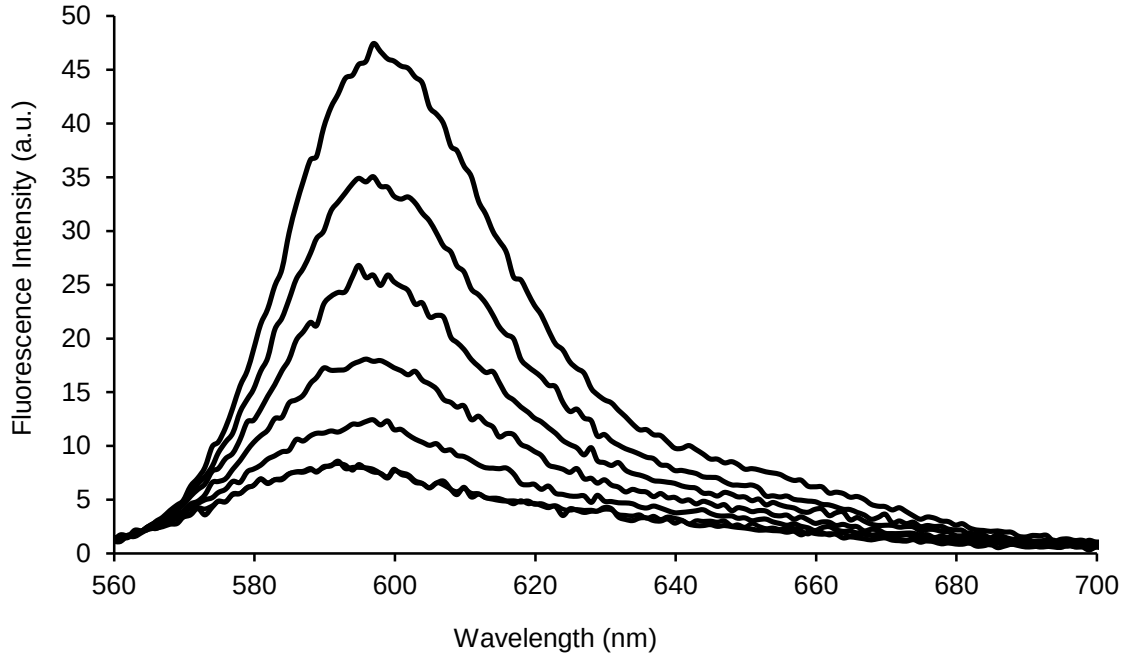

Figure 4.11. Rh101 emission spectra variation over time in presence of AuNPs. Fluorescence spectra (excitation at λ=546 nm) of the mixture Rh101:AuNPs recorded at two hour intervals for 10 hours and then after 16 hours. The emission spectrum with highest value at 596 nm was recorded immediately after mixing (0 hours).

A decrease in fluorescence is observed throughout 10 hours and then stabilizes. The relative quantum yield can be directly calculated from these data: considering that the in the first spectrum no or very little interaction between Rh101 and AuNPs occurs, the fluorescence intensity can be considered to correspond to free Rh101 with Φ_F (Rh101)=1 [177]. Note that the same solution is always being measured and the global absorbance remains constant because excitation is occurring at the isosbestic point. Knowing that the measured fluorescence intensity is the sum of the fluorescence of Rh101 interacting with AuNPs and the fluorescence of free Rh101,

$$I_F(\text{solution}) = I_F(\text{Rh101@AuNP}) + I_F(\text{Rh101}) \qquad \text{(Equation 4.24)}$$

and that

$$I_F = I_0 \Phi_F A \qquad \text{(Equation 4.25),}$$

then

$$I_0 \Phi_F A(\text{solution}) = I_0 \Phi_F A(\text{rh101@AuNP}) + I_0 \Phi_F A(\text{Rh101}) \qquad \text{(Equation 4.26)}$$

where I_F is the fluorescence intensity, I_0 is the light reaching the sample, Φ_F is the fluorescence quantum yield and A is the absorbance at the excitation wavelength. I_0 is the same in all cases and the absorbance depends on the concentration according to the Lambert-Beer law ($A=\varepsilon bC$). The optical

path is the same for both cases and ε(Rh101@AuNP) and ε(Rh101) was calculated to be 26912 $M^{-1}cm^{-1}$ at the excitation wavelength (calculated from Figure 1). Therefore, if equation 4.26 is divided by the overall (free and bound) concentration of Rh101, C(solution), a dependence with the molar fractions is obtained:

$$\Phi_F\varepsilon(\text{solution}) = \Phi_F\varepsilon X(\text{Rh101@AuNP}) + \Phi_F\varepsilon X(\text{Rh101}) \qquad \text{(Equation 4.27)}$$

and Φ_F(solution) can be calculated. Considering that the initial fluorescence intensity corresponds to Rh101 alone and that the final intensity corresponds to the final mixture, a direct relation between Φ_F(solution) and Φ_F(Rh101) can be established and Φ_F(solution)=0.153. From Equation 4.25., results Φ_F(Rh101@AuNP)=0.072. In order to calculate the rate constants associated with the excited state deactivation processes, fluorescence decays were measured in the absence and presence of AuNPs at different proportions (Table 4.3.). The use of more than one concentration in this case ensures that we can assign the decay times to each form of Rh101. The fluorescence decay of the solution containing Rh101 alone is well fitted to a single exponential with a decay time of 4.1 ns. Addition of the NP and equilibration overnight leads to double exponential decays, with a decay time identical to that obtained in absence of AuNPs, whose pre-exponential factor decreases with the increase of AuNP:Rh101 ratio, and a second shorter decay time (~2 ns) whose pre-exponential factor increases with the increase of AuNP:Rh101 ratio. The decays for all concentrations are well fitted to the same decay times and the results from the global analysis are summarized in Table 4.3.

Table 4.3. Decay times, τ_1 and τ_2, and normalized pre-exponential factors, a_1 and a_2, for different concentrations of Rh101 in presence of AuNPs (different AuNP:Rh101 ratios)

	τ (ns)		Normalized Amplitudes		χ^2
[AuNP]:[Rh101]	τ_1	τ_2	a_1	a_2	
0nM:1μM	-	4.10	-	1	1.07
1nM:10μM	1.95[a]	4.17[a]	0.43	0.57	1.06
1nM:5μM	1.95[a]	4.17[a]	0.61	0.39	1.10
1nM:2μM	1.95[a]	4.17[a]	0.91	0.08	1.25

[a]global analysis of the decays for 1nM:10μM, 1nM:5μM and 1nM:2μM

In absence of AuNPs, a single decay time that corresponds to free Rh101 is obtained, whereas in the presence of AuNPs an additional decay time is obtained, which can be attributed to Rh101@AuNP. In the presence of 1 nM of AuNPs and for Rh101 concentrations less than 2 μM, almost all Rh101

molecules are adsorbed to the AuNPs. This result strengthens the previous data retrieved from the supernatant analysis, where only ~6 % of free Rh101 was recovered when a 1.3 μM solution of Rh101 was equilibrated with 1 nM AuNPs (see section 4.4.3.2.1).

4.4.3.2.3. Determination of k_r and k_{nr} of Rhodamine101@AuNPs

Similarly to what was described in chapter 4.4.2.3. k_r and k_{nr} can be estimated for both Rh101 bulk in solution and Rh101@AuNP using equations 4.9 and 4.13.. k_r of Rh101@AuNP is calculated using the calculated Φ_F(Rh101@AuNP) and τ_1 in equation 4.9, and then k_{nr} is calculated using equation 4.13. As for Rh101, the procedure is similar but the result is obtained using Φ_F(Rh101) from the literature [D16] and the measured decay time, τ_2. The calculated radiative and non-radiative rate constants are presented in Table 4.4.

Table 4.4. Radiative and non-radiative rate constants of Rh101 in presence and absence of AuNPs

	Rh101	Rh101@AuNP
k_r (s^{-1})	2.44×10^8	3.69×10^7
k_{nr} (s^{-1})	6.10×10^7	4.76×10^8

It is interesting to notice that the radiative constant (apparent or not) appears to decrease in a factor of 6.6 when in presence of AuNPs. This is coherent with the variation observed in absorption either considering that the cause is aggregation of Rh101 or coupling between plasmonic oscillator and the optical transition of Rh101. According to the Strickler-Berg equation:

$$k_r = 2.88 \times 10^{-9} n^2 \langle v_f^{-3} \rangle \int \varepsilon(\bar{\nu}) d\ln\bar{\nu} \qquad \text{(Equation 4.28.)}$$

a direct relation between ε and k_r can be established. What was observed via differential spectroscopy was a substantial decrease in ε together with a decrease in k_r if the refractive index (n) does not change appreciably. However, if the cause of this change is Rh101 aggregation, then the set of molecules being analysed is different form the initial set, and it is reasonable that it ought to have different photophysical properties.

As to the k_{nr}, a 7.8-fold increase in presence of AuNPs is observed even without significant superimposition of Rh101 emission spectra with the AuNPs absorption spectra. Energy transfer cannot be discarded as it may be occurring between Rh101 and AuNPs in such close proximity, despite the

fact that that the spectral overlap between Rh101 emission spectrum and AuNPs absorption spectrum is low.

Furthermore, the amount of light reaching the fluorophores before and after interaction with AuNPs should also be taken into account. The light scattered from the AuNPs, which will be more important to the adsorbed molecules, has not been accounted for in the fluorescent quantum yield determined above. As a consequence, Φ_F(Rh101@AuNP) is the product of the real quantum yield by the ratio I/I_0, where I is the light reaching the adsorbed Rh101 and I_0 is the light reaching the bulk solution. However, this effect cannot be appropriately accounted for and can only be corrected by an estimate of a light dilution factor as was previously described in section 4.4.2.4. So, considering that the light scattered back from the AuNP reaching the Rh101@AuNP is stronger than the average light reaching bulk Rh101, the calculated k_r value is overestimated. Still, the observed value decreases when compared to bulk Rh101.

4.4.4. Nanoparticle-DNA-fluorophore systems

In this chapter, the effects of gold nanoparticles on fluorescence of molecules chemically bonded to them were assessed. A successful method to experimentally determine the fluorescence quantum yield in presence of gold nanoparticles while accounting for the optical interference of AuNPs was also achieved. However, the problem of the amount of light reaching a fluorophore when bonded to a AuNP was not completely tacked and as result only a radiative enhancement factor can be calculated rather than the real radiative rate constant. Even when AuNPs are in solution but not bonded to the fluorophores, the light reaching each fluorophore is different from the case where bonding occurs due to a light dilution factor through space. Since this factor is dependent on the distance to the nanoparticle, the key to calculate the radiative rate constant may lie on the behaviour of the system at several distances from the AuNPs.

To explore this idea, five nanoprobes with fluorophores at different distances were synthesized (as mentioned in Chapter 2.4.2.1) and the relative Φ_F and τ were determined for each case as previously described in this chapter. The fluorophore:AuNP ratio was calculated for each distance and solutions containing 1nM of AuNPs and the correspondent amount of oligonucleotides for each case (hence assuring that the absorbance of both AuNPs and fluorophores is the same in both solutions) were prepared and its fluorescence intensity measured. This allowed for the determination of the apparent Φ_F of the nanoprobes as shown in Table 4.5. Distance was calculated from both the centre of the nanoparticle and its surface and also accounts for the Thiol-C6 spacer and a base-stacking distance of 4Å between two consecutive bases [183].

Table 4.5. Φ_F, τ, and respective distances from the fluorophore to the AuNP for SNSET probes

Nanoprobe	Distance Surface (Å)	Distance Centre (Å)	Fluorophores/AuNP	Φ_F	τ (ps)
SNSET12	55.1	125.1	63.44±3.77	0.028 ± 0.003	26.61 ± 10.68
SNSET15	67.1	137.1	61.64±6.85	0.041 ± 0.002	57.94 ± 38.83
SNSET20	87.1	157.1	52.27±4.31	0.058 ± 0.003	138.74 ± 45.34
SNSET25	107.1	177.1	44.92±3.26	0.098 ± 0.001	323.18 ± 60.22
SNSET50	207.1	277.1	37.81±1.80	0.140 ± 0.002	496.92 ± 59.85

4.4.4.1. Quantum yield and fluorescence lifetime ruler

The behaviour of both Φ_F and τ in function of distance to the nanoparticle can be predicted:

$$\tau_F = \frac{1}{\frac{1}{\tau_0}(1+(\frac{R}{R_0})^n)} \qquad \text{(Equation 4.29.)}$$

$$\Phi_F = \frac{k_r}{\frac{1}{\tau_0}(1+(\frac{R}{R_0})^n)} \qquad \text{(Equation 4.30.)}$$

where τ_0 is the fluorescence lifetime of the fluorophores when not affected by the nanoparticle, R_0 is the Förster distance, R is the distance between the nanoparticle and the fluorophore and n is the distance dependence factor. The distance factor, n, usually is 6 if a typical energy transfer phenomenon is considered or 4 if a nanosurface energy transfer mechanism is considered. By modelling the k_r, τ_0 and R_0, theoretical curves of both Φ_F and τ were fitted simultaneously into the data obtained as presented in Figure 4.12.A and 4.12.B using n=4 (dashed line) and n=6 (full line).

There are several factors that can affect the analysis of this question. The most important one is how distance is measured. DNA molecules are known to be semi-rigid with a defined structure in dsDNA. However, ssDNA is more flexible and harder to study. The reference used to choose the distance between two consecutive bases in a ssDNA strand is itself loose, referring a range of distances from 2-6 Å. The average value was chosen but some uncertainty is present nonetheless. More on this topic is related to where the measurement should start at the centre or the surface of the AuNP. Usually, the dispute lays on whether FRET or NSET is observed. In the former case a dipole-dipole interaction is considered. As such, a AuNP must be considered to provide a dipole and that is observed at the surface of the AuNPs. On the contrary, the former case is based on the idea that a point-dipole interaction occurs. Thus, AuNPs are to be considered as point particles and so distance is counted from

the centre of the AuNP. Figure 4.12 clearly shows that both fittings match the experimental results obtained for both Φ_F and τ. Both curves were determined simultaneously for each case and using the same parameters showing that the results are not only coherent but very robust.

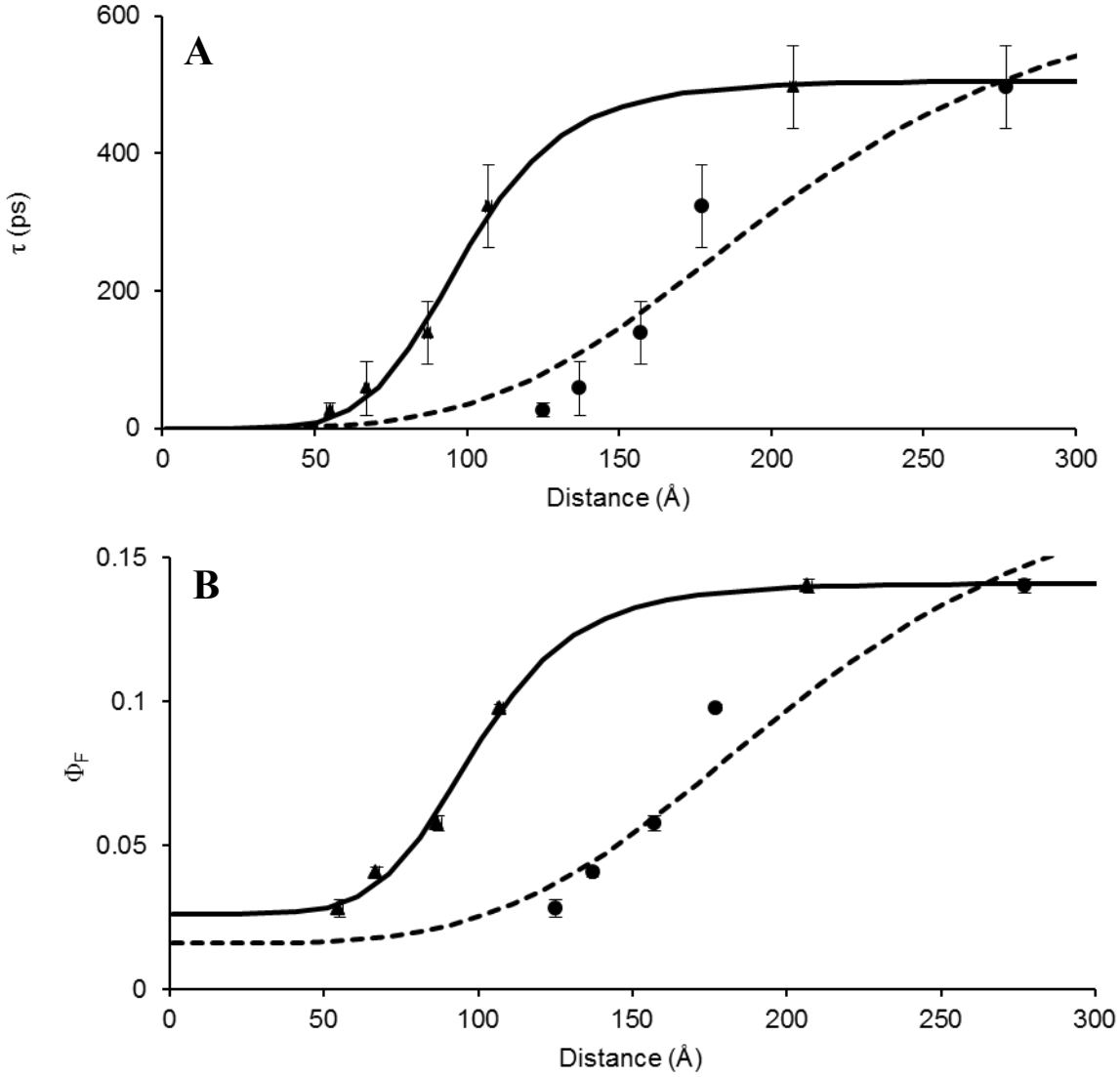

Figure 4.12. τ and Φ_F as a dependence of distance to the nanoparticle. Determined τ (A) and Φ_F (B) are shown as black circles when distance is assessed from the centre of the AuNPs and black triangles when assessed from the surface. Simulation of τ and Φ_F was executed using equations 4.29. and 4.30. with n=6 (black lines) or n=4 (dashed lines). The distance values were considered from the surface of the AuNP for n=6 and from the centre for n=4. Curves of Φ_F and τ were calculated simultaneously and using the same parameters for each n value. Error bars represent triplicates for Φ_F and duplicates in different experimental apparatus for τ.

The fitting was achieved using the least squares method. As such one way to analyse if n=6 or n=4 fit the experimental data better is to look at the error obtained in the fitting. Using n=6 fitting an error of 0.37% was obtained with an R_0 of 99.19 Å while for n=4 an error of 0.48% was found with an R_0 of 114.00 Å. Both errors are very small but a FRET-like mechanism appears to fit the data better.

Looking at Figure 4.12., the triangles appear to fit the solid line better than the circles fit the dashed line. However, in this specific case, the dimension of the AuNPs relative to the DNA strands size leads to the thought that the AuNPs' surface presents a dipole that greatly influences the fluorophore. This way, the interaction between the fluorophores and the nanoparticle should be first sensed at the surface of the AuNPs unlike what is considered in cornerstone theoretical works on the subject [93].

Similar assessments are found in literature using different nanoparticles, spacers and fluorophores [95,104,112]. This fact lead to several results but no unquestionable evidence was ever found. A clue about what may be happening is already in literature as well. Single-nanoparticle studies show that the modulation of fluorescence by AuNPs lies on a balance between enhancement and quenching [96,97]. Also, the spectral overlap between the plasmonic band and the emission of the fluorophores has been described as key for the energy transfer between them [108]. In this study, the emission of the chosen fluorophores and the plasmonic band are almost completely overlapped which should be favourable to the energy transfer mechanism and hence to a typical quenching of fluorescence through FRET. The results presented here support this idea. In a case with less spectral overlap, it can be hypothesised that the energy transfer mechanism would not be so extensive and the enhancement factor could be of greater notice.

One detail to be noticed is the stabilization of τ at around 490 ps. The influence of the AuNPs in τ of a molecule in its vicinity is dependent with distance as shown in Figure 4.12. This being the case, at longer distances the effect should be less effective and, in the limit, no effect should be observed. The stabilization of τ should be around 3.8 ns, as measured in section 4.4.2 and not at 496.92 ps. The explanation to this fact may lie on the protonation state of FAM. Fluorescein derivatives are known to have a pKa $\approx$ 6.5 [184]. At solution pH FAM would be in its dianionic form that would present a fluorescence lifetime around 4 ns. However, this lifetime can decrease in acidic pH when protonated species are formed. If the local pH is changed due to electrostatic considerations, the apparent pKa's can change dramatically. As was shown before AuNPs have local pH at the surface due to its negative charge. Also, ssDNA presents a negatively-charged backbone which added to the AuNPs could cause the pH to change enough for FAM to protonate and change its τ values.

4.4.4.2. Radiative and non-Radiative constant analysis

The data shown in Table 4.5. can also be used to calculate k_r and k_{nr}. It was previously suggested that the incident light on each fluorophore is affected by the light scattered back from the AuNPs' surface hence varying with the distance to the nanoparticle. By dividing the determined Φ_F by a light dilution factor a value closer to the real Φ_F of each fluorophore when bonded to the AuNP may be assessed. Assuming that in each probe the ssDNA used as spacer is rigid enough and that every fluorophore is in

radial disposition towards the AuNP's centre, one can calculate the sphere total area using the radius provided by each spacer. The ratio between the total area obtained for one distance and the total area obtained from another distance is directly related to the dilution of light between these two distances. So, from the measured Φ_F it is still only possible to calculate a radiative enhancement factor ($k_{r'}$, Figure 4.13.A – black circles) but if using Φ_F values corrected with a factor for the distance effect, new k_r values can be calculated and a quite different trend appears (Figure 4.13.A – white squares). Surprisingly, when comparing k_r with k_r' a clear difference is observable. While k_r appears to change only slightly with distance, k_r' decreases sharply until about 100 Å. These results suggest that the scattered light can be a major factor in the apparent increase of fluorescence rather than an effectual photophysical modulation of the radiative rate constant. Instead, AuNPs seem to increase the amount of light received by the fluorophores in its vicinity.

Taking into account that the radiative rate constant is not likely to be changing a question rises on how the non-radiative rate constant changes. When calculating non-radiative rate constant using the real radiative rate constant the differences are negligible when compared to the ones obtained using the radiative enhancement factor. This indicates that the major contribution to the k_{nr} value is not dependent on the amount of light reaching each fluorophore, strengthening the idea that k_{nr} is mostly constituted of an energy transfer process from the fluorophore to the AuNP.

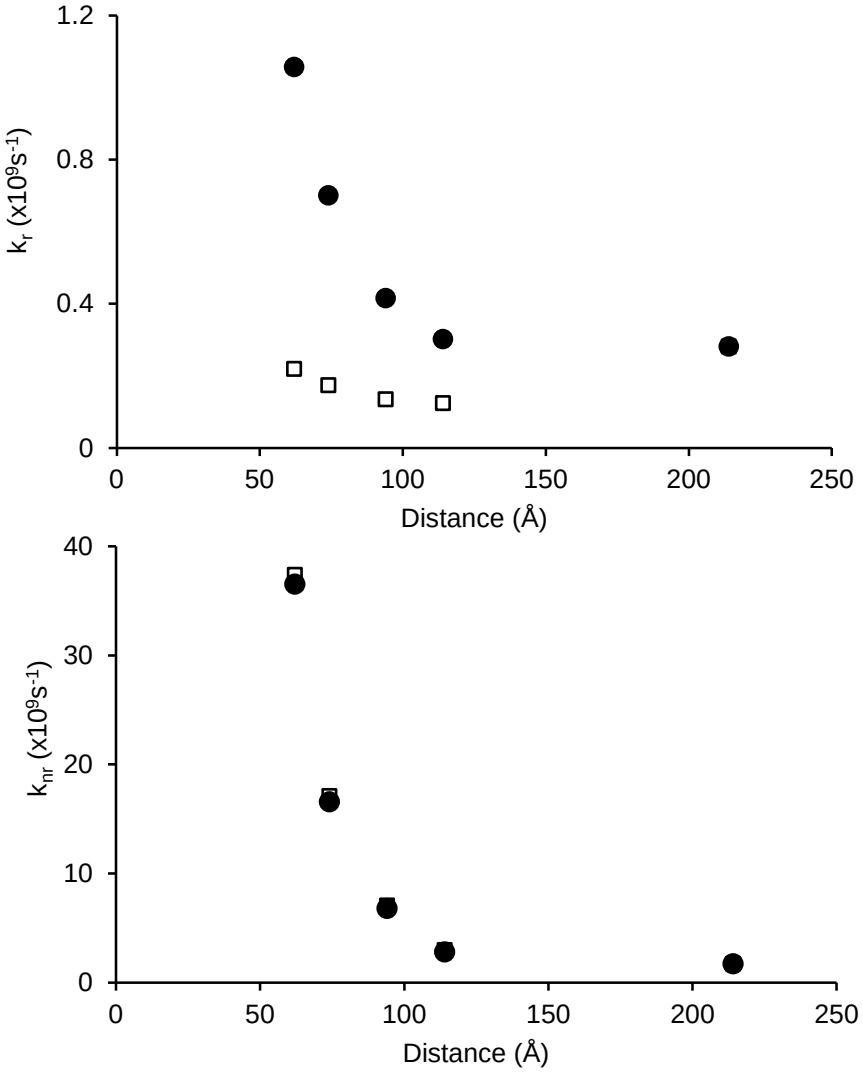

Figure 4.13. Radiative and non-radiative rate constants of FAM at different distances from AuNPs' centre. A – Radiative enhancement (black circles) and radiative rate constant (white squares) at different distances of AuNP. B- Non-radiative rate constant considering the effect of the space dilution factor (white squares) and not (blue circles).

CHAPTER 5. Nanobiophotonics

Publications associated with this chapter:

Rosa J, Conde J, de la Fuente JM, Lima JC, Baptista PV (2012) Gold-nanobeacons for real-time monitoring of RNA synthesis. *Biosensors and Bioelectronics*, **36**(1), 161-167

Conde J, Rosa J, de la Fuente JM, Baptista PV (2013) Gold-nanobeacons for simultaneous gene specific silencing and intracellular tracking of the silencing events. *Biomaterials*, **34**(10):2516-23

Systems composed by AuNPs, fluorophores and DNA are ideal for the development of theranostics methods. The combination of the properties of each of the elements produces the potential to exceed the existing methods. The final goal of this project was to apply the knowledge gathered on modulation of fluorescence by AuNPs to recognition and characterisation of biomolecules. As demonstrated throughout this thesis, AuNPs and fluorophores share a modulation relation that is distance dependent. Simultaneously, AuNPs provide scaffold for ssDNA, modulating properties for fluorophores and can provide protection against destabilization agents, *i.e.,* nucleases [185]. On the other hand, self-complementary of DNA is ideal for spontaneous hybridisation and recognition of other nucleic acids. Together, these properties may allow for more sensitive recognition of nucleic acids, discriminate different conformation of DNA or even detect small nucleotide deletions.

The work developed through this thesis unveiled some information about the photophysical rate constants and the existence of distance-dependent effects. Nonetheless, real k_r and k_{nr} could not be successfully determined. Based on the information available, the best way to explore the studied system at this point, in terms of application, is to use fluorescence emission directly. Not only is it a simpler way to analyse the system but it is also the more suitable if the proper corrections are considered. If one batch of AuNPs functionalised with oligonucleotides modified with the same fluorophore is used in the same optical conditions but in two different biological scenarios, *i.e.,* presence and absence of a complementary target, any variations observed in fluorescence should be caused by conformational changes in the DNA structure.

5.1. Gold-nanobeacons for real-time monitoring of RNA synthesis*

An area that could particularly benefit from a new age of nano-based devices is RNA theranostics. RNA synthesis is one of the key steps in Crick's central dogma of molecular biology [187]. Although through the development of molecular biology it was proved that this dogma is not accurate [188], it is undeniable that monitoring and understanding RNA synthesis is of great relevance for life sciences. The synthesis of an RNA chain using a DNA double helix as template is called transcription. The synthesised strand is complementary to its template strand and is, therefore, identical to the other strand of that duplex. RNA is a central player in gene expression. It was first characterized as an intermediate in protein synthesis, but since then many other RNA types have been discovered that play structural or functional roles at other stages of gene expression [189]. The meaning of the presence or absence of RNA molecules may be as critical as health or disease. In most cases, as important as qualitative detection of RNA is the quantitative aspect of the procedure. Often, dysregulation of the expression of regulatory genes leads to cancer. For that purpose, the importance of a sensitive tool that can quantitatively report this type of behaviour is extremely relevant. RNA molecules play a particularly important role in cell regulation. The absence of controlled regulation of RNA molecules

*Adapted from [186]

can sometimes lead to cancer. As such, developing a robust, sensitive and adaptable system to monitor and regulate RNA is vital in the prevention and treatment of cancer.

One of the genes known to be involved in cancer when dysregulated is *c-myc*. The *c-myc* gene was discovered as the homolog of the retroviral v-myc oncogene for cells 20 years ago [190-193]. The *c-myc* proto-oncogene was later found to be active in and related to several animal and human tumors [194,195]. Targeted homozygous deletion of the murine *c-myc* gene results in embryonic lethality, suggesting that it is critical for development [196]. Homozygous inactivation of *c-myc* in rat fibroblasts caused a marked prolongation of cell doubling time, further suggesting a central role for *c-myc* in regulating cell proliferation [197].

Dysregulation of *c-myc* expression was directly linked to increased cell replication via coordinated activation of different cyclin and cyclin-dependent kinases. Recent evidence has provided evidence that *c-myc* directly increases the expression of proteins that induce cell replication. *c-myc* is able to activate the expression of cyclin E as well as increase the expression of cyclin A [198-203]. Lately, cdc25A gene was also described as a direct target of *c-myc* [204,205]. This gene produces a protein phosphatase that activates important cell cycle regulator proteins, such as CDK2 and CDK4. On the contrary, *c-myc* was described as a downregulator of p27 expression [203,206,207], a protein that controls the cell cycle by forming a complex with CDK proteins. These activities of *c-myc* are all compatible with the ability of *c-myc* to promote cell entry into S phase of the cell cycle.

Monitoring and controlling RNA synthesis is of great relevance for understanding the cell (and the organism) homeostasis. The ability to scrutinize cellular processes *in vitro* has become an important tool for novel approaches to gene studies and for molecular therapeutics [208-210]. Several techniques to analyse RNA synthesis *in vitro* have been described, *e.g.* Northern Blot [211], RT-PCR [212,213] and cDNA microarrays [214]. In addition, molecular beacons have provided a rapid and sensitive system capable of efficient quantitative monitoring of RNA synthesis and/or inhibition in real-time. A molecular beacon is a stem-loop DNA single-stranded-oligonucleotide that carries a fluorophore and a quencher at both ends: in absence of target, the stem-loop structure is closed forcing the fluorophore and the quencher to close proximity, resulting in fluorescence quenching; upon hybridisation to a complementary target the stem-loop sequence opens, the fluorophore and quencher are spatially separated and the fluorescence is restored [215,216]. Fluorescence monitoring allows quantitative kinetic analysis of the conformation changes occurring in the molecular beacon under various situations such as real-time monitoring of DNA cleavage caused by enzymes [217], protein–DNA interaction studies [218], real-time *in vitro* transcription monitoring [219,220] and real-time PCR detection [221].

Although very fruitful for *in vitro* experiments, utilization of molecular beacons *in vivo* has not been so successful, probably due to the poor chemical stability of nucleic acids in biological media and

weak protection against action by nucleases. AuNPs can provide the possibility for *in vivo* studies of molecular beacon-like structures as they offer some protection against degradation [185] and can act as vectors for transfection into cells [222]. Such gold nanoparticle-based molecular beacons have been shown to detect sequence-specific DNA targets [223] and even be more sensitive in detecting single-mismatch than regular molecular beacons [152].

Transcription of a gene into mRNA is highly regulated and can be switched on and off by blocking the respective promoter. The RNA promoter determines the maximal rate of RNA synthesis and is the site of binding for RNA polymerase. By controlling the enzymatic access to the promoter region, transcription can also be modulated.

A system composed of AuNPs functionalised with several fluorophore-modified DNA strands each was devised. If each DNA strands on the surface of the AuNP can provide a signal then the total amount of signal will be proportional to the amount of targets in solution. Therefore, theoretically, the developed system should be able to provide quantitative information about a sample that is set to hybridise to. Having this in mind, AuNP based molecular beacon structures (Au-nanobeacons) were developed. First, Au-nanobeacons constituted by AuNPs with an average diameter of 14 nm (see Section 3.1.4) were designed. In one Au-nanobeacon, the loop in the hairpin structure is complementary to a fragment of the *c-myc* proto-oncogene mRNA produced by *in vitro* transcription (reporter); as transcription occurs, the presence of mRNA target induces the opening of the reporter's structure with concomitant fluorescence intensity increment. A second one was designed to silence gene transcription: an inhibitor Au-nanobeacon complementary to the promoter region recognized by the T7-RNA polymerase, thus capable of blocking the transcriptional machinery at the specific promoter site and obstructing transcription. This design is for *in vitro* transcription but the same rationale may be used to target any specific gene sequence of choice.

This double-Au-nanobeacon system can be used for real-time monitorization of RNA transcription and inhibition simultaneously: the reporter Au-nanobeacon monitors the transcription level while the second Au-nanobeacon acts as inhibitor of transcription while quantitatively assessing the number of sequences being inhibited. Because the inhibitor reports on the number of targets it binds to, real time quantification of the number of sequences being silenced at one time is obtained, and the consequent effect on transcription is provided by the reporter Au-nanobeacon as presented in Figure 5.1.

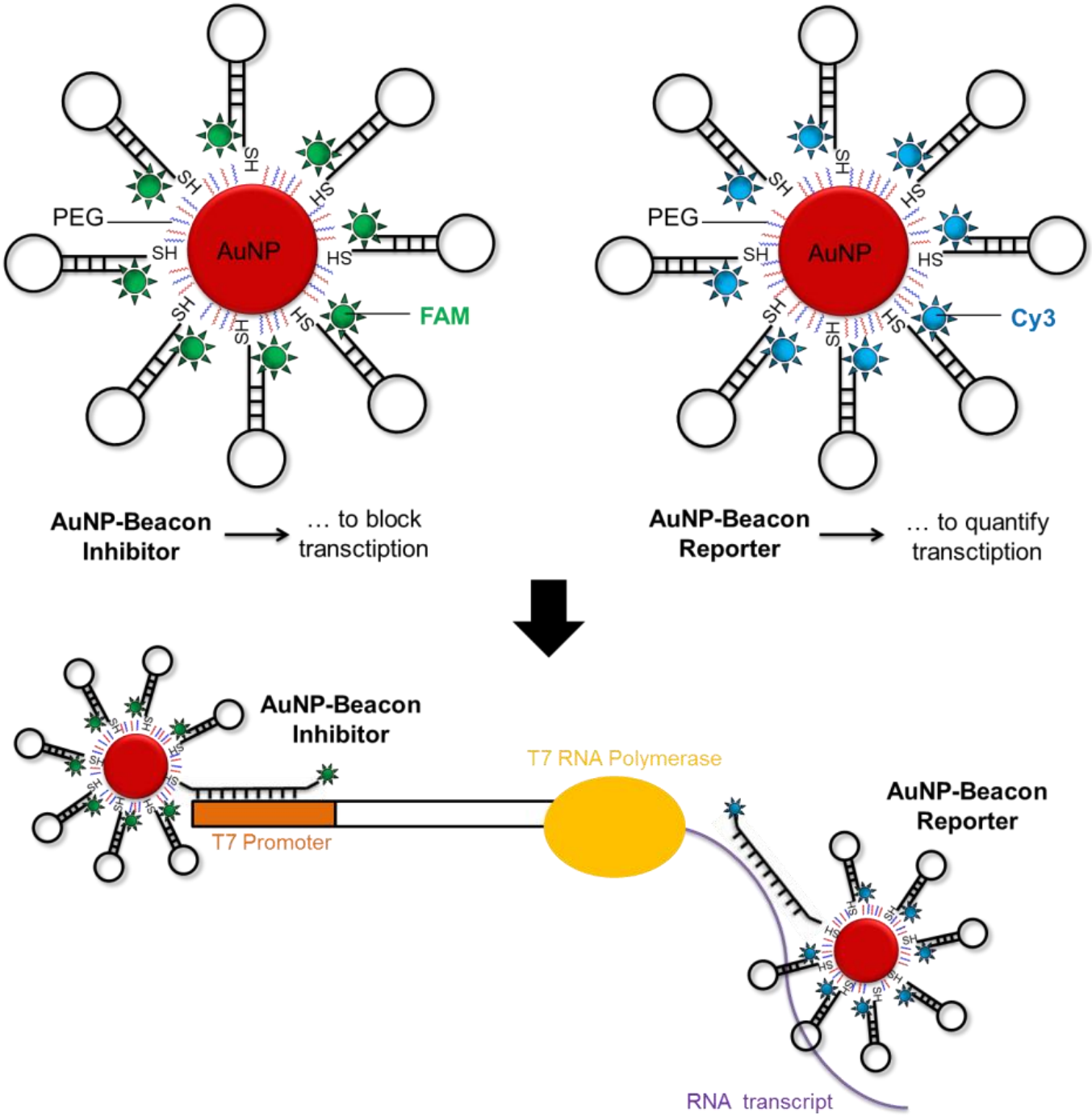

Figure 5.1. Gold-nanobeacons for monitoring and inhibition of real-time RNA synthesis. An Au-nanobeacon is composed by a hairpin DNA structure with a gold nanoparticle at 5' and a fluorophore at 3'. When the hairpin has its stem-loop structure formed the fluorophore is forced to be in close proximity with gold nanoparticles and fluorescence is quenched due to gold nanoparticles modulation properties on standard organic fluorophores. On the other hand, in the presence of a target that can hybridise with the loop sequence of the hairpin the stem-loop structure is opened and the fluorophore is parted from the gold nanoparticles resulting in restoration of fluorescence. A cy3-labeled Au-nanobeacon hybridises with the RNA transcript as it is formed in an *in vitro* reaction acting as a reporter of the levels of transcription. Simultaneously, a FAM-labelled Au-nanobeacon is used to hybridise with the T7 promoter region of the dsDNA template which results in inhibition of *in vitro* transcription. The fluorescence of both Au-nanobeacons is measured and quantification of both how many T7 promoter sites are being blocked and how many RNA products are being formed is retrieved.

Much like standard molecular beacons, in the native conformation the hairpin structure is designed to be closed and the fluorophore and AuNP are brought together. The secondary structure prediction was performed using NUPACK [224] for the oligonucleotides of both Au-nanobeacons (see Reporter_NB and Inhibitor_NB in section 2.2. for sequence) and the free energy obtained in both cases indicates the spontaneous formation of the stem-loop structure at 37°C as shown in Figure 5.2.

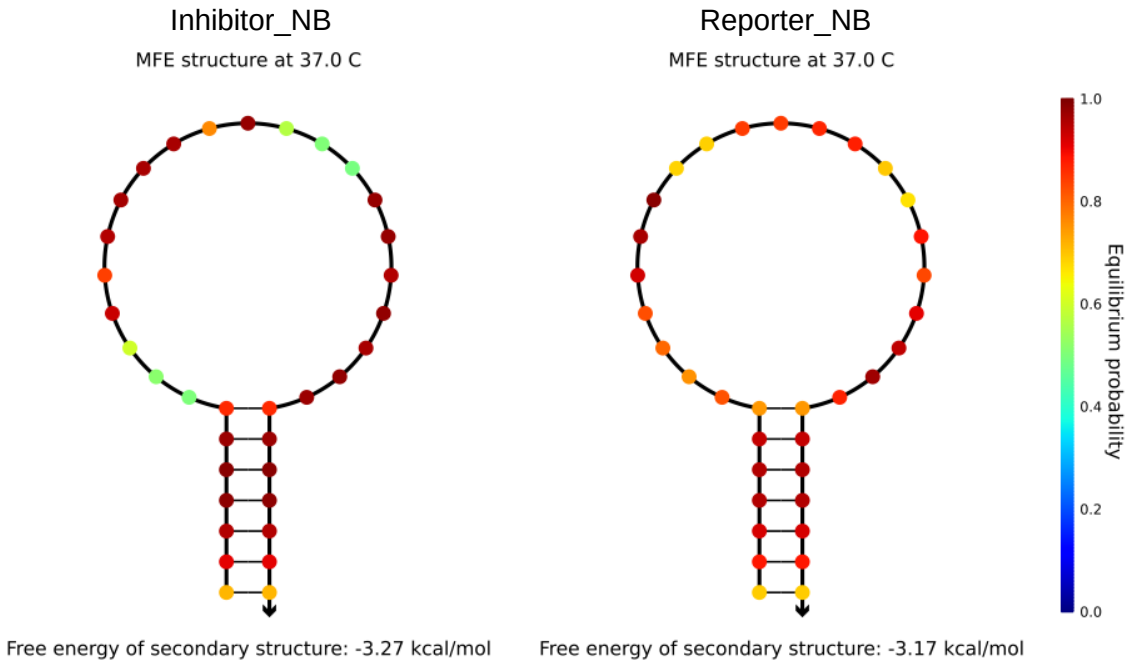

Figure 5.2. Hairpin structure of the oligonucleotides of both Au-nanobeacons. Two-dimensional structures of inhibitor_NB and reporter_NB oligonucleotides (used to synthesise both Au-nanobeacons) at 37ºC as predicted by NUPACK [224]. The free energy of secondary structure of both hairpins is negative, which implies a spontaneous structure at 37˚C.

Since both Au-nanobeacons are to be used simultaneously the fluorophores that constitute reporter and inhibitor Au-nanobeacon must be different in order to have distinct signals from inhibition and transcription levels. This way, the choosing of fluorescein derivative 6-FAM was a logical consequence of the work developed in the previous chapters and was used to construct the inhibitor Au-nanobeacon. On the contrary, the choosing of cy3 as the other reporter molecule was a decision based on the relation between the technical properties required to perform the task, time to acquire the labelled-oligonucleotide and price. On one hand, from the possible fluorophores available at the time it was the cheaper that could be ordered in a double labelled oligonucleotide with a thiol-C6 group in 5'. According to this, cy3 was opted as the fluorophore for the reporter Au-nanobeacon. Figure 5.3

illustrates the absorption and emission spectra of both fluorophores used. FAM was excited at λ=490nm to explore the maximum absorbance of the fluorophore and cy3 was excited at λ=530nm to allow the visualization of the full emission spectra of the fluorophore and simultaneously avoid spectral contaminations of the inhibitor Au-nanobeacon.

Another important factor to consider is the stability of the Au-nanobeacons in biological medium. Until this point in this thesis, every experiment was conducted under low salt medium that do not compromise the stability of either AuNPs or Au-nanoprobes. Changing to an environment that is favourable to enzymes usually means the increase of pressure to the stability of the AuNPs. Having this in mind, the Au-nanobeacons were co-functionalised with PEG molecules that should enhance the protection of the AuNPs against aggregation when compared to simple Au-nanoparticles probes.

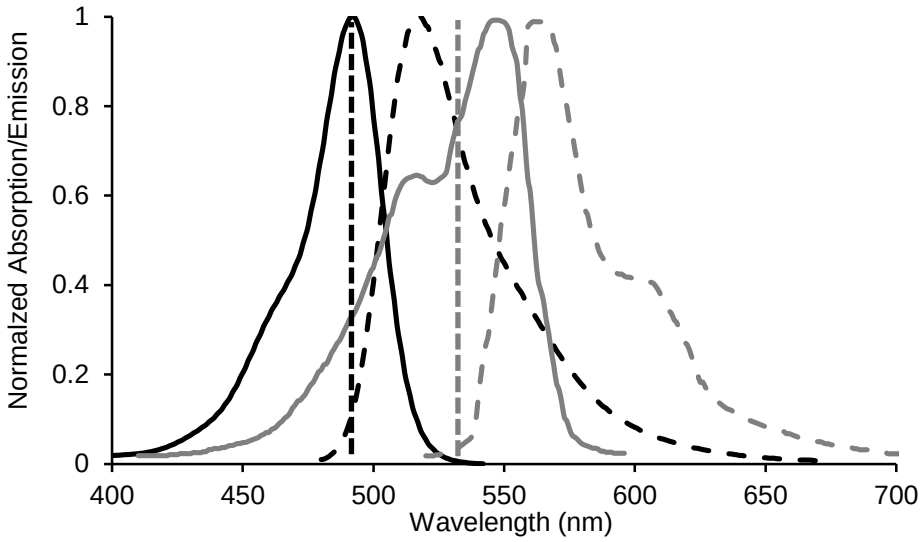

Figure 5.3. Absorption and emission spectra of the fluorophores. Absorption (full lines) and emission (dashed lines) spectra of FAM (black lines) and cy3 (grey lines). Vertical lines represent the excitation wavelength of each fluorophore (λ=490 nm for FAM and λ=530 nm for cy3).

5.1.1. Au-nanobeacon calibration

The response of the reporter Au-nanobeacon to the presence of complementary target (RepNB_comp) was calibrated using the DNA template that was subsequently used for *in vitro* transcription – Figure 5.4. A 10-fold increase in fluorescence was detected upon hybridisation of the Au-nanobeacon to the complementary target at 37 ˚C when compared to hybridisation to non-related target, showing that the Au-nanobeacon is capable of specific sequence recognition. To ensure that, during transcription, the Au-nanobeacon in solution would not be totally hybridised to the DNA template alone before transcription started, a fixed amount of Au-nanobeacon was added to crescent target concentrations, heated and cooled-down to induce maximum hybridisation before transcription. Then, the

fluorescence intensity of the total system before and after transcription was measured. The fluorescence intensity consistently increases after transcription indicating that, although higher quantities of template correspond to higher fluorescent intensities, there are still hairpin-structures available for specific hybridisation to the newly formed transcript.

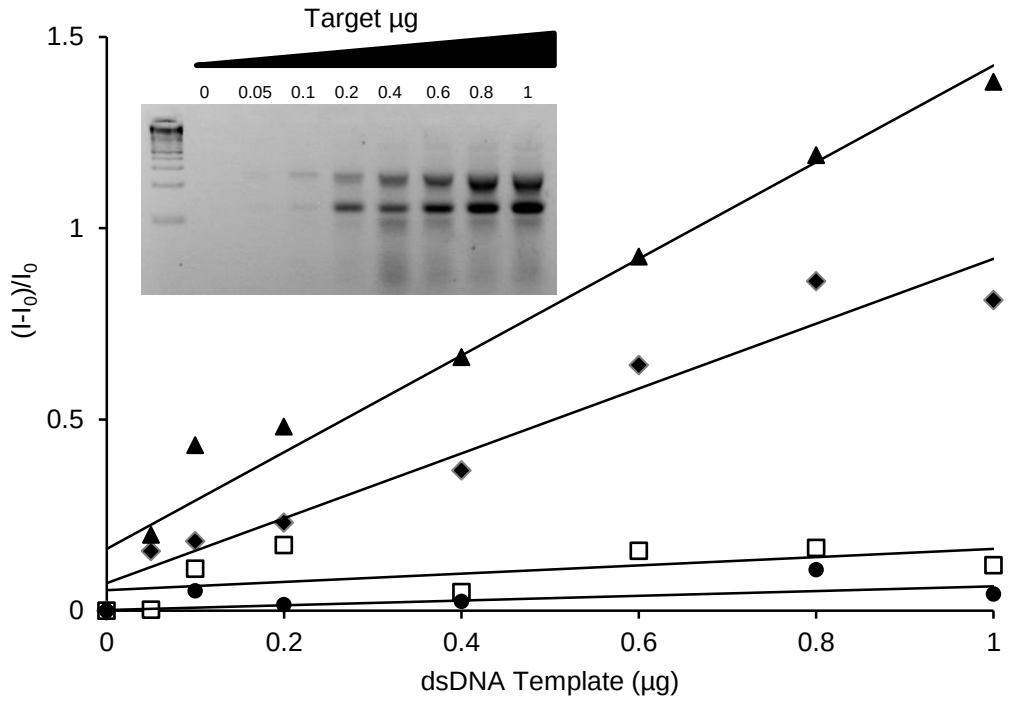

Figure 5.4. Au-nanobeacon calibration. Reporter Au-nanobeacon normalized emission before and after transcription of dsDNA templates that generate complementary (black diamonds, y = 0.8482x + 0.0719; and black triangles, y = 1.2634x + 0.1614, respectively) and non-complementary (black circles, y = 0.0618x + 0.0018; and white squares, y = 0.1076x + 0.0539, respectively) RNA products for increasing transcription template. Inset: Agarose gel demonstrating an increase in the intensity of the band corresponding to the transcript for higher template mass.

Au-nanobeacons have more than one hairpin-oligonucleotide per nanoparticle, which results in better signal to background noise when compared to traditional molecular beacons, *i.e.*, better capability to detect complementary targets that has also been previously reported by others [225]. From these calibrating experiments, a working concentration of 0.6 µg of template for the real-time assay was selected. The reporting signal obtained from the reporter Au-nanobeacon was further validated by i) hybridisation to total RNA containing complementary target – Figure 5.5; and ii) real-time quantitative PCR, the gold standard technique for transcript quantification – Figure 5.6. Results corroborate the quantification capability of the reporter Au-nanobeacon.

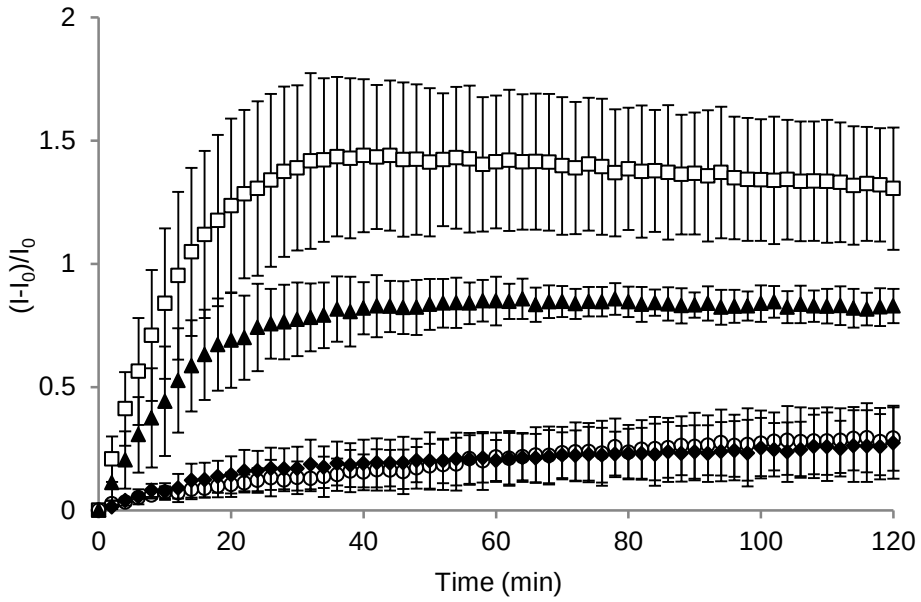

Figure 5.5. Reporter Au-nanobeacon calibration via hybridisation to total RNA. Reporter Au-Nanobeacon normalized emission for 120 minutes at 37ºC in presence of increasing concentrations of total RNA (0 ng/μL – white circles, 6.7 ng/μL – black diamonds, 13.3 ng/μL – black triangles, 26.7 ng/μL – white squares). Error bars represent at least 3 independent assays.

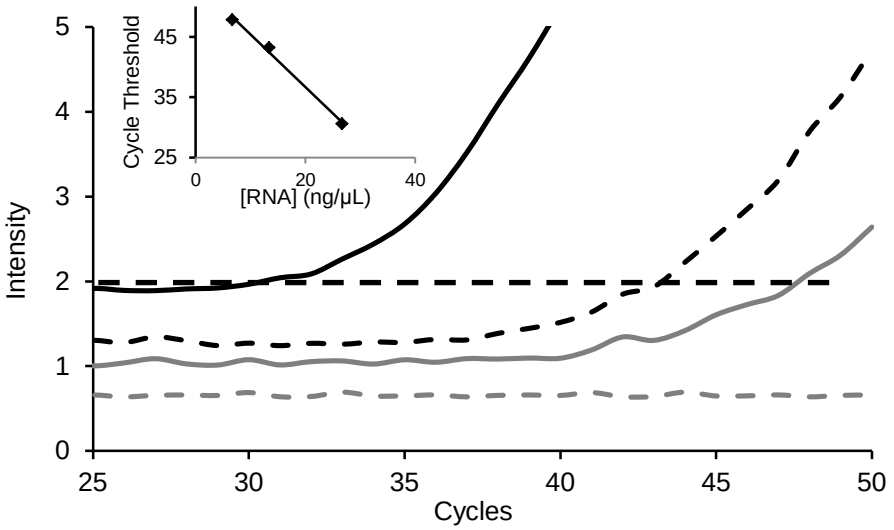

Figure 5.6. Reporter Au-nanobeacon calibration via real-time quantitative PCR. Real-time PCR of the total RNA samples tested with the reporter Au-nanobeacon (0 ng/μL – grey dashed line, 6.7 ng/μL – grey full line, 13.3 ng/μL – black dashed line, 26.7 ng/μL – black full line). Inset: Plot of Cycle Threshold vs. [total RNA], y = -0.8721x + 54.1, R^2 = 0.9948. The Threshold Cycle (Ct) represents the cycle number at which the fluorescence produced within a reaction crosses the threshold line (horizontal dotted line at Intensity = 2).

The inhibitor Au-nanobeacon presents an average of 4.95±0.66 oligomer per AuNP (Appendix II, Figure A5). The inhibitor Au-nanobeacon was calibrated as described above for the reporter Au-nanobeacon, showing its capability to specifically detect its complementary target sequence inducing a 4.3-fold increase in fluorescence, while not hybridising to a non-complementary target (Figure 5.7).

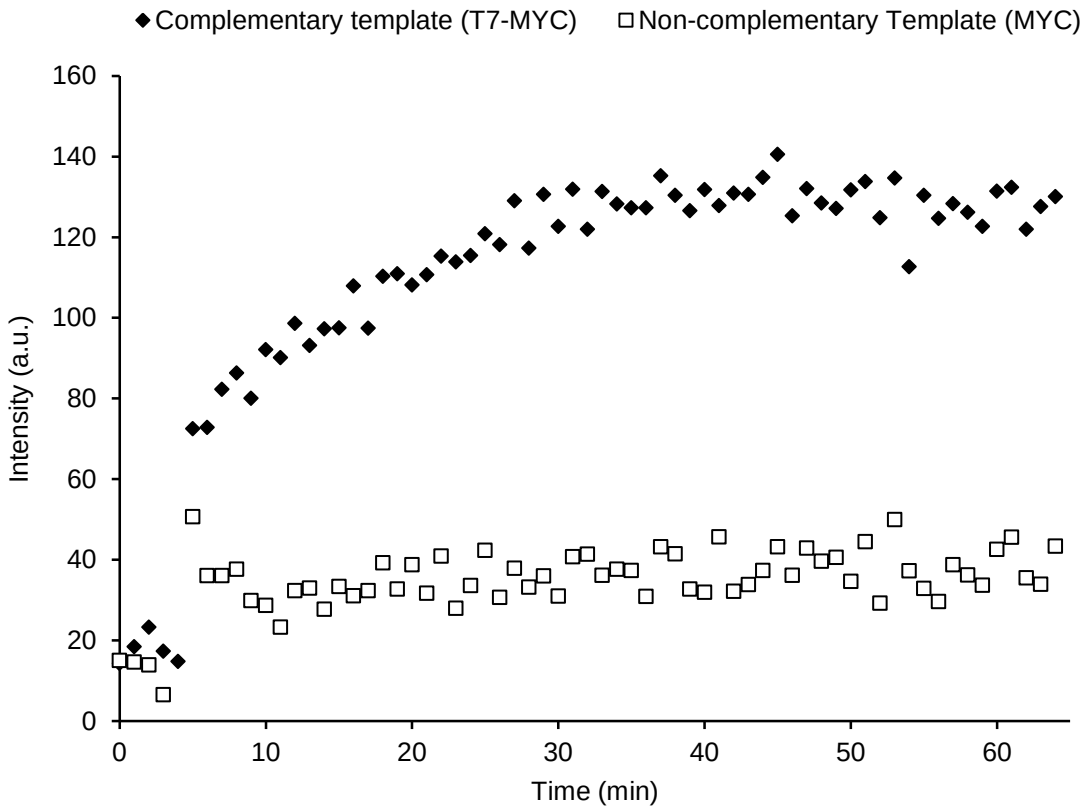

Figure 5.7. Inhibitor Au-nanobeacon specificity. Hybridisation kinetics of the inhibitor Au-nanobeacon at 37º C in presence of the complementary target (T7 primer; black diamonds) and non-complementary target (NEG; white squares).

In a typical inhibition assay, the dsDNA template (T7-MYC) is incubated with increasing concentrations of inhibitor Au-nanobeacon and then the transcription reaction is carried out. Following agarose gel electrophoresis, quantification of the amount of mRNA produced in each transcription showed a steady decrease with increasing amount of inhibitor Au-nanobeacon, as expected – Figure 5.8. It is clear that the inhibitor Au-nanobeacon can effectively compete with the template DNA sequence for RNA polymerase and drastically reduce the level of transcription. This is in clear agreement with previous reports that demonstrate that AuNPs enhance the silencing capability of oligonucleotides, while conveying protection against nucleases [185]. At the same time it blocks transcription, the inhibitor Au-nanobeacon simultaneously signals out the amount of target it is binding to, *i.e.*, the fraction of promoters being blocked at any given time.

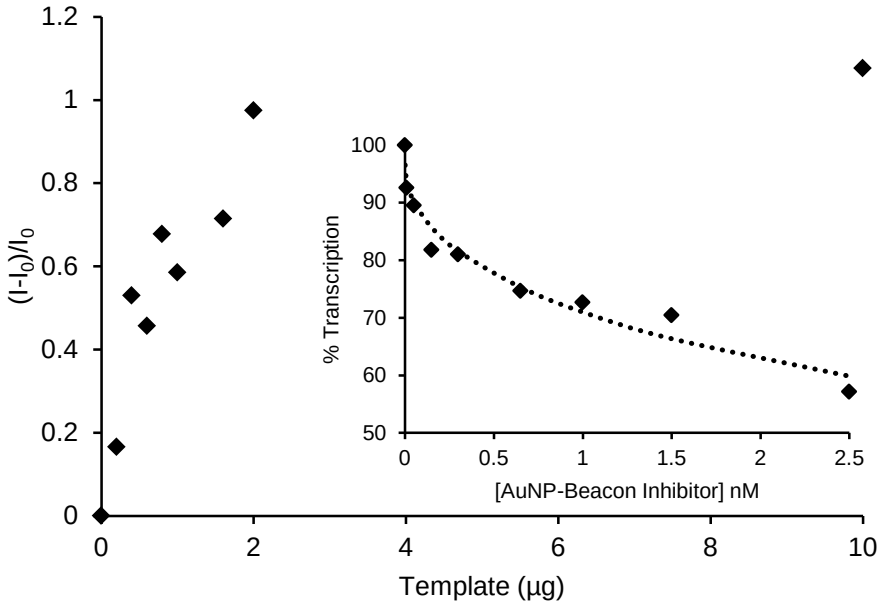

Figure 5.8. Inhibitor Au-nanobeacon calibration via real-time quantitative PCR. Inhibitor Au-nanobeacon normalized emission in presence of increasing dsDNA template. Inset: Transcription inhibition with increasing amounts of inhibitor Au-nanobeacon.

5.1.2. Monitoring of RNA synthesis inhibition

The reporter and the inhibitor Au-nanobeacons were used simultaneously in the same reaction vial in order to assess transcription and transcription inhibition as shown in Figure 5.9. Data show increasing fluorescence output from the reporter Au-nanobeacon with increasing concentrations of template that correlates with increasing levels of transcription. The presence of the inhibitor Au-nanobeacon (1 nM) can be noted by a decrease in fluorescence from the reporter (1 nM) Au-nanobeacon, showing that it is blocking transcription.

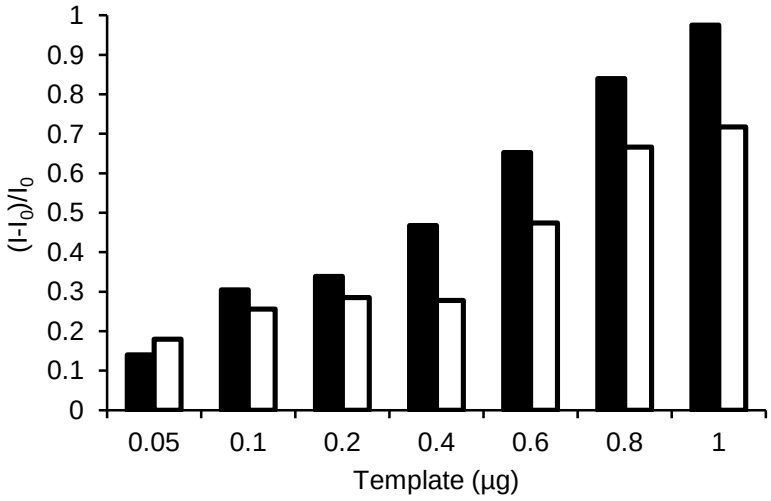

Figure 5.9. Au-nanobeacon effect on *in vitro* transcription. *In vitro* transcription in the presence of the reporter Au-nanobeacon (black bars) and in the presence of both reporter (1 nM) and inhibitor (1 nM) Au-nanobeacons (white bars) with increasing amounts of DNA template, measuring the fluorescent intensity of cy3 (λ=530 nm).

As the concentration of template increases, the level of transcription also increases showing that the same amount of inhibitor Au-nanobeacon is blocking a smaller percentage of all the available templates present in the reaction medium. In fact, considering that each AuNP of the inhibitor Au-nanobeacon possess an average of five hairpins on its surface, one may assume that all the hairpins per AuNP are in the open conformation if each Au-nanobeacon is blocking five promoters. In this situation the inhibitor Au-nanobeacon is saturated and ceases to respond to incremental increases in target concentration, which happens for a concentration of target of about 10 μg (6.43×10^{-11} mol) (see Figure 5.8). Taken this into account and retrieving the fluorescence of the inhibitor Au-nanobeacon, it is possible to determine the ratio of promoters being effectively blocked − Table 5.1. The percentage of promoters being blocked is lower for the higher template concentrations, which correlates to lower inhibition and consequent higher levels of transcription, thus demonstrating that this system can effectively quantify the level of RNA synthesis and simultaneously assess the ratio of blocked promoters. This is the first time a DNA-AuNP conjugate is used to simultaneously silence transcription and quantify the percentage of promoters being effectively blocked, as far as can be searched in literature.

Table 5.1. *In vitro* transcription inhibition vs. inhibited Au-nanobeacon hybridisation.

Added template (mol $\times10^{-12}$)	1.29 (0.2 μg)	2.57 (0.4 μg)	3.86 (0.6 μg)	5.14 (0.8 μg)	6.43 (1 μg)
Inhibited template (mol $\times10^{-12}$)	0.23 (17.63%)	0.35 (13.79%)	0.42 (10.79%)	0.36 (6.91%)	0.49 (7.64%)
Inhibition of transcription (%)	96.14	90.69	66.49	62.00	56.39
Inhibitor saturation (%)	45.34	70.95	83.23	71.08	98.28

5.1.3. Real-time assessment of transcription and inhibition

Based on the previous results, the same approach was used to follow the *in vitro* transcription in real-time. The results are shown in Figure 5.10. The fluorescence of the reporter Au-nanobeacon was measured first during the 120 minutes immediately after the addition of T7 enzyme and NTPs to a previously stabilized solution containing the Au-nanobeacon and template**.** The reporter Au-nanobeacon signals the continuous synthesis of the complementary mRNA, whilst the production of a non-related transcript induces no changes to the fluorescence intensity. Because of the calibration of the Au-nanobeacon previously described it is possible at any time point to correlate directly to the actual amount of RNA being produced (as number of moles or mass). The complementary RNA

product caused a linear response (y=0.1066x−0.1336) corresponding to the formation of 10.6 fmol of RNA/min. This is extremely relevant if one is to study the regulatory and controlling elements of transcription of a given gene.

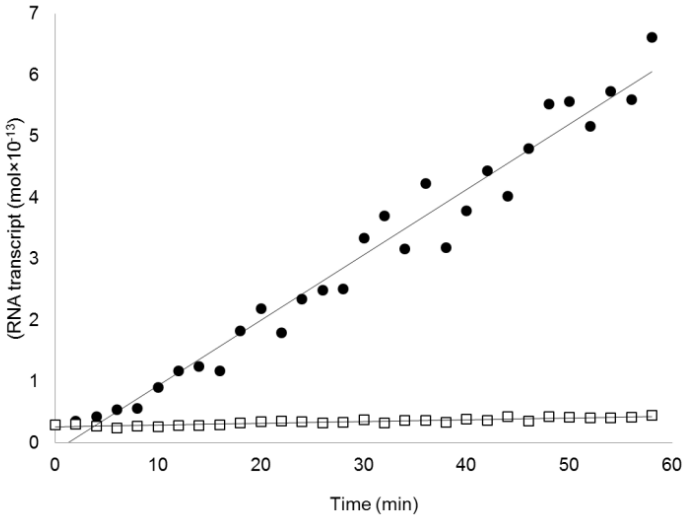

Figure 5.10. Real-time monitorization with the reporter Au-nanobeacon. Real-time measurement of *in vitro* transcription of RNA products showing complementarity to the reporter (black circles) and without any complementarity to the reporter (white squares). The complementary RNA product caused a linear response (y=0.1066x−0.1336) corresponding to the formation of 10.6 fmol of RNA/min

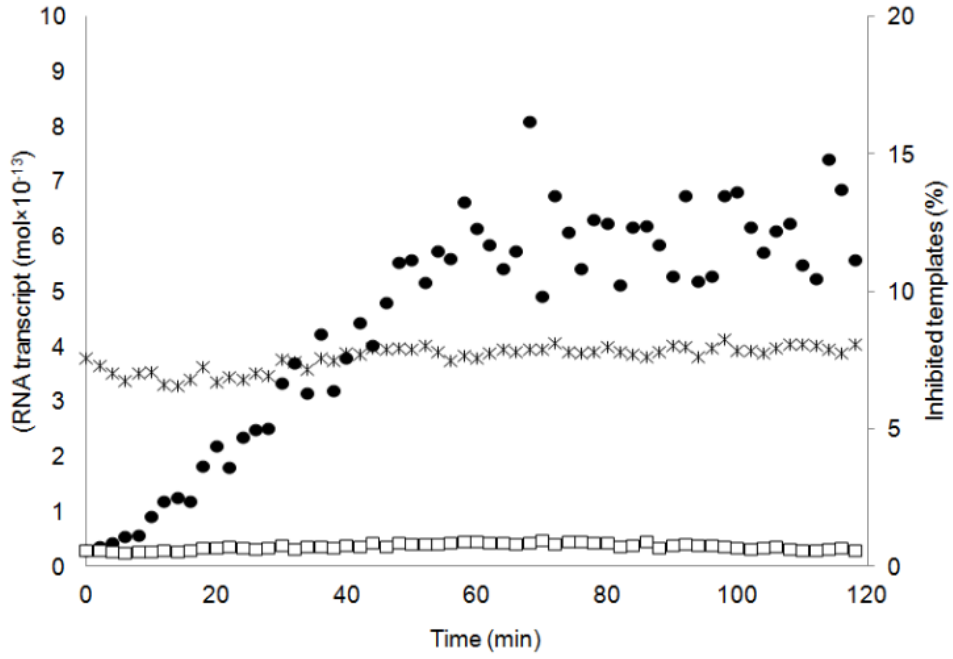

Figure 5.11. Real-time *in vitro* transcription and inhibition using Au-nanobeacons. *In vitro* transcription was measured (excitation wavelength of 530 nm, primary axis) in real-time in presence of the reporter Au-nanobeacon (black circles) and in simultaneous presence of the reporter and inhibitor Au-nanobeacons (white squares). The emission of the inhibitor Au-nanobeacon was also measured throughout the experience (black stars, secondary axis, excitation wavelength 490 nm).

Both Au-nanobeacons were then placed in the same RNA synthesis reaction towards a dual-colour system for the real time monitoring of both RNA synthesis and level of inhibition. The inhibitor Au-nanobeacon (also 1 nM) was then combined in one *in vitro* transcription reaction and measured the fluorescent intensity of both fluorophores with excitation at 490 and 530 nm. During the entire reaction time there was no rise in fluorescence associated with production of transcript (reporter Au-nanobeacon), showing that the inhibitor Au-nanobeacon is effectively blocking the promoter as shown in Figure 5.11. The inhibitor's emission is constant throughout the entire time lapse, and the percentage of blocked promoters can be easily determined via the procedure described above (7.61%). The level of inhibition of transcription can be easily calculated for each time point. What is more, as can be seen in Figure 5.12B, a normalized intensity curve can be plotted as function of the resulting transcription product retrieved from the agarose gel electrophoresis - Figure 5.12A.

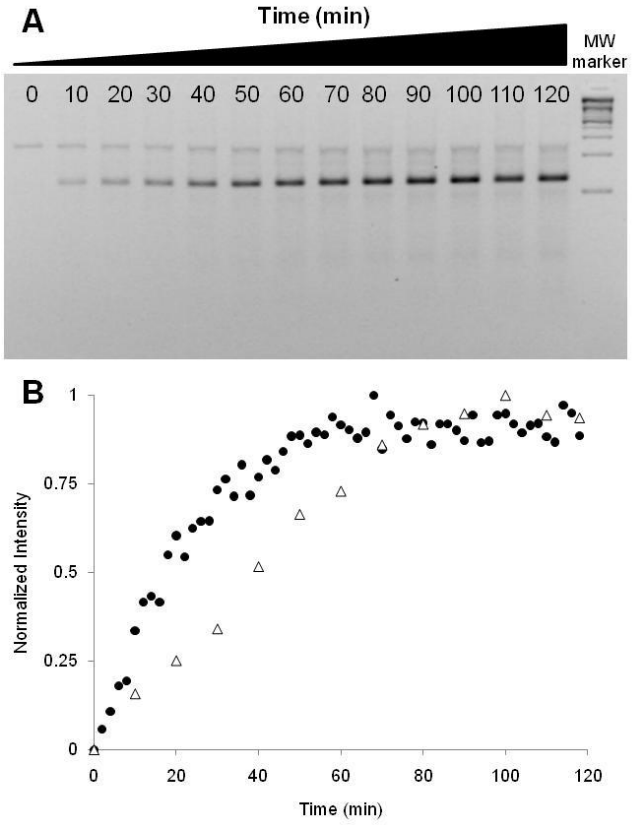

Figure 5.12. Confirmation of transcription. A. Agarose gel electrophoresis of the transcription product as function of time. **B.** Normalized intensity curve plotted as function of the resulting transcription product retrieved from the agarose gel electrophoresis (white triangles) and with the fluorescence intensity measurements of the reporter Au-nanobeacon (black circles) for 120 minutes immediately after the addition of T7 enzyme and NTPs to a previously stabilized solution containing the Au-nanobeacon and template. All transcription reaction products were also evaluated on a 3% agarose gel electrophoresis with GelRed™ staining. Product quantity determination was performed by pixel intensity/counting using ImageJ™ imaging software as previously described [164].

Real-time monitoring of RNA transcription reactions gave fluorescence plots with an initial lag phase, followed by a first-order increase. The initial lag may be due to assay sensitivity and kinetics of double-helix formation between the Au-nanobeacon and its RNA target. Comparison between the linear phase of the RNA synthesis for the reporter Au-nanobeacon (black circles) and reporter + inhibitor (white squares) demonstrate that we can achieve a 14.1-fold decrease in RNA synthesis after 60 minutes of transcription (~618 fmol of RNA and ~43.9 fmol of RNA, respectively). These results were confirmed through quantification of transcription via agarose gel electrophoresis as depicted in Figure 5.13.

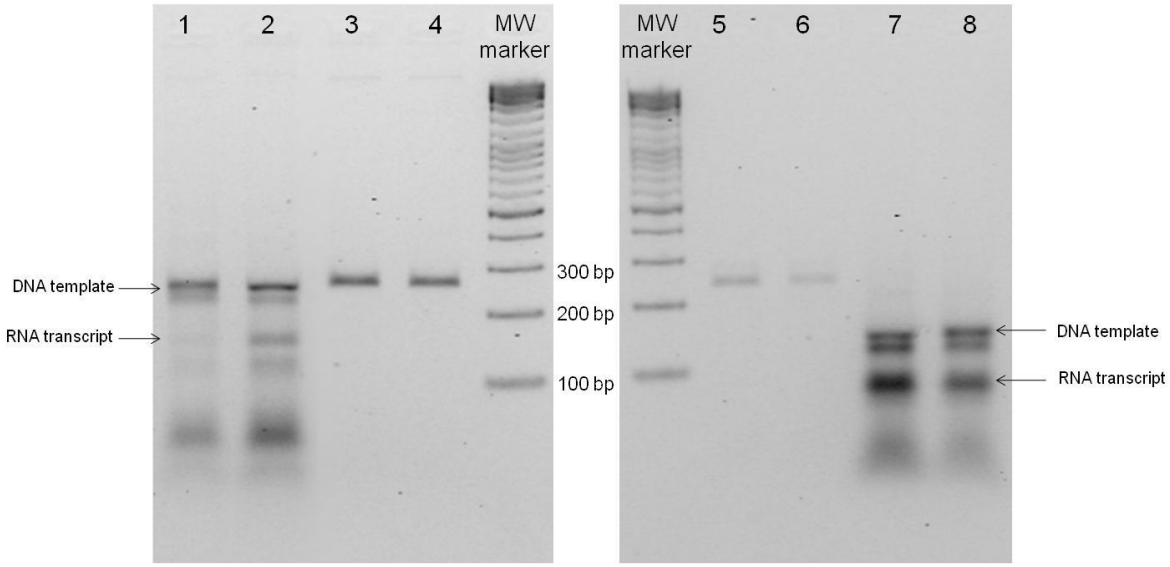

Figure 5.13. Agarose gel electrophoresis of end-point measurements of RNA synthesis and inhibition using active and non-active (denaturated) T7 RNA polymerase. Data show that fluorescence is strictly dependent of transcription of the added template. Lane 1 – Reporter + Inhibitor with active T7 Pol., Complementary target (T7-MYC); Lane 2 – Reporter with active T7 Pol., Complementary target (T7-MYC); Lane 3 – Reporter + Inhibitor with non-active T7 Pol., Complementary target (T7-MYC); Lane 4 – Reporter with non-active T7 Pol., Complementary target (T7-MYC); Lane 5 – Reporter with active T7 Pol., Non-complementary target I (X); Lane 6 – Reporter + Inhibitor with active T7 Pol., Non-complementary target I (X); Lane 7 – Reporter with active T7 Pol., Non-complementary target II (T7-Y); Lane 8 – Reporter + Inhibitor with active T7 Pol., Non-complementary target II (T7-Y).

5.2. Gold-nanobeacons for simultaneous gene specific silencing and intracellular tracking of the silencing events*

The potential of Au-nanobeacons for *in vitro* RNA detection was demonstrated in the last section. One logical step in the development of this type of biosensors is to explore the advantages provided by the AuNPs as potential vector. As such, going for an *in situ* detection system seems appropriate. In this specific scenario, when one Au-nanobeacon hybridises with a target it will not only provide the signal associated with change in its conformation but also block the function of the target. As such, besides performing its function as sensor, the Au-nanobeacon also works as an effector therapeutical agent turning it into a very promising theranostics approach.

Three potential targets were devised in order to show the versatility of the system. Au-nanobeacons were designed to intersect mRNA, siRNA and miRNA. Depending on the target, Au-nanobeacons can be used either to downregulate a specific gene or to silence the silencers of a specific pathway, allowing for recovery of previously downregulated gene expression while simultaneously tracking cell internalization and identifying the cells where silence is occurring. A scheme of the strategies that were followed is shown in Figure 5.14.

5.2.1. Theranostics system on mRNA pathways

To assess the potential of the Au-nanobeacons for *in situ* detection and simultaneous gene silencing, HCT-116 cells were transfected with EGFP. The antisense Au-nanobeacon was designed to target the Kozak consensus translation initiation site and start codon of the EGFP expression vector. This is intended to turn the Au-nanobeacon capable of blocking the transcriptional machinery in the colorectal cell-line in addition to its biomolecular recognition function. Stable AuNPs with an average diameter of 14.6±1.7 nm (third batch of cit1, see section 3.1.4) were synthesized and functionalised with poly(ethylene glycol) (PEG) spacers to increase stability, biocompatibility and grant chemical functionality as well as avoid opsonisation (PEG coverage in Appendix II, Figure A6) [227,228]. PEGylated AuNPs were then functionalised with a Cy3-labelled hairpin-DNA and calibrated to respond to the specific complementary target – Figure 5.15.

A substantial increase in fluorescence was detected upon hybridisation of the Au-nanobeacon to the complementary target (ssRNA, siRNA and microRNA oligonucleotides) at 37 ˚C, showing that the Au-nanobeacons are capable of specific sequence recognition. The number of beacons per AuNP was determined for all constructs, together with the hydrodynamic diameter by Dynamic light Scattering (DLS), gold core diameter by Transmission Electron Microscopy and surface charge by Zeta-potential (see Appendix II, Table A1).

*Adapted from [226]

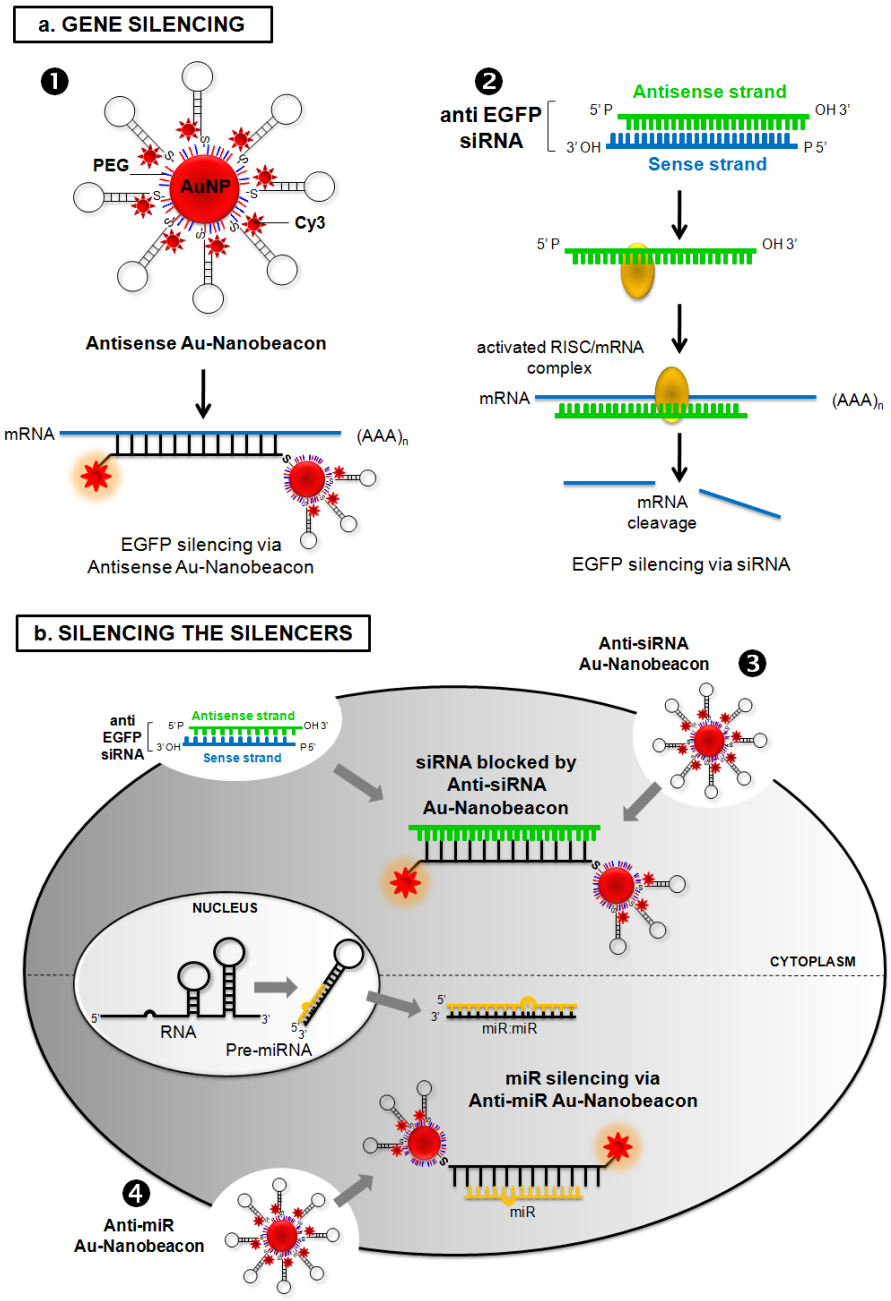

Figure 5.14. Au-nanobeacons as multi-targeting tools for RNAi: from specific gene silencing to Silencing the Silencers. (a) GENE SILENCING – Human cancer cells (HCT-116) efficiently transfected with EGFP expression vector were used for assessing the gene silencing potential of Au-nanobeacons – Antisense Au-nanobeacon (1) and by traditional siRNA approach (2). Upon hybridisation to the target sequence, the beacons' conformation change leads to fluorescence emission that signals target recognition and that silencing is occurring. (b) SILENCING THE SILENCERS – specific Au-nanobeacons are capable of intersecting both pathways – siRNA (3) and miRNA (4), leading to recovery of previously downregulated gene expression while simultaneously discriminating cells where silencing is occurring. The fluorescence signal may allow for tracking cell internalization and sub-cellular localization. The Au-nanobeacons' potential for anti-cancer therapeutics via the silencing of the silencers is demonstrated by blocking the endogenous microRNA pathway via an Anti-miR Au-nanobeacon complementary to the mature microRNA-21 (miR-21), commonly upregulated in cancer phenotypes [229].

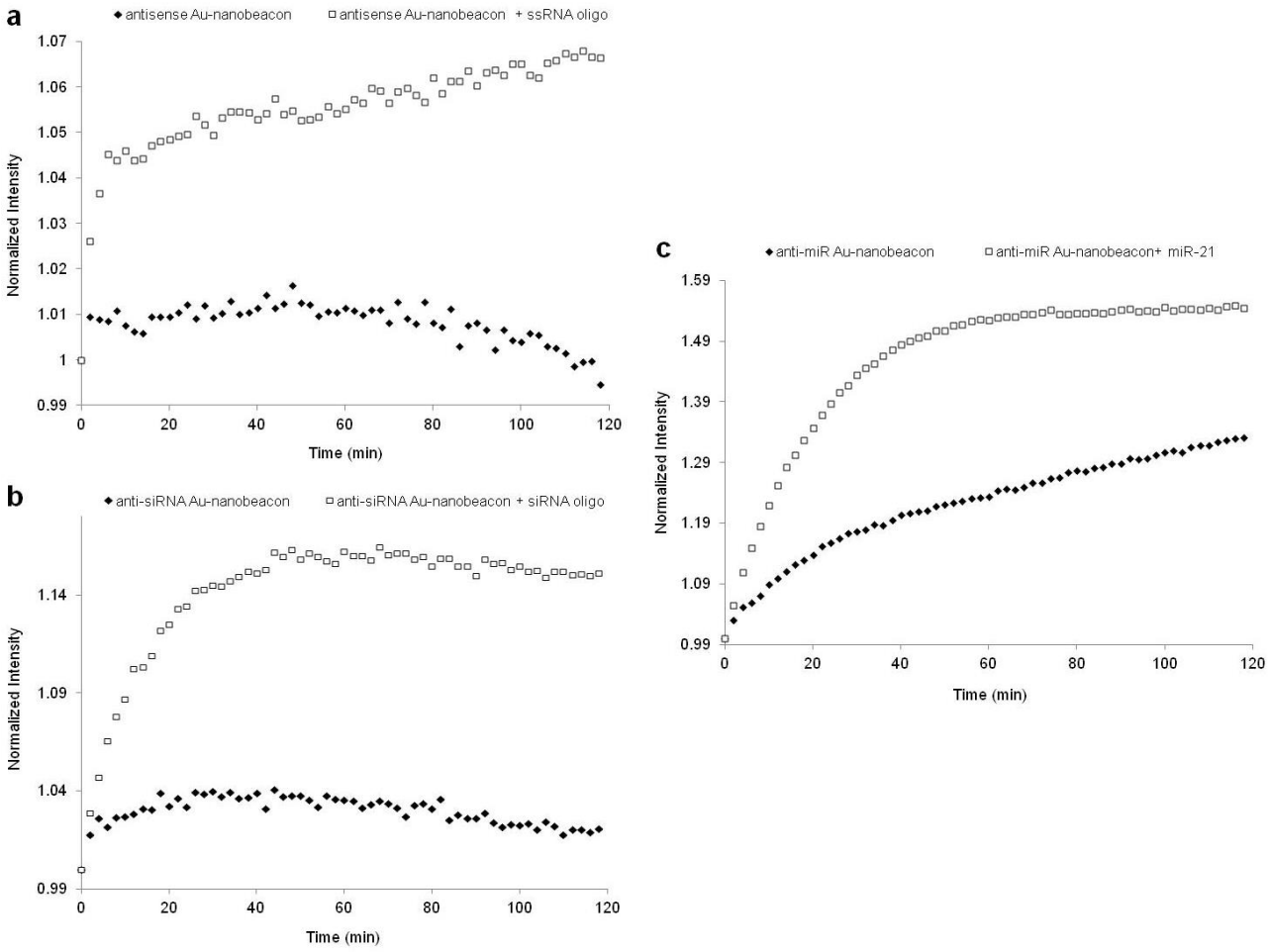

Figure 5.15. Au-nanobeacons specificity for target. Fluorescence emission as function of hybridisation time with (a) the antisense Au-nanobeacon, (b) anti-siRNA Au-nanobeacon, and (c) anti-miR Au-nanobeacon at 37ºC in presence of the complementary target (white squares) or a non-complementary target . Target sequences are depicted in Table 1.

The silencing effect of these antisense Au-nanobeacons (58±4 beacons per nanoparticle) was compared to that of traditional siRNA transfection using lipofectamine. All cellular uptake assays were carried out with serum-free media to avoid unspecific binding of serum proteins to the Au-nanobeacons and compromise cell uptake. Results show that both approaches are effective at blocking EGFP expression. After 24 hours of EGFP vector transfection, cells were treated with 30 nM of antisense Au-nanobeacons or 10 nM of siRNA for optimal EGFP silencing (Appendix III, Figure A11). After 48 hours of Au-nanobeacons exposure, the cells were lysed and the bulk fluorescence of the lysate was measured in the emission range of the EGFP protein (Excitation/Emission, 480/510 nm) and collected for total RNA extraction. Quantification of EGFP expression by direct measurement of EGFP fluorescence levels in bulk cell lysates at 48 hours – Figure 5.16b – reveals similar silencing for both approaches: 39.7±12.5% and 37.9±12.6% for antisense Au-nanobeacon and siRNA, respectively.

These data are corroborated by qRT-PCR (Figure 5.16a). EGFP expression is not affected by a nonsense Au-nanobeacon (32±3beacons per NP) or nonsense siRNA indicating that the knockdown is sequence specific. No changes in cell viability that would indicate off-target effects were observed (see Appendix III, Figure A12).

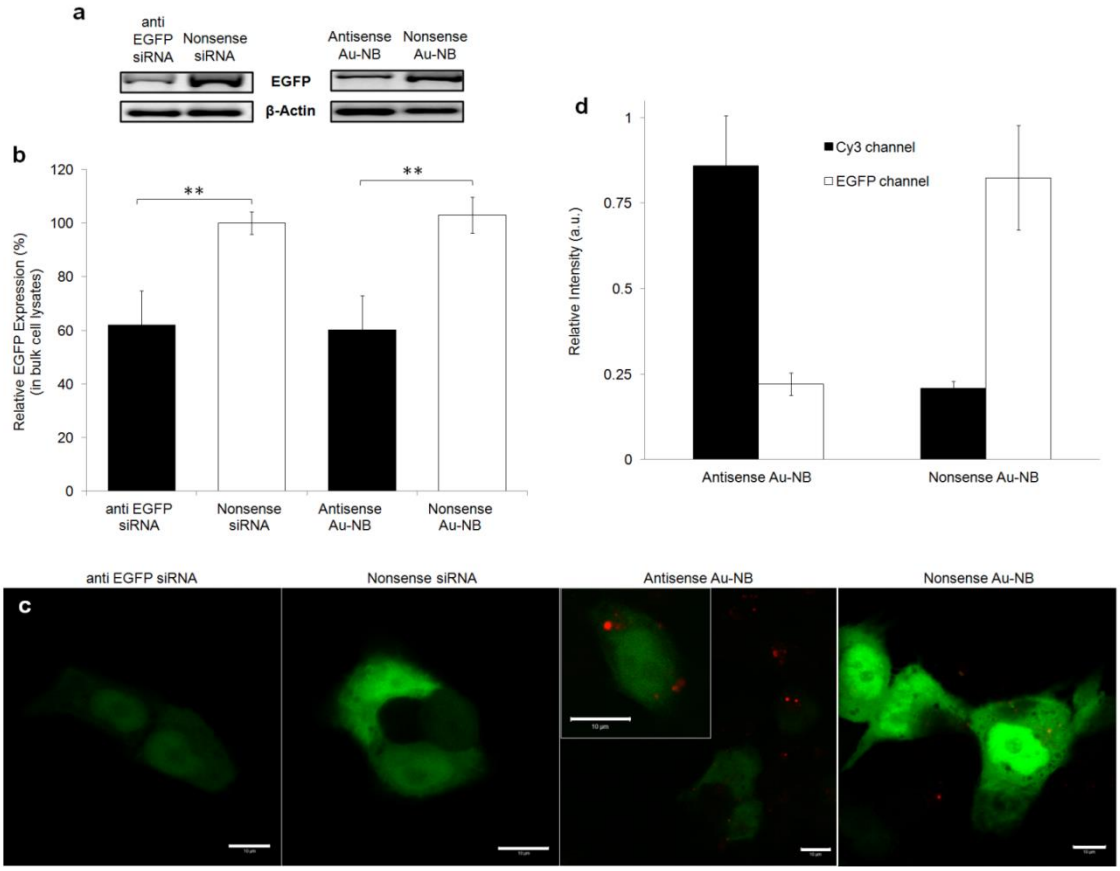

Figure 5.16. Au-nanobeacon silencing of specific gene expression in colorectal carcinoma cell line (HCT-116). HCT-116 cells were transfected with EGFP expression vector and mRNA expression confirmed by qRT-PCR before and (a) after siRNA and Antisense Au-nanobeacon transfection, using β-actin as reference. (b) EGFP silencing was confirmed by significant fluorescence decrease (**, $P \leq 0.005$) in bulk cell lysates (as percentage of original EGFP fluorescence levels), using an unrelated siRNA (Nonsense siRNA) or unrelated hairpin DNA bound onto AuNPs (Nonsense Au-nanobeacon). Values are means ± s.d. from 6 independent experiments. (c) Confocal imaging (scale bar, 10 μm) show HCT-116 cells expressing EGFP after transfection with siRNA 10 nM, Nonsense siRNA 10 nM, Antisense Au-nanobeacon 30 nM and Nonsense Au-nanobeacon 30 nM. EGFP expression levels can be evaluated by the intensity of its fluorescence (green) and Au-nanobeacons in open conformation (red, Cy3) can be identified as fine punctuation dispersed throughout the cytoplasm. (d) Relative fluorescence intensity of Au-nanobeacons (Cy3, black bars) and EGFP (white bars) obtained after individual colour channel analysis of the same confocal images using ImageJ software.

Confocal imaging clearly shows specific EGFP knockdown by siRNA anti EGFP and antisense Au-nanobeacon (Figure 5.16c). Cells show a punctuate fluorescence pattern indicating that the antisense Au-nanobeacons are distributed evenly in the cytoplasm (Figure 5.16c), and a closer examination

revealed more fluorescence in perinuclear regions. It should be noted that Au-nanobeacons require no transfection agent to enter cells. The intensity of fluorescence signals was broken down by specific channels that show striking differences for Cy3 and EGFP emissions related to the antisense and nonsense Au-nanobeacons, *i.e.*, silencing occurs upon hairpin conformational change due to specific hybridisation to the target sequence, which can be identified via the fluorescence emission. This way, effective silencing can be evaluated by the beacons' fluorescence (Figure 5.16d). Measuring the intensity of the Cy3 and EGFP channels, a decrease in EGFP fluorescence can be observed together with an increase in antisense Au-nanobeacons signal. The opposite occurs with the respective control, the nonsense Au-nanobeacon. This data demonstrates that silencing is attained only when the Au-nanobeacon opens and emits fluorescence that in turn signals out the localization and effectiveness of silencing (Figure 5.17).

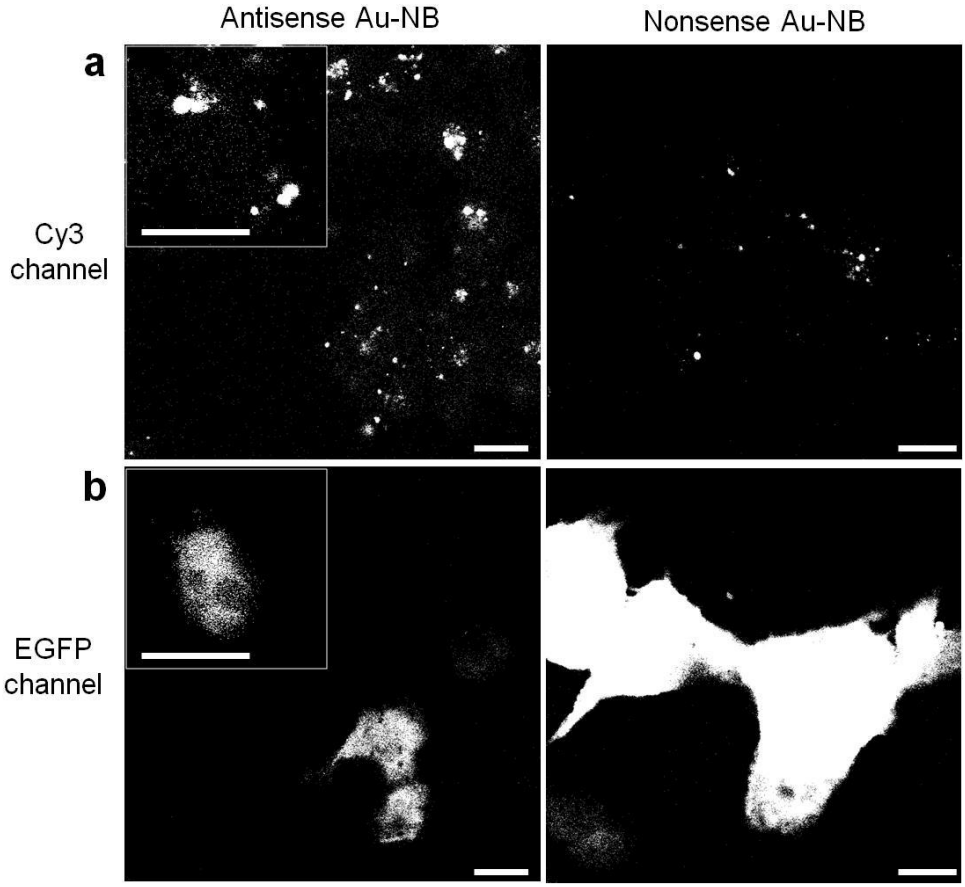

Figure 5.17. Antisense Au-nanobeacon silencing of EGFP. Striking differences for Cy3 and EGFP emissions related to the antisense and nonsense Au-nanobeacon effect can be observed, thus confirming that silencing occurs upon hairpin conformational change due to specific hybridisation to the target sequence. Black and white imaging of each channel allows each signal to be observed separately. The intensity of each individual signal can then be quantified. This process confirms that the effect of Au-nanobeacons on gene expression modulation is only felt in presence of target-induced opening of the structure. Scale bar, 10 μm.

Once EGFP expression had been blocked by siRNA, the silencing effect was reversed and EGFP expression was recovered via an anti-siRNA Au-nanobeacon that blocks siRNA. A specific anti-siRNA Au-nanobeacon was synthesized with 31±5 anti-siRNA beacons per nanoparticle. Quantification of the number of beacons at the AuNPs' surface is crucial to match the siRNA being used to silence. Therefore, 10 nM (beacon concentration on AuNP) of anti-siRNA Au-nanobeacon were added to the cell media previously incubated with 10 nM of siRNA at several delays of incubation (0.5h, 1h, 3h, 6h and 24 hours). After 48 hours, the cells were lysed and collected for analysis of EGFP recovery (Figure 5.18). Silencing of the silencer, *i.e.*, blockage of the siRNA, is most effective for the first 3 hours of incubation, where maximum EGFP recovery is accomplished after 0.5 hours of siRNA transfection (80.6±14.8% recovery of EGFP expression) and barely detected after 24 hours. Expression of the EGFP was also confirmed by qRT-PCR analysis of transfected HCT-116 cells (Figure 5.18a and b). Again, confocal imaging (Figure 5.18d and e) clearly shows EGFP recovery using an anti-siRNA Au-nanobeacon, particularly when compared with a non-sense Au-nanobeacon for 0.5 and for 24 hours. Surprisingly, EGFP recovery decreases in a time dependent manner showing almost no recovery at 24 hours of incubation after adding the "silencer". The high levels of expression recovery by silencing the silencer with an anti-siRNA Au-nanobeacon, which successfully blocks the antisense strand of siRNA, together with the persistent recovery of EGFP may be the result of the stabilization of hairpin-DNA on nanoparticle. Gold nanobeacons provide significant protection from nuclease degradation in an extracellular context, probably due to the hairpin configuration and to the proximity of the oligonucleotide to the gold surface, increasing the resistance to nuclease degradation and the oligonucleotide lifetime in the cell [185,230]. This data shows that the Au-nanobeacon approach uses the beacon's fluorescence to track the silencing inside the cell whilst evaluating whether the target is effectively being silenced. It is clear that the beacon's fluorescence increases for increased levels of silencing (Figure 5.18f). Once again, the fluorescence intensity in each channel shows an increase (recovery) in EGFP fluorescence when there is an increase in anti-siRNA Au-nanobeacon signal (Cy3). And that the reverse is also true, *i.e.*, the nonsense Au-nanobeacon that does not silence the siRNA, is not capable to promote EGFP recovery (Figures 5.18f and 5.19).

Single-stranded RNA oligonucleotides were used to silence the antisense Au-nanobeacon and a 70.3±15.5% of EGFP recovery was attained. Interestingly, for the first hour of incubation, the silencing of the Au-nanobeacon by ssRNA oligonucleotides was more effective than that of the anti-siRNA Au-nanobeacon (Supporting Information Figure S8 and FigureS11c and d). However, the recovery of EGFP due to silence of the siRNA seems to last for longer and 10-20% more than that observed when the antisense Au-nanobeacon is silenced by the ssRNA, which might be due to increased degradation of naked ssRNA by nucleases [185,231].

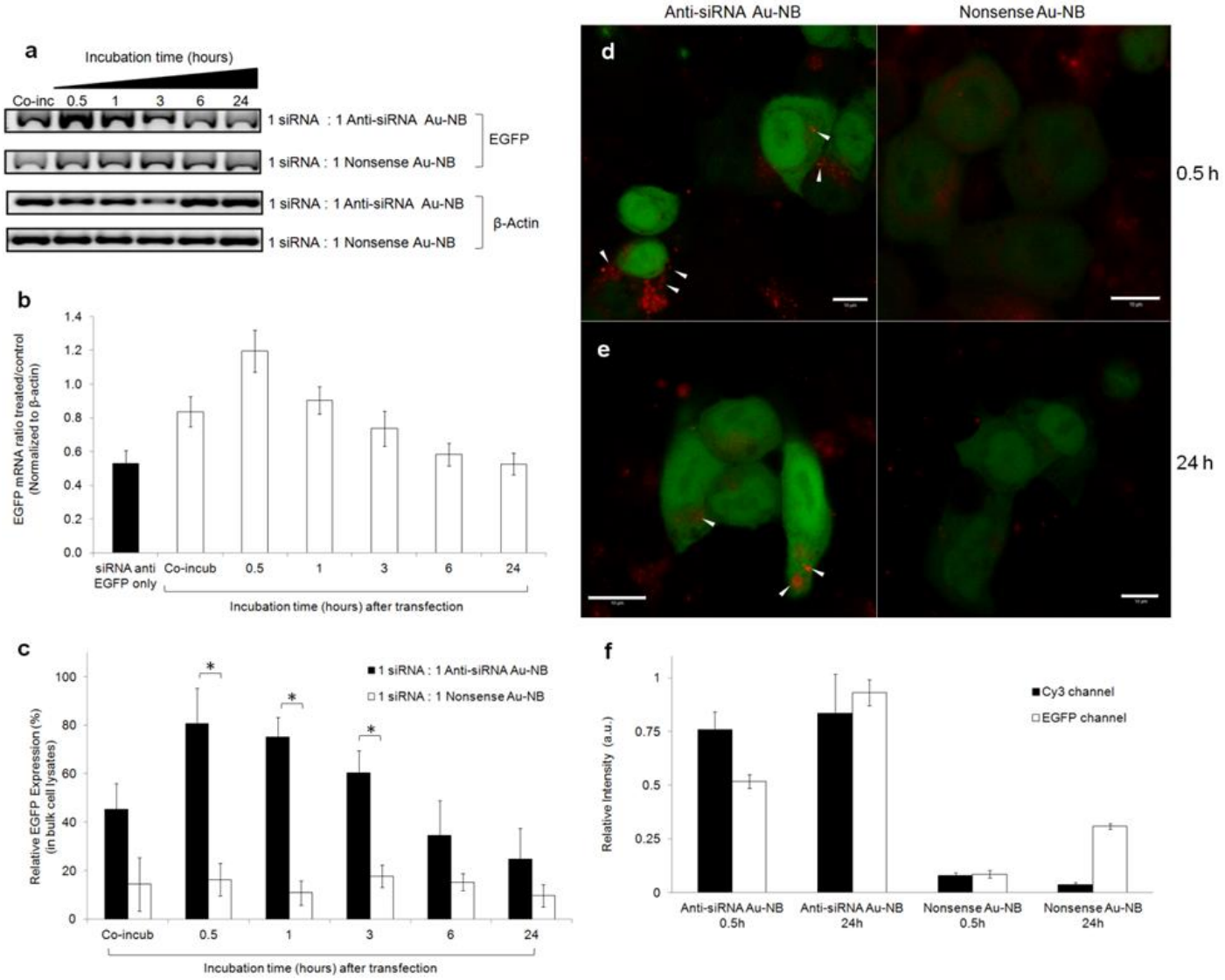

Figure 5.18. Au-nanobeacons silencing of siRNA leads to EGFP expression recovery. HCT-116 cells were transfected with EGFP expression vector, followed by co-transfection with 10 mM anti-EGFP siRNA and 10 nM (concentration of beacon on AuNP) Anti-siRNA Au-nanobeacon or Nonsense Au-nanobeacon and points measured with several delays of incubation (0.5, 1, 3, 6 and 24 hours). (a) EGFP recovery confirmed by qRT-PCR after treatment with Anti-siRNA Au-nanobeacon or Nonsense Au-nanobeacon using β-actin as reference. (b) Maximal effect of the Au-nanobeacon on siRNA silencing is attained almost immediately (0.5 h), which then decreases levelling at circa 40% EGFP recovery. (c) Significant EGFP recovery (asterisk, $P \leq 0.05$) as function of time from incubation with anti-siRNA Au-nanobeacon is corroborated by fluorescence evaluation in bulk cell lysates (as percentage of original EGFP fluorescence levels), using a Nonsense Au-nanobeacon as control. Values are means ± s.d. from 3 independent experiments. Confocal imaging (scale bar, 10 μm) show EGFP recovery at (d) 0.5 and (e) 24 hours delay incubation. Arrows point to Au-nanobeacons (Cy3) only observable in the cytoplasm of cells with high levels of EGFP recovery. (f) Silencing of silencers effect is corroborated by the relative fluorescence intensity of Au-nanobeacons (Cy3, black bars) and

EGFP (white bars) after individual colour channel analysis of the same confocal images using ImageJ software.

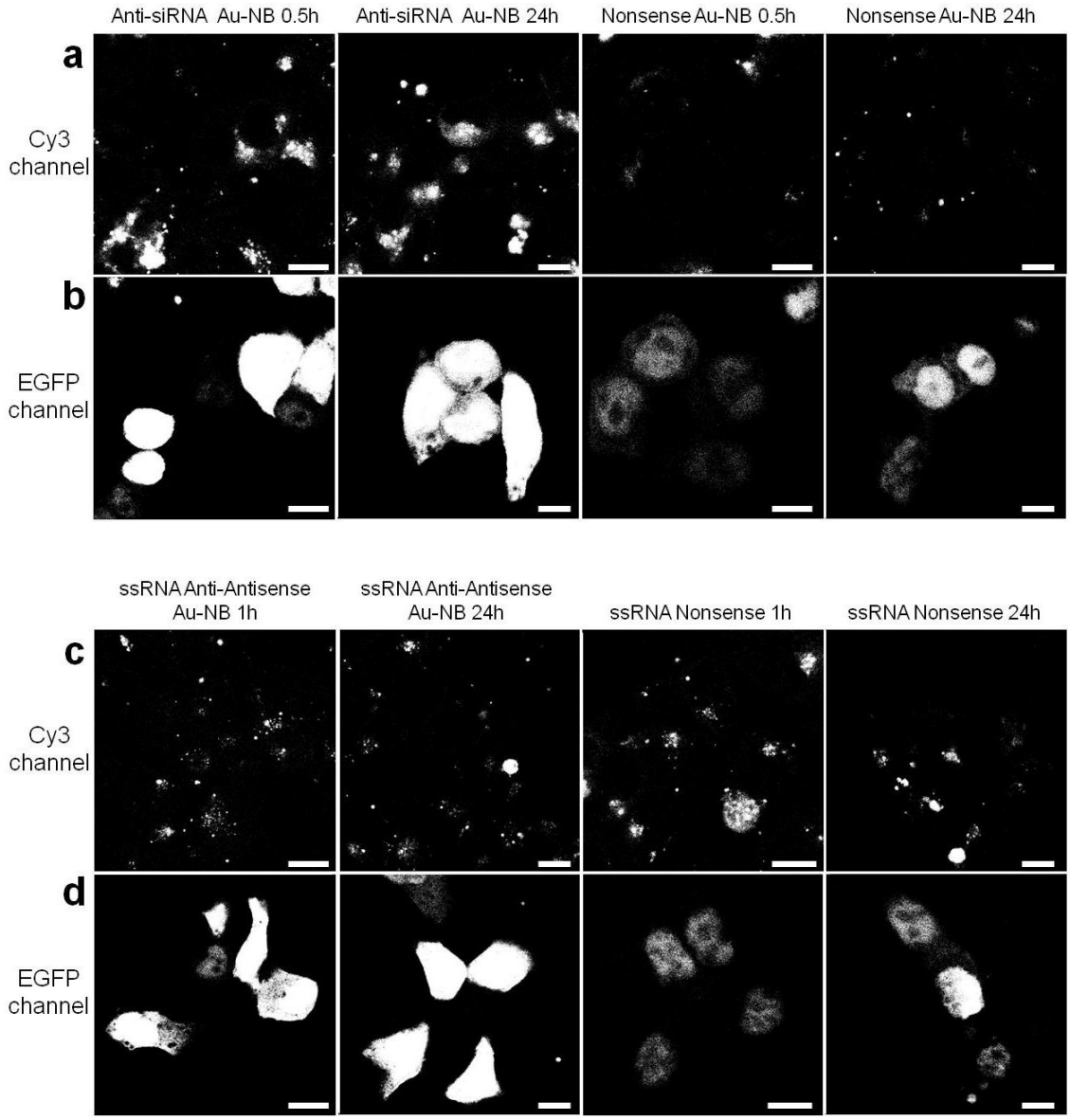

Figure 5.19. EGFP recovery due to anti-siRNA Au-nanobeacon silencing of siRNA. It can be clearly seen that only when the anti-siRNA Au-nanobeacon is emitting fluorescence, thus silencing siRNA, EGFP recovery is observed. The nonsense Au-nanobeacon shows no effect. Regarding the EGFP recovery by ssRNA oligonucleotides used to silence the antisense Au-nanobeacon, there is no difference in Cy3 channel (c) once all cells are incubated with 30 nM of antisense Au-nanobeacon. The EGFP channel (d) clear demonstrates that EGFP recovery was attained only by ssRNA oligonucleotides anti-antisense Au-nanobeacon, when compared to ssRNA nonsense. Scale bar, 10 μm.

5.2.2. Theranostics system on miRNA pathways*

Au-nanobeacon strategy effectiveness was also tested at targeting and silencing an endogenous miRNA. This could represent an important step towards modulation of miRNA pathways in a simple and straightforward way, making the Au-nanobeacon a valid therapeutic approach against oncomiRs. MiRNAs are a class of small non-coding RNAs whose mature products are ~22 nucleotides long. They negatively regulate gene expression by inducing translational inhibition or transcript degradation. MiRNA-21 was one of the first miRNAs to be identified as transcribed by RNA polymerase II, which subsequently has been identified as a major driver of miRNA transcription [229,232]. miR-21 has been found to be upregulated in many pathological conditions including cancer and cardiovascular diseases [229,233]. A non-transcriptional mechanism for miR-21 regulation implying gene amplification, rather than promoter hyper-activation, has been proposed [234]. However, most of the available data suggest that miR-21 expression is maintained by transcriptional and post-transcriptional regulation.

Due to its ubiquitous role in various biological processes, the interest in miRNA-21 has dramatically increased during recent years, especially in cancer and cardiovascular diseases. [233,235,236]. In a subsequent large scale study from 540 human samples, it was found that miR-21 is the only miRNA that is overexpressed in six solid cancers including that of lung, breast, stomach, prostate, colon and pancreas. In later studies miR-21 was established as an oncogenic miRNA and its overexpression was shown in most cancer types analysed so far. miR-21 has also been described to play important roles in regulation of the immune system, development and epithelial-to-mesenchymal transition [229].

To apply the Au-nanobeacon strategy, an anti-miR-21 Au-nanobeacon (33±3 anti-miR beacons per nanoparticle, see Appendix II) was used to block miR-21, which is upregulated in the HCT-116 cell line. The miR-21, referred as an "oncomiR" has been found to be over-expressed in most epithelial cancers and therefore, believed to play a pivotal role in the progression of many malignancies, including colon cancer and in colorectal carcinoma cells [237]. Quantitative expression and silencing efficiency of miR-21 was performed by qRT-PCR using 10, 30 and 50 nM of anti-miR-21 Au-nanobeacon during 24, 48 and 72 hours of incubation. Data shows that steady state expression of miR-21 was transiently but substantially inhibited by the specific Au-nanobeacon at 48 hours (88.5±1.4% miR-21 down regulation) and barely reduced at 72 hours (Figure 5.20d and e). Confocal microscopy results (Figure 5.20a and b) show that miR-21 silencing is associated with increased Au-nanobeacon fluorescence that can be used to assess the silencing effect (Figure 5.21). Data from the Cy3 channel shows that specific target recognition by anti-miR-21 Au-nanobeacon leads to higher signal intensity than that of the nonsense Au-nanobeacon (Figure 5.20c), demonstrating that miR-21 silencing is attained only when the anti-miR-21 Au-nanobeacon opens and emits fluorescence (Figure 5.22).

*Adapted from [226]

To reassure that the Au-nanobeacon fluorescence emission is due to the specific recognition of the target inside cells, thus avoiding false positive signals, the Au-nanobeacons were incubated with increasing concentrations of dithiothreitol (DTT) or glutathione (GST) to mimic the reductive cell milieu (Appendix II, Figure A10). Incubation of anti-miR Au-nanobeacon with 5 mM (physiological concentration), 10 mM and 100 mM of DTT at 37ºC during 24 hours, showed no increase in fluorescence, which demonstrates that, at physiological reductive conditions, the Au-nanobeacons' emission is due to hybridisation to the specific target sequence. Data shows no increase in fluorescence up to 24h incubation, which demonstrates that, at physiological reductive conditions, the Au-nanobeacons' emission is due to hybridisation to the specific target.

For all experiments, cell survival rates upon siRNA and Au-nanobeacon exposure were determined via the MTT assay on HCT-116 cells, with the same experimental conditions of both silencing and recovery of expression. No cell cytotoxicity was detected up to 48 and 72 hours incubation for all Au-nanobeacons and oligonucleotides (Appendix III, figure A12).

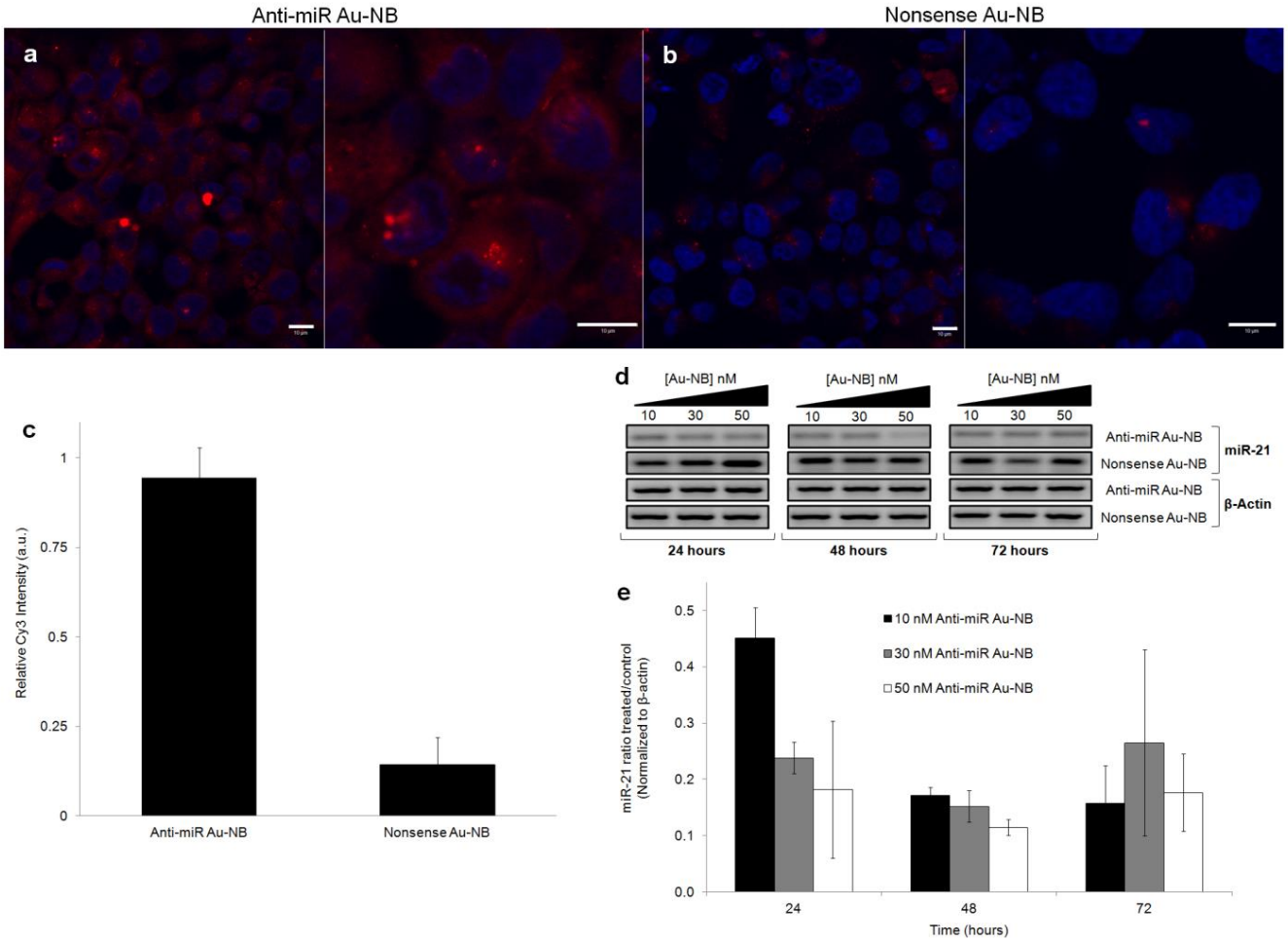

Figure 5.20. Au-nanobeacons silencing of miR-21. Confocal imaging (scale bar, 10 μm) shows internalization of 50 nM (a) Anti-miR Au-nanobeacon 50 nM and (b) Nonsense Au-nanobeacon. Target (mature miR-21) recognition leads to change of Anti-miR Au-nanobeacon conformation in the cytoplasm with concomitant fluorescence signal (red, Cy3) encircling the cell nuclei (blue, DAPI). (c) Specificity of target recognition is corroborated by the relative fluorescence intensity of Au-nanobeacons reading in the Cy3 channel (black bars). (d) Quantitative assessment of miR-21 silencing in colorectal carcinoma cells (HCT-116) induced by 10, 30 and 50 nM of Anti-miR Au-nanobeacon for 24, 48 and 72 hours of incubation using β-actin as reference was confirmed by RT-PCR followed by agarose gel electrophoresis. (e) qRT-PCR analysis of assay versus control normalized for β-actin expression for the same conditions depicted as in (d), error bars indicate ± s.d. from 3 independent experiments.

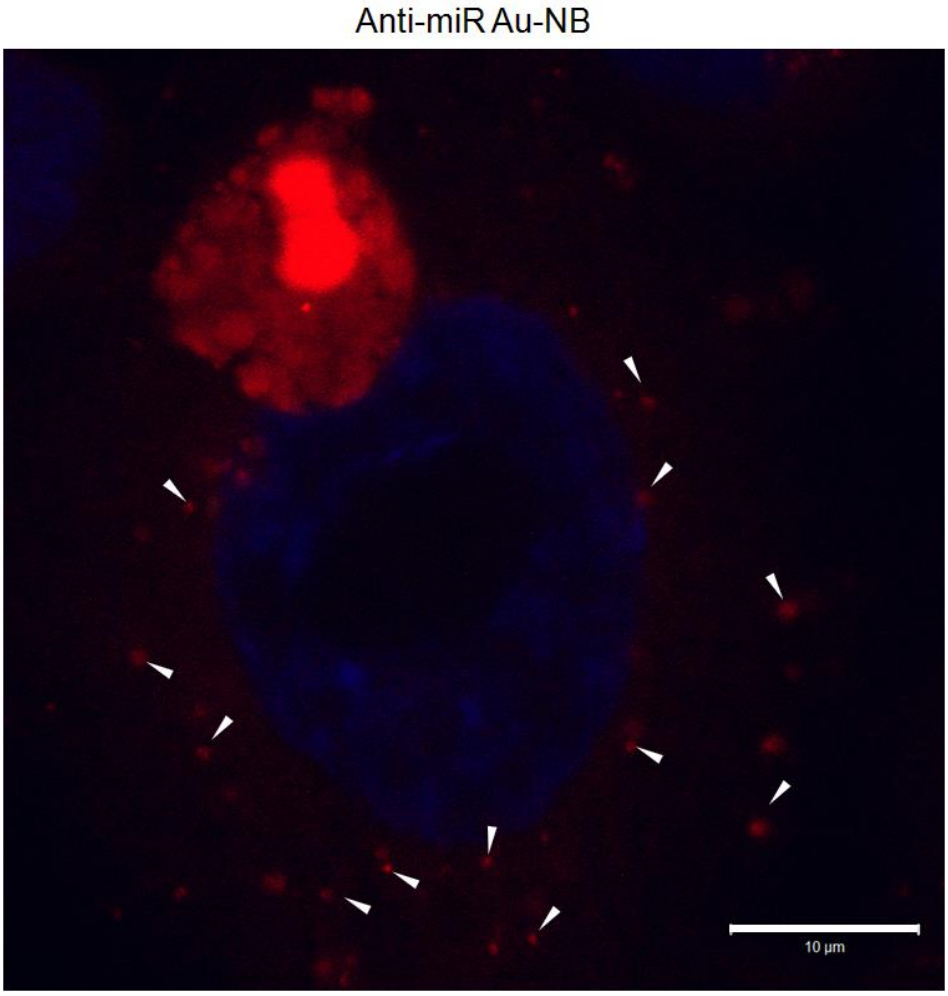

Figure 5.21. Intracellular localization of the anti-miR-21 Au-nanobeacon. Cell show a punctuate fluorescence pattern indicating that the anti-miR Au-nanobeacons distributed evenly in the cytoplasm (white arrows) following hairpin conformational change due to specific hybridisation to the miR-21 target sequence. A large amount of fluorescence seems to be engulfed in a localized compartment above the plan of the nucleus, possibly indicating entrapment in cell vesicle.

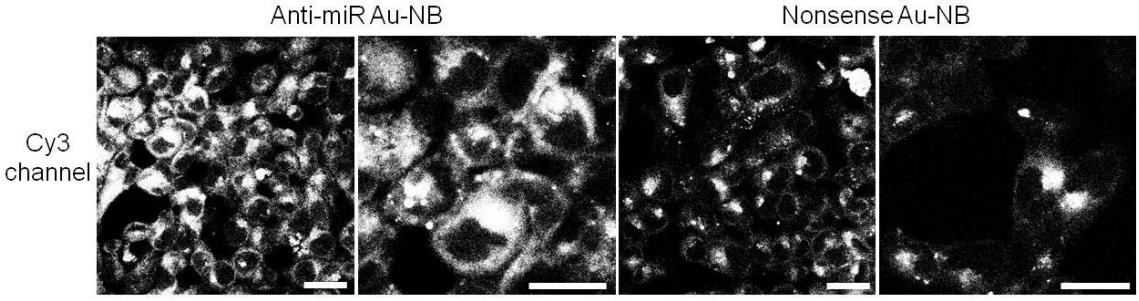

Figure 5.22. Silencing the silencers via anti-miR Au-nanobeacons. Silencing of miR-21 is clearly observed when the Anti-miR Au-nanobeacon is open due to hybridisation to the target, shown by the increased fluorescence intensity in Cy3 channel. These results corroborate what is shown above (Figure 5.20). The nonsense Au-nanobeacon only shows residual fluorescence hardly observable above background. Scale bar, 10 µm.

5.3. Gold nanobeacons for RNA isoform detection

The developed system proved to be versatile and applicable to *in vitro* and *in situ* theranostics applications. The photophysical parameters of the Au-nanoprobes cannot be used due to the impossibility to separate the scattering component from the k_r. However, the system was shown to have potential as an *in vitro* diagnostics tool and potentially therapeutic tool as well. The same principle that fluorescence intensity can be used directly to measure the behaviour of the Au-nanobeacons should also be applicable to a distance analysis. On a similar note to what is described earlier in this work, if a batch of Au-nanobeacons is used throughout the experiments then any variation in observed fluorescence should be regarded as being caused by a change in conformation of the Au-nanobeacon.

The *WT1* was chosen as target to test the applicability of these systems to distance analysis. The *WT1* gene encodes proteins carrying four C-terminal zinc-fingers and is characterized by multiple alternative isoforms. Combinations of alternative exons, alternative start codons, alternative splice sites and RNA editing can theoretically give rise to 36 different proteins [238]. The physiological relevance of most variations remains to be confirmed, with the exception of the KTS isoforms. In this case, the presence (+) or absence (-) of the three aminoacids lysine (K), threonine (T) and serine (S) results in two distinct isoforms: +KTS or –KTS. This variation is conserved throughout vertebrate evolution, and targeted mouse models specifically removing the +KTS or −KTS isoforms show different phenotypes in the homozygous state [239,240], confirming at least partially differing functions for these isoforms. The zinc fingers have been found to function in the sequence-specific binding of nucleic acids. The +KTS isoform's functions appear to be related to post-transcriptional functions, as they can be found in splicing speckles and can directly bind to splicing factors [241–244]. The –KTS form can act as an activator or a repressor of target genes in a cell type-dependent context [238,241].

The ratio of +KTS/−KTS isoforms is conserved across tissues, ranging from 1.10 to 1.49 in humans [245]. A disruption of the equilibrium of both isoforms can bear severe consequences. For example, Frasier Syndrome – characterized by unspecific focal segmental glomerular sclerosis, male-to-female sex reversal (female external genitals, gonads of reduced size, XY karyotype), and a high risk of gonadoblastoma [246] –results from a heterozygous point mutation in the splice donor site in intron 9, resulting in the loss of +KTS isoform expression from one allele [245]. This results in a reduction of the amount of WT1+KTS which leads to the severe developmental abnormalities seen in Frasier Syndrome patients. The importance of the ratio of WT1 isoforms has been further highlighted by the generation of mouse strains in which the ability to express specific isoforms has been removed. Heterozygous mice with a reduction in WT1+KTS isoform expression develop glomerulosclerosis and represent a model for Frasier Syndrome, and homozygous mice not able to express +KTS isoforms

show complete XY sex reversal [245]. In 1990, the *WT1* gene, inactive in 15–20% of Wilms' tumour cases, was identified on chromosome 11 (11p13) [247-250]. Early work on the expression pattern of the gene in humans [251] and mice [252] immediately gave important clues on the biology of the disease and led to important hypotheses on the developmental functions of the gene. Since then, WT1 has been confirmed to be involved in a variety of developmental processes [247].

The possibility of using the potential of distance dependence fluorescence modulation of WT1_S_FAM Au-nanobeacon as molecular rulers was tested by using 2 synthetic oligonucleotides. The WT1_S_FAM was designed to target a part of the mRNA molecule resultant from the transcription of *WT1*. As was explained before, this fragment can be expressed in two isoforms: one including 9 nucleotides coding for Lys-Thr-Ser (+KTS) and one excluding those nucleotides (-KTS). Since RNA oligonucleotides are more expensive and less stable for long periods, two DNA oligonucleotides with the same sequence of the biological target (WT1+KTS and WT1-KTS) were designed to hybridise with Au-nanobeacon at 15˚C in order to assess the feasibility of this system to detect specific minor differences in the sequence size – see Figure 5.23. When hybridised to WT1+KTS, the Au-nanobeacon should form a hybrid DNA-RNA double helix. On the contrary, when hybridised with WT1-KTS there will be 9 nucleotides in the middle of the sequence of the Au-nanobeacon that will not be paired and a different secondary structure should appear.

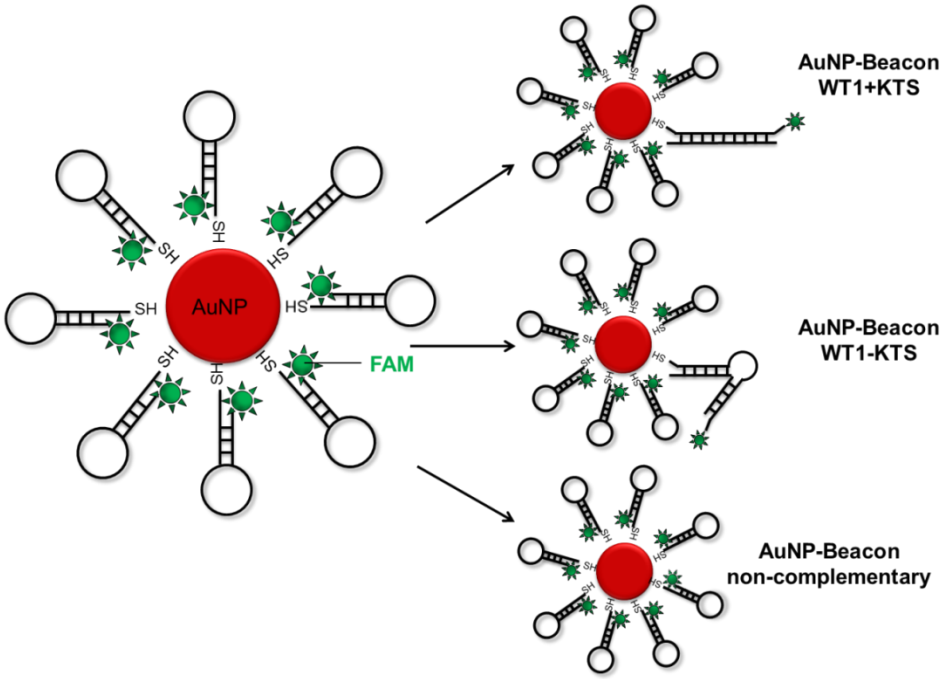

Figure 5.23. Gold nanobeacons for RNA isoform detection. The WT1_S_FAM Au-nanobeacon labelled with FAM will hybridise completely with a fully complementary target (WT1+KTS) or only partially with a partially complementary target (WT1-KTS). In the presence of a non-complementary target the signal configuration should remain similar to the initial one. The hybridisation of the WT1_S_FAM Au-nanobeacon with WT1+KTS should form a hybrid DNA-RNA double helix. On the contrary, when hybridised with WT1-KTS there will be 9 nucleotides of the sequence of the Au-nanobeacon that will remain unpaired and a different secondary structure may occur.

Following the strategy used before in this chapter, Au-nanobeacons were synthesised using WT1_S_FAM and AuNPs with an average diameter of 14.4±2.0 nm (second batch of cit2, see Section 3.1.4) were designed. WT1_S_FAM was designed to be a hairpin DNA structure whose loop is complementary to the part of the mRNA transcript from *WT1* that contains the KTS area. The structure of the Au-nanobeacon was predicted using NUPACK. The result is shown in Figure 5.23A. The predictable secondary structure of the product of the hybridisation with both target oligonucleotides is shown in Figure 5.23B (WT1+KTS) and Figure 5.23C (WT1-KTS). The Au-nanobeacon hairpin sequence is fully complementary to the oligonucleotide WT1+KTS. The hybridisation between the Au-nanobeacon and WT1+KTS is predicted result in a double helix with full and direct complementarity to the Au-nanobeacon. On the contrary, WT1-KTS will only hybridise with both ends of the Au-nanobeacon which is predicted to result in a more unstable structure as can be seen by the lower free energy of the secondary structure. According to the results obtained with NUPACK (used to predict secondary structures of nucleic acids) the hybridisation of WT1_S_FAM will disrupt the hairpin structure promote the formation of a two independent structures: one that is linear and semi-rigid such as the double helix and another with 9 unpaired nucleotides that should force an angle to appear in double helix. It is legitimate to hypothesise that these two structures will put the fluorophore at different distances from the AuNP. Besides the designed stem sequences, WT1_S_FAM also shows weak self-complementarity within the sequence designed to hybridise to *WT1* mRNA. Regardless of this fact, both thiol group (where the AuNP will bond) and the fluorophore will still be forced to be together at this temperature.

5.3.1. WT1_S_FAM Au-nanobeacon characterization

Hybridisation was performed by heating the samples at 95˚C for 5 minutes and letting it cool down to 15˚C. Fluorescence spectra were subsequently measured at the same temperature for all the samples as shown in Figure 5.24A. The spectra obtained show 4 distinct signals. Hybridisation with WT1+KTS and WT1-KTS increases the fluorescence intensity of the Au-nanobeacons when compared to the Au-nanobeacon alone. On the contrary, a similar protocol with a non-complementary target decreases emission comparing with the initial state. From Figure 5.24A it is possible to distinguish the fluorescence intensity that corresponds to WT1+KTS and WT1-KTS but the signals show only a 10% difference and could be within the experimental error. The experiment was triplicated in order to ascertain the level of error within the measurements. The area under the curve of all spectra was calculated for a more accurate quantification and the average values are shown in Figure 5.24B. The error bars correspond to the standard deviation of the measurements which should clarify whether the differences are larger than the experimental error.

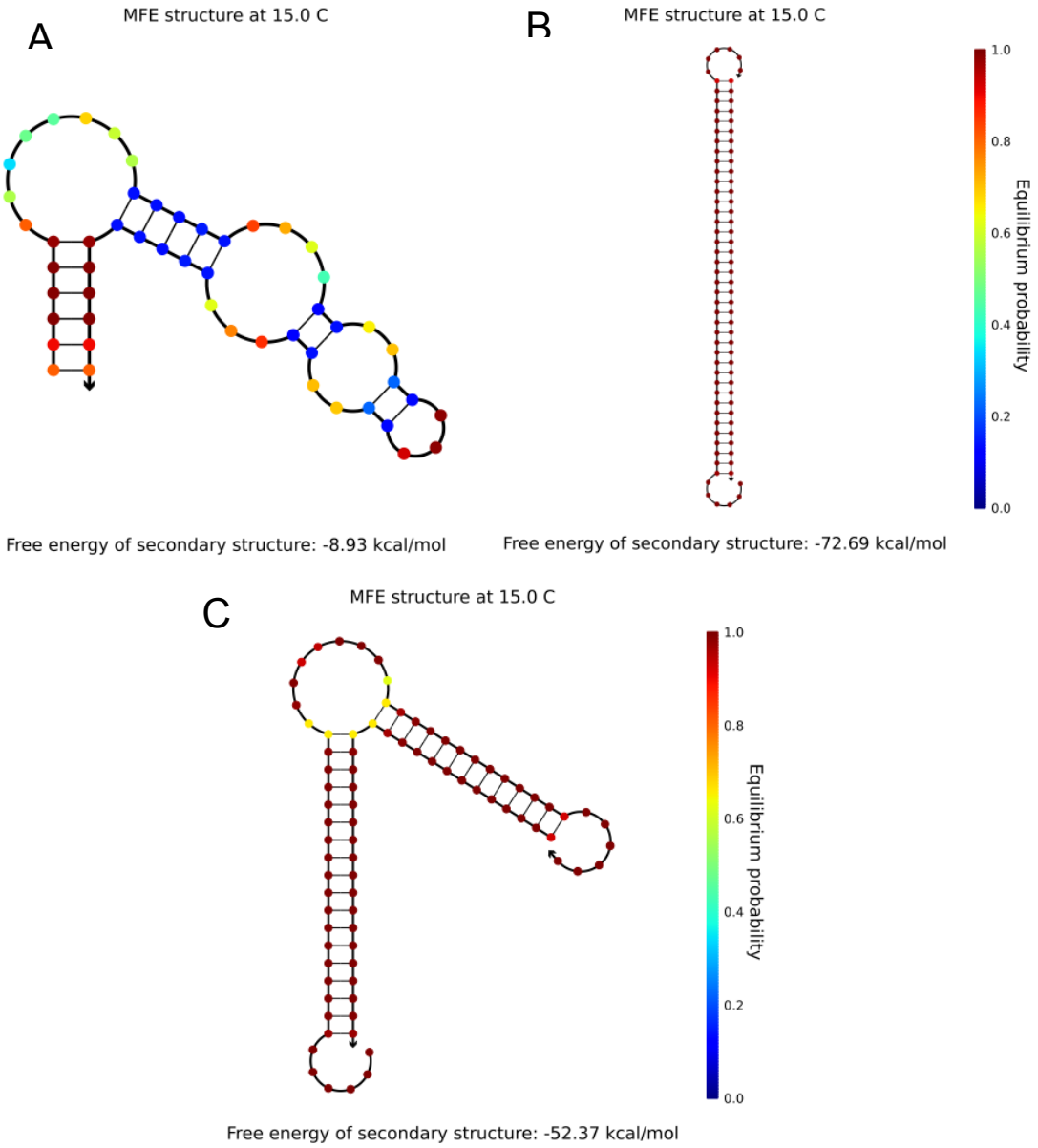

Figure 5.23. Secondary structure of WT1_S_FAM in presence and absence of complementary targets. Two-dimensional structure of the WT1_S_FAM oligonucleotide in absence (A) and presence of complementary targets (B and C) at 15ºC as predicted by NUPACK [224]. In B a fully complementary target (WT1+KTS) is hybridised with WT1_S_FAM forming a double helix while in C a partially complementary sequence (WT1-KTS) is hybridised to WT1_S_FAM forming a double helix with a gap of 9 nucleotides. The free energies of secondary structures presented are negative, which implies that all structures are spontaneous at 15˚C.

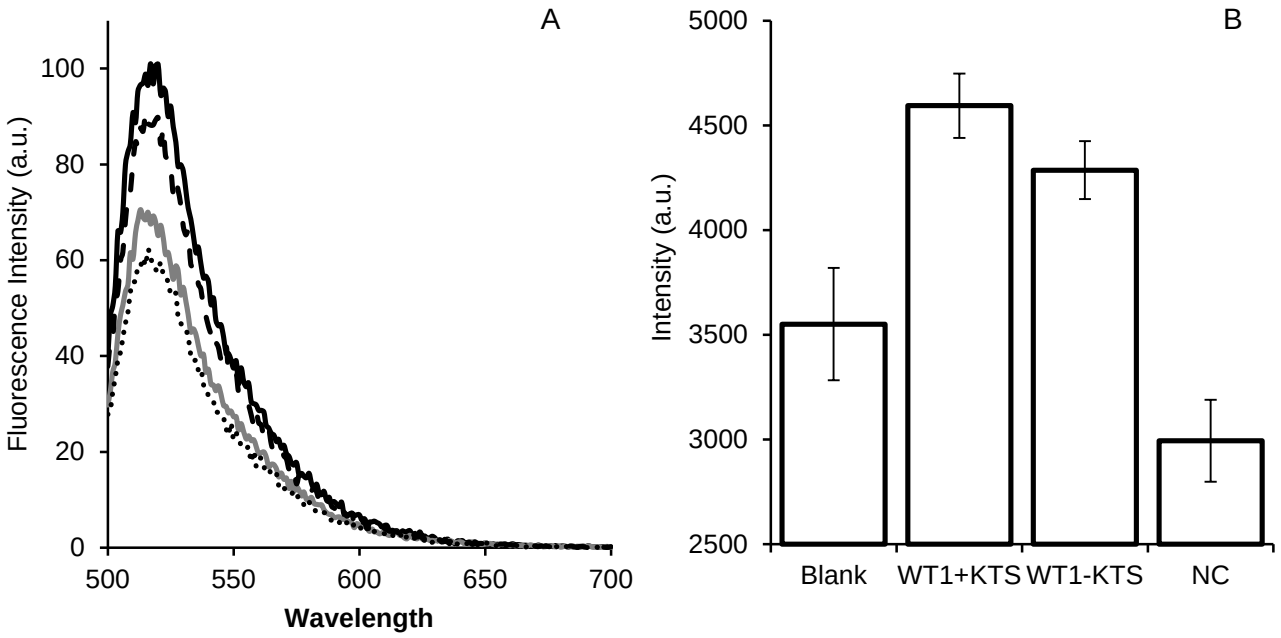

Figure 5.24. WT1 Au-nanobeacon specificity. A - Fluorescence intensity after hybridisation of the WT1 Au-nanobeacon at 15º C in Phosphate buffer 10 mM (pH 8) in presence of a fully complementary target (WT1+KTS, full line line), a partially complementary target (WT1-KTS, dashed line) and non-complementary target (dotted line). The fluorescence intensity in the absence of target is also shown (grey line). B – Area under the fluorescence curves shown in A. Error bars show the standard deviation of triplicate experiments.

These results are very promising and show three independent signals for three types of target. Even if the differences are very thin, they are still outside the experimental error. If anything is to be learned throughout the work in this thesis is that all the possibilities must be accounted for. This means that although the signals are different in direct fluorescence measurement, it is still possible that this difference is not due to a distance variation. One other very plausible cause for the observed results may be that the number of targets hybridised to each Au-nanobeacon is different for all three tested targets. If for NEG2 it is rational that no hybridisation has occurred, for WT1+KTS and WT1-KTS this may not be the case. As shown in Figures 5.23B and C, the hybridisation between the Au-nanobeacon and WT1+KTS and WT1-KTS is associated to different free energies. This suggests that the number of strands hybridised to the Au-nanobeacon could be different for both targets. In that case the increase in intensity could be due to an increase of hairpins that are dislodge from the surface of the AuNP rather than information about the distance at which the AuNP is from the fluorophore. To be sure that the difference in the observed fluorescence intensity is due to a distance effect, it is necessary to assess the number of fluorophores hybridised to the Au-nanobeacon in each case.

Table 5.2. Quantification of the number of strands hybridised to WT1 Au-nanobeacon in presence of a fully complementary target (WT1+KTS), a partially complementary target (WT1-KTS) and non-complementary target (NEG2).

Target	[non-hybridised target] (μM)	[hybridised target] (nM)
WT1+KTS	0.987 ± 0.070	0.013 ± 0.070
WT1-KTS	1.038 ± 0.286	-0.038 ± 0.286
Non-complementary	1.040 ± 0.020	-0.040 ± 0.020

The procedure used to analyse the fluorescence signal of the Au-nanoprobes when hybridised to the targets was repeated using oligonucleotides labelled with cy5. The samples were later centrifuged to remove the excess of target. The number of non-hybridised strands was determined by analysing the supernatants after washing the Au-nanobeacons. The amount of target that did not interact with the Au-nanoprobes was determined by comparing the fluorescence of the supernatants with that of a calibration curve – see Appendix IV. Table 5.2 shows how the template partitioned between the Au-nanobeacon and the supernatant.

The error associated with the determinations is too big for any conclusions. The experiment has been repeated in order to clarify if the errors were sporadic or associated with the experiment. The results were similar. Not knowing the amount of target hybridised with the Au-nanobeacon in each case negates further advance in the understanding of the system, *i.e.,* knowing how intense is the fluorescence intensity associated to each WT1_S_FAM strand when hybridised with both targets. Other strategies could be developed to try to estimate the amount of targets hybridised with the Au-nanobeacon. A more sensitive alternative strategy could lie on the use of radioactive-labelled synthetic target.

The development of an Au-nanobeacon analytical system for distances could follow a different path. The characterization of the system was not successfully achieved but the results concerning the fluorescence intensity signals from the Au-nanobeacons seem promising as biosensor. Since this Au-nanobeacon was only tested using synthetic DNA oligonucleotides it may be important to explore the evolution of its signal when hybridising to RNA samples, since the biological samples it was designed for are RNA samples.

RNA produced using *in vitro* transcription are a more appropriate targets to test the feasibility of the system as detection and analysis system than DNA oligonucleotides as they are more similar. To be able to produce RNA transcripts, it was necessary to clone the desired sequence. RNA was extracted from HCT-116 cell line and from kidney of patient of Wilms Tumour. Reverse Transcription was applied to the product of the RNA extraction and followed by PCR reaction using the conditions explained in Section 2.6.1.1.2 of this work. Although several conditions were tested, it was never possible to obtain a PCR product that could be ligated to the vector. Only a very faint band could be

seen in one gel but the product of ligation was never successfully reamplified for confirmation. As a last resort, a transfection of the vectors ligated with the PCR products obtained was tested but no viable colonies were detected. A reason for the absence of an effective PCR product can be speculated for the two sources of biological material that were tested. The kidney sample used to extract RNA was stored at -80˚C for over 10 years and the extracted RNA could be degraded. As for the RNA extracted from the HCT-116 cell line, it is possible that *WT1* was not being expressed. HCT-116 cells are epithelial cells derived from colorectal carcinoma cells while *WT1* has an essential role in the normal development of the urogenital system. It is plausible to argue that *WT1* may not be activated in HCT-116 cells.

CHAPTER 6. General Discussion and Conclusions

The advances in nanoscience brought significant impact on many other scientific fields, with particular interest in biomedical applications ranging from biomolecular detection, characterisation of interaction between biomolecules both *in vivo* and *in vitro*, and towards the development of therapeutics. Amongst these topics, the interaction of nanomaterials with light appeared as the chance to develop more sensitive and robust biomolecular diagnostics.

The main objective of this thesis was to study the fluorescence modulation induced by gold nanoparticles (AuNPs) on fluorophores nearby and/or bonded to the AuNPs' surface through nucleic acid molecules. The understanding of the effect of distance in the spectral properties of fluorophores would allow the development of a biosensor for the characterisation of DNA and/or RNA sequences towards the development of diagnostics and/or molecular therapy approaches. Throughout the work presented in this thesis, data was obtained regarding the modulation properties of gold nanoparticles on fluorescence and their application for nucleic acid detection. The experimental work developed in this thesis provided valuable information about AuNP-fluorophores systems. An experimental-based approach was devised to characterise AuNP-fluorophore systems and clarifying the events associated with AuNP-induced fluorescence modulation for a broader evaluation of the system:

- The AuNPs in solution strongly compete for the incident light and may affect the photophysical characterization of AuNP-fluorophore systems. Physically separating AuNPs and fluorophores while maintaining the optical path in a two-chambered cuvette showed that the mere presence of AuNPs in solution reduces the amount of light available for the fluorophores.

- The photophysics of AuNP-fluorophore systems can be drastically affected by other physical and chemical phenomena other than fluorescence modulation. The surface of the AuNPs was demonstrated to modify the absorption spectra of fluorophores on their surface. SAMSA was shown to change its spectrum due to a local pH effect at the surface of the AuNPs, Rhodamine B suffers multimodal coupling of optical transitions with the LSPR and Rhodamine 101 changes its absorption spectrum dramatically.

- Scattered light absorption may play an influential role in this interaction. Scattered light is about 4200 times more intense at the surface than at the average distance in the used conditions. The designed experimental approach is based on the assumption that reference molecules and samples are in the same optical conditions. However, the effect of the dilution of the light scattered from the AuNP with distance was not accounted for. Even considering that the scattered light is only one of the sources of light available to the fluorophores, the presented simulation on the matter questions whether the increase of the radiative rate constant does in fact occur. The simulated dilution factor is about 717 times larger than the increase in the measured radiative constant.

- Despite the setbacks, the method developed during this thesis allowed for the determination of a radiative enhancement (k_r'), directly dependent on the k_r and the amount of light reaching each fluorophores, and k_{nr}'. Both radiative and non-radiative phenomena are involved in the observed fluorescence modulation.

- The effect of distance on the modulation caused by the AuNPs on the fluorescence of 5-FAM was determined to be dependent on r^6. Both Φ_F and τ variation showed a better fitting into an r^6 distance dependence to the surface of the AuNP than into an r^4 distance dependence to the centre of the AuNP. This behaviour is closer to the one observed in a typical FRET mechanism than to the SET mechanism proposed in literature. A simulation on the effect of scattered light in k_r and k_{nr} reinforces the relevance of taking into account the light scattered back from the nanoparticles.

One of the main conclusions of this work is that AuNP-fluorophores systems are more complex than just the metallic surface interaction with the fluorophore. Most of the literature on this topic is usually based on theoretical models that consider the electromagnetic interaction between the plasmonic band of the AuNPs and the fluorophores but disregard that AuNPs are more than just a metallic core. The importance of the theoretical models is not questionable but the transition to practical application clearly requires a careful experimental characterisation of each system. The work described throughout this thesis incites a consideration on what is indeed being measured when studying AuNP-fluorophore systems. All the unexpected phenomena that were described can effectively mislead the interpretation of collected data if not taken into account. The presence of AuNPs filters the light available to the fluorophores in the sample even without physical contact. Also, the fluorophores that directly interacted with the surface of the AuNPs changed their absorption spectra due to interactions with the AuNPs that are unrelated with the photophysical modulation induced by the metallic surface. All these phenomena can directly influence the determination of Φ_F and, consequently, k_r and k_{nr}.
It is must be stressed that all of fluorophores appear to interact due to different causes, such as pH effects, coupling of the oscillator with the optical transition of the fluorophore and apparent fluorophore aggregation. This idea suggests that each fluorophore may interact differently with each set of AuNPs and that every combination of fluorophores and AuNPs may result in an unexpected interaction between them. Unfortunately, all the tested fluorophores were non-photophysically affected by the AuNPs and a direct characterisation could not be performed.

Despite the breakthroughs, some issues were not successfully tackled. The contribution of light intensity could not be split from k_r. The inability to effectively quantify the contribution of scattering allowed only the determination of a measurable constant (k_r') that contains both k_r and incident light intensity. In what concerns the understanding of the system in terms of photophysical modulation this represents a major setback that could not be experimentally countered. The fact that k_r' of a molecule

increases when in presence of the AuNPs still does not clarify whether this increase is in fact an increase in the emission rate or merely an increase in the number of photons that reach the fluorophores. Nonetheless, the increase in k_r' represents the potential of increasing emissivity of a molecule by placing it in the vicinity of a nanosurface. This is even more relevant considering that the growth observed in k_{nr}' is two orders of magnitude higher than the one observed in k_r'.

The nature of the LSPR in the AuNP-fluorophore interaction is crucial. Not only the position and intensity of the LSPR peak is a major factor in the energy transfer mechanism, but whether the scattering component or the absorption component are predominant is also very important. The optical interference caused by the AuNPs would also be affected. The data obtained in this work supports the idea that the absorption component is the cause for the quenching in fluorescence and the scattering component is associated to the measurable enhancement. A change in AuNP size, shape or composition would change the LSPR band and, consequently, change the interaction with a fluorophore. One can speculate that a drastic increase in the AuNPs' size could result in the predominance of the scattering component which could lead to a more noticeable enhancement. On the contrary, a decrease in the AuNPs' size would reinforce the absorption component predominance and which should result in an even more extensive quenching.

The experiments with fluorophores at different distances allowed for the determination of the distance-dependence rule of the studied system. With the used AuNPs and fluorophore the system varied its fluorescence with r^6, similarly to what happens in FRET. One possible evaluation of this result is that the AuNPs are not big enough for the fluorophore to interact with them as a nanosurface but rather as a dipole. Adding to all the mentioned effects, increasing the AuNPs size could also result in a change of the nature of the interaction between AuNPs and fluorophores as the AuNPs could start behaving as a nanosurface.

The use of AuNPs to measure distances with energy transfer mechanisms could improve the range of distances that can be measured. The results presented in this thesis indicate that with this set of AuNPs and fluorophores distances in the range of 50-140Å can be measured. This range is complementary to the one usually obtained with typical FRET pairs and, if explored and optimized correctly, could provide an important tool to measure distance in biologic environments.

An initial approach to the development of a nanobiophotonics sensor was attempted. The results obtained during this work allowed the acknowledgment that, with proper corrections, the observed emission variation could be used by itself for the development of a detection system for nucleic acids. The use of DNA hairpin-structure offered a system that would be more quenched in the absence of a complementary target and less quenched in its presence, allowing for positive/negative discrimination. The used Au-nanobeacons were capable of semi-quantitatively recognizing specific complementary sequences. Moreover, by using a second Au-nanobeacon it was also possible to create a dual colour

system capable of quantify transcription and the level of inhibition in a single reaction vial. The described Au-nanobeacon biosensor allows for fast, accurate and sensitive RNA transcript expression profiling. An interesting feature of this sensor is that the probes do not generate a signal from unrelated nucleic acids and polymerase activities can be distinguished from promoter-specific RNA polymerization. The simplicity and speed of the sensor are also great advantages.

This system evolved to an *in situ* approach where a new and versatile concept for genes specific silencing was devised. In this case, the Au-nanobeacons also allowed for intracellular tracking of the silencing events. A significant attribute of these Au-nanobeacons is the ability to hybridise to endogenous and exogenous nucleic acids with noticeably small amounts of Au-nanobeacons and without chemical co-transfectants. This extraordinary efficiency without adverse side effects is probably due to the fact that each nanoparticle is functionalised with several oligonucleotides.

The use of Au-nanobeacons for detection and silencing is simple, inexpensive and straightforward as adjustment to any specific target, be it a specific mRNA or an endogenous or exogenous silencing nucleic acid, can be easily made simply by changing the sequence of the oligonucleotide used to functionalise the AuNPs. The presence of AuNPs confer resistance to nuclease degradation, these sensors may be used to follow gene silencing *in vivo*, thus providing additional information to assist modelling of actual gene therapy protocols.

Finally, the possibility of silencing the silencers and of discriminating specific cells, where silencing is occurring, offers future prospects for studying and modulating cellular mechanisms involved in cancer. Combination of Au-nanobeacons with other chemical functionalisations, *e.g.* targeting moieties, may enhance the therapeutic potential of this concept.

As often occurs in science, more answers lead to more questions. All of the proposed objectives were addressed but there is a lot more to know about nanoparticle-fluorophore systems. The aforementioned issues about the importance of scattering and absorption components in the plasmonic bands of the AuNPs raise questions on the nature of nanoparticle-fluorophore interactions. Is there a real enhancement or is it an increase in absorbed light? Can the energy transfer be reduced without losing the enhancement factor? It is clear that more experiments using different AuNPs sizes and fluorophores in other regions of the spectrum would be central in the comprehension of the nanoparticle-fluorophore interaction. Using different materials for the synthesis of the nanoparticles may also help in the understanding of the system.

The usefulness of Au-nanobeacons for diagnostics *in vitro* and *in situ* was clearly demonstrated. The natural course of this research envisions the possibility of using Au-nanobeacons in full organisms. A full theranostics approach can result from these systems. By combining the demonstrated proficiency

in target detection with the potential therapeutic approach may result in a tool that effectively modulates nucleic acid pathways and simultaneous provides a signal that localises the event. The span of targets that can be chosen is endless which can transform the Au-nanobeacons approach into a valuable technique not only as an actual theranostics vessel but also a biological and biotechnological research tool.

A different perspective provides a future sight into other applications. The combination of molecules with nanosurfaces is not exclusive to the fluorescence modulation or nanodiagnostics. The interaction of Rhodamine 101 demonstrated that AuNPs can provide the conditions to facilitate other reactions. If the modulation of the rate constants involved in the several photophysical phenomena of a molecule can be properly understood, it is possible that AuNPs can be used to modulate photochemical reactions as well. More importantly, it is possible that AuNPs can be used to modulate how light interacts with molecules, *i.e.*, changing radiative rate constants, increasing amount of light absorbed by neighbour molecules, which could result in more controlled and efficient photochemical reactions or brighter emission.

In summary, this thesis has successfully achieved its objectives by providing important information on the modulation of fluorescence induced by AuNPs. An experimental method was developed and successfully applied, allowing a closer understanding to how AuNPs influence nearby molecules, not only photophysically but also chemically. A nanodiagnostics system was successfully designed and tested *in vitro* and *in situ* and may pave the way for a new era of nanotheranostics approaches. There is still a lot to understand and explore about AuNP-DNA-fluorophore systems and I hope that the work here presented can contribute to a clearer and more comprehensive study in the field.

REFERENCES

1. Feynman RP (1960) There's plenty of room at the bottom. *Engineering and Science*, **23**:22-36

2. Faraday M (1857) On the color of colloidal goal. *Phil. Trans. R. Soc. Lond.*, **147***:*145-181

3. Edwards PP, Thomas JM (2007) Gold in a metallic divided state – from Faraday to present-day nanoscience. *Angew. Chem. Int. Ed.*, **46**(29):5480-6

4. Shen Y, Friend CS, Jiang Y, Jakubczyk D, Swiatkiewicz J, Prasad PN (2000) Nanophotonics: Interactions, Materials, and Applications. *J.Phys.Chem.B.* **104**: 7577-7587

5. Ohtsu M, Kobayashi K, Kawazoe T, Yatsui T and Naruse M (2008) Principles of nanophotonics. 1st ed., *Taylor & Francis Group Press*, London, UK

6. Shen,Y and Prasad PN (2002) Nanophotonics: a new multidisciplinary frontier. *Appl.Phys.B.*, **474**: 641-645.

7. Jain KK (2007) Applications of nanobiotechnology in clinical diagnostics. *Clin Chem*, **53**:2002-2009

8. Jain KK (2008) Nanomedicine: application of nanobiotechnology in medical practice. *Med Princ Pract*, **17**:89-101

9. Jain KK (2003) Nanodiagnostics: application of nanotechnology in molecular diagnostics. *Expert Rev Mol Diagn*, **3**:153-161

10. Valeur B (2001) Molecular fluorescence: principles and applications. 1st ed., *Wiley-VCH*, Weinheim, Germany

11. Miller JN (1981) Standards in fluorescence spectrometry. 1st ed., *Chapman and Hall Ltd*, New York, USA

12. Lambert JH (1760) Photometria sive de mensura et gradibus luminis, colorum et umbrae (Photometry, or, One the measure and gradations of light, colors and shade). Augsburg, Germany

13. Beer A (1852) Bestimmung der Absorption des rothen Lichts in farbigen flüssigkeiten (Determination of the absorption of red light in colored liquids). *Annalen der Physik und Chemie*, **86**:78-88

14. Rohatgi-Mukherjee KK (1986) Fundamentals of photochemistry, Revised ed., *Wiley Eastern Limited*, New Delhi, India

15. Lakowicz JR (2006) Principles of fluorescence spectroscopy, 3rd ed., *Springer*, Singapore

16. Kasha M (1950) Characterization of electronic transitions in complex molecules. *Disc Faraday Soc*, **9**:14–19

17. Berlman IB (1971) *Handbook of fluorescence spectra of aromatic molecules*, 2nd ed., *Academic Press*, New York, USA

18. Morris KJ, Roach MS, Xu W, Demas JN, deGraaf BA (2007) luminescence lifetime standards for the nanosecond to microsecond range and oxygen quenching of ruthenium(II) complexes. *Anal. Chem.*, **79**:9310-9314

19. Nakashima N, Yoshihara K, Tanaka F, Yagi K (1980) Picosecond fluorescence lifetime of the coenzyme of D-amino acid oxidase. *J. Biol. Chem.*, **255**(11):5261-5263

20. Kandori H, Katsuta Y, Ito M, Sasabe H (1995) Femtosecond fluorescence study of the rhodopsin chromophore in solution. *J. Am. Chem. Soc.*, **117**(9):2669–2670

21. Wang A (2008) Measurement of the fluorescence quantum yield using a spectrometer with an integrating sphere detector. *J. Res. Natl. Inst. Stand. Technol.*, **113**(1):17-28

22. Olmsted J (1979) Calorimetric determinations of absolute fluorescence quantum yields. *J. Phys. Chem.*, **83**(20):2581–2584

23. Weber G, Teale FWJ (1957) Determination of the absolute quantum yield of fluorescent solutions. *Trans. Farad. Soc.*, **53**:646-655

24. Dawson WR, Kropp JL (1965) Measurement of fluorescence yields of europic ion upon excitation to selected levels. *J.Opt. Soc. Amer.*, **55**:822-828

25. Dawson WR, Windsor MW (1968) Fluorescence yields of aromatic compounds. *J. Phys. Chem.*, **72**(9):3251-3260

26. Arden-Jacob J, Drxhage KH, Druzhinin SI, Ekimova M, Flender O, Lenzer T, Oum K, Scholz M (2013) Ultrafast photoinduced dynamics of the 3,6-diaminoacridinium derivative ATTO 465 in solution. *Phys. Chem. Chem. Phys.*, **15**:1844-1853

27. Ware WR (1971) Transient luminescence measurements. In creation and detection of the excited state, Vol. 1A. Editor Lamola AA. *Marcel Dekker*, New York, USA

28. Verity B, Bigger SW (1996) The dependence of quinine fluorescence quenching on ionic strength. *Int. J. Chem. Kinet.*, **28**(12):919–923

29. Seidel CAM, Schulz A, Sauer MHM (1996) Nucleobase-specific quenching of fluorescent dyes, 1: nucleobase one-electron redox potentials and their correlation with static and dynamic quenching efficiencies. *J. Phys. Chem.*, **100**:5541–5553

30. Visser AJWG (1984) Kinetics of stacking interactions in flavin adenine dinucleotide from time-resolved flavin fluorescence. *Photochem. Photobiol.*, **40**(6):703–706

31. Marras SAE, Kramer FR, Tyagi S (2002) Efficiencies of fluorescence resonance energy transfer and contact-mediate quenching in oligonucleotide probes. *Nucleic Acids Res.*, **30**:21

32. Grellmann KH, Watkins AR, Weller A (1972) Electron-transfer mechanism of fluorescence quenching in polar solvents. I. Dicyanobenzene as quencher. *J. Phys. Chem.*, **76**(4):469-473

33. Kearvell A, Wilkinson F (1968) Fluorescence quenching and external spin-orbit coupling effects. *Mol. Crystals*, **4**:69-81

34. Antonov L, Gergov G, Petrov V, Kubista M and Nygren J (1999) UV-Vis spectroscopic and chemometric study on the aggregation of ionic dyes in water. *Talanta*, **49**(1):99-106

35. Arbeloa FL, Ojeda PR, Arbeloa IL (1988) On the aggregation of rhodamine B in ethanol. *Chem. Phys. Lett.*, **148**(2–3) 253–258

36. Förster T (1948) Intermolecular energy migration and fluorescence (Translation by Knox RS). *Ann. Phys.*, **2**:55–75.

37. Ge S, Lu J, Yan M, Yu F, Yu J, Sun X (2011) Fluorescence resonance energy transfer sensor between quantum dot donors and neutral red acceptors and its detection of BSA in micelles. *Dyes and Pigments*, **91**:304-308

38. Bruchez M, Moronne M, Gin P, Weiss S, Alivisatos AP (1998) Semiconductor nanocrystals as fluorescent biological labels. *Science*, **281**:2013–2016

39. Clegg RM (2009) Förster resonance energy transfer – FRET what is it, why do it, and how it's done. Laboratory Techniques in Biochemistry and Molecular Biology, Volume **33**:1-57. FRET and FLIM Techniques. Editor Gadella TWJ.*Academic Press*, Burlington, USA

40. Dexter DL (1953) A theory of sensitized luminescence in solids. *J.Chem.Phys.*, **21**:836-850

41. Vollath D (2008) Nanomaterials: an introduction to synthesis, properties and applications. 1st ed., *Wiley-VCH*, Weinheim, Germany

42. Baptista P, Pereira E, Eaton P, Doria G, Miranda A, Gomes I, Quaresma P, Franco R (2008) Gold nanoparticles for the development of clinical diagnosis methods. *Anal Bioanal Chem*, **391**:943-950

43. Boisselier E, Astruc D (2009) Gold nanoparticles in nanomedicine: preparations, imaging, diagnostics, therapies and toxicity. *Chem Soc Rev*, **38**:1759-1782

44. Sperling RA, Rivera Gil P, Zhang F, Zanella M, Parak WJ (2008) Biological applications of gold nanoparticles. *Chem Soc Rev*, **37**:1896-1908

45. Huang X, Jain PK, El-Sayed IH, El-Sayed MA (2007) Gold nanoparticles: Interesting optical properties and recent applications in cancer diagnostics and therapy. *Nanomed*, **2**:681-693

46. Murray RW (2008) Nanoelectrochemistry: Metal Nanoparticles, Nanoelectrodes, and Nanopores. *Chem.Rev.*, **108**:2688-2720

47. Ouyang J, Chu CW, Szmanda CR, Ma L, Yang Y (2004) Programmable polymer thin film and non-volatile memory device. *Nature Mater.*, **3**:918-922

48. Bozano LD, Kean BW, Beinhoff M, Carter KR, Rice PM, Scott JC (2005) Organic materials and thin-film structures for cross-point memory cells based on trapping in metallic nanoparticles. *Adv. Funct. Mater.* **15:**1933-1939

49. Leong WL, Lee PS, Mhaisalkar SG, Chen TP, Dodabalapur A (2007) Charging phenomena in pentacene-gold nanoparticle memory device. *Appl. Phys. Lett.* **90**:042906

50. Gittins DI, Bethell D, Schiffrin DJ, Nichols RJ (2000) A nanometre-scale electronic switch consisting of a metal cluster and redox addressable groups. *Nature*, **408**:67-69

51. Chen M, Goodman DW (2006) Catalytically active gold: from nanoparticles to ultrathin films. *Acc. Chem. Res.*, **39**:739-746

52. Daniel MC, Astruc D (2004) Gold nanoparticles: assembly, supramolecular chemistry, quantum-size-related properties, and applications toward biology, catalysis, and nanotechnology. *Chem. Rev,*. **104**(1):293-346

53. Turkevich J, Stevenson PC, Hillier J (1951) A study of the nucleation and growth processes in the synthesis of colloidal gold. *Discuss. Faraday. Soc.*, **11**:55-75

54. Frens G (1973) Controlled nucleation for the regulation of the particle size in monodisperse gold suspensions. *Nat. Phys. Sci.*, **241**:20-22

55. Wilcoxon JP, Abrams BL (2006) Synthesis, structure and properties of metal nanoclusters. *Chem. Soc. Rev.*, **35**:1162-1194

56. Kimling J, Maier M, Okenve B, Kotaidis V, Ballot H, Plech A (2006) Turkevich method for gold nanoparticle synthesis revisited. *J. Phys. Chem. B*, **110**(32):15700-15707

57. Tréguer-Delapierre M, Majimel J, Mornet S, Duguet E, Ravaine S (2008) Synthesis of non-spherical gold nanoparticles. *Gold Bull.* 2008, **41**:195-207

58. Yuan Q, Wang X (2010) Aqueous-based route toward noble metal nanocrystals: Morphology-controlled synthesis and their applications. *Nanoscale*, **2**:2328-2335

59. Sau TK, Rogach AL (2010) Nonspherical noble metal nanoparticles: Colloid-chemical synthesis and morphology control. *Adv. Mater.*, **22**:1781-1804

60. Murphy CJ, Sau TK, Gole AM, Orendorff CJ, Gao J, Gou L, Hunyadi SE, Li T (2005) Anisotropic metal nanoparticles: Synthesis, assembly, and optical applications. *J. Phys. Chem. B*, **109**:13857-13870

61. Pelton M, Aizpurua J, Bryant G (2008) Metal-nanoparticle plasmonics. *Laser & Photon Rev.2.*, **3**:136-159

62. Jain PK, Lee KS, El-Sayed IH, El-Sayed MA (2006) Calculated absorption and scattering properties of gold nanoparticles of different size, shape, and composition: applications in biological imaging and biomedicine. *J. Phys. Chem. B*, **110**:7238-7248

63. Link S, El-Sayed MA (2000) Shape and size dependence of radiative, non-radiative and photothermal properties of gold nanocrystals. *Int. Rev. Phys. Chem.*, **19**:409-453

64. Liang A, Liu Q, Wen G, Jiang Z (2012) The surface-plasmon-resonance effect of nanogold/silver and its analytical applications. *Trends in Anal. Chem.*, **37**:32–47

66. Hu M, Chen J, Li Z, Au L, Hartland GV, Li X, Marquez M, Xia Y (2006) Gold nanostructures: engineering their plasmonics properties for biomedical applications. *Chem. Soc. Rev.*, **35**:1084-1094

67. Eustis S, El-Sayed MA (2006) Why gold nanoparticles are more precious than pretty gold: noble metal surface plasmon resonance and its enhancement of the radiative and nonradiative properties of nanocrystals of different shapes. *Chem.Soc.Rev.*, **35**: 209-217

68. Ghosh SK, Pal T (2007) Interparticle coupling effect on the surface plasmon resonance of gold nanoparticles: from theory to applications. *Chem.Rev.*, **107**: 4797-4862

69. Zhao W, Brook MA, Li Y (2008) Design of gold nanoparticle-based colorimetric biosensing assays. *Chembiochem.*, **9**: 2363-2371

70. Jain PK, Huang W, El-Sayed MA (2007) On the universal scaling behavior of the distance decay of plasmon coupling in metal nanoparticle pairs: A plasmon ruler equation. *Nano Lett.*, **7**:2080-2088

71. Liz-Marzan LM (2006) Tailoring surface plasmons through the morphology and assembly of metal nanoparticles. *Langmuir*, **22**:32-41

72. Mie G (1908) Beiträge zur optik trüber medien, speziell kolloidaler metallösungen. *Ann. Phys.*, **330**:377-445

73. Link S, Burda C, Wang ZL, El-Sayed MA (1999) Electron dynamics in gold and gold-silver alloy nanoparticles: the influence of a nonequilibrium electron distribution and the size dependence of the electron:phonon relaxation. *J. Chem. Phys.*, **111**:1255-1264

74. Voisin C, Del Fatti N, Christofilos D, Vallée F (2001) Ultrafast electron dynamics and optical nonlinearities in metal nanoparticles. *J. Phys. Chem. B*, **105**:2264-2280

75. Ahmadi TS, Logunov SL, El-Sayed MA (1996) Picosecond dynamics of colloidal gold nanoparticles. *J. Phys. Chem.,* **100**:8053-8056

76. Perner M, Bost P, Lemmer U, von Plessen G, Feldmann J, Becker U, Mennig M, Schmitt M, Schmidt H (1997) Optically induced damping of the surface plasmon resonance in gold colloids. *Phys. Rev. Lett.,* **78**:2192-2195

77. Logunov SL, Ahmadi TS, El-Sayed MA, Khoury JT, Whetten RL (1997) Electron dynamics of passivated gold nanocrystals probed by subpicosecond transient absorption spectroscopy. *J. Phys. Chem. B,* **101**:3713-3719

78. Hodak JH, Martini I, Hartland GV (1998) Spectroscopy and dynamics of nanometer-sized noble metal particles. *J. Phys. Chem. B,* **102**:6958-6967

79. Mohamed MB, Ahmadi TS, Link S, Braun M, El-Sayed MA (2001) Hot electron and phonon dynamics of gold nanoparticles embedded in a gel matrix. *Chem. Phys. Lett.,* **343**:55-63

80. Wilcoxon JP, Martin JE, Parsapour F, Wiedenman B, Kelley DF (1998) Photoluminescence from nanosize gold clusters. *J. Chem. Phys.*, **108**:9137

81. Bigioni TP, Whtten RL, Dag Ö (2000) Near-infrared luminescence from small gold nanocrystals. *J. Phys. Chem. B,* **104**:6983-6986

82. Sperling RA, Parak WJ (2010) Surface modification, functionalisation and bioconjugation of colloidal inorganic nanoparticles. *Phil. Trans. R. Soc. A,* **368**:1333-1383

83. Subbiah R, Veerapandian M, Yun KS (2010) Nanoparticles: Functionalisation and multifunctional applications in biomedical sciences. *Curr. Med. Chem.,* **17**:4559-4577

84. Ipe BI, Thomas KG, Barazzouk S, Hotchandani S, Kamat PV (2002) Photoinduced charge separation in a fluorophore-gold nanoassembly. *J. Phys. Chem. B,* **106**:18-21

85. Aguila A, Murray RW (2000) Monolayer-protected clusters with fluorescent dansyl ligands. *Langmuir*, **16**:5949-5954

86. Gu T, Whitesell JK, Fox MA (2003) Energy transfer fro a surface-bound arene to the gold core in ω-fluorenyl.alkane-1-thiolate monolayer-protected gold clusters. *Chem. Mater.*, **15**:1358-1366

87. Jennings TL, Singh MP, Strouse GF (2006) Fluorescent lifetime quenching near d=1.5 nm gold nanoparticles: probing NSET validity. *J. Am. Chem. Soc.*, **128**:5462-5467

88. Häkkinen H (2012) The gold-sulfur interface at the nanoscale. *Nature Chem.,* **4**:443-455

89. DeLong RK, Reynolds CM, Malcolm Y, Schaeffer A, Severs T, Wanekaya A (2010) Functionalized gold nanoparticles for the binding, stabilization, and delivery of therapeutic DNA, RNA, and other biological macromolecules. *Nanotech. Sci. Appl.*, **3**:53-63

90. Chen H, Ming T, Zhao L, Wang F, Sun L, Wang J, Yan C (2010) Plasmon-molecule interactions. *Nano Today*, **5**:494-505

91. McDonagh C, Stranik O, Nooney R, MacCraith BD (2009) Nanoparticle strategies for enhancing the sensitivity of fluorescence-based biochips. *NanoMedicine*, **4**(6):645-656

92. Dulkeith E, Ringler M, Klar TA, Feldmann J, Javier AM, Parak WJ (2005) Gold nanoparticles quench fluorescence by phase induced radiative rate suppression. *Nano Lett.*, **5**:585-589

93. Gersten J and Nitzan A (1981) Spectroscopic properties of molecules interacting with small dielectric particles. *J. Chem. Phys.*, **75**:1139–1152

94. Chance RR, Prock A, Silbey R (1978) Molecular Fluorescence and Energy Transfer Near Interfaces. *Adv. Chem. Phys.*, **37**, 1–65

95. Kang KA, Wang J, Jasinski JB, Achilefu S (2011) Fluorescence manipulation by gold nanoparticles: from complete quenching to extensive enhancement. *J. Nanobiotech.*, **9**:16

96. Anger P, Bharadwaj P, Novotny L (2006) Enhancement and quenching of single-molecule fluorescence. *Phys. Rev. Lett*., **96**:113002

97. Bharadwaj P, Anger P, Novotny L (2007) Nanoplasmonic enhancement of single-molecule fluorescence. *Nanotechnology*, **18**(4):044017

98. Ipe BI, Thomas KG (2004) Investigations on nanoparticle-chromophore and interchromophore interactions in pyrene-capped gold nanoparticles. *J. Phys. Chem. B*, **108**:13265-13272

99. Barazzouk S, Kamat PV, Hotchandani S, Kamat PV (2002) Photoinduced charge separation in a fluorophore-gold nanoassembly. *J. Phys. Chem. B*, **106**:18-21

100. Pons T, Medintz IL, Sapsford KE, Higashiya S, Grimes AF, English DS, Mattoussi H (2007) On the quenching of semiconductor quantum dot photoluminescence by proximal gold nanoparticles. *Nano Lett.*, **7**:3157-3164

101. Fermi E. (1950). *Nuclear Physics*. University of Chicago Press.

102. Yun CS, Javier A, Jennings T, Fisher M, Hira S, Peterson S, Hopkins B, Reich NO, Strouse GF (2005) Nanometal surface energy transfer in optical rulers, breaking the FRET barrier. *J. Am. Chem. Phys.*, **127**:3115-3119

103. Sen T, Patra A (2008) Resonance energy transfer from rhodamine 6G to gold nanoparticles by steady-state and time-resolved spectroscopy. *J. Phys. Chem. C*, **112**:3216-3222

104. Dulkeith E, Morteani A, Niederreichholz T, Klar TA, Feldmann J, Levi SA, van Veggel FCJM, Reinhoudt DN, Möller M, Gittins DI (2002) Fluorescence quenching of dye molecules near gold nanoparticles: radiative and nonradiative effects. *Phys. Rev. Lett.*, **89**:203002

105. Vukovic S, Corni S, Mennucci B (2009) Relative rightness of a chromophore near gold nanoparticles. *J. Phys. Chem. C*, **113**:121-133

106. Persson BNJ, Lang ND (1982) Electron-hole-pair quenching of excited states near a metal. *Phys. Rev. B*, **26**, 5409–5415

107. Lakowicz JR (2005) Radiative decay engineering 5: metal-enhanced fluorescence and plasmon emission. *Anal. Biochem*., **337**(2):171–194

108. Singh MP, Strouse GF (2010) Involvement of the LSPR spectral overlap for energy transfer between a dye and Au nanoparticle. *J. Am. Chem. Soc*., **132**(27):9383-9331

109. Olejnik M, Bujak L, Mackowski S (2012) Plasmonic Molecular Nanohybrids—Spectral Dependence of Fluorescence Quenching. *Int. J. Mol. Sci.*, **13**:1018-1028

110. Tabor C, Haute D V, El-Sayed MA (2009) Effect of Orientation on Plasmonic Coupling between Gold Nanorods. *ACS Nano*, **3**(11):3670–3678

111. Kuhn S, Akanson SUH, Rogobete L, Sandoghdar V (2006) Enhancement of Single-Molecule Fluorescence Using a Gold Nanoparticle as an Optical Nanoantenna. *Phys. Rev. Lett.*, **97**:017402

112. Chhabra R, Sharma J, Wang H, Zou S, Lin S, Yan H, Lindsay S, Liu Y (2009) Distance-dependent interactions between gold nanoparticles and fluorescent molecules with DNA as tunable spacers. *Nanotechnology*, **20**:485201

113. Zou S, Schatz GC (2005) Silver nanoparticle array structures that produce giant enhancements in electromagnetic fields. *Chem. Phys. Lett.*, **403**:62-67

114. Zou S, Schatz GC (2006) Metal nanoparticle array waveguides: proposed structures for subwavelength devices. *Phys Rev. B*, **74**(12):125111

115. Zhang F, Ali Z, Amin F, Feltz A, Oheim M, Parak WJ (2010) Ion and pH sensing with colloidal nanoparticles: influence of surface charge on sensing and colloidal properties. *Chem. Phys. Chem*., **11**(3):730-735

116. Li H, Rothberg LJ (2004) Label-free colorimetric detection of specific sequences in genomic DNA amplified by the polymerase chain reaction. *J. Am. Chem. Soc.*, **126**:10958-10961

117. Lee H, Joo SW, Lee SY, Lee CH, Yoon KA, Lee K (2010) Colorimetric genotyping of single nucleotide polymorphism based on selective aggregation of unmodified gold nanoparticles. *Biosens. Bioelectron.*, **26**:730-735

118. Lee H, Kang T, Yoon KA, Lee SY, Joo SW, Lee K (2010) Colorimetric detection of mutations in epidermal growth factor receptor using gold nanoparticle aggregation. *Biosens. Bioelectron.*, **25**:1669-1674

119. Kim JH, Chung BH (2011) Naked eye detection of mutagenic DNA photodimers using gold nanoparticles. *Biosens. Bioelectron.*, **26**:2805-2809

120. Shawky SM, Bald D, Azzazy HM (2010) Direct detection of unamplified hepatitis C virus RNA using unmodified gold nanoparticles. *Clin. Biochem.*, **43**:1163-1168

121. Xia F, Zuo X, Yang R, Xiao Y, Kang D, Vallée-Bélisle A, Gong X, Yuen JD, Hsu BB, Heeger AJ, Plaxco KW (2010) Colorimetric detection of DNA, small molecules, proteins, and ions using unmodified gold nanoparticles and conjugated polyelectrolytes. *Proc. Natl. Acad. Sci. USA*, **107**:10837-10841

122. Mirkin CA, Letsinger RL, Mucic RC, Storhoff JJ (1996) A DNA-based method for rationally assembling nanoparticles into macroscopic materials. *Nature*, **382**:607-609

123. Storhoff JJ, Elghanian R, Mucic RC, Mirkin CA, Letsinger RL (1998) One-pot colorimetric differentiation of polynucleotides with single base imperfections using gold nanoparticle probes. *J. Am. Chem. Soc.*, **120**:1959-1964

124. Thaxton CS, Georganopoulou DG, Mirkin CA (2006) Gold nanoparticle probes for the detection of nucleic acid targets. *Clin. Chim. Acta*, **363**:120-126

125. Li JS, Deng T, Chu X, Yang RH, Jiang JH, Shen GL, Yu R (2010) Rolling circle amplification combined with gold nanoparticle aggregates for highly sensitive identification of single-nucleotide polymorphisms. *Anal. Chem.*, **82**:2811-2816

126. Sato K, Hosokawa K, Maeda M (2003) Rapid aggregation of gold nanoparticles induced by non-cross-linking DNA hybridization. *J. Am. Chem. Soc.*, **125**:8102-8103

127. Doria G, Franco R, Baptista P (2007) Nanodiagnostics: Fast colorimetric method for single nucleotide polymorphism/mutation detection. *IET Nanobiotechnol.*, **1**:53-57

128. Costa P, Amaro A, Botelho A, Inácio J, Baptista PV (2010) Gold nanoprobe assay for the identification of Mycobacteria of the *Mycobacterium tuberculosis* complex. *Clin. Microbiol. Infect.*, **16**:1464-1469

129. Conde J, de la Fuente JM, Baptista PV (2010) RNA quantification using gold nanoprobes – Application to cancer diagnostics. *J. Nanobiotechnol.*, **8**:5

130. Baptista PV, Koziol-Montewka M, Paluch-Oles J, Doria G, Franco R (2006) Gold-nanoparticle-probe-based assay for rapid and direct detection of *Mycobacterium tuberculosis* DNA in clinical samples. *Clin. Chem.*, **52**:1433-1434

131. Baptista P, Doria G, Henriques D, Pereira E, Franco R (2005) Colorimetric detection of eukaryotic gene expression with DNA-derivatized gold nanoparticles. *J. Biotechnol.*, **119**:111-117

132. Veigas B, Machado D, Perdigão J, Portugal I, Couto I, Viveiros M, Baptista PV (2010) Au-nanoprobes for detection of SNPs associated with antibiotic resistance in *Mycobacterium tuberculosis*. *Nanotechnology*, **21**(41):415101

133. Doria G, Larguinho M, Dias JT, Pereira E, Franco R, Baptista PV (2010) Gold-silver-alloy nanoprobes for one-pot multiplex DNA detection. *Nanotechnology*, **21**(25):255101

134. Fleischmann M, Hendra PJ, McQuillan AJ (1974) Raman spectra of pyridine adsorbed at a silver Electrode. *Chem. Phys. Lett.*, **26**:163-166

135. Bantz KC, Meyer AF, Wittenberg NJ, Im H, Kurtuluş O, Lee SH, Lindquist NC, Oh SH, Haynes CL (2011) Recent progress in SERS biosensing. *Phys. Chem. Chem. Phys.*, **13**:11551-11567

136. Vo-Dinh T, Wang HN, Scaffidi J (2010) Plasmonic nanoprobes for SERS biosensing and bioimaging. *J. Biophotonics.*, **3**:89-102

137. Hossain MK, Ozaki Y (2009) Surface-enhanced Raman scattering: facts and inline trends. *Current Science*, **97**(2):192-201

138. Jeanmaire DL, Van Duyne RP (1977) Surface Raman spectroelectrochemistry: Part I. Heterocyclic, aromatic, and aliphatic amines adsorbed on the anodized silver electrode. *J. Electroanal. Chem.*, **84**:1-20

139. Albrecht MG, Creighton JA (1977) Anomalously intense Raman spectra of pyridine at a silver electrod. *J. Am. Chem. Soc.*, **99**:5215-5217

140. Pettinger B (1986) Light scattering by adsorbates at Ag particles: quantum-mechanical approach for energy transfer induced interfacial optical processes involving surface plasmons, multipoles, and electron-hole pairs. *J. Chem. Phys.*, **85**:7442-7451

141. Michaels AM, Brus LE (1999) Surface-enhanced Raman spectroscopy of individual Rhodamine6G molecules on large Ag nanocrystals. *J. Am. Chem. Soc.*, **121**:9932-9939

142. Etchegoin P, Liem H, Maher RC, Cohen LF, Brown RJC, Hartigan H, Milton MJT, Gallop JC. A novel amplification mechanism for surface enhanced Raman scattering. *Chem. Phys. Lett.*, **366**(1-2):115-121

143. Otto A (2003) On the electronic contribution to single molecule surface enhanced Raman spectroscopy. *Indian J. Phys.*, **77B**:63-73

144. Vitol EA, Brailoiu E, Orynbayeva Z, Dun NJ, Friedman G, Gogotsi Y (2010) Surface-enhanced Raman spectroscopy as a tool for detecting Ca^{2+} mobilizing second messengers in cell extracts. *Anal. Chem.*, **82**:6770-6774

145. Guven B, Basaran-Ajgul N, Temur E, Tamer U and Boyaci IH (2011) SERS-based sandwich immunoassay using antibody coated magnetic nanoparticles for Escherichia coli enumeration. *Analyst*. **136(4)**:740-748

146. Ray PC, Darbha GK, Ray A, Walker J, Hardy W (2007) Gold Nanoparticle Based FRET for DNA Detection. *Plasmonics*, **2**:173-183

147. Tang B, Zhang N, Chen Z, Xu K, Zhuo L, An L, Yang G (2008) Probing hydroxyl radicals and their imaging in living cells by use of FAM-DNA-Au nanoparticles. *Chemistry*, **14**(2):522-528

148. Wu ZS, Jiang JH, Fu L, Shen GL, Yu RQ (2006) Optical detection of DNA hybridization based on fluorescence quenching of tagged oligonucleotide probes by gold nanoparticles. *Anal. Biochem.*, **353**:22-29

149. Phillips RL, Miranda OR, You CC, Rotello VM, Bunz UH (2008) Rapid and efficient identification of bacteria using gold-nanoparticle-poly(para-phenyleneethynylene) constructs. *Angew. Chem. Int. Ed. Engl.*, **47**:2590-2594

150. Mo ZH, Yang XC, Guo KP, Wen ZY (2007) A nanogold-quenched fluorescence duplex probe for homogeneous DNA detection based on strand displacement. *Anal. Bioanal. Chem.*, **389**:493-497

151. Doria G, Conde J, Veigas B, Giestas L, Almeida C, Assunção M, Rosa J, Baptista PV (2012) Noble metal nanoparticles for biosensing applications. *Sensors*, **12**:1657-1687

152. Dubertret B, Calame M, Libchaber AJ (2001) Single-mismatch detection using gold-quenched fluorescent oligonucleotides. *Nat. Biotechnol.*, **19**:365-370

153. Benia V, Hayesa K, Lerga MT, O'Sullivan CK (2010) Development of a gold nano-particle-based fluorescent molecular beacon for detection of cystic fibrosis associated mutation. *Biosen. Bioelectron.*, **26**:307-313

154. Lacerda SHD, Park JJ, Meuse C, Pristinski D, Becker ML, Karim A, Douglas JF (2010) Interaction of gold nanoparticles with common human blood proteins. *ACS Nano*, **4**(1):365-379

155. Mayilo S, Kloster MA, Wunderlich M, Lutich A, Klar TA, Nichtl A, Kurzinger K, Stefani FD, Feldmann J (2009) Long-range fluorescence quenching by gold nanoparticles in a sandwich immunoassay for cardiac troponin T. *Nano Lett.*, **9**(12):4558-4563

156. He X, Gao J, Gambhir SS, Cheng Z (2010) Near-infrared fluorescent nanoprobes for cancer molecular imaging: status and challenges. *Trends Mol. Med.*, **16**(12):574-83

157. Guirgis BS, Cunha CS, Gomes I, Cavadas M, Silva I, Doria G, Blatch GL, Baptista PV, Pereira E, Azzazy HM, Mota MM, Prudêncio M, Franco R (2011) Gold nanoparticle-based fluorescence immunoassay for malaria antigen detection. *Anal. Bioanal. Chem.*, **402**(3):1019-1027

158. Lee PC, Meisel D (1982) Adsorption and surface-enhanced Raman of dyes on silver and gold sols. J. Phys. Chem., **86**:3391-3395

159. Zou X, Ying E, Dong S (2006) Seed-mediated synthesis of branched gold nanoparticles with the assistance of citrate and their surface-enhanced Raman scattering properties. *Nanotechnology*, **17**:4758–4764

160. Ellman GL (1959) Tissue sulfhydryl groups. *Arch. Biochem. Biophys.*, **82**(1): 70–7

161. Melo JS, Fernandes PF (2001) Spectroscopy and Photophysics of 4- and 7-hydroxycoumarins and their Thione Analogs. *J. Mol. Struct.*, **565-566**:69-78

162. Striker G, Subramaniam V, Seidel CAM, Volkmer A (1999) Photochromicity and Fluorescence Lifetimes of Green Fluorescent Protein. *J. Phys. Chem. B*, **103**:8612-8617

163. Inoue H, Nojima H, Okayama H (1990) High efficiency transformation of Escherichia coli with plasmids. *Gene*, **96**:23-28

164. Luhtala N,Parker R(2009) LSM1 over-expression in *Saccharomyces cerevisae* depletes U6 snRNA levels. *Nucl. Acids Res.*, **37**(16):5529-5536

165. Schmittgen TD, Livak KJ (2008) Analyzing real-time PCR data by the comparative CT method. *Nat. Protocols*, **3**:1101-08

166. Dong J, Qu S, Zhang Z, Liu M, Liu G, Yan X, Zheng H (2012) Surface enhanced fluorescence on three dimensional silver nanostructure substrate. *J. Appl. Phys.*, **111**:093101

167. Fu Y, Zhang J, Lakowicz JR (2009) Silver-enhanced fluorescence emission of single quantum dot nanocomposites. *Chem. Comm.*, **21**(3):313-315

168. Aslan K, Lakowicz JR, Geddes CD (2005) Metal-enhanced fluorescence using anisotropic silver nanostructures: critical progress to date. *Anal. Bioanal. Chem.*, **382**:926-933

169. Wang J, Polsky R, Xu D (2001) Silver-enhanced colloidal gold electrochemical stripping detection of DNA hybridization. *Langmuir*, **17**:5739-5741

170. Bar-Ilan O, Albrecht RM, Fako VE, Furgeson DY (2009) Toxicity assessments of multisized gold and silver nanoparticles in zebrafish embryos. *Small*, **5**(16):1897-1910

171. Chen H, Kou X, Yang Z, Ni W, Wang J (2008) Shape- and Size-Dependent Refractive Index Sensitivity of Gold Nanoparticles. *Langmuir*, **24**:5233-5237

172. Sun YN, Wang CD, Zhang XM, Ren L, Tian XH (2011) Shape dependence of gold nanoparticles on *in vivo* acute toxicological effects and biodistribution. *J Nanosci Nanotechnol.*, **11**(2):1210-6

173. Laven P, MiePlot (v4.107), http://www.philiplaven.com/mieplot.htm

174. Gutiérrez-Wing C, Velázquez-Salazar JJ, José-Yacaman M (2012) Procedures for the synthesis and capping of metal nanoparticles. *Meth. Mol.Biol.*, **906**:3-19

175. Cannone F, Chirico G, Bizzari AR and Cannistraro S (2006) Quenching and blinking of fluorescence of a single dye molecule bound to gold nanoparticles. J. Phys. Chem. B, 110:16941-16498

176. Tanemura M (1986) On the stereology of the radial distribution function of hard-sphere systems. *Procedings of the First International Symposium for Science*, KTK Scientific Publishers: Tokyo, 157-165

177. Magde D, Rojas GE, Seybold PG (1999) Solvent dependence of the fluorescence lifetimes of xanthene dyes photochemistry and photobiology **70(**5):737-744

178. Karstens T, Kobs K (1980) Rhodamine B and rhodamine 101 as reference substances for fluorescence quantum yield measurements. *J. Phys. Chem.*, **84**:1871-1872

179. Li L, Liu S, Zhu T (2010) Application of activated carbon derived from scrap tires for adsorption of rhodamine B. *J. of Env. Sci.*, **22**(8):1273–1280

180. Stobiecka M, Hepel M (2011) Multimodal coupling of optical transitions and plasmonic oscillations in rhodamine B modified gold nanoparticles. *Phys. Chem. Chem. Phys.* **13**:1131-1139

181. Arbeloa FL, Aguirresacona IU, Arbeloa IL (1989) Influence of the molecular structure and the nature of the solvent on the absorption and fluorescence characteristics of rhodamines. *Chem. Phys.* **130**(1–3):371–378

182. deMello AJ, Elliott JA, Rumbles G (1997) Evanescent wave-induced fluorescence study of rhodamine 101 at dielectric interfaces. *J. Chem. SOC., Faraday Trans.* **93**(23):4723-4731

183. Jing TW, Jeffrey AM, DeRose JA, Lyubchenko YL, Shlyakhtenko LS, Harrington RE, Appella E, Larsen J, Vaught A, Rekesh D (1993) Structure of hydrated oligonucleotides studied by in situ scanning tunneling microscopy. *Proc. Natl. Acad. Sci.USA*, **90**(19):8934-8938

184. Han J, Burgess K (2010) Fluorescent indicators for intracellular pH. *Chem. Rev.*, **110**(5):2709-28

185. Conde J, de la Fuente JM, Baptista PV (2010) *In vitro* transcription and translation inhibition via DNA functionalized gold nanoparticles. *Nanotechnology*. **21**:1-6

186. Rosa J, Conde J, de la Fuente JM, Lima JC, Baptista PV (2012) Gold-nanobeacons for real-time monitoring of RNA synthesis. *Biosens. Bioelectron.*, **36**(1):161-167

187. Crick F (1956) Ideas on protein synthesis. *Symp. Soc. Exp. Biol. XII*, 139-163

188. Crick F (1970) Central dogma of molecular biology. *Nature*, **227**:561-563

189. Lewin (2004) Genes VIII. 1st ed. *Pearson Prentice Hall*, Upper Saddle River, USA

190. Dang CV (1999) c-Myc Target Genes Involved in Cell Growth, Apoptosis, and Metabolism. *Mol. Cell. Biol.*, **19**(1):1-11

191. Bishop JM (1982) Retroviruses and cancer genes. *Adv. Cancer Res.*, **37**:1–32

192. Bister K, Jansen HW (1986) Oncogenes in retroviruses and cells: biochemistry and molecular genetics. *Adv. Cancer Res.*, **47**:99–188

193. Sheiness D, Fanshier L, Bishop JM (1978) Identification of nucleotide sequences which may encode the oncogenic capacity of avian retrovirus MC29. *J. Virol.*, **28**:600–610

194. Cole MD (1986) The myc oncogene: its role in transformation and differentiation. *Annu. Rev. Genet.*, **20**:361–384

195. Dalla-Favera R, Gelmann EP, Martinotti S, Franchini G, Papas TS, Gallo RC, Wong-Staal F (1982) Cloning and characterization of different human sequences related to the onc gene (v-myc) of avian myelocytomatosis virus (MC29). *Proc. Natl. Acad. Sci. USA*, **79**:6497–6501

196. Davis AC, Wims M, Spotts GD, Hann SR, Bradley A (1993) A null c-myc mutation causes lethality before 10.5 days of gestation in homozygotes and reduced fertility in heterozygous female mice. *Genes Dev.*, **7**:671–682

197. Mateyak MK, Obaya AJ, Adachi S, Sedivy JM (1997) Phenotypes of c-Myc-deficient rat fibroblasts isolated by targeted homologous recombination. *Cell Growth Differ.* **8**:1039–1048

198. Daksis JI, Lu RY, Facchini LM, Marhin WW, Penn LJ (1994) Myc induces cyclin D1 expression in the absence of de novo protein synthesis and links mitogen-stimulated signal transduction to the cell cycle. *Oncogene*, **9**:3635–3645

199. Hanson KD, Shichiri M, Follansbee MR, Sedivy JM (1994) Effects of c-myc expression on cell cycle progression. *Mol. Cell. Biol.*, **14**:5748–5755

200. Hoang AT, Cohen KJ, Barrett JF, Bergstrom DA, Dang CV (1994) Participation of cyclin A in Myc-induced apoptosis. *Proc. Natl. Acad. Sci. USA*, **91**:6875–6879

201. Jansen-Durr P, Meichle A, Steiner P, Pagano M, Finke D, Botz J, Wessbecher J, Draetta G, Eilers M (1993) Differential modulation of cyclin gene expression by MYC. *Proc. Natl. Acad. Sci. USA*, **90**:3685–3689

202. Leone G, DeGregori J, Sears R, Jakoi L, Nevins JR (1997) Myc and Ras collaborate in inducing accumulation of active cyclin E/Cdk2 and E2F. *Nature*, **387**:422–426

203. Perez-Roger I, Solomon DLC, Sewing A, Land H (1997) Myc activation of cyclin E/Cdk2 kinase involves induction of cyclin E gene transcription and inhibition of p27Kip1 binding to newly formed complexes. *Oncogene*, **14**:2373–2381

204. Galaktionov K, Chen X, Beach D (1996) Cdc25 cell-cycle phosphatase as a target of c-myc. *Nature*, **382**:511–517

205. Amati B, Alevizopoulos K, Vlach J (1998) Myc and the cell cycle. *Front. Biosci.*, **3**:D250–D268

206. Rudolph B, Saffrich R, Zwicker J, Henglein B, Muller R, Ansorge W, Eilers M (1996) Activation of cyclin-dependent kinases by Myc mediates induction of cyclin A, but not apoptosis. *EMBO J.*, **15**:3065–3076

207. Vlach J, Hennecke S, Alevizopoulos K, Conti D, Amati B (1996) Growth arrest by the cyclin-dependent kinase inhibitor p27Kip1 is abrogated by c-Myc. *EMBO J.*, **15**:6595–6604

208. Agrawal S (1996) Antisense oligonucleotides: towards clinical trials. *Trends Biotechnol.*, **14**(10):376–387

209. Fichou Y, Ferec C (2006) The potential of oligonucleotides for therapeutic applications. *Trends Biotechnol.*, **24**:563-570

210. Tamm I, Dorken B, Hartmann G (2001) Antisense therapy in oncology: New hope for an old idea? *Lancet*, **358**:489-497

211. Bor YC, Swartz J, Li Y, Coyle J, Rekosh D, Hammarskjold M (2006) Northern Blot analysis of mRNA from mammalian polyribosomes. *Nature Protocols*, (protocol exchange)

212. Freeman WM, Walker SJ, Vrana KE (1999) Quantitative RT-PCR: pitfalls and potential. *Biotechniques*, **26**:112-115

213. Weis JH, Tan SS, Martin BK, Wittwer CT (1992) Detection of rare mRNAs via quantitative RT-PCR. *Trends Genet.*, **8**:263-264

214 - E62 - Schena M, Shalon D, Davis RW, Brown PO (1995) Quantitative monitoring of gene expression patterns with a complementary DNA microarray. *Science*, **270**:467-470

215. Tan W, Wang K, Drake TJ (2004) Molecular beacons. *Curr. Opin. Chem. Biol.*, **8**:547-553

216. Tyagi S, Kramer FR (1996) Molecular beacons: probes that fluoresce upon hybridization. *Nat Biotechnol*., **14**:303-308

217. Li JJ, Fang X, Schuster SM, Tan W (2000) Molecular Beacons: A Novel Approach to Detect Protein - DNA Interactions This work was partially supported by a U.S. NSF Career Award (CHE-9733650) and by a U.S. Office of Naval Research Young Investigator Award (N00014-98-1-0621). *Angew. Chem. Int. Ed.*, **39**:1049-1052

218. Li JJ, Geyer R, Tan W (2000) Using molecular beacons as a sensitive fluorescence assay for enzymatic cleavage of single-stranded DNA. *Nucleic Acids Res.*, **28**:e52

219. Liu J, Feldman P, Chung TC (2002) Real-time monitoring *in vitro* transcription using molecular beacons. *Anal. Biochem.*, **300**:40-45

220. Marras SAE, Gold B, Kramer FR, Smith I, Tyagi S (2004) Real-time measurement of *in vitro* transcription. *Nucleic Acids Res.*, **32**:e72

221. Waltz TL, Marras SAE, Rochford G, Nolan J, Lee E, Melegari M, Pollack H (2005) Development of a molecular-beacon assay to detect the G1896A precore mutation in hepatitis B virus-infected individuals. *J. Clin. Micro.*, **43**:254-258

222. Paciotti GF, Myer L, Weinreich D, Goia D, Pavel N, McLaughlin RE, Tamarkin L (2004) Colloidal Gold: A Novel Nanoparticle Vector for Tumor Directed Drug Delivery. *Drug. Deliv.*, **11**(3):169-183

223. Song S, Liang Z, Zhang J, Wang L, Li G, Fan C (2009) Gold-Nanoparticle-Based Multicolor Nanobeacons for Sequence-Specific DNA Analysis. *Angew. Chem. Int. Ed.*, **48**:8670 –8674

224. Zadeh JN, Steenberg, CD, Bois JS, Wolfe BR, Pierce MB, Khan AR, Dirks RM, Pierce NA (2011) NUPACK: analysis and design of nucleic acid systems. *J. Comput. Chem.*, **32**:170–173

225. Cheng Y, Stakenborg T, Van Dorpe P, Lagae L, Wang M, Chen H, Borghs G (2011) Fluorescence near gold nanoparticles for DNA sensing. *Anal Chem.*, **83**:1307-1314

226. Conde J, Rosa J, de la Fuente JM, Baptista PV (2013) Gold-nanobeacons for simultaneous gene specific silencing and intracellular tracking of the silencing events. *Biomaterials*, **34**(10):2516-23

227. Conde J, Ambrosone A, Sanz V, Hernandez Y, Marchesano V, Tian F, Child H, Berry CC, Ibarra MR, Baptista PV, Tortiglione C, de la Fuente JM (2012) Design of Multifunctional Gold Nanoparticles for *In vitro* and *In vivo* Gene Silencing. *ACS Nano*, **6**:8316–8324

228. Sanz V, Conde J, Hernandez Y, Baptista PV, Ibarra MR, de la Fuente JM (2012) Effect of PEG biofunctional spacers and TAT peptide on dsRNA loading on gold nanoparticles. *J. Nanopart. Res.*, **14**:1-9

229. Kumarswamy R, Volkmann I, Thum T (2011) Regulation and function of miRNA-21 in health and disease. *RNA Biology*, **8**(5):706-713

230. Giljohann DA, Seferos DS, Prigodich AE, Patel PC, Mirkin CA (2009) Gene regulation with polyvalent siRNA-nanoparticle conjugates. *J. Am. Chem. Soc.*, **131**:2072-2073

231. Rosi NL, Giljohann DA, Thaxton CS, Lytton-Jean AK, Han MS, Mirkin CA (2006) Oligonucleotide-modified gold nanoparticles for intracellular gene regulation. *Science*, **312**:1027-1030

232. Ambros V, Lee RC, Lavanway A, Williams PT, Jewell D (2003) MicroRNAs and other tiny endogenous RNAs in *C. elegans*. *Curr. Biol.*, **13**:807-18

233. Jazbutyte V, Thum T (2010) MicroRNA-21: from cancer to cardiovascular disease. *Curr. Drug Targets*, **11**:926-935

234. Haverty PM, Fridlyand J, Li L, Getz G, Beroukhim R, Lohr S, Wu TD, Cavet G, Zhang Z, Chant J (2008) High-resolution genomic and expression analyses of copy number alterations in breast tumors. *Genes Chromossomes Cancer*, **47**(6):530-542

235. Ribas J, Lupold SE (2010) The transcriptional regulation of miR-21, its multiple transcripts, and their implication in prostate cancer. *Cell Cycle*, **9**:923-9

236. Selcuklu SD, Donoghue MT, Spillane C (2009) miR-21 as a key regulator of oncogenic processes. *Biochem. Soc. Trans.*, **37**:918-25

237. Yan LX, Huang XF, Shao Q, Huang MY, Deng L, Wu QL, Zeng YX, Shao JY (2008) MicroRNA miR-21 overexpression in human breast cancer is associated with advanced clinical stage, lymph node metastasis and patient poor prognosis. *RNA*, **14**:2348-236

238. Hohenstein P, Hastie ND (2006) The many facets of the Wilms' tumour gene, WT1. *Hum. Mol. Genet.*, **15**(special no 2):R196-201

239. Hammes A, Guo JK, Lutsch G, Leheste JR, Landrock D, Ziegler U, Gubler MC, Schedl A (2001) Two splice variants of the Wilms' tumor 1 gene have distinct functions during sex determination and néfron formation. *Cell*, **106**(3):319-329

240. Hastie ND (2001) Life, sex, and WT1 isoforms – three amino acids can make all the difference. *Cell*, **106**:391-394

241. Roberts SG (2005) Transcriptional regulation by WT1 in development. *Curr. Opin. Genet. Dev.*, **15**:542-547

242. Davies RC, Calvio C, Bratt E, Larsson SH, Lamond AI, Hastie ND (1998) WT1 interacts with the splicing factor U2AGF65 in an isoform-dependent manner and can be incorporated into spliceosomes. *Genes Dev.*, **12**(20):3217-3225

243. Ladomery MR, Slight J, McGhee S, Hastie ND (1999) Presence of WT1, the Wims' tumor suppressor gene product, in a muclear poly(A)(+) ribonucleoprotein. *J. Biol. Chem.*, **274**(51):36520-36526

244. Larsson SH, Charlieu JP, Miyagawa K, Engelkamp D, Rassoulzadegan M, Ross A, Cuzin F, van Heyningen V, Hastie ND (1995) Subnuclear localization of WT1 in splicing or transcription factor domains is regulated by alternative splicing. *Cell*, **81**:391-401

245. Morrison AA, Viney RL, Saleem MA, Ladomery MR (2008) New insights into the function of the Wilms tumor suppressor gene WT1 in podocytes. *AJP - Renal Physiol.*, **295**(1):F12-F17

246. Moorthy AV, Chesney RW, Lubinsky M (1987) Chronic renal failure and XY gonadal dysgenesis: “Frasier” syndrome—a commentary on reported cases. *Am. J. Med. Genet. Suppl.*, **3**:297–302

247. Miller-Hodges E, Hohenstein P (2012) WT1 in disease: shifting the epithelial–mesenchymal balance. *J. Pathol.*, **226**:229–240

248. Call KM, Glaser T, Ito CY, Buckler AJ, Pelletier J, Haber DA, Rose EA, Kral A, Yege H, Lewis WH (1990) Isolation and characterization of a zinc finger polypeptide gene at the human chromosome 11 Wilms' tumor locus. *Cell*, **60**:509–520

249. Gessler M, Poustka A, Cavenee W, Neve RL, Orkin SH, Bruns GA (1990) Homozygous deletion in Wilms tumours of a zinc-finger gene identified by chromosome jumping. *Nature*, **343**(6260):774-778

250. Haber DA, Buckler AJ, Glaser T, Call KM, Pelletier J, Sohn RL, Douglass EC, Housman DE (1990) An internal deletion within an 11p13 zinc finger gene contributes to the development of Wilms’ tumor. *Cell*, **61**(7):1257-1269

251. Pritchard-Jones K, Fleming S, Davidson D, Bickmore W, Porteous D, Gosden C, Bard J, Buckler A, Pelletier J, Housman D, Van Heyningen V, Hastie N (1990) The candidate Wilms’ tumour gene is involved in genitourinary development. *Nature*, **346**(6280):194-197

252. Armstrong JF, Pritchard-Jones K, Bickmore WA, Hastie ND, Bard JB (1993) The expression of the Wilms’ tumour gene, WT1, in the developing mammalian embryo. *Mech. Dev.*, **40**(1-2):85-97

APPENDICES

APPENDIX I

WT1–KTS mRNA (isoform A)

>gi|309951094|ref|NM_000378.4| Homo sapiens Wilms tumor 1 (WT1), transcript variant A, mRNA

AGCUGGGGUAAGGAGUUCAAGGCAGCGCCCACACCCGGGGGCUCUCCGCAACCCGACC
GCCUGUCCGCUCCCCCACUUCCCGCCCUCCCUCCCACCUACUCAUUCACCCACCCACCC
ACCCAGAGCCGGGACGGCAGCCCAGGCGCCCGGGCCCCGCCGUCUCCUCGCCGCGAUCC
UGGACUUCCUCUUGCUGCAGGACCCGGCUUCCACGUGUGUCCCGGAGCCGGCGUCUCA
GCACACGCUCCGCUCCGGGCCUGGGUGCCUACAGCAGCCAGAGCAGCAGGGAGUCCGG
GACCCGGGCGGCAUCUGGGCCAAGUUAGGCGCCGCCGAGGCCAGCGCUGAACGUCUCC
AGGGCCGGAGGAGCCGCGGGGCGUCCGGGUCUGAGCCGCAGCAAAUGGGCUCCGACGU
GCGGGACCUGAACGCGCUGCUGCCCGCCGUCCCCUCCCUGGGUGGCGGCGGCGGCUGU
GCCCUGCCUGUGAGCGGCGCGGCGCAGUGGGCGCCGGUGCUGGACUUUGCGCCCCCGG
GCGCUUCGGCUUACGGGUCGUUGGGCGGCCCCGCGCCGCCACCGGCUCCGCCGCCACCC
CCGCCGCCGCCGCCUCACUCCUUCAUCAAACAGGAGCCGAGCUGGGGCGGCGCGGAGC
CGCACGAGGAGCAGUGCCUGAGCGCCUUCACUGUCCACUUUUCCGGCCAGUUCACUGG
CACAGCCGGAGCCUGUCGCUACGGGCCCUUCGGUCCUCCUCCGCCCAGCCAGGCGUCAU
CCGGCCAGGCCAGGAUGUUUCCUAACGCGCCCUACCUGCCCAGCUGCCUCGAGAGCCA
GCCCGCUAUUCGCAAUCAGGGUUACAGCACGGUCACCUUCGACGGGACGCCCAGCUAC
GGUCACACGCCCUCGCACCAUGCGGCGCAGUUCCCCAACCACUCAUUCAAGCAUGAGG
AUCCCAUGGGCCAGCAGGGCUCGCUGGGUGAGCAGCAGUACUCGGUGCCGCCCCCGGU
CUAUGGCUGCCACACCCCCACCGACAGCUGCACCGGCAGCCAGGCUUUGCUGCUGAGG
ACGCCCUACAGCAGUGACAAUUUAUACCAAAUGACAUCCCAGCUUGAAUGCAUGACCU
GGAAUCAGAUGAACUUAGGAGCCACCUUAAAGGGCCACAGCACAGGGUACGAGAGCGA
UAACCACACAACGCCCAUCCUCUGCGGAGCCCAAUACAGAAUACACACGCACGGUGUC
UUCAGAGGCAUUCAGGAUGUGCGACGUGUGCCUGGAGUAGCCCCGACUCUUGUACGGU
CGGCAUCUGAGACCAGUGAGAAACGCCCCUUCAUGUGUGCUUACCCAGGCUGCAAUAA
GAGAUAUUUUAAGCUGUCCCACUUACAGAUGCACAGCAGGAAGCACACUGGUGAGAAA
CCAUACCAGUGUGACUUCAAGGACUGUGAACGAAGGUUUUCUCGUUCAGACCAGCUCA
AAAGACACCAAAGGAGACAUACAGGUGUGAAACCAUUCCAGUGUAAAACUUGUCAGCG
AAAGUUCUCCCGGUCCGACCACCUGAAGACCCACACCAGGACUCAUACAGGUGAAAAG
CCCUUCAGCUGUCGGUGGCCAAGUUGUCAGAAAAAGUUUGCCCGGUCAGAUGAAUUAG
UCCGCCAUCACAACAUGCAUCAGAGAAACAUGACCAAACUCCAGCUGGCGCUUUGAGG
GGUCUCCCUCGGGGACCGUUCAGUGUCCCAGGCAGCACAGUGUGUGAACUGCUUUCAA

GUCUGACUCUCCACUCCUCCUCACUAAAAAGGAAACUUCAGUUGAUCUUCUUCAUCCA
ACUUCCAAGACAAGAUACCGGUGCUUCUGGAAACUACCAGGUGUGCCUGGAAGAGUUG
GUCUCUGCCCUGCCUACUUUUAGUUGACUCACAGGCCCUGGAGAAGCAGCUAACAAUG
UCUGGUUAGUUAAAAGCCCAUUGCCAUUUGGUGUGGAUUUUCUACUGUAAGAAGAGC
CAUAGCUGAUCAUGUCCCCCUGACCCUUCCCUUCUUUUUUUAUGCUCGUUUUCGCUGG
GGAUGGAAUUAUUGUACCAUUUUCUAUCAUGGAAUAUUUAUAGGCCAGGGCAUGUGU
AUGUGUCUGCUAAUGUAAACUUUGUCAUGGUUUCCAUUUACUAACAGCAACAGCAAG
AAAUAAAUCAGAGAGCAAGGCAUCGGGGGUGAAUCUUGUCUAACAUUCCCGAGGUCA
GCCAGGCUGCUAACCUGGAAAGCAGGAUGUAGUUCUGCCAGGCAACUUUUAAAGCUCA
UGCAUUUCAAGCAGCUGAAGAAAAAAUCAGAACUAACCAGUACCUCUGUAUAGAAAUC
UAAAAGAAUUUUACCAUUCAGUUAAUUCAAUGUGAACACUGGCACACUGCUCUUAAG
AAACUAUGAAGAUCUGAGAUUUUUUUGUGUAUGUUUUUGACUCUUUUGAGUGGUAAU
CAUAUGUGUCUUUAUAGAUGUACAUACCUCCUUGCACAAAUGGAGGGGAAUUCAUUU
UCAUCACUGGGAGUGUCCUUAGUGUAUAAAAACCAUGCUGGUAUAUGGCUUCAAGUU
GUAAAAAUGAAAGUGACUUUAAAAGAAAAUAGGGGAUGGUCCAGGAUCUCCACUGAU
AAGACUGUUUUUAAGUAACUUAAGGACCUUUGGGUCUACAAGUAUAUGUGAAAAAAA
UGAGACUUACUGGGUGAGGAAAUCCAUUGUUUAAAGAUGGUCGUGUGUGUGUGUGUG
UGUGUGUGUGUGUGUGUGUUGUGUUGUGUUUUGUUUUUUAAGGGAGGGAAUUUAUUA
UUUACCGUUGCUUGAAAUUACUGUGUAAAUAUAUGUCUGAUAAUGAUUUGCUCUUUG
ACAACUAAAAUUAGGACUGUAUAAGUACUAGAUGCAUCACUGGGUGUUGAUCUUACA
AGAUAUUGAUGAUAACACUUAAAAUUGUAACCUGCAUUUUUCACUUUGCUCUCAAUU
AAAGUCUAUUCAAAAGGAAAAAAAAAAAA

WT1+KTS mRNA (isoform F)

>gi|309951098|ref|NM_001198552.1| Homo sapiens Wilms Tumor 1 (WT1), Transcript variant F, mRNA

AGGCGCUUUCACCACUGCCCCUCCCGGGGGGACCUGAAGGAGAGGGUUUGAGGCCGGU
CUUUGCCCGCCGAGGUCUGCGUGUCCGGUCUGGGAGGAGGCCUAGGAGGGCUCGCGGG
CCACGGGCAUCCUUGGGCCCGAGUUCUGGGGUGCGGACGGACGUCUCGAGAGUGGGUG
CCGCGACUCGGGACCCACGGCCCUCGCCGGGCACGGACAGUUGCGGAGCAGGGCUCUG
AGGAUUGUGCAGUGCCCUGGGUCCCUGCCUACUCCUGGGCUCAGGAAUGGAGAAGGGU
UACAGCACGGUCACCUUCGACGGGACGCCCAGCUACGGUCACACGCCCUCGCACCAUG
CGGCGCAGUUCCCCAACCACUCAUUCAAGCAUGAGGAUCCCAUGGGCCAGCAGGGCUC
GCUGGGUGAGCAGCAGUACUCGGUGCCGCCCCCGGUCUAUGGCUGCCACACCCCCACC
GACAGCUGCACCGGCAGCCAGGCUUUGCUGCUGAGGACGCCCUACAGCAGUGACAAUU

UAUACCAAAUGACAUCCCAGCUUGAAUGCAUGACCUGGAAUCAGAUGAACUUAGGAGC
CACCUUAAAGGGCCACAGCACAGGGUACGAGAGCGAUAACCACACAACGCCCAUCCUC
UGCGGAGCCCAAUACAGAAUACACACGCACGGUGUCUUCAGAGGCAUUCAGGAUGUGC
GACGUGUGCCUGGAGUAGCCCCGACUCUUGUACGGUCGGCAUCUGAGACCAGUGAGAA
ACGCCCCUUCAUGUGUGCUUACCCAGGCUGCAAUAAGAGAUAUUUUAAGCUGUCCCAC
UUACAGAUGCACAGCAGGAAGCACACUGGUGAGAAACCAUACCAGUGUGACUUCAAGG
ACUGUGAACGAAGGUUUUCUCGUUCAGACCAGCUCAAAAGACACCAAAGGAGACAUAC
AGGUGUGAAACCAUUCCAGUGUAAAACUUGUCAGCGAAAGUUCUCCCGGUCCGACCAC
CUGAAGACCCACACCAGGACUCAUACAGGUAAAACAAGUGAAAAGCCCUUCAGCUGUC
GGUGGCCAAGUUGUCAGAAAAAGUUUGCCCGGUCAGAUGAAUUAGUCCGCCAUCACAA
CAUGCAUCAGAGAAACAUGACCAAACUCCAGCUGGCGCUUUGAGGGGUCUCCCUCGGG
GACCGUUCAGUGUCCCAGGCAGCACAGUGUGUGAACUGCUUUCAAGUCUGACUCUCCA
CUCCUCCUCACUAAAAAGGAAACUUCAGUUGAUCUUCUUCAUCCAACUUCCAAGACAA
GAUACCGGUGCUUCUGGAAACUACCAGGUGUGCCUGGAAGAGUUGGUCUCUGCCCUGC
CUACUUUUAGUUGACUCACAGGCCCUGGAGAAGCAGCUAACAAUGUCUGGUUAGUUAA
AAGCCCAUUGCCAUUUGGUGUGGAUUUUCUACUGUAAGAAGAGCCAUAGCUGAUCAU
GUCCCCCUGACCCUUCCCUUCUUUUUUUAUGCUCGUUUUCGCUGGGGAUGGAAUUAUU
GUACCAUUUUCUAUCAUGGAAUAUUUAUAGGCCAGGGCAUGUGUAUGUGUCUGCUAA
UGUAAACUUUGUCAUGGUUUCCAUUUACUAACAGCAACAGCAAGAAAUAAAUCAGAG
AGCAAGGCAUCGGGGGUGAAUCUUGUCUAACAUUCCCGAGGUCAGCCAGGCUGCUAAC
CUGGAAAGCAGGAUGUAGUUCUGCCAGGCAACUUUUAAAGCUCAUGCAUUUCAAGCAG
CUGAAGAAAAAAUCAGAACUAACCAGUACCUCUGUAUAGAAAUCUAAAAGAAUUUUA
CCAUUCAGUUAAUUCAAUGUGAACACUGGCACACUGCUCUUAAGAAACUAUGAAGAUC
UGAGAUUUUUUUGUGUAUGUUUUUGACUCUUUUGAGUGGUAAUCAUAUGUGUCUUUA
UAGAUGUACAUACCUCCUUGCACAAAUGGAGGGGAAUUCAUUUUCAUCACUGGGAGU
GUCCUUAGUGUAUAAAAACCAUGCUGGUAUAUGGCUUCAAGUUGUAAAAAUGAAAGU
GACUUUAAAAGAAAAUAGGGGAUGGUCCAGGAUCUCCACUGAUAAGACUGUUUUUAA
GUAACUUAAGGACCUUUGGGUCUACAAGUAUAUGUGAAAAAAAUGAGACUUACUGGG
UGAGGAAAUCCAUUGUUUAAAGAUGGUCGUGUGUGUGUGUGUGUGUGUGUGUGUG
UGUGUUGUGUUGUGUUUUGUUUUUUAAGGGAGGGAAUUUAUUAUUUACCGUUGCUUG
AAAUUACUGUGUAAAUAUAUGUCUGAUAAUGAUUUGCUCUUUGACAACUAAAAUUAG
GACUGUAUAAGUACUAGAUGCAUCACUGGGUGUUGAUCUUACAAGAUAUUGAUGAUA
ACACUUAAAAUUGUAACCUGCAUUUUUCACUUUGCUCUCAAUUAAAGUCUAUUCAAAA
GGAAAAAAAAAAAAA

APPENDIX II

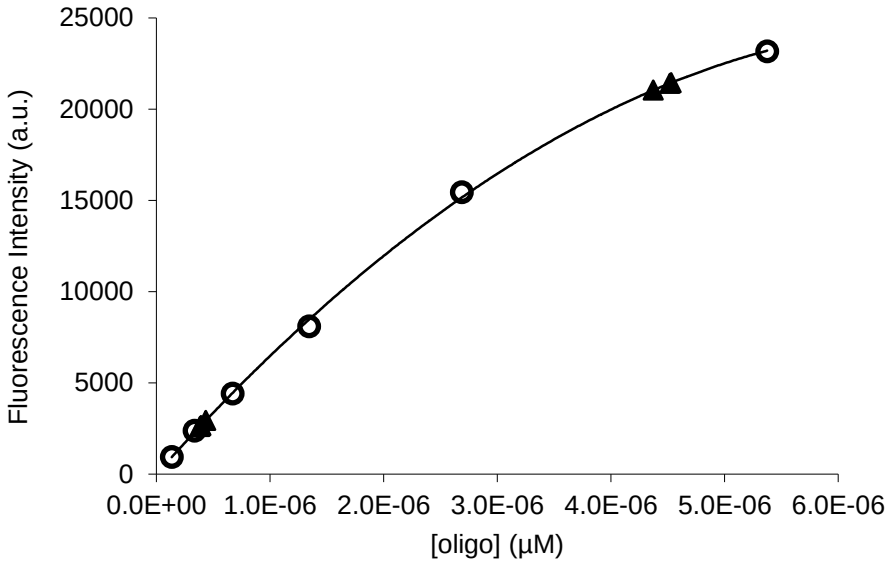

Figure A1. Quantification of SAMSA@AuNPs by differential analysis. Calibration curve of SAMSA in phosphate buffer 10mM (pH8), 0.05% SDS (circles, y = -4.921E+14x^2 + 6.961E+09x, R^2=0.9994) and fluorescence intensities (λ_{exc}= 490 nm) measured in the supernatants of SAMSA@AuNP (triangles).

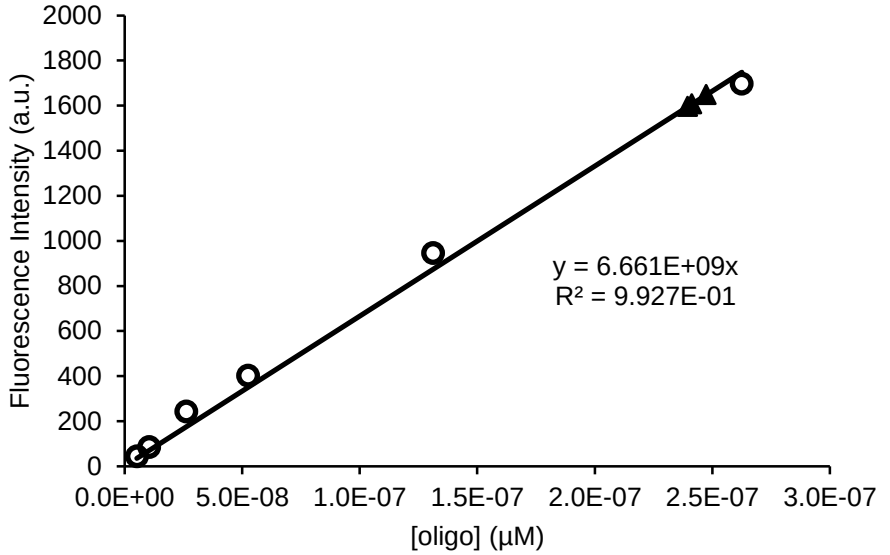

Figure A2. Quantification of SAMSA@AuNPs by DTT reduction. Calibration curve of SAMSA in phosphate buffer 10mM (pH 8), DTT 0.1M (circles y = 6.661E+09x, R^2=0.9927) and fluorescence intensities (λ_{exc}= 490 nm) measured in the supernatants of SAMSA@AuNP (triangles).

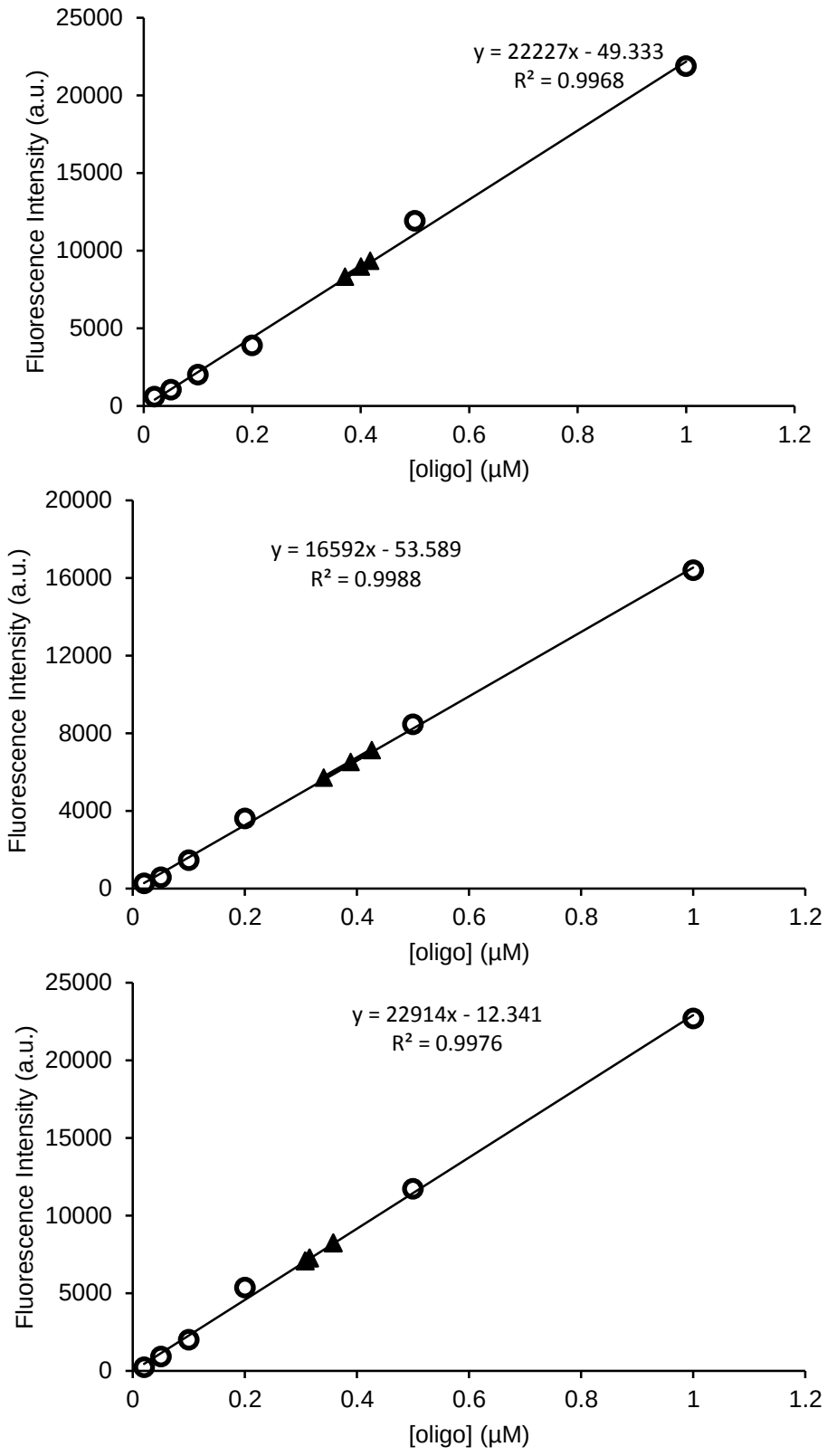

Figure A3. Oligonucleotides density – SNSET10, 15 and 20. Calibration curve of FAM-labeled oligonucleotides SNET10, 15 and 20 (from top to bottom) (circles: y=22227x-49.333, R^2=0.9968; y=16592x-53.589, R^2=0.9988; y=22914x-12.341, R^2 = 0.9976) and fluorescence intensities measured (λ_{exc}= 490 nm) in the supernatants of the Au-nanoprobes (triangles).

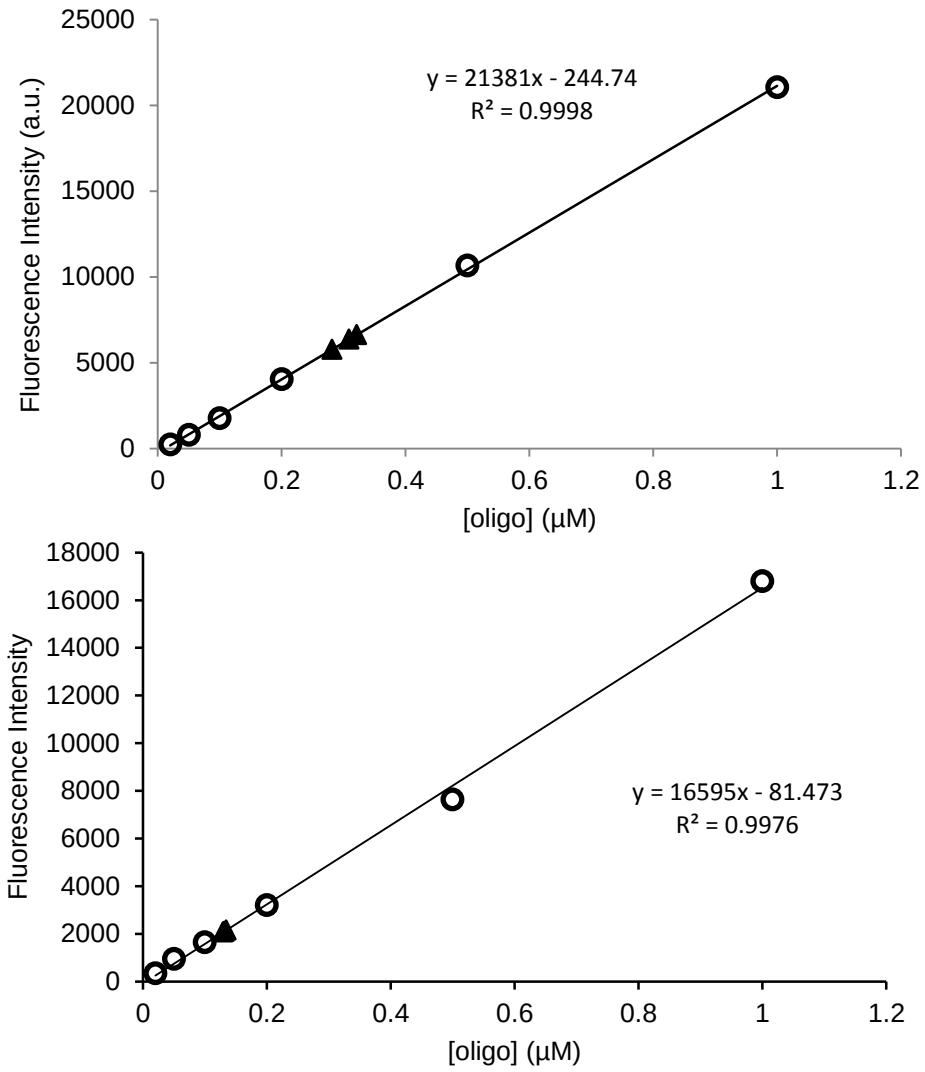

Figure A4. Oligonucleotides density – SNSET25 and 50. Calibration curve of FAM-labeled oligonucleotides SNET25 and 50 (from top to bottom) (circles: y=21381x-244.74, R^2=0.9998; y=16595x-81.473, R^2=0.9976) and fluorescence intensities (λ_{exc}= 490 nm) measured in the supernatants of the Au-nanoprobes (triangles).

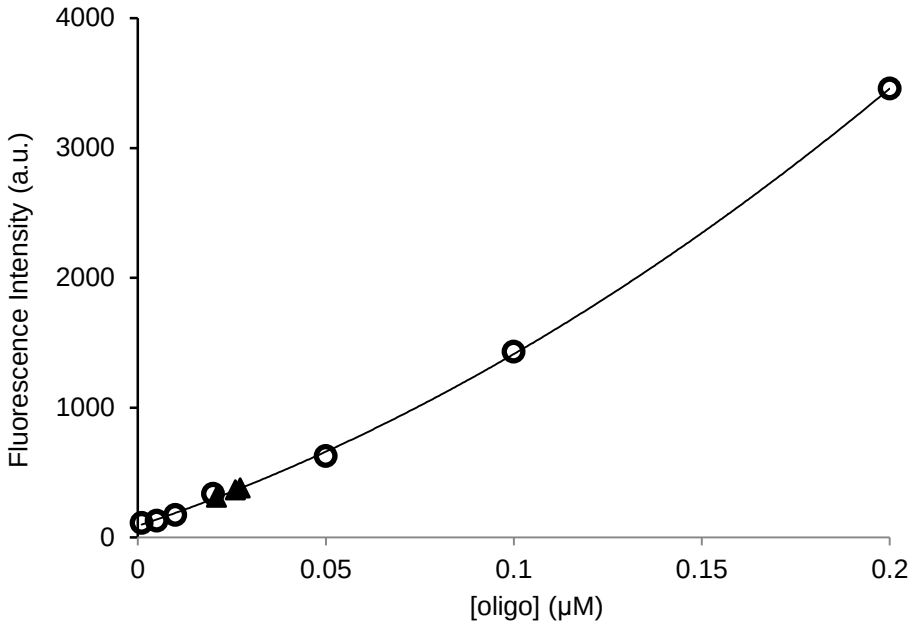

Figure A5. Oligonucleotides density - *inhibitor* Au-nanobeacon. Calibration curve of FAM-labeled oligonucleotide (circles, $y=36090.0x^2+9625.8x+89.7$, $R^2=0.9996$) and fluorescence intensities measured (λ_{exc}= 490 nm) in the supernatants of Au-nanobeacon (circles). A ratio of 4.96±0.66 oligonucleotides per gold nanoparticle was calculated.

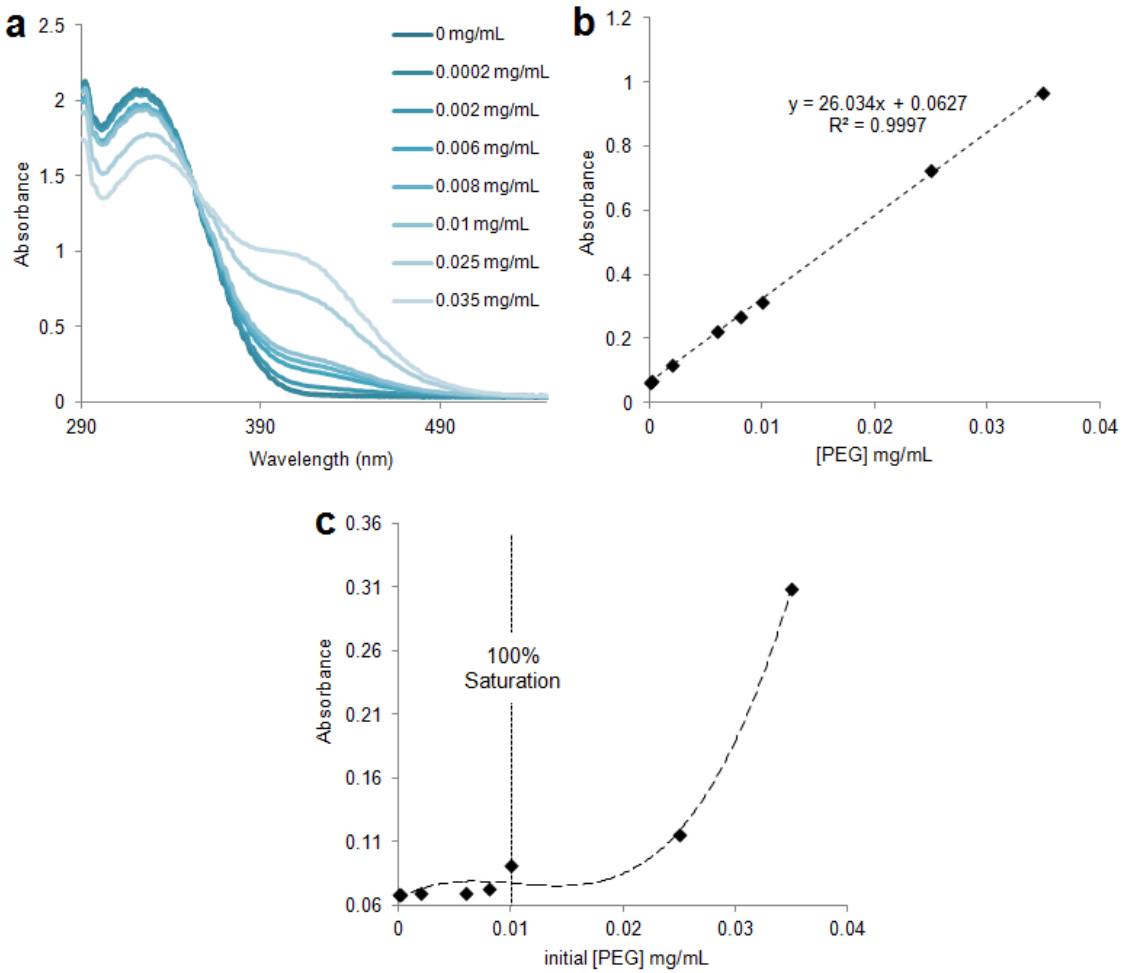

Figure A6. PEG coverage of AuNP surface. (a) Absorbance spectra of DTNB after reaction with the thiolated PEG. (b) Standard calibration curve for PEG chains, whose concentration can be calculated via the following equation Abs412nm = 26.034x [PEG, mg/mL] + 0.0627. (c) Variation of the excess of PEG thiolated chains as a function of the initial concentration in the incubation with 10 mM AuNPs. The dashed vertical line indicates the 100% saturation, *i.e.*, the PEG concentration above which no more PEG can be bonded to the AuNPs' surface.

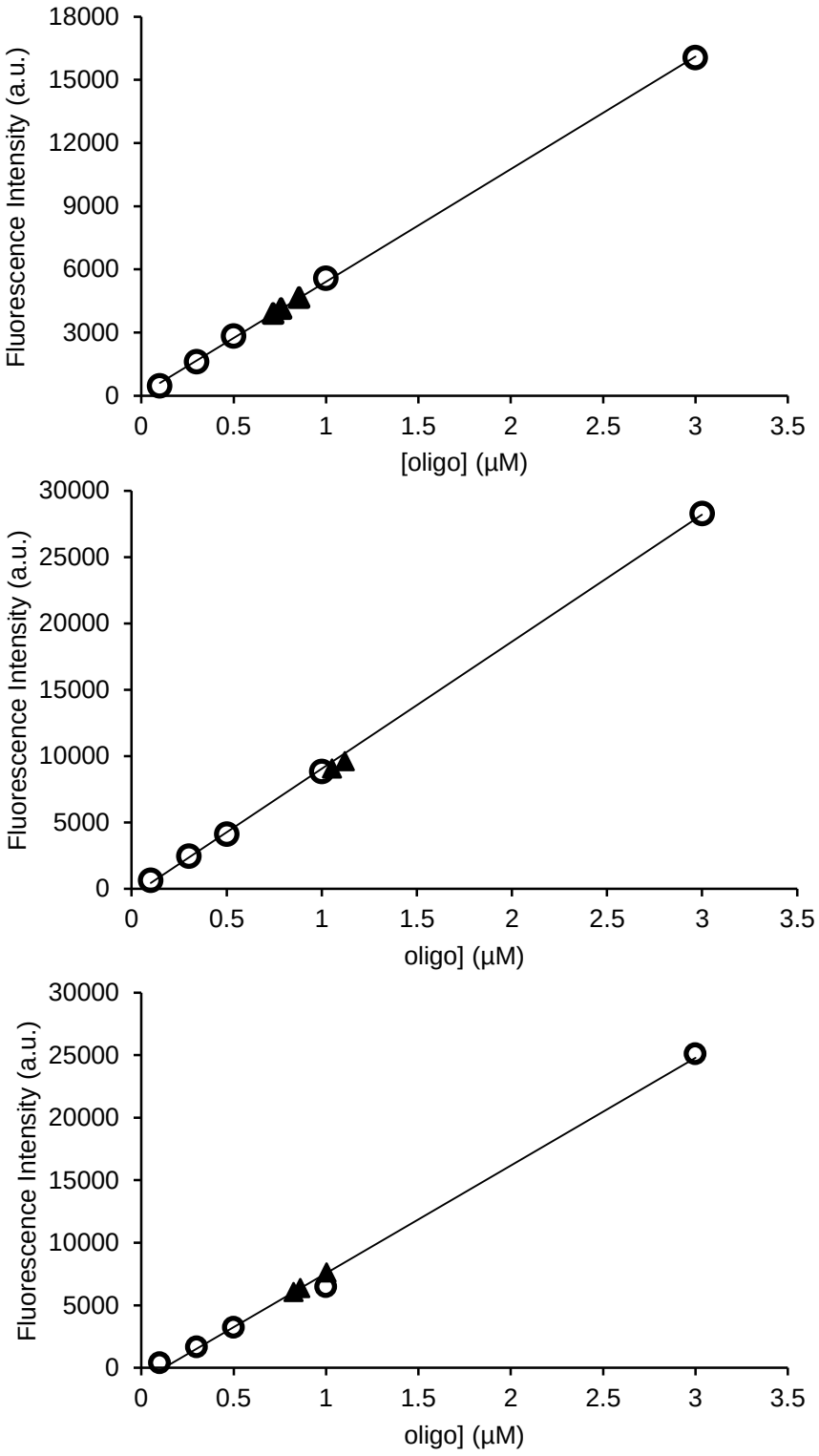

Figure A7. Oligonucleotides density – antisense, anti-siRNA and non-complementary Au-nanobeacons. Calibration curve of cy3-labeled oligonucleotides used in the synthesis of the antisense (circles, y = 5348.86x + 66.75, R^2=0.9996), anti-siRNA (circles, y = 9570.18x + 510.09, R^2=0.9997) and non-complementary (circles, y = 8615.91x + 1053.73, R^2=0.9961) Au-nanobeacons; and fluorescence intensities (λ_{exc}= 530 nm) measured in the supernatants of Au-nanobeacon (triangles). A ratio of 4.96 ± 0.66 oligonucleotides per gold nanoparticle was calculated.

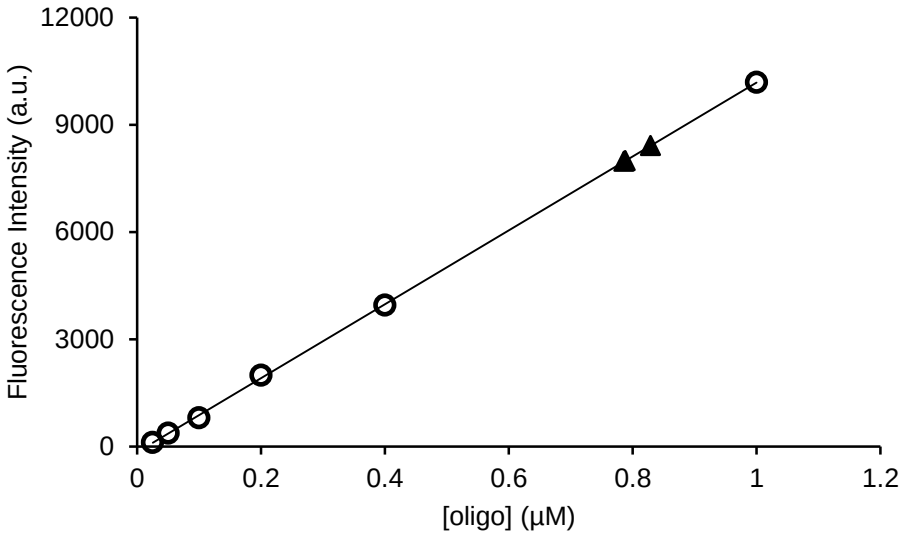

Figure A8. Oligonucleotides density – anti-miR21 Au-nanobeacon. Calibration curve of cy3-labeled oligonucleotides used in the synthesis of the anti-miR21 (circles, y = 10340.00x + 158.73, R2=0.9998) Au-nanobeacon and fluorescence intensities (λexc= 490 nm) measured in the supernatants of Au-nanobeacon (triangles). A ratio of 4.96±0.66 oligonucleotides per gold nanoparticle was calculated.

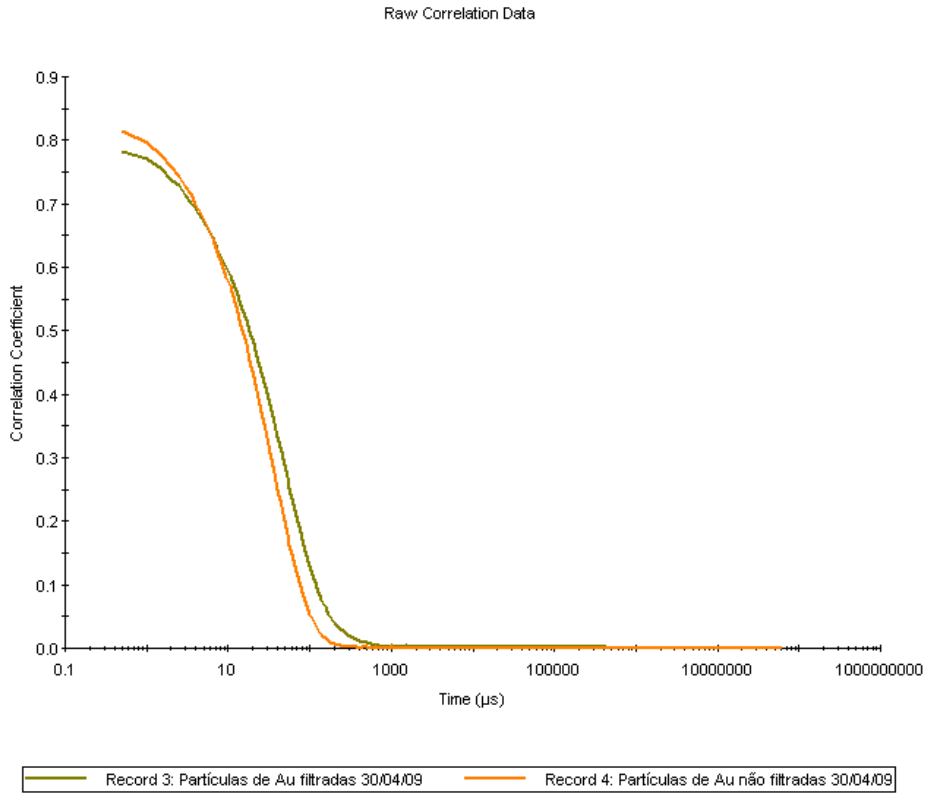

Sample Name:	Partículas de Au não filtradas 30/04/09		
SOP Name:	Manual measurement settings		
File Name:	joao rosa.dts	**Dispersant Name:**	Water
Record Number:	4	**Dispersant RI:**	1,330
Material RI:	0,47	**Viscosity (cP):**	0,8872
Material Absorbtion:	0,03	**Measurement Date and Time:**	quinta-feira, 14 de Maio de 2009

Temperature (°C):	25,0	**Duration Used (s):**	60
Count Rate (kcps):	309,0	**Measurement Position (mm):**	4,65
Cell Description:	Disposable sizing cuvette	**Attenuator:**	7

			Diam. (nm)	% Intensity	Width (nm)
Z-Average (d.nm):	21,5	**Peak 1:**	27,2	100,0	10,2
PdI:	0,225	**Peak 2:**	0,00	0,0	0,00
Intercept:	0,899	**Peak 3:**	0,00	0,0	0,00

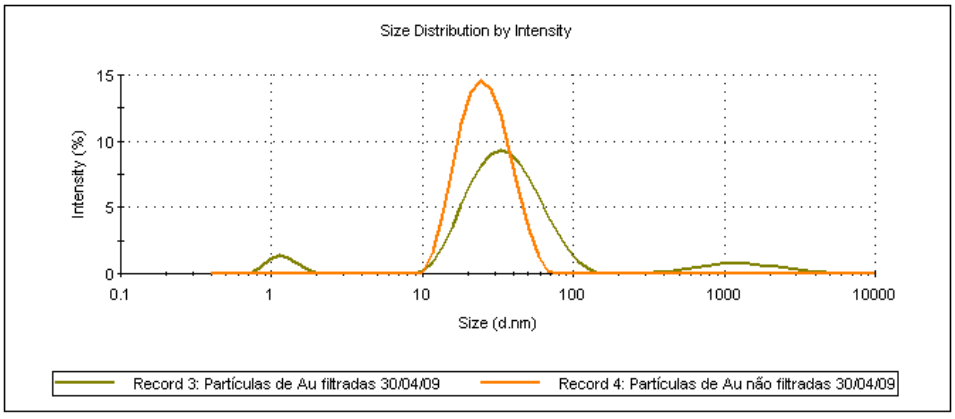

Figure A9. DLS measurement. DLS measurement of a sample of AuNPs.

Table A1. Quantification of the PEG chains and beacon for all Au-nanobeacons, together with DLS and Zeta-potential measurements.

Au-nanobeacons	PEG chains/NP	Hairpin DNA (Beacons)/NP	DLS Diameter (nm)	Zeta Potential (mV)
antisense Au-nanobeacon	190.29 ± 19.56	57.87 ± 3.92	33.95 ± 7.10	-36.53 ± 1.24
anti-siRNA Au-nanobeacon	190.29 ± 19.56	30.78 ± 4.84	40.77 ± 4.42	-37.73 ± 1.34
anti-miR Au-nanobeacon	190.29 ± 19.56	33.04 ± 2.99	52.65 ± 8.08	-21.87 ± 1.41
nonsense Au-nanobeacon	190.29 ± 19.56	31.64 ± 3.49	34.86 ± 1.21	-33.76 ± 2.37

To mimic the behaviour in the intra-cellular milieu, 1 nM of the Anti-miR-21 Au-nanobeacon was incubated with 5, 10 and 100 mM of DTT (Sigma-Aldrich) at 37°C for up to 24 h. Fluorescence intensity was measured in a PerkinElmer LS45 Fluorescence Spectrometer (Varian) using an Ultra-Micro quartz cell (Hëllma) programmed to incubate the reactions for 1440 min (24 hours) at 37°C at 15 minutes intervals (excitation/emission, 530 nm/560 nm).

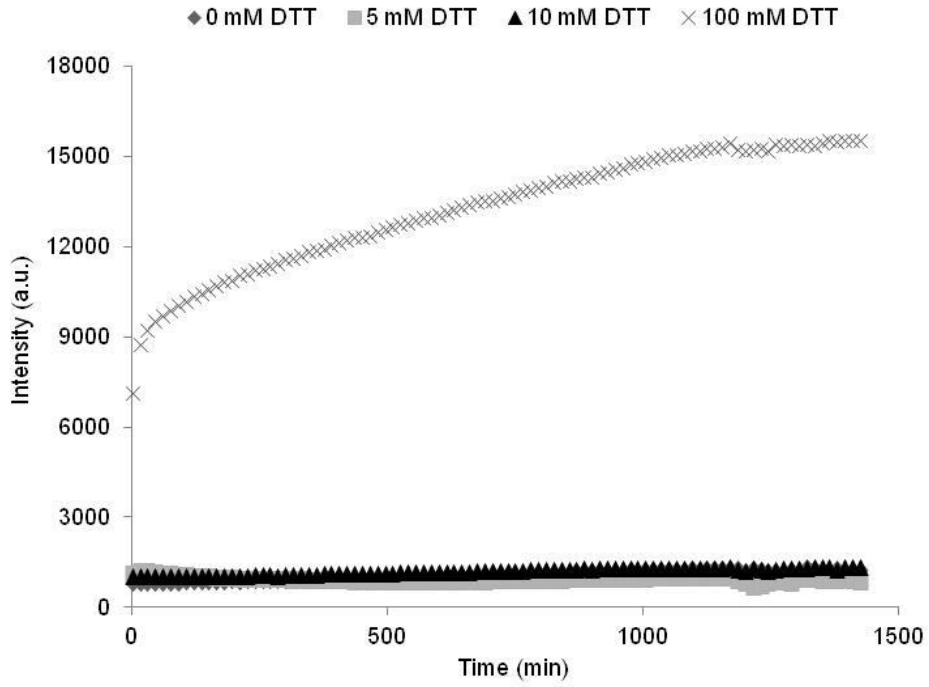

Figure A10. Au-nanobeacon behaviour in presence of increasing concentration of DTT (reducing agent). The anti-miR Au-nanobeacon was incubated with 5 mM (physiological concentration), 10 mM and 100 mM of DTT, at 37ºC during 24 hours, and fluorescence plotted as function of time. The curves show that for concentrations of reducing agent between 5 and 10 mM, the Au-nanobeacon remains in its closed conformation, which demonstrate that, under physiologic intracellular conditions, observable Au-nanobeacon fluorescence is solely due to hybridization to specific target.

APPENDIX III

Recovery of EGFP expression by ssRNA anti-antisense Au-nanobeacon

To evaluate EGFP recovery, 30 nM of ssRNA complementary to the Antisense Au-nanobeacon was added to the media together with 30 nM of the Au-nanobeacon with several delays of incubation (0.5, 1, 3, 6 and 24 hours). After 48 hours, EGFP fluorescence was evaluated as for the silencing experiments. Expression of the EGFP was confirmed by qRT-PCR analysis of transfected HCT-116 cells using β-actin as reference. Evaluation of EGFP recovery in bulk cell lysates following Antisense Au-nanobeacon silencing was performed by addition of 30 nM of anti-antisense ssRNA to the cell media with 30 nM of antisense Au-Nanobeacon at several delays of incubation (0.5, 1, 3, 6 and 24 hours). Bioactivity of anti-antisense ssRNA oligo was compared to that of a nonsense ssRNA oligo.

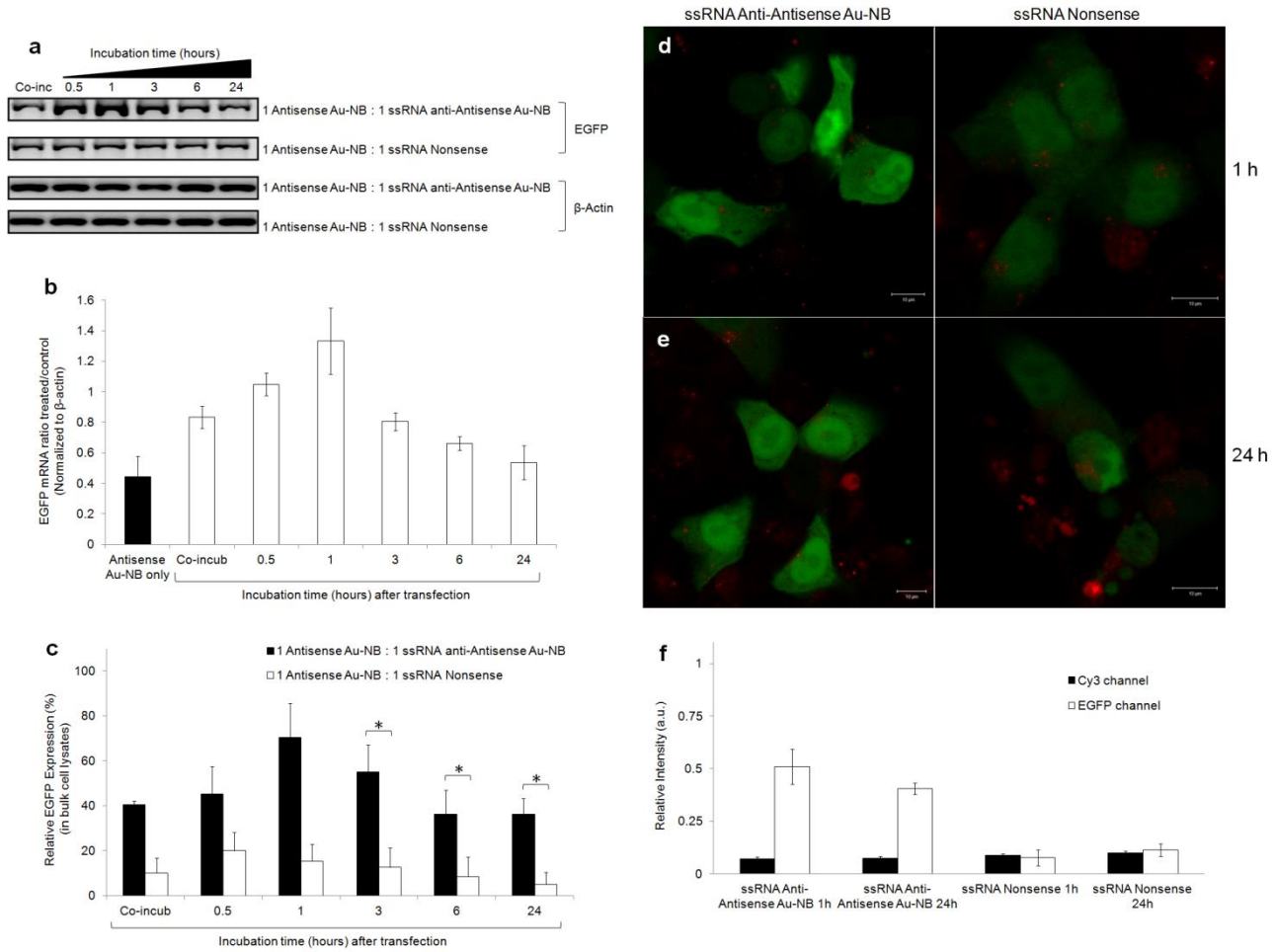

Figure A11. Recovery of EGFP expression by ssRNA anti-antisense Au-nanobeacon. Evaluation of EGFP recovery by (a,b) qRT-PCR and (c) in bulk cell lysates in presence of ssRNA oligo nonsense (grey bars), ssRNA oligo anti-antisense Au-Nanobeacon (black bars) indicating statistically significant difference as calculated by Paired-Sample T-test (asterisk, $P \leq 0.05$). Values are means ± s.d. from 3 independent experiments. Confocal imaging (scale bar, 10 μm) show EGFP recovery at (d) 1 and (e) 24 hours delay incubation. (f) blocking of Antisense Au-nanobeacon by ssRNA oligomer is corroborated by the relative fluorescence intensity of Au-nanobeacons (Cy3, black bars) and EGFP (white bars) after individual colour channel analysis of the same confocal images using ImageJ software.

Acute cytotoxicity evaluation by the MTT assay

Living cells' enzymes cleave the tetrazolium salts from the MTT reagent to yield formazan, which directly correlates to the number of metabolically active cells in culture. An expansion in the number of viable cells results in an increase in the overall activity of mitochondrial dehydrogenases, thus increasing the formation of formazan dye.

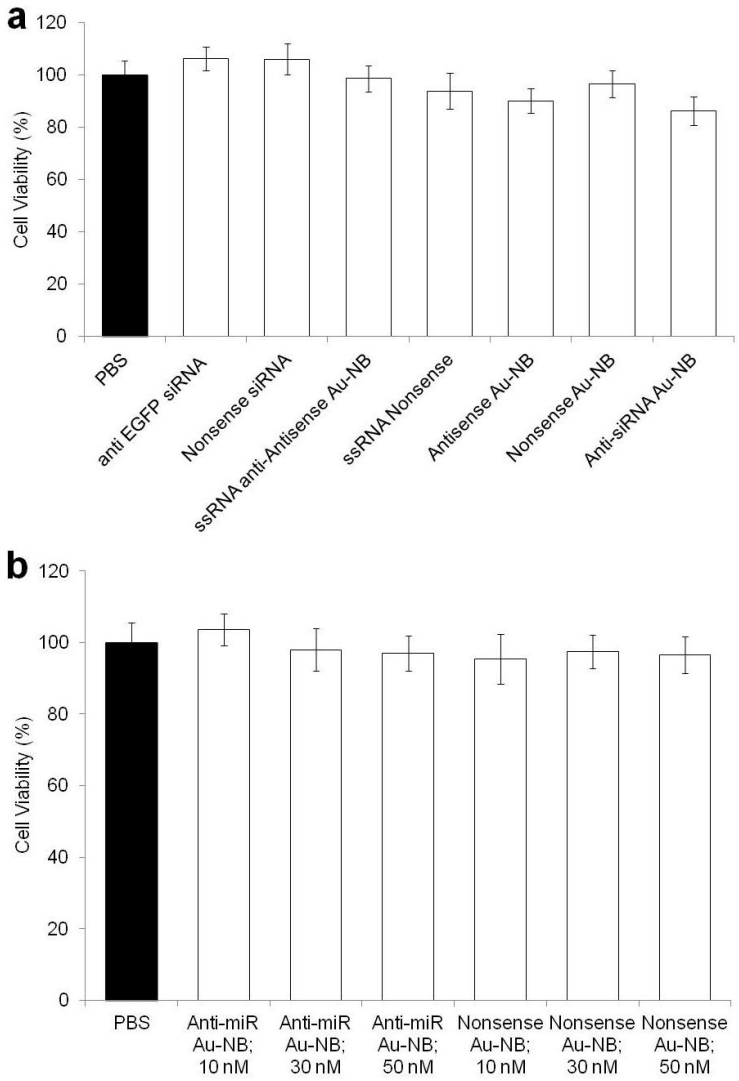

Figure A12. Cytotoxicity evaluation of the biomolecular assemblies administered to culture cells. Cytotoxicity evaluation of all biomolecular assemblies administered to human colorectal cancer cells (HCT-116 cell line) in the present study via the MTT assay at 48 (a) and 72 hours (b) of exposure. Negligible influence in cell viability is observed for all assemblies tested when compared to untreated cells (black bar).

APPENDIX IV

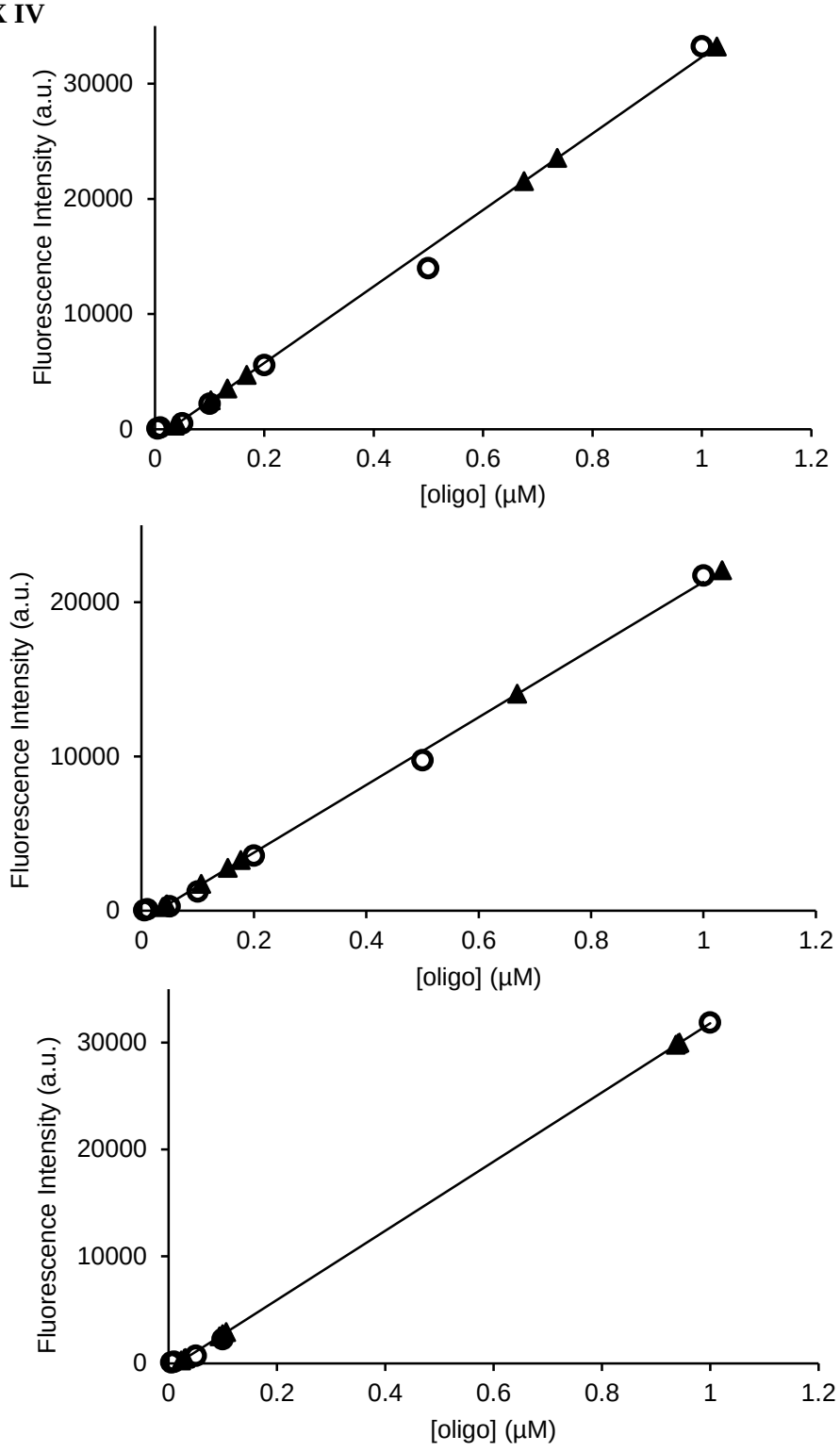

Figure A13. Quantification of the number of strands hybridised to WT1 Au-nanobeacon. Calibration curves of cy5-labeled oligonucleotides used in thedetermination of the number of strands hybridised to WT1 Au-nanobeacon in presence of WT1+KTS (circles, y = 33198.161x + 895.48, R^2=0.9943), WT1-KTS (circles, y = 21935.67x + 618.30, R^2=0.9968) and NEG2 (circles, y = 32343.26x + 549.55, R^2=0.9992), from top to bottom; and fluorescence intensities (λ_{exc}= 650 nm) measured in the supernatants of Au-nanobeacon (triangles).

APPENDIX V

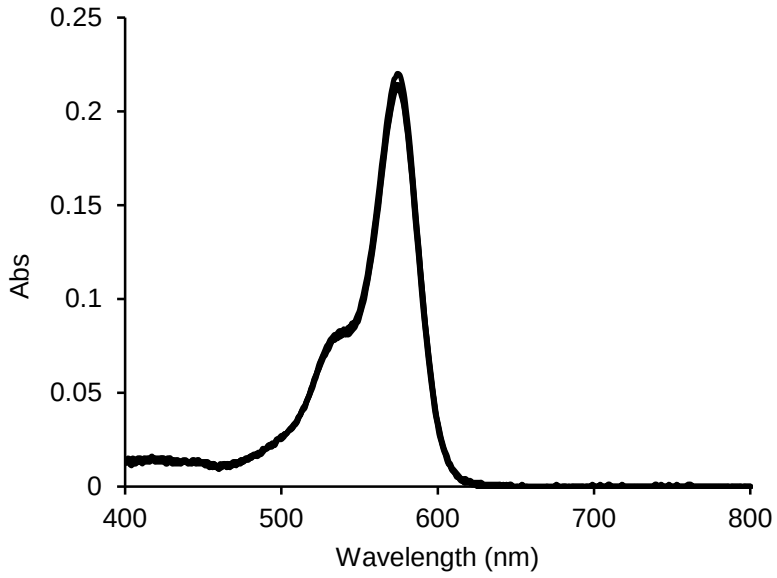

Figure A14. Titration of Rh101. Titration of Rh101 with citrate within a pH range of 5 to 8.